Development of a *Para*-hydrogen Delivery System for *in situ* SABRE with Low-Field NMR Detection

James M^{c}Call

Doctor of Philosophy

University of York

Chemistry

September 2025

Abstract

Low-field and benchtop Nuclear Magnetic Resonance (NMR) spectrometers offer significant advantages in terms of cost and accessibility, but their widespread application is limited by their inherently low sensitivity. Hyperpolarisation techniques like Signal Amplification By Reversible Exchange (SABRE) can overcome this limitation by boosting NMR signals by several orders of magnitude, creating new opportunities for chemical analysis and process monitoring outside of specialist laboratories. However, to realise this potential, methods for generating and measuring hyperpolarised signals must be robust and reproducible.

This work details the development of an automated *para*-hydrogen gas flow system to enable the probing of polarisation transfer and relaxation dynamics in SABRE. The system was developed to overcome the limitations of *ex situ* measurements, with applications for both *in situ* ultra-low-field studies and experiments on benchtop NMR spectrometers. The system provides reproducible *para*-hydrogen delivery with precise control over experimental parameters, enabling time-resolved studies of the hyperpolarisation process.

Application of this system to a solution of SABRE catalyst and pyridine enabled the indirect observation of *para*-hydrogen spin-order relaxation at the Earth's field. The decay of the hyperpolarised signal followed a biexponential model, dominated by a fast relaxation process ($t \approx 1-4\,\mathrm{s}$). This relaxation rate appears to be governed by the competitive exchange of ligands at the iridium catalyst, providing insight into the solution-state dynamics of *para*-hydrogen.

The utility and modularity of the polariser unit were further established by its integration with a 1.4 T benchtop spectrometer with an integrated motor-driven sample shuttle and capillary bubbling system. Software was developed for the motor system, spectrometer and user interface to make all components compatible for synchronous motor-driven polarisation transfer, bubbling and detection. This integrated hardware implementation demonstrates a viable pathway for performing advanced, automated SABRE experiments on accessible low-field platforms, moving beyond the limitations of manual sample handling.

Contents

List of Tables

List of Figures

Acknowledgements

I would like to thank my supervisor, Dr Meghan Halse, for giving me the opportunity to undertake this research project, and for all the support, direction, advice and endless patience across the course of this project. I have learned so much over the course of this project, and I am a better researcher for everything you've taught me. The last five years in the group have been excellent and I will miss being a part of it.

As part of this I am grateful to the University of York for the PhD studentship funding opportunity which allowed me to undertake the project.

From the Halse group, I would particularly like to thank Matheus and Alastair for their support and for his warm welcome to the group at the start of this project; Ana, who has been the most constant friendly presence for the duration of this project, Dan, for all his contributions, especially to my writing, and for his building the motor setup, and Fraser, whose work on the valves provided the starting point for much of the work presented here. I would also like to thank everyone else who has been part of the Halse group during my time as part of it: Dan, Izzy, Izzy, Greg, Alastair, Adrian, Luke, Aminata, Sam, Jonathan and Emma, as well as everyone else in PhysChem and CHyM. Everyone has made my time in the Halse group as enjoyable and fulfilling an experience as I could hope for, and I have learned so much from everyone.

I must acknowledge the use of Google Gemini for proofreading this report in line with the University Policy on Transparency in Authorship in PGR Programmes.

Outside the office, my deepest appreciation and gratitude to Lauren and Mum for all the proofreading and all the rest of the unwavering help and support they have given throughout, along with all the rest of my friends and family.

Author Declaration

I declare that this thesis is a presentation of original work and I am the sole author. This work has not previously been submitted for an award at this, or any other, University. All sources are acknowledged as References.

CHAPTER 1

Introduction

1.1 NMR

Nuclear Magnetic Resonance (NMR) spectroscopy is a powerful, non-invasive analytical technique that provides detailed information on molecular structure and dynamics. Its applications include medical imaging,[1] molecular structure elucidation,[2–5] reaction monitoring,[6–9] and mixture analysis.[10]

Relative to other spectroscopy techniques, such as optical spectroscopies and mass spectrometry, NMR is comparatively insensitive. This limitation arises from the weak Zeeman interaction between nuclear magnetic moments and an external magnetic field, B_0. The very small energy differences between the nuclear spin states result in a correspondingly small population difference between them, which is the ultimate source of the NMR signal. For routine ^{1}H NMR experiments, sample concentrations are typically in the millimolar (mM) range, while quantitative analysis of less sensitive nuclei like ^{13}C can require molar concentrations.

The sensitivity of an NMR experiment is fundamentally governed by the level of nuclear spin polarisation, P_0, which describes the fractional population difference between the spin states. For a spin-$I = \frac{1}{2}$ nucleus at thermal equilibrium, this polarisation can be estimated by the high-temperature approximation (Equation 1.1):

$$P_0 \approx \frac{\gamma B_0 \hbar}{2 k_B T} \tag{1.1}$$

where γ is the gyromagnetic ratio of the target nucleus, $\hbar$ is the reduced Planck's constant, k_B is the Boltzmann constant, and T is the temperature of the system. This relation-

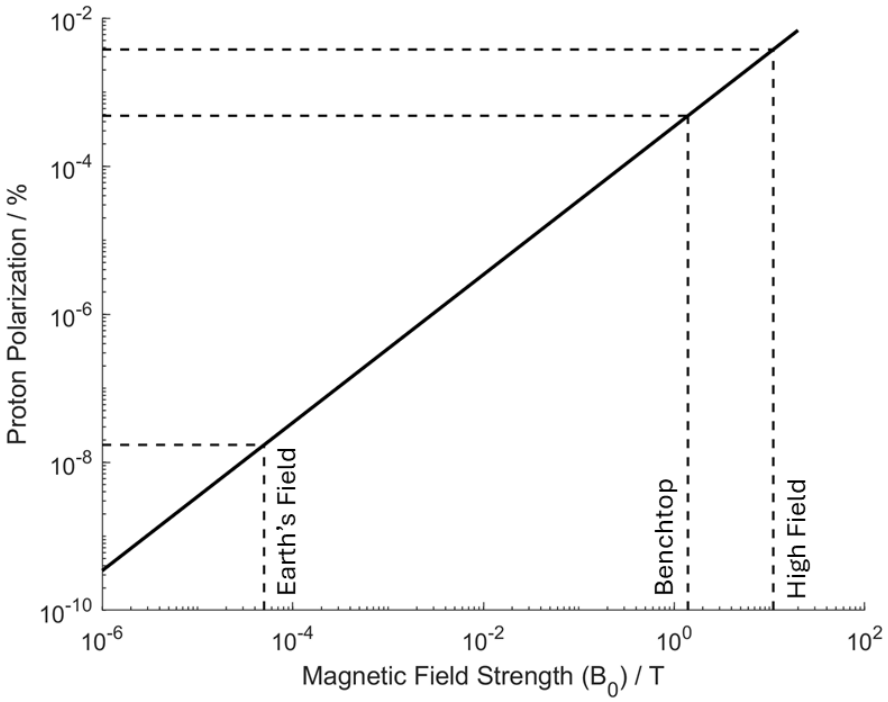

Figure 1.1: Plot of ^{1}H thermal polarisation $P_0/\%$ against field strength B_0 for field strengths 1 μT to 15 T at 298 K. Polarisation levels for detection fields relevant to this thesis are shown with dashed lines at 50 μT (Earth's field, 1.70×10^{-8} %), 1.4 T (typical benchtop field, 4.8×10^{-4} %), and 11 T (Typical high field, 3.8×10^{-3} %).

ship is fundamental to NMR, as it shows that polarisation, and therefore the observable signal strength, is directly proportional to the magnetic field strength B_0 and inversely proportional to the temperature T.

To make NMR more sensitive, a "brute force" approach is therefore often used, which involves using high-field instruments (commonly 7 - 11.2 T), with the strongest fields reaching up to 28.2 T.[11,12] These spectrometers boost sensitivity and give improved chemical shift resolution by further separating signals from different chemical environments. This is illustrated in Figure 1.1, which shows the thermal polarisation against field strength. Marked on Figure 1.1 are the thermal polarisations of nuclei at different detection fields for NMR instruments discussed in this thesis: Earth's field (50 μT), benchtop (1.4 T), and high field (11 T).

The highly homogeneous fields generated by these instruments, when combined with careful shimming, can yield very sharp spectral linewidths of less than 0.5 Hz, corresponding to a field homogeneity of better than 10 ppb on benchtop (1-2 T) or less than 1 ppb for a typical 500 MHz system. These fields are generated through the use of large, superconducting magnets. This makes these instruments expensive (with high costs for the instrument itself and for cryogens), complex to operate, and require a significant spatial footprint. This expense and complexity makes high-field NMR spectroscopy less than ideal in scenarios where budget, space, or access to specially trained personnel are limited. Consequently, there is demand for more compact, simpler, and more portable spectrometers.[13]

Benchtop spectrometers fulfil this need, typically operating at fields of 1-2.4 T with permanent magnets coupled with sophisticated shimming electronics.[13–17] This allows them to achieve highly homogeneous B_0 fields with homogeneity better than 10 ppb, yielding narrow spectral linewidths (< 0.5 Hz).[18–20] Benchtop spectrometers have found numerous applications in NMR[13,21] and MRI.[22] The reduced size makes benchtop NMR spectroscopy particularly useful for *in situ* reaction monitoring to study reaction completion, pathways and rates, as the instruments can be set up in fume hoods or integrated into a flow system for time-resolved spectroscopy.[23–25] Further to this, the external lock used in benchtop spectrometers also allows the use of standard non-deuterated solvents,[26] which further reduces the cost of consumables. However, the lower magnetic field of benchtop spectrometers introduces two primary challenges: reduced resolution and reduced sensitivity. Regarding resolution, the lower field strength results in fewer Hz per ppm in a spectrum compared to high-field counterparts. Consequently, J-coupling effects become dominant relative to chemical shift dispersion, leading to increased peak overlap. As the spectrum enters the strong coupling regime, second-order effects further distort the shape of coupled peaks. Regarding sensitivity, the lower field results in lower thermal polarisation (Equation 1.1). Polarisation is field-dependent and is very small under standard conditions, with a value of only 3.5 ppm T^{-1} for ^{1}H nuclei at room temperature. (the equivalent of 3.5 nuclei per million contribute to the observable NMR signal)[27] This limitation means that applications of NMR where sample concentration or volume is highly constrained can benefit significantly if signal sensitivity is decoupled from field strength.

Figure 1.2 shows a comparison of spectra for quinine recorded on high-field (top) and benchtop (bottom) spectrometers. In the high-field spectrum, signal dispersion is better and spectral linewidth on the chemical shift axis is narrower. The benchtop spectrum still provides clear structural information, albeit with more peak overlap due to the lower field strength.

1.2 Hyperpolarisation

Hyperpolarisation techniques are a class of methods used to enhance nuclear spin polarisation, creating a non-equilibrium state with greater polarisation than the thermal equilibrium at a given magnetic field and temperature. Most hyperpolarisation techniques generate this non-equilibrium state by transferring high spin order from a source to a target molecule. The simplest method is brute force hyperpolarisation, where a sample is polarised in a strong magnetic field and then rapidly moved to a weaker field for detection. The enhanced polarisation persists for a time dictated by the spin-lattice relaxation (T_1), allowing for sensitive detection at low field.[28] Other methods include Dynamic Nuclear Polarisation (DNP)[29,30], which uses the thermal polarisation of electrons as a source of spin order, and Spin-Exchange Optical Pumping (SEOP), which allows hyperpolarisation of noble gases,[31,32] useful especially in imaging applications[31,33,34] and biomedical NMR.[33]

Other hyperpolarisation techniques use *para*-hydrogen (p-H_2), a nuclear spin isomer of H_2 as their source of high spin order. These are called *Para*-hydrogen- Induced Polarisa-

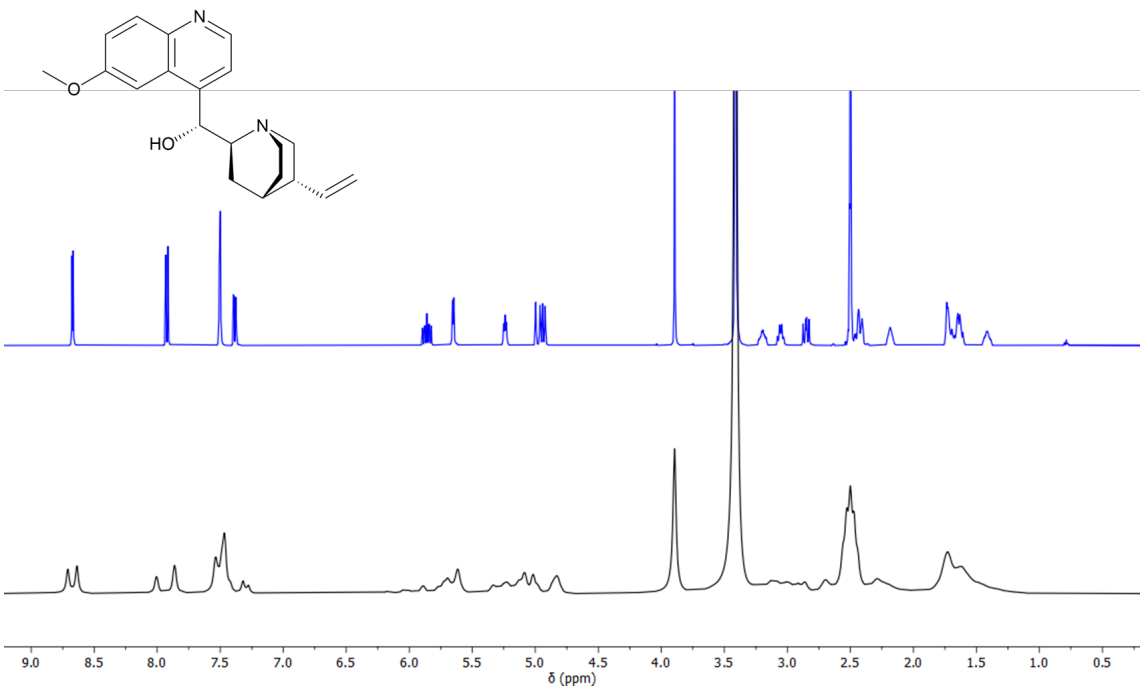

Figure 1.2: Comparison of ^{1}H NMR spectra of quinine recorded at high field (top, blue, 11 T, 1 scan), and low-field (bottom, black, 1.4 T, 16 scans). Spectra recorded by Dr. Daniel A. Taylor.

tion (PHIP) techniques. They are particularly useful as p-H_2 is inexpensive and simple to produce, and can be generated at point of use or stored with a long lifetime. The hyperpolarisation generated is not dependent on the B_0 field, allowing the use of less complex instrumentation.[35,36] PHIP can be carried out through hydrogenation reactions[37,38] or reversible catalytic spin exchange.[39] Hydrogenation reactions offer a simple, single-shot method to give strongly enhanced NMR signals via addition of p-H_2 to an unsaturated bond, supported by a hydrogenation catalyst such as platinum or iridium.[40–42]

1.3 SABRE

PHIP can also be performed non-hydrogenatively through a method called Signal Amplification By Reversible Exchange (SABRE).[43] This technique, like PHIP, relies on p-H_2 as the source of hyperpolarisation, but does not require chemical modification of the target analyte. Instead, a metal-centred catalyst is used to mediate the transfer of hyperpolarisation from p-H_2 to the target by simultaneously and reversibly binding them. In the presence of a weak magnetic field, known as the Polarisation Transfer Field (PTF), Level Anti-Crossings (LACs) occur between the nuclear spin states of the *para*-hydrogen-derived hydrides and the co-bound substrate.[44] This allows the transfer of spin order from p-H_2 to the substrate, mediated by the J-coupling network, to give enhanced NMR signals. The exchange and transfer process is illustrated in Figure 1.3 and explored in more detail in Chapter 2.

The reversibility of the substrate and p-H_2 binding enables replacement of the ther-

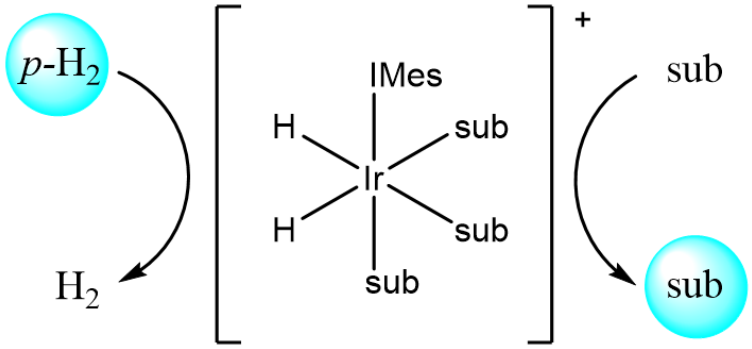

Figure 1.3: The SABRE (Signal Amplification By Reversible Exchange) cycle. The active SABRE catalyst is $[Ir(IMes)(H)_2(sub)_3]^+$,where IMes = 1,3-Bis(2,4,6-trimethylphenyl)-1,3-dihydro-2H-imidazol-2-ylidene. High spin order *para*-hydrogen and a target substrate (sub), commonly pyridine, reversibly bind to the iridium centre on the catalyst. This high spin-order, highlighted in blue, is transferred from the p-H_2 to the substrate through the J-coupling network. the hyperpolarised substrate dissociates resulting in a build-up of hyperpolarised substrate in solution, and allowing exchange of fresh p-H_2 and substrate to the catalyst.

mally polarised hydrides (depleted of hyperpolarisation due to transfer) and hyperpolarised substrate with fresh p-H_2 and thermally polarised substrate. This process allows for the continuous build-up of hyperpolarised substrate in solution from a single sample, provided there is a constant supply of p-H_2. Consequently, SABRE has a broader range of suitable target molecules compared to PHIP, as they are not required to contain an unsaturated bond for hydrogenation, but only need the ability to bind reversibly to the metal catalyst.

SABRE was first demonstrated in 2009 by Adams *et al.*,[43] by charging an NMR tube with *para*-hydrogen and shaking in the stray field of a high field magnet before detection. This method is very effective and simple to carry out. Since the initial demonstration, an improved understanding of the reaction mechanism has driven several developments including improved catalysts,[45,46] dedicated PTF magnet arrays for more efficient transfer[47], and a significant broadening of substrate range through processes such as SABRE-SHEATH for heteronuclear hyperpolarisation[48] and SABRE-Relay, which allows SABRE hyperpolarisation through labile H exchange without requiring the target to directly bind to the catalyst.[49] The ongoing development of SABRE has allowed it to find practical applicability for reaction monitoring,[50,51] and forensics,[52,53] and progress towards clinical imaging.[54]

Performance of SABRE through the manual shake-and-drop method is limited by poor control and reproducibility, even if an operator has had significant practice. Automated systems allow a much more precise level of control, enabling automated, timed experiments (for example, for 2D NMR) with faster and more reproducible transfer than manual methods. This includes shuttling systems,[55–58] and flow systems[59,60], which allow for integration of SABRE into flow chemistry[61]. For these systems, with polarisation transfer outside the detection region of the magnet (*ex-situ*), travel time (even if rapid) obscures the observation of very fast relaxation dynamics which occur post p-H_2 delivery of post transfer. Transfer through inhomogeneous magnetic field can potentially

cause unwanted polarisation transfer or relaxation, such as has been shown in d-DNP[62] Polarisation transfer fields for *ex-situ* systems can be generated through stray field or permanent magnets as above, or through the use of electromagnets[48,52,59,60,63] and mu-metal shields,[48,64,65] which allow a controllable transfer field to be applied. With stable, controllable fields, field-sweep experiments can be performed allowing the optimisation of the PTF to a target substrate.[47]

One way of avoiding sample transfer is to recreate the conditions required for SABRE polarisation transfer in the bore of the magnet using calibrated radiofrequency (RF) pulses. By manipulating the effective fields, these pulses create a Level Anti-Crossing (LAC) in the rotating frame, allowing polarisation to transfer. This process, referred to as RF-SABRE,[66] eliminates shuttling entirely, simplifying hardware and allowing for straightforward implementation of multi-scan experiments. While powerful, RF-SABRE does not allow direct exploration of the spin dynamics in the native ULF/mT regime where spontaneous polarisation transfer is most efficient. Enhancements in RF-SABRE are lower than those achieved with optimised low-field transfer, and the transfer is much less efficient than its spontaneous counterpart, reducing the effectiveness of these methods.[66,67]

To analyse SABRE polarisation transfer occurring spontaneously in its native state, ultra-low-field (ULF) detection methods are required. Low field SABRE has been performed by several groups. Barskiy *et al.*[68–70] studied the kinetics of polarisation transfer and demonstrated SABRE-based imaging at 5.75 mT, at which SABRE transfer occurs. More recent work has focused on detecting SABRE signals directly at zero- and ultra-low-field using magnetometers such as superconducting quantum interference devices (SQUIDs)[71,72] or optically pumped magnetometers (OPMs) to observe couplings to natural abundance heteronuclei,[64,71,73] or by using the Earth's magnetic field. Hill-Casey *et al.*[74] used Earth's Field NMR (EFNMR) to study the activation of the SABRE catalyst, the build-up of signal in the polarisation transfer field (PTF), the dependence of the hyperpolarisation level on the strength of the PTF, and the rate of the hyperpolarisation's decay in the ultra-low-field regime. The work in this thesis follows on from Hill-Casey's developments. These papers use a variety of complex, custom instrumentation for p-H_2 delivery for their own particular setups. This thesis aims to develop a simple, flexible apparatus for p-H_2 delivery, compatible with a variety of instruments. This will allow the exploration of SABRE mechanics in the Earth's field/ultra-low-field regime using inexpensive, accessible instrumentation. Comparable studies can be conducted on benchtop instruments, where shuttling mechanisms can be implemented to access homonuclear chemical shift information. With the instrumentation platform developed in this thesis, it would also be possible to use in other spectrometers with appropriate B_0 fields to probe SABRE dynamics while polarisation transfer is occurring. A method for *in-situ* exploration of SABRE dynamics is needed, with gas delivery and field application as a controllable part of the NMR experiment, coupled to a low-field detector in which the rapid processes around p-H_2 interaction and polarisation transfer can be observed. The ability to directly and systematically observe SABRE dynamics (both polarisation build-up and subsequent relaxation) in-situ will allow for a deeper understanding of SABRE mechanisms, kinetics, and relaxation phenomena, essential for optimising the technique for future applications.

1.4 Project Goals and Thesis Outline

The primary goal of this project is to develop, implement, and optimise a system for performing *in situ* and shuttled SABRE experiments across a variety of NMR systems. It will be implemented for the direct exploration of SABRE relaxation dynamics in the Ultra Low Field (ULF) regime. This work aims to improve the fundamental understanding of SABRE and provide methodologies to more effectively implement the technique in a variety of systems.

Chapter 2 gives a background overview of NMR fundamentals and instrumentation, hyperpolarisation, and provides a detailed theoretical framework for the SABRE mechanism, including its kinetics and spin dynamics.

Chapter 3 details the design, construction, and validation of the core instrumentation developed for this research: a versatile and electronically controllable para-hydrogen delivery system, or "polariser unit". It also outlines the hardware, including the p-H_2 generator and electronic valve network, and the software developed to provide precise, automated gas flow in time with an NMR pulse sequence. The system's functionality, including pressure monitoring and leak testing protocols, is thoroughly characterised to establish its robustness for subsequent experiments.

In Chapter 4, the polariser unit is integrated with a commercial Earth's Field NMR (EFNMR) spectrometer to create a complete platform for in-situ SABRE studies. A series of optimisation experiments are performed to establish a robust methodology for achieving consistent para-hydrogen concentration and maximum reproducible signal enhancement. It also details the use of Magnetic Resonance Imaging (MRI) to investigate gas mixing dynamics within the reaction cell and evaluates strategies, such as an in-line solvent reservoir and overnight nitrogen pressurisation, to extend sample lifetimes.

With this validated methodology, Chapter 5 applies the *in situ* SABRE system with EFNMR detection to investigate the relaxation dynamics of para-hydrogen in a SABRE solution at the Earth's magnetic field. The dependence of this relaxation process on reactant concentrations is explored to determine the origin of the complex relaxation dynamics of p-H_2 in solution.

Chapter 6 demonstrates the versatility and modularity of the polariser unit by adapting it for use with a 1.4 T benchtop NMR spectrometer. This section details the necessary hardware modifications, including a specialised capillary bubbling cell for a 5 mm NMR tube, and the development of a semi-automated control system for instruments lacking TTL capability. Furthermore, the design and implementation of a motor-driven shuttling system is presented, enabling the performance of SABRE with spontaneous polarisation transfer and benchtop detection.

Finally, Chapter 7 presents the conclusions of this work, summarising the key instrumental developments and scientific findings. It also discusses the implications of the observed relaxation phenomena and outlines opportunities for future research, including further development of the shuttling system and its application to higher field studies.

CHAPTER 2

Background Theory

2.1 Fundamentals of NMR

Elementary particles have a quantised intrinsic angular momentum, or "spin". Composite particles, including protons and neutrons, thus also have an intrinsic spin, as do atomic nuclei, made of protons and neutrons. An atomic nucleus has its spin described by quantum number I, taking half-integer and integer values. The total intrinsic angular momentum of a nucleus $\hat{\mathbf{I}}$ is a vector which can be decomposed into Cartesian direction components, $\hat{I}_x, \hat{I}_y$ and $\hat{I}_z$.

$$\hat{\mathbf{I}}^2 = \hat{I}_x^2 + \hat{I}_y^2 + \hat{I}_z^2. \tag{2.1}$$

Nuclei with a non-zero spin ($I \neq 0$) also have a magnetic moment, $\hat{\mu}$. $\hat{\mu}$ is proportional to the spin angular momentum $\hat{\mathbf{I}}$, with the gyromagnetic ratio γ as the constant of proportionality. This ratio is a unique property of each isotope with non-zero spin.

$$\hat{\mu} = \gamma \hat{\mathbf{I}} \tag{2.2}$$

Magnetic moments interact with magnetic fields. A magnetic moment, placed in an external magnetic field $1B$, will precess about the external field axis at an angular frequency ω. The corresponding Larmor frequency, ν_{Larmor} (in Hz), is described by Equation 2.3.

$$\nu_{Larmor} = \frac{\omega}{2\pi} = \frac{|\gamma B|}{2\pi} \tag{2.3}$$

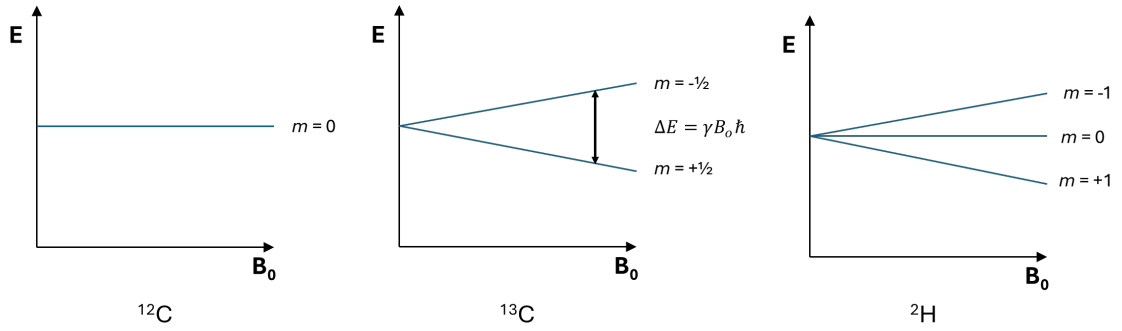

Figure 2.1: Zeeman levels of nuclei with various spins. Left: Nucleus with spin quantum number $I = 0$, such as ^{12}C. Centre: Nucleus with spin quantum number $I = \frac{1}{2}$, such as ^{13}C. Right: Nucleus with spin quantum number $I = 1$, such as ^{2}H.

Magnetic fields cause the spin states to become non-degenerate, and separate into discrete energy levels. This is called Zeeman splitting. A nucleus with spin I will split into $2I+1$ discrete energy levels or spin states (hence at $I = 0$, $2I + 1 = 1$, giving one energy level, and no splitting). Instead of simply aligning with or against the a magnetic field B_0 (usually B_0 denotes the main, static magnetic field), each magnetic moment experiences a torque. Due to their angular momentum, this torque causes them to precess around the B_0 field. The energy of each spin state, E_m, can be calculated through Equation 2.4, where m is the magnetic quantum number, taking values from $-I$ to $+I$ (where I is the spin quantum number), γ is the gyromagnetic ratio, B_0 is applied magnetic field strength, and $\hbar$ is the reduced Planck constant. Figure 2.1 illustrates the splitting of spin state energy levels for various nuclei as B_0 field is applied.

$$E_m = -m\gamma B_0\hbar \tag{2.4}$$

A spin-$\frac{1}{2}$ nucleus with positive γ (for example, ^{1}H, ^{13}C) therefore has two energy levels at $m = +\frac{1}{2}$ and $m = -\frac{1}{2}$. The lower energy state ($m = +\frac{1}{2}$) is aligned with the external field and is commonly referred to as "spin-up" or α. Conversely, the higher energy state ($m = -\frac{1}{2}$) is opposed to the field and referred to as "spin-down" or β. The energy difference between these states is $\gamma B_0\hbar$ (equation 2.5). This is the energy required for a transition between the two spin states. For nuclei with a negative γ, spin-down (β) is the lower energy state.

and the higher energy spin state β. While nuclei with higher spin numbers have additional transitions, the remainder of this discussion will focus on the spin-$\frac{1}{2}$ case for clarity.

$$\Delta E_{\alpha\to\beta} = \hbar\gamma B_0 \tag{2.5}$$

Planck's equation, equation 2.6, can be used to calculate the frequency of this transition, as shown in equation 2.7: the Larmor equation. Units of frequency (ν/Hz) and angular frequency (ω/radians s^{-1}), can be interconverted using $\omega = 2\pi\nu$.

$$E = h\nu = \hbar\omega \tag{2.6}$$

$$\omega = \gamma B_0 \tag{2.7}$$

The Larmor equation shows that the frequency of a spin-state transition is only dependent on the gyromagnetic ratio of the nucleus and the local magnetic field. For nuclei of the same type, only the local magnetic field will impact the frequency of this transition. Within a molecule, the local magnetic field is impacted by shielding effects, in which electrons induce a small, opposing magnetic field to an applied magnetic field.

2.1.1 Chemical shift

Nuclei of the same isotope at different positions in a molecule are differently shielded depending on the electron density at their nucleus, and so have different Larmor frequencies. For example, proximity to strongly electronegative oxygen or fluorine (-OH, -CHF_2 groups) reduces electron density. This is de-shielding, and will raise the Larmor frequency of local H nuclei, while shielding groups, such as long chain alkanes will lower Larmor frequency. Additionally, shielding is influenced by neighbour anisotropy effects, where circulation currents in adjacent bonds create direction-dependent magnetic fields. This is expressed in equation 2.8[3,75], where B_{local} is the local field experienced by the nucleus, B_0 is the main magnetic field and σ is the shielding constant.

$$B_{local} = B_0(1 - \sigma) \tag{2.8}$$

Larger values of σ correspond to greater shielding. Substituting Equation 2.8 into the Larmor equation (2.7) gives the relationship between frequency and ω and B_{local}:

$$\omega = \gamma B_{local} = \gamma B_0(1 - \sigma) \tag{2.9}$$

This dependency shows that the frequency of nuclei with the same σ varies depending on the applied field B_0. This means that nuclei observed at different B_0 frequencies will appear differently spaced at different B_0. To account for this, a chemical shift (δ) scale can be used. Chemical shift expresses resonance frequency relative to a standard reference compound, making its value independent of B_0. Chemical shift in ppm is calculated following equation 2.10, where ω_{sample} is the taregt nucleus frequency, ω_{ref} is the frequency of the reference, and ω_{spec} is the spectrometer frequency. The factor of 10^6 gives the value in parts per million (ppm).

$$\delta(\text{ppm}) = \frac{\omega_{sample} - \omega_{ref}}{\omega_{ref}} \times 10^6 \tag{2.10}$$

This cancels out the dependence on B_0 and gives a single δ value for a nucleus in a given chemical environment. Nuclei which are more shielded (larger σ) have larger positive δ values.

2.1.2 *J*-coupling

So far, we have been considering an ensemble of independent spins. In practice, nuclei exist within molecules, connected by bonds. Magnetically active nuclei can influence each other through bonds in an interaction called J-coupling or scalar coupling. This interaction is not a direct through-space effect. Instead, the magnetic moment of one nucleus polarises its surrounding bonding electrons. Because these electrons are shared in a chemical bond with a neighbouring nucleus, this polarisation is transmitted, slightly altering the local magnetic field experienced by that neighbour. The effect is mutual and its magnitude is given by the coupling constant, J.[2,75,76]

Take an $I = \frac{1}{2}$ nucleus **A** coupled to n chemically equivalent nuclei **X** with $I = \frac{1}{2}$, while in a magnetic field B_0. The nucleus in environment **X** can be either spin-up or spin-down. Nuclei in environment **A** will experience a small addition to the main B_0 field when **X** is spin-up, and a small reduction when **X** is spin-down. Across an entire sample of molecules containing AX_n, the spin-up and spin-down states of **X** will be approximately equally populated. The Larmor frequencies of nucleus A will therefore be split approximately equally into $n + 1$ peaks centred at δ_A, with a separation of J_{AX} Hz, with the relative intensity of the lines following Pascal's triangle, due to the different possible combinations of the **X** spin states. For example, if $n = 3$, A will be split into a quadruplet (4 peaks) with intensity ratio 1:3:3:1.

This only applies when the chemical shift difference ($\Delta\nu$) is much larger than the coupling constant J. This is the weak coupling regime. For coupling between two nuclei A and X the condition for weak coupling is:

$$|\nu_A - \nu_X| \gg |J_{AX}| \tag{2.11}$$

When the chemical shift difference ($\Delta\nu$) is on a similar order of magnitude to the coupling constant (J), the system enters the strong coupling regime. Under these conditions, the simple first-order analysis is no longer sufficient; the simple first-order splitting rules (e.g., the $n + 1$ rule) are no longer valid, and the relative intensities of peaks no longer follow simple statistical patterns like Pascal's triangle. Multiplets become more complex, often exhibiting second-order patterns with distorted intensities. A "roofing" effect also becomes prominent, where the inner peaks of two coupled multiplets are enhanced relative to the outer peaks.

This complexity arises because the individual spin states can no longer be considered independent and the secular approximation, used to simplify the Hamiltonian at high field, breaks down. Under strong coupling, the Zeeman product states (e.g., $|\alpha\beta\rangle$ and $|\beta\alpha\rangle$) become mixed, leading to new eigenstates and allowing for transitions that are forbidden under weak coupling conditions. These second-order effects require analysis using the full spin Hamiltonian. Because the chemical shift difference $\Delta\nu$ (in Hz) scales with the external magnetic field B_0, while J does not, strong coupling effects are most pronounced in spectra acquired at lower field strengths.[77,78]

2.2 Vector model

While the previous section treats the fundamental interactions that govern individual and coupled nuclei in magnetic fields, an approach is needed to treat the millions of nuclei in a sample as a single ensemble. The vector model is a semi-classical model that achieves this by considering the vector sum of all individual nuclear magnetic moments. This yields a single bulk or net magnetisation vector, $\mathbf{M}$.

In the absence of an external magnetic field, the individual magnetic moment vectors are randomly oriented, and thus their vector sum is zero. When an external magnetic field, B_0, is applied (conventionally along the z-axis), it becomes slightly energetically favourable for spins to align with the field. This creates a small population excess aligned with B_0, resulting in a net equilibrium magnetisation, M_0, directed along the z-axis.

The individual spins still precess around the B_0 field at the Larmor frequency, ω_0. However, at equilibrium, the phase of this precession is random for each nucleus. Consequently, the individual magnetic moment components in the transverse (xy) plane are randomly oriented and their vector sum is zero. At equilibrium, the net magnetisation has only a longitudinal component ($M_z = \mathbf{M} = M_0$) and no transverse component ($M_{xy} = 0$). As there is no rotating transverse component, no signal can be detected.

To generate a detectable signal, a non-zero transverse component (M_{xy}) must be created. This is achieved by applying a second, oscillating magnetic field, B_1, perpendicular to B_0. This field, known as the radiofrequency (RF) pulse, applies a torque to the net magnetisation vector. This pulse is critical because it not only tips the magnetisation vector away from the z-axis but also forces the individual spins to begin precessing with the same phase. This creation of phase coherence is what allows a non-zero M_{xy} component to form.

The behaviour of $\mathbf{M}$ under the influence of both B_0 and B_1 can be difficult to visualise. To simplify this, it is convenient to switch from the static "laboratory frame" of reference to a "rotating frame" of reference. This frame is defined by a set of Cartesian axes (labelled x', y', z') that rotates around the lab frame's z-axis at the Larmor frequency, ω_0. In this rotating frame, the precessing magnetisation vector appears static, making the effect of the B_1 pulse much easier to follow. The two frames are illustrated in Figure 2.2.

The angle of rotation, θ, (also called the flip angle) is determined by the gyromagnetic ratio (γ) of the nucleus, the amplitude of the B_1 field, and the pulse duration, t:

$$\theta = \gamma B_1 t \tag{2.12}$$

For example, a pulse with a flip angle of $\theta = \frac{\pi}{2}$ radians, or 90°, is known as a 90° pulse. If this pulse is applied along the y'-axis of the rotating frame, it rotates the magnetisation vector entirely into the transverse plane. Starting with $M_z = M_0$, after the 90° pulse, the net magnetisation vector will lie along the $-x'$ axis. The longitudinal magnetisation becomes zero ($M_z = 0$), and the magnitude of the transverse magnetisation is now at its maximum, equal to the initial equilibrium magnetisation, $|M_{xy}| = M_0$. This rotation is

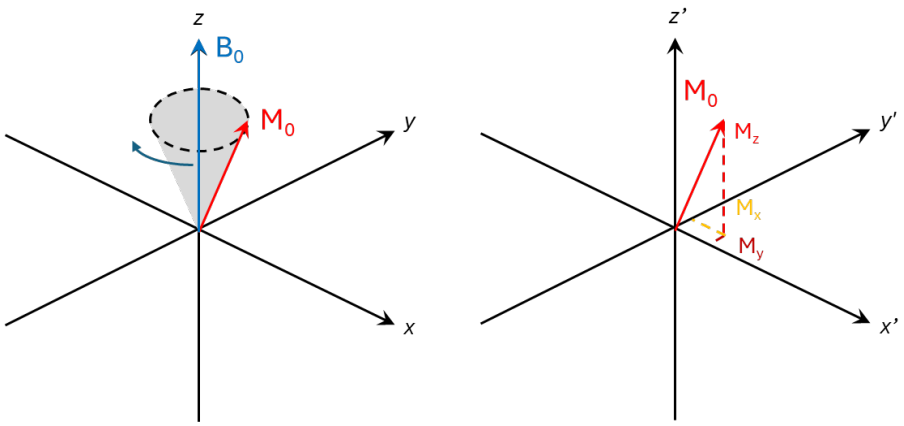

Figure 2.2: Representation of the vector model of net magnetisation M_0 precessing about B_0. Left: Shown in the laboratory frame (x,y,z). Right: shown in the rotating frame (x', y', z'), which rotates at the Larmor frequency. In the rotating frame, the precessing vector appears stationary.

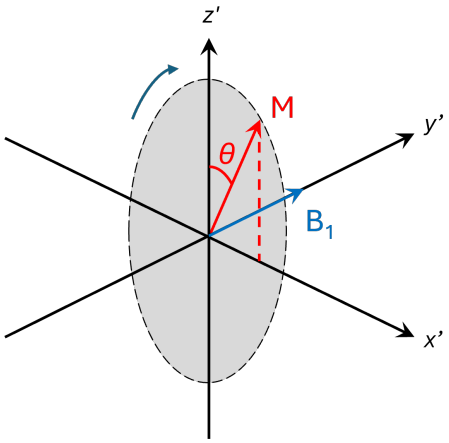

Figure 2.3: Rotation of the net magnetisation vector **M** in the rotating frame under an applied field B_1. The B_1 field is applied along the y'-axis, causing the magnetisation vector (initially along z') to rotate by an angle θ in the z'x' plane.

illustrated in Figure 2.3. The relationship between the transverse component and the flip angle is given by:

$$|M_{xy}| = M_0 \sin(\theta)$$

The vector model effectively describes the manipulation of the bulk magnetisation vector to produce a detectable signal. The amplitude of this signal is fundamentally constrained by the initial magnitude of the equilibrium magnetisation, M_0. Before this vector can be manipulated by radiofrequency pulses, it must first be established from a sample of randomly oriented nuclear spins. The following section will therefore examine the physical process responsible for creating this initial net magnetisation: the polarisation of nuclear spins within the static magnetic field, B_0.

2.2.1 Polarisation

The energy difference between nuclear spin states is very small. Consequently, at thermal equilibrium, both the lower and higher energy states are significantly populated. The probability p_m of a given spin state m being occupied is governed by the Boltzmann distribution, shown in Equation 2.13, where E_m is the spin state Zeeman energy, k_B is the Boltzmann constant and T is temperature.[3]

$$p_m = \exp \frac{-E_m}{k_B T} \tag{2.13}$$

The exact polarisation P_0 for a spin-$\frac{1}{2}$ system can be expressed using the hyperbolic tangent function:

$$P_0 = \tanh\left(\frac{\Delta E}{2k_B T}\right) = \tanh\left(\frac{\gamma B_0 \hbar}{2k_B T}\right) \approx \frac{\gamma B_0 \hbar}{2k_B T} \tag{2.14}$$

At temperatures and magnetic fields typically used in NMR, the magnetic energy is much smaller than the thermal energy, meaning the argument of the hyperbolic tangent is very small ($|\gamma B_0 \hbar| \ll 2k_B T$). In this high-temperature regime, we can use the linear first - order Taylor approximation: $\tanh(x) \approx x$ for small values of x. This simplifies the expression for polarisation to the approximation given in the introduction (Chapter 1), in Equation 1.1.

Equation 2.14 gives the number of nuclei which contribute to M_0, the number of excess nuclei in the more highly populated state. For example, at 298 K in a B_0 field of 1 T, $P_0 = 0.0000035$, or 3.5 ppm; this means the observed M_0 is the statistical equivalent of 3.5 nuclei in every million contribute constructively to the net magnetisation of the ensemble, with the remainder cancelling out.

2.2.2 NMR Detection

Once the net magnetisation (M_0) has been manipulated to create a precessing transverse component (M_{xy}), the final step is to understand how this magnetisation is detected and how it returns to equilibrium. The detection process is governed by Faraday's Law of Induction, which states that a changing magnetic field will induce a voltage in a nearby coil.

The precessing M_{xy} vector acts as a tiny rotating magnet. As its magnetic field sweeps past a receiver coil, the changing magnetic flux induces a small, oscillating voltage. This is the raw NMR signal, known as the Free Induction Decay (FID). As its name suggests, the FID is not a continuous wave; it decays over time. This decay is a direct consequence of two simultaneous relaxation processes, which describe how the spin system releases the energy it absorbed from the RF pulse and returns to thermal equilibrium. These processes dictate the shape and duration of the FID and are therefore critical to understanding the appearance of the final NMR spectrum.

Finally, the spectrometer's electronics amplify this faint FID. A mathematical procedure, the Fourier Transform, is then applied to convert this time-domain signal (the FID) into the familiar frequency-domain spectrum, where each unique Larmor frequency appears as a distinct peak.

2.2.3 Relaxation

The B_1 pulse rotates the net magnetisation vector away from the z' axis. Once the pulse ends, the vector begins returning to thermal equilibrium. This process involves two distinct and simultaneous relaxation mechanisms: the spin-lattice recovery of the longitudinal component (M_z) back towards its equilibrium value along the z-axis, and the spin-spin decay of the transverse component (M_{xy}) in the xy-plane. Figure 2.4 illustrates the changing amplitude of M_x, M_y and M_z following a $\frac{\pi}{2}$ nutation of M_0 through a B_1 pulse applied along y (this illustrated in 2.4).

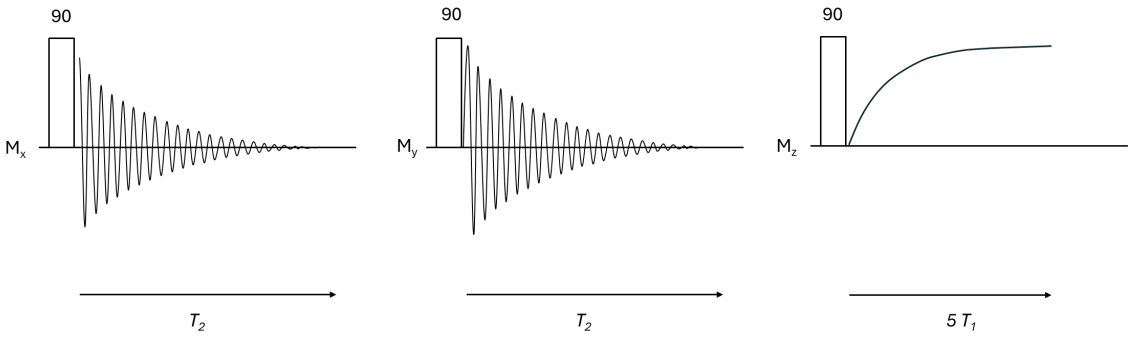

Figure 2.4: Plot of the amplitude of the M_x, M_y and M_z components of the net magnetisation vector M in the x, y and z axes, following a 90° pulse along the y-axis, rotating M_0 from the z-plane into the x-plane, as shown in Figure 2.3. The transverse components (M_x, M_y) exhibit a Free Induction Decay (FID) characterised by the spin-spin relaxation time T_2. The longitudinal component (M_z) returns to equilibrium exponentially according to the spin-lattice relaxation time T_1. Note that for full signal recovery ($> 99\%$), a delay of approximately $5 \times T_1$ is required.

2.2.3.1 Spin-lattice (T_1) relaxation

Over time, the net magnetisation of the M_z component relaxes back to alignment with B_0 through exchange of energy with surrounding molecules (the lattice). After a 90° pulse, there is no M_z magnetisation, and both spin states are equally populated. This recovery occurs as spins in the higher-energy state exchange energy with the lattice and return to the lower-energy state (α), thus restoring the slight population excess defined by the Boltzmann distribution at B_0.[79] This relaxation process is called T_1 relaxation, or spin-lattice relaxation. The time taken for this decay is characteristic of each nucleus in its magnetic (chemical) environment. This is described by Equation 2.15, where $M_z(t)$ is net magnetic moment along the z-axis at time t; M_0 is the equilibrium magnetic moment, t is time, and T_1 is the relaxation constant. This is the same mechanism responsible for

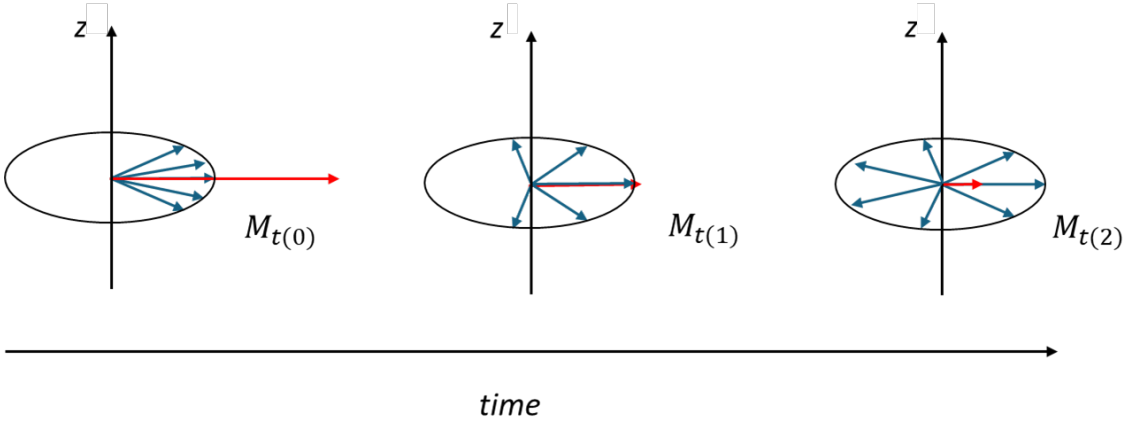

Figure 2.5: Cartoon of T_2 relaxation of an ensemble of nuclei, following a rotation of M_0 into the xy plane. Vectors are shown at three arbitrary time points, $t(0)$, $t(1)$, and $t(2)$. Individual nuclear spin vectors shown in blue and the net magnetisation vector at each time point (M_t) of the ensemble shown in red. At the initial time point $t(0)$, immediately following the B_1 pulse, phase coherence is highest. Following a time interval to $t(1)$, the net magnetisation vector diminshes in magnitude due to loss of phase coherence. As further time passes to $t(2)$, the phases of individual spins become incoherent, and net magnetisation in the xy plane diminshes significantly. After a sufficient duration all phase coherence will be lost and M_{xy} will become 0.

the initial establishment of the net magnetisation (M_0) when the sample is first placed in the magnetic field.

$$\frac{\mathrm{d}M_z(t)}{\mathrm{d}t} = -\frac{M_z(t) - M_0}{T_1} \tag{2.15}$$

2.2.3.2 Spin-spin (T_2) relaxation

After the initial RF pulse, the individual nuclear spins that form the transverse magnetisation are precessing with a shared phase, a state known as phase coherence. This coherence is lost over time because small, random variations in the local magnetic field—caused by molecular interactions—lead to slight differences in the precession rates of individual nuclei. As the spins "fan out" and lose their phase relationship, as illustrated in Figure 2.5, the net transverse magnetisation (M_{xy}) decays. This process, which represents an irreversible loss of order to the molecular environment, is called spin-spin relaxation and is characterised by the time constant T_2. In practice, dephasing is also accelerated by static spatial inhomogeneities in the main magnetic field (B_0) across the sample volume. These spatial variations mean that nuclei in different parts of the sample precess at slightly different, but constant, frequencies, leading to a further, reversible loss of phase coherence. The combined effect of natural T_2 relaxation and dephasing from magnet inhomogeneity is described by the effective transverse relaxation time, T_2^*, which is what is actually observed in an experiment. The relationship between these rates is given by Equation 2.16, where γ is gyromagnetic ratio and B_i is the inhomogeneity of the local magnetic

field.

$$\frac{1}{T_2^*} = \frac{1}{T_2} + \gamma \Delta B_i \tag{2.16}$$

The loss of phase coherence and decay of M_{xy} over time occurs with an exponential decay characterised by the T_2^* constant, described by Equation 2.17.

$$M_{xy}(t) = M_{xy}(0) \exp\left(-\frac{t}{T_2^*}\right) \tag{2.17}$$

2.3 NMR detection - instrumentation

For a thermally polarised sample, this combination of chemical shift and J-coupling information allows for the relative populations of nuclei to be quantified through proportionality of signal intensity. In addition, the fine structure of a peak, induced by splitting through J-coupling, can be used to infer the connectivity of molecular fragments. For example, a -CH_2- group adjacent to a -CH_3 group will appear as a quartet, while the signal for the -CH_3 will appear as a triplet.

To maximise the polarisation and therefore the observed signal ($P \propto B_0$), NMR spectroscopy is typically performed at very high magnetic fields. A typical high-field spectrometer is built around a powerful superconducting electromagnet, which is cooled by liquid helium and nitrogen to generate a strong and highly stable B_0 field, commonly in the region of 7–14 T, with maximum strengths approaching 28 T.[80] The sample is placed within a probe, which is inserted into the bore of the magnet; this probe contains precisely engineered coils to transmit the B_1 pulses and detect the resulting FID. The entire experiment is controlled by the spectrometer console, which houses the electronics required to generate precisely shaped RF pulses, amplify the weak NMR signal, and convert it into digital form for processing. The frequency separation between NMR spectral peaks scales with B_0, while, J-coupling splitting (in Hz) is independent of the B_0 field strength. Therefore, at higher fields, overlapping multiplets are better resolved, as can be seen in Figure 1.2.

2.3.1 Low-Field and Zero-Field NMR

The high cost, large footprint, and operational complexity of high-field superconducting systems have driven demand for more accessible NMR technology.[13,35] Recent advancements in magnet technology and electronics have enabled the production of a new class of compact, lower-field spectrometers. While sacrificing the ultimate sensitivity of high-field systems, these modern instruments benefit from a comparable level of electronic sophistication, resulting in a significant reduction in instrument cost, size, and operational complexity.[35] Low-field NMR can be broadly classed into the benchtop regime ($\sim$ 0.1 -

2.4 T), and Ultra Low Field (ULF) regime (pT to mT), which includes the Earth's field (EF) regime at $\sim 50\mu T$, and zero-field (ZF) spectroscopy.

The benchtop regime occupies an intermediate space between high-field and ultra-low-field NMR. While chemical shift is still resolved, the lower magnetic field strength means that the difference between resonance frequencies (in Hz) is reduced, causing spin systems to frequently enter the strong J-coupling regime. This results in spectra that retain the general appearance of their high-field counterparts, with recognizable splitting patterns, but often exhibit significant second-order effects such as multiplet distortion, as previously illustrated in Figure 1.2. At ultra-low fields, the Zeeman interaction becomes weaker and can be comparable to, or even smaller than, the J-coupling interaction. This leads to spectra that are qualitatively different from their high-field counterparts. Advantages of benchtop NMR include reduced cost, portability, and diminished magnetic susceptibility artifacts, which are particularly problematic at the interface of different materials.[81,82] The external locking system used in some benchtop spectrometers can also allow the use of protiated solvents, further reducing cost and complexity, as no solvent deuterium signal is needed to maintain the lock frequency.[26,50]

2.4 NMR in the Ultra-Low-Field Regime

A distinct spectroscopic environment exists at magnetic fields substantially weaker than those of high-field or benchtop spectrometers. This is the ultra-low-field (ULF) or zero-field (ZF) regime, which includes the Earth's magnetic field (EF) ($B_0 \approx 50\,\mu$T), and is governed by an altered balance of spin interactions.

2.4.1 Sensitivity

The most immediate challenge of ULF NMR is the significant loss of sensitivity. As established in Equation 1.1, thermal polarisation is directly proportional to the magnetic field strength ($P_0 \propto B_0$). Moving from the tesla regime of high-field and benchtop instruments to the microtesla regime results in a reduction in polarisation, and thus signal, by a factor of 10^5 to 10^6.

Sensitivity is further limited by the inefficiency of conventional NMR detection. The signal is detected via Faraday induction, where the voltage induced in the receiver coil is proportional to the rate of change of magnetic flux.[83] At ULF, the Larmor frequencies are in the low kilohertz range, meaning the magnetisation precesses very slowly. This slow rate of change induces a very small voltage, rendering the detection of thermally polarised signals practically impossible. Consequently, the application of hyperpolarisation techniques is not merely beneficial in the ULF regime; it is an absolute necessity for acquiring signals with a usable signal-to-noise ratio.

In the Earth's Field ($B_E \approx 50\,\mu$T) regime and below, chemical shift collapses as fre-

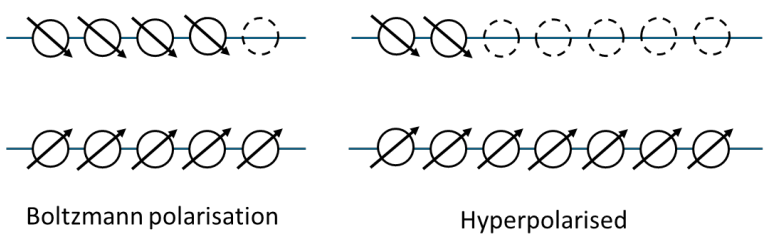

Figure 2.6: Illustration (not to scale) of Boltzmann and hyperpolarised distribution of spins under the same B_0. Boltzmann polarisation is typically on the order of parts per million, while hyperpolarised samples may reach polarisation levels of parts per hundred.

quency differences between nuclear environments become narrower than spectral peaks (1 ppm = 0.002 Hz at 50 μT).[74,84] In this regime, all nuclei of the same isotope become effectively magnetically equivalent. This results in spectra that would normally show complex strong homonuclear J-coupling resolving into singlet peaks at the Larmor frequency (determined only by the field B_0.) Couplings to heteronuclei remain visible[85] due to the large difference in gyromagnetic ratio, but homonuclear couplings become visible only if the magnetic equivalence is broken through heteronuclear coupling.[86] In this regime, strongly coupled, second-order spectra of unlike spins are observed.[87] Further, the polarisation at Earth's field is incredibly weak, at approximately 175 ppt at $B_E \approx 50$ μT. As a result, generating a detectable signal from such a small net magnetic moment requires the use of very large sample volumes (typically 100s of mL compared to 0.6 mL in a standard NMR tube).

Further, in the ultra-low field (ULF) regime below the Earth's Field, and the zero-field (ZF) regime, the nuclear precession frequency is so low that conventional inductive detection is ineffective, as the rate of change of magnetic flux ($\frac{d\Phi_B}{dt}$) is too small to induce a measurable current.[72] Detection in this regime relies on highly sensitive instruments, such as Superconducting Quantum Interference Devices (SQUIDs) or Optical Magnetometers (OPMs), which can directly measure the static or slowly oscillating magnetic field produced by the sample.[88,89]

The low intrinsic sensitivity of all low-field techniques, a direct consequence of the low thermal polarisation, presents a significant challenge. To make these methods practical for chemical analysis, this limitation must be overcome, which provides the primary motivation for the development of hyperpolarisation techniques, which allow a significant increase to sensitivity without changing detection field.

2.5 Hyperpolarisation

Conventional NMR experiments use very high magnetic fields ($B_0 > 7$ T) to increase the NMR signal. The very high magnetic field raises the difference in nuclear energy levels, increasing the population of the lower energy state. High fields are achieved using cryogenically cooled superconducting electromagnets. This makes conventional spectrometers very expensive to purchase and operate, as well as very large in physical

footprint. Smaller, cheaper and more portable NMR devices are available but these have lower magnetic fields ($B_0 < 3$ T) and therefore lower sensitivity. However, significant signal enhancements can be achieved, even in weaker detection fields, using alternative methods called hyperpolarisation techniques. Hyperpolarisation is a general name for all methods that boost NMR signals by temporarily increasing the population difference beyond thermal equilibrium in the detection field.[35,37,90,91] Hyperpolarisation techniques can increase polarisation from parts per million to tens of percent.[13]

Hyperpolarisation significantly broadens scope of what is possible with NMR: for example, enabling real-time metabolic imaging *in vivo* with ^{13}C-labelled substrates,[92] allowing for rapid, single-scan acquisition of multidimensional spectra,[93] or making low-cost, portable NMR devices practical for chemical analysis outside of a specialised lab.[53,94] This also allows the use of less sensitive equipment without loss of signal.

Hyperpolarisation techniques include *para*-hydrogen induced polarisation (PHIP),[37,43] and Dynamic Nuclear Polarisation (DNP).[30,95] A brief overview of hyperpolarisation techniques is given in Table 2.1

2.5.1 Methods

There are a number of methods in which non-equilibrium spin-order can be reached. The simplest method is brute force polarisation, in which a sample is subjected to a high field or a low temperature and then transferred to the detector. Both methods reach a new Boltzmann equilibrium with a higher sample polarisation, and detection is performed before T_1 relaxation following field switching and/or sample reheating allows the spins to return to equilibrium. Brute force hyperpolarisation is very simple to perform, and retains the (T_1 weighted) proportionality of signal in different chemical environments. It is limited in its applicability: high field systems require cryogens and a sample amenable to freezing, and by field switching being only applicable when using low-field detection.

Most hyperpolarisation techniques rely on transferring spin order from a more highly polarised source. There are two common sources of enhanced spin order for hyperpolarisation: spin-polarised electrons and *para*-hydrogen (p-H_2). The earliest discovered method of hyperpolarisation is Dynamic Nuclear Polarisation (DNP), proposed by Overhauser and implemented by Carver & Slichter in 1953.[30,90,95–97] DNP uses unpaired electrons as a source of spin hyperpolarisation. Electrons have a much higher gyromagnetic ratio γ than atomic nuclei ($\gamma_e \approx 660\gamma_{^1H}$). DNP provides a mechanism by which this higher intrinsic polarisation can be transferred to target nuclei for detection. The unpaired electrons are generally sourced from a stable free radical such as TEMPO ((2,2,6,6-Tetramethylpiperidin-1-yl)oxyl) which can be mixed with the target. At very low temperatures ($\sim 1-2\,\mathrm{K}$) and under application of a moderate field (3.4 T) the polarising agent can reach near-100% polarisation.[35] Irradiation of the sample at very low ($< 4.2K$) temperature with microwave frequency radiation at the electron paramagnetic resonance (EPR) transition frequency of the polarising agent then allows transfer of spin polarisation from the agent to the target. This can occur via the solid effect, cross effect, or thermal mixing, depending on experimental conditions.[96–98] The maximum polarisation

that can be reached by DNP is the ratio between gyromagnetic ratios, 660 for transfer to ^{1}H and 2615 for ^{13}C. DNP using polarisation in the solid state and detection in the solution state (dissolution DNP, d-DNP) is a much more recent development.[30] It uses a rapid dissolution of the hyperpolarised target in hot solvent, followed by rapid transfer to a spectrometer and detection, to allow liquid state DNP NMR prior to analyte relaxation to thermal polarisation. d-DNP gives very large signal enhancements (up to 10 000 fold) and has broad applicability, with examples of use in materials science[99], structural biology[100], and metabolic imaging[101]. However, DNP is a complex and expensive technique to perform, still requiring cryogens, high-field NMR magnets and separate high field microwave sources. Samples can also be limited by short T_1 lifetimes, poor interactions between analyte and polarising agent, or by damage through freezing, particularly for biological samples.

Spin Exchange Optical Pumping allows for hyperpolarisation of noble gases. To generate high spin order, alkali metal vapour (Rb or Cs) is optically pumped using circularly polarised laser light. This selectively excites valence electrons of a specific spin state to higher energy levels to give a spin-polarised population of alkali metal vapour.[34,102,103] Following mixing of polarised alkali metal vapour and noble gas, spin exchange from metal to noble gas can occur through through Fermi-contact interaction during gas-phase collisions.[32,103] The subsequently hyperpolarised noble gas can then be used for NMR or MRI experiments. Hyperpolarisation in this manner is very effective and can have very long polarisation lifetimes, but the target range is limited to only noble gases. Because of this, SEOP predominantly finds use in clinical applications, including respiratory disease imaging.[104–109]

As discussed in Chapter 1, the other major source of hyperpolarisation is the singlet nuclear spin isomer of dihydrogen, *para*-hydrogen, which possesses a unique form of spin order. This spin isomer can be enriched to create a non-equilibrium population at room temperature, which serves as the source of hyperpolarisation The focus of this thesis is on hyperpolarisation using *para*-hydrogen, which will now be explored in more detail.

Table 2.1: A comparison of common hyperpolarisation methods.

Method	Polarisation Source	Mechanism	Advantages	Limitations
Brute force	Enhanced nuclear polarisation from high-field and/or low temperature.	Rapid field/temperature switching between build-up and detection.	Retains signal proportionality; very simple.	Requires variable field apparatus; largely limited to low-field detection; enhancement factors limited by strength of pre-polarising field or temperature that can be reached.

Dynamic Nuclear Polarisation (DNP)	Unpaired electrons	Microwave irradiation.	Potential for high polarisation; broad range of targets.	Long polarisation times; d-DNP requires large, expensive instrumentation; ODNP gives lower enhancements
Spin-exchange optical pumping (SEOP)	Optically pumped alkali metal (Rb) vapour.	Spin exchange collisions between noble gases and pumped metal vapour.	Near-100% polarisation; very long polarisation lifetimes.	Only applicable to noble gas nuclei.
Hydrogenative PHIP	*Para*-hydrogen	Hydrogenation reaction in solution.	Room temperature operation; no high fields required.	Requires an unsaturated target; chemically modifies the sample.
Signal Amplification By Reversible Exchange (SABRE)	*Para*-hydrogen	Reversible exchange reaction in a weak polarisation transfer field (0–10 mT).	Continuous hyperpolarisation is possible; no high T or field required.	Limited range of substrates; requires rapid exchange on catalyst.

2.5.2 *Para*-hydrogen

Molecular hydrogen consists of a pair of ^{1}H nuclei each with spin $\frac{1}{2}$. ^{1}H atoms are fermions: identical particles with half-integer spins. A combination of fermions must follow the Pauli exclusion principle, that the overall wavefunction must be antisymmetric with respect to exchange of nuclei.[110] The Born-Oppenheimer approximation allows the overall wavefunction to be split into components: electronic, rotational, vibrational, translational and spin wavefunctions.[111]

$$\psi_{total} = \psi_{elec}\psi_{vib}\psi_{rot}\psi_{trans}\psi_{spin} \tag{2.18}$$

In H_2, the electronic, translational and vibrational wavefunctions are symmetric with respect to nuclear exchange. For the overall wavefunction to be antisymmetric, the product of the rotational and spin wavefunctions must be antisymmetric. This can occur either through coupling a symmetric rotational wavefunction with an antisymmetric spin wavefunction, or an antisymmetric rotational wavefunction with a symmetric spin wavefunction. This is shown in Table 2.2. Rotational wavefunctions are symmetric at even rotational quantum numbers (J = 1,3,5...) and antisymmetric at odd rotational quantum numbers (J = 0,2,4...).

A spin-$\frac{1}{2}$ nucleus can exist in α or β spin states. These combine into four product spin states for a diatomic molecule: $\alpha\alpha$, $\alpha\beta$, $\beta\alpha$, and $\beta\beta$. Because the two nuclei are

Table 2.2: Table showing the coupling of rotational and spin wavefunctions $\psi_{rotational}$ & ψ_{spin} to produce an overall antisymmetric wavefunction ψ_{total}.

ψ_{total}	$\psi_{rotational}$	ψ_{spin}
antisymmetric	symmetric	antisymmetric
antisymmetric	antisymmetric	symmetric

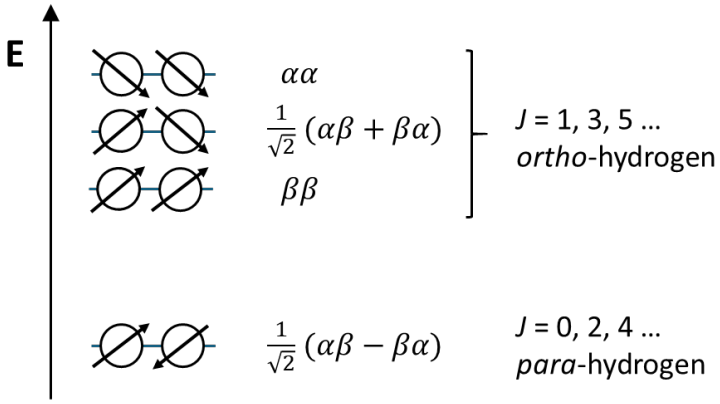

Figure 2.7: Cartoon of energy levels of H_2 in the presence of a magnetic field, with the associated nuclear spin eigenstates. J is the rotational quantum number of the states.

indistinguishable, the simple product states $\alpha\beta$ and $\beta\alpha$ are not valid eigenstates of the system. Instead, the true nuclear spin eigenstates must be constructed as normalised linear combinations which have a defined symmetry upon exchange of the two nuclei: the symmetric $\frac{1}{\sqrt{2}}(\alpha\beta + \beta\alpha)$ and the antisymmetric $\frac{1}{\sqrt{2}}(\alpha\beta - \beta\alpha)$. Both $\alpha\alpha$ and $\beta\beta$ are inherently symmetric spin states. This gives a set of three symmetric spin states, with total nuclear spin quantum number $I = 1$, and one antisymmetric spin state with total nuclear spin $I = 0$. The wavefunction is kept antisymmetric through coupling the symmetric triplet spin states with antisymmetric rotational states, and the antisymmetric singlet spin state with symmetric rotational states. The rotational states are characterised by the rotational quantum number, J, where even values of J correspond to symmetric rotational states and odd values of J correspond to antisymmetric states. Figure 2.7 illustrates this coupling for the nuclear energy levels at the $J = 0$ and $J = 1$ rotational states.

Population of the rotational spin states is determined by Boltzmann's distribution law for rotational states (Equation 2.19).[112]

$$N_J = N_{G_J} \exp\left(-\frac{J(J+1)\theta_R}{T}\right) \tag{2.19}$$

$$\theta_R = \frac{\hbar^2}{2Ik_B}$$

At room temperature, the small difference in energy between rotational states gives equal population of all nuclear states, with the triply degenerate *ortho-* state being approximately three times more abundant than the singlet *para-* state, splitting the population 75% *ortho-* to 25% *para-*hydrogen at equilibrium.

Interconversion between the *ortho-* and *para-* states is symmetry forbidden, as one of the ^{1}H nuclei must reverse spin states. Inversion only of ψ_{spin} without a simultaneous change of ψ_{rot} would result in a forbidden symmetric ψ_{total}.

Interconversion only becomes allowed through perturbation of the molecular symmetry by providing a locally inhomogeneous magnetic field, allowing the mixing of the *ortho-* and *para-* spin states through a hyperfine coupling between the hydride nuclear spins and catalyst electron spins. This is often achieved through the presence of a paramagnetic catalyst, which provides a local inhomogeneous magnetic field. This allows for simultaneous, coupled changes in ψ_{rot} and ψ_{spin}, conserving the antisymmetric total wavefunction ψ_{total} and allowing interconversion.[113,114]

Iron (III) Oxide[115,116] and activated charcoal[117,118]are common catalysts. To increase the population of *para*-hydrogen, the lower energy singlet state, H_2 gas is cooled in the presence of such a catalyst. As temperature falls, occupation of the lowest energy $J = 0$ rotational state becomes increasingly favourable, up to 99.75% occupation at 19 K. Figure 2.8 shows the change in enrichment (p-H_2 fraction) as temperature falls. At 77 K, the temperature of liquid nitrogen, H_2 gas is $\approx 51\%$ p-H_2. As the transition remains symmetry forbidden away from the catalyst, moving the enriched *para*-hydrogen gas away from the catalyst and then allowing temperature to rise allows production of p-H_2-enriched H_2 gas. The forbidden transition allows the gas to be stored for long periods (up to months).[119,120]

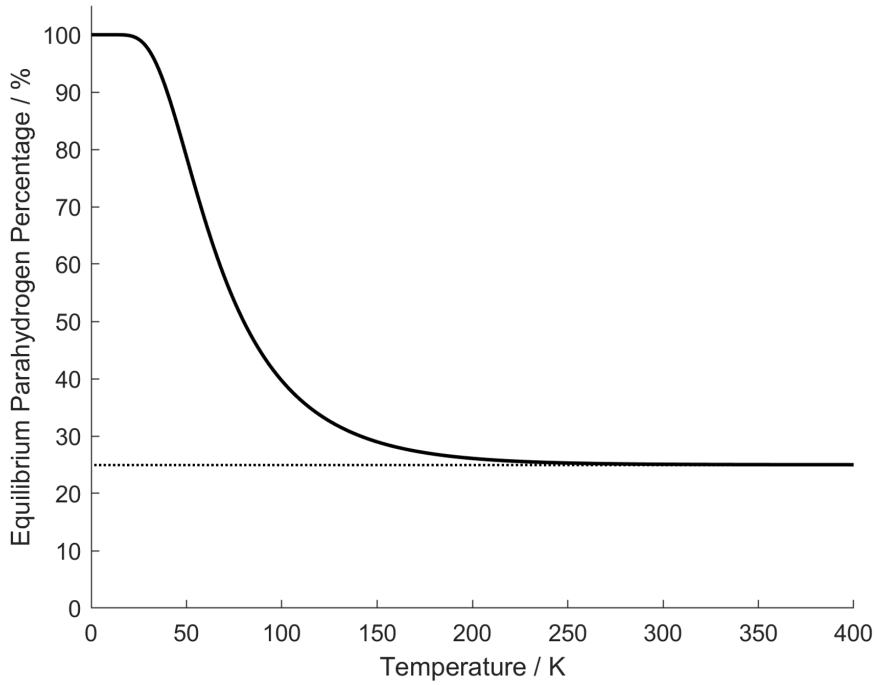

Figure 2.8: The equilibrium fraction of *para*-hydrogen in H_2 gas as a function of temperature, across range 0-400 K. The *para*-hydrogen fraction approaches 25% (indicated by the dashed line) as temperature increases.

2.5.3 *Para*-hydrogen Induced Polarisation

Para-hydrogen is highly ordered but has no net angular momentum, and so is NMR silent. It must be used in a chemical reaction to create hyperpolarisation. This was first demonstrated by Bowers and Weitekamp in 1986-1987, establishing the *Para*-hydrogen Induced Polarisation (PHIP) as a technique.[37,38] p-H_2 has high spin order that can be transformed into hyperpolarisation by breaking the magnetic symmetry of the two ^1H nuclei in the p-H_2 molecule. This can be done through hydrogenation, or reversibly through spin exchange across a catalyst. In hydrogenative PHIP, the irreversible, pairwise addition of the two hydrogen atoms across an unsaturated bond allows observation of strongly enhanced signals.[35,38] For SABRE, the two atoms bind to a central metal catalyst in a reversible, non-hydrogenative process, allowing the target molecule to remain chemically unmodified.[43] The two ^1H nuclei must also be chemically inequivalent ($\Delta\nu_{H_1H_2}$) or magnetically inequivalent after they have been added to the target molecule or catalyst complex. Where no inequivalence is experienced, no enhancement of NMR signals is observed.

2.6 Signal Amplification by Reversible Exchange

Signal Amplification By Reversible Exchange (SABRE) is a method of *para*-hydrogen-induced polarisation developed by Adams *et al.* in 2009.[43] It offers a reversible, catalysed alternative to hydrogenation for the generation of hyperpolarised species in solution.

2.6.1 Mechanics of SABRE

Figure 2.9 illustrates the activation of the [Ir(COD)Cl(IMes)] SABRE pre-catalyst to form the active Ir(IMes) SABRE catalyst, followed by the complete catalytic cycle. IMes = 1,3-bis(2,4,6-trimethylphenyl)imidazol-2-ylidine; COD = cis,cis-1,5-cyclooctadiene).

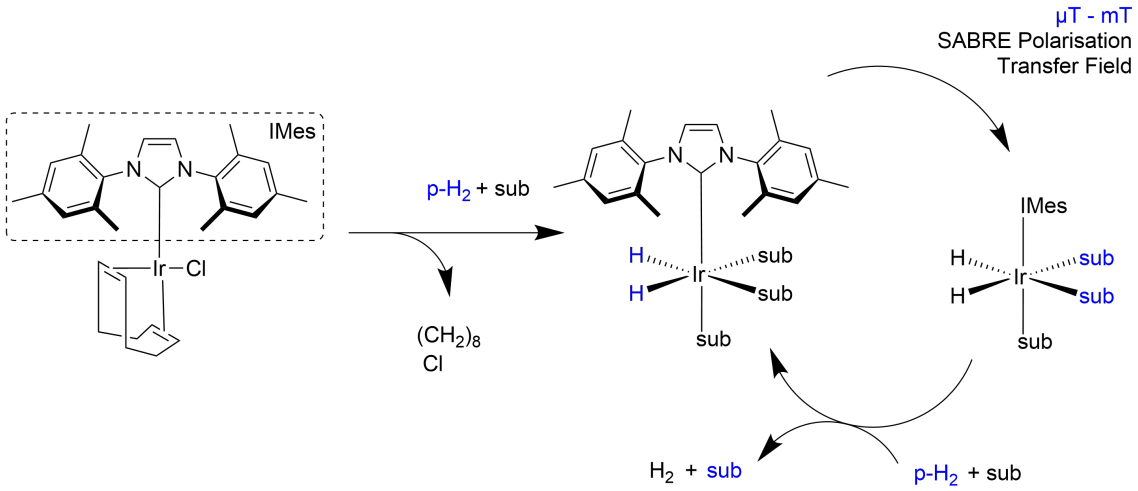

Figure 2.9: The SABRE catalytic cycle. The inactive precatalyst [Ir(IMes)(COD)Cl] is activated by H_2 to form the active catalyst species. The substrate (sub) and *para*-hydrogen reversibly bind to this active catalyst. In a weak magnetic field (the PTF), spin order is transferred from the *para*-hydrogen-derived hydrides to substrate nuclei. The hyperpolarised substrate dissociates into solution, allowing the catalytic cycle to continue. Hyperpolarised species are indicated in blue.

In SABRE, the transfer of polarisation from *para*-hydrogen to the substrate is only possible when the two hydrides derived from *para*-hydrogen have different J-coupling interactions with the target nucleus on the bound substrate ($J_{H_AB} \neq J_{H_{A'}B}$). This is illustrated in Figure 2.10, using a model Ir(IMes) SABRE catalyst with pyridine substrate. SABRE catalysts are designed to create this condition.[121] The structure ensures that the two hydrides are positioned asymmetrically with respect to other ligands, making them magnetically inequivalent. This difference in their magnetic environment is what allows them to couple differently to the substrate, enabling the polarisation transfer to occur.[39]

SABRE achieves continuous, renewable hyperpolarisation through a catalytic cycle, shown in Figure 2.9. SABRE catalyst activation happens through substrate displacement of the Cl ligand on the Ir catalyst. Oxidative addition of H_2 to a vacant site on the catalyst gives the octahedral complex, and the active catalyst is formed by subsequent hydrogenation of the unsaturated bonds in the cyclooctadiene (COD) ligand to cyclooctane, which binds weakly and causes its removal from the Ir complex. The active catalyst is shown in Figure 2.9.[122,123]

Exposure of the active SABRE catalyst to a weak Polarisation Transfer Field in the ULF regime (μT or mT, depending on target)[44,48,74,124] allows coherent polarisation transfer between the *para*-hydrogen singlet state and the substrate Zeeman states. The mechanism for this spin order transfer, which occurs at a Level Anti-Crossing (LAC), is discussed in Section 2.6.2. For transfer to ^{1}H nuclei with the Ir(IMes) catalyst, this LAC generally occurs at approximately 6 mT.[123] Spontaneous dissociation of a substrate ligand from the fully coordinated SABRE catalyst leaves a vacant site. This coordinatively unsaturated intermediate is then rapidly trapped by species in the bulk solution, for which "fresh" *p*-H_2 and substrate compete for addition. This competition drives both the substrate exchange and hydride replenishment pathways. Oxidative addition of fresh

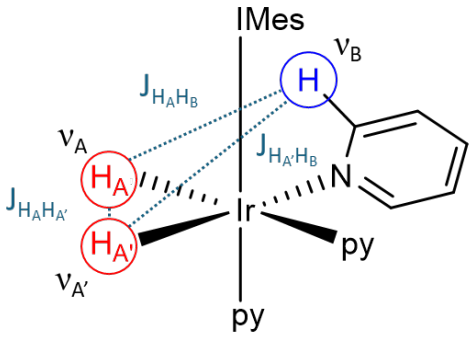

Figure 2.10: Schematic of the AA'B spin system in the active SABRE catalyst. The hydrides are chemically equivalent ($\nu_A = \nu'_A$) spins A and A' and nucleus B (with Larmor frequency ν_B) is an *ortho* nucleus on a pyridine substrate. The magnetic equivalence is broken by the difference in scalar coupling: $J_{AB} \neq J_{A'B}$)

p-H_2 (through its bond) at the vacant site regenerates the dihydride species, replenishing the source of spin order on the catalyst. Ligand exchange of the substrate allows the hyperpolarised ligand to return to solution and be replaced by "fresh", non-hyperpolarised substrate and *p*-H_2 molecules. Through continuous repetition of this process, hyperpolarised substrate can be built up in solution as long as there is available *p*-H_2. This is only possible as all binding processes are reversible and the substrate is not chemically altered by the exchange process.

2.6.2 Level Anti-crossings (LACs) and polarisation transfer condition

In 2012, Pravdivtsev *et al.*[44] developed a theory to explain the magnetic field dependence of SABRE using LACs. The enhancement and sign of SABRE-hyperpolarised NMR signal was shown to be dependent on the magnetic field at which polarisation transfer occurs. The evolution of the nuclear spins within the active complex is governed by the spin Hamiltonian. For a simplified model system comprising two hydrides (H_1, H_2) and a target ligand nucleus (L), the Hamiltonian in a static magnetic field, B_0,[44,121,125,126] oriented along the z-axis can be written as:

$$\hat{H} = -\omega_H(\hat{I}_{1z} + \hat{I}_{2z}) - \omega_L\hat{L}_z + 2\pi J_{H_1H_2}(\hat{I}_1 \cdot \hat{I}_2) + 2\pi J_{H_1L}(\hat{I}_1 \cdot \hat{L}) + 2\pi J_{H_2L}(\hat{I}_2 \cdot \hat{L}) \quad (2.20)$$

Here, ω_H and ω_L are the Larmor frequencies of the hydride and ligand nuclei, respectively, and the J terms represent the scalar couplings. A Level Anti-Crossing (LAC), or avoided crossing, occurs when two energy levels in the system that would otherwise cross as a function of the magnetic field are coupled by an interaction term. This coupling causes the states to mix and repel each other, preventing them from becoming degenerate. At high magnetic fields, the Zeeman Interaction (difference in chemical shift) is much larger than the J-coupling ($|\Delta\nu| \gg |J|$). In this "weak coupling" regime, the spin states are well-defined by their individual Zeeman energies, and there is very little mixing. The J-coupling only causes splitting of resonance lines. At the LAC, the magnitude of the energy of the Zeeman interaction becomes very close to or isoenergetic with the energy of the field-independent J-coupling. At the anti-crossing point, the Hamiltonian terms for

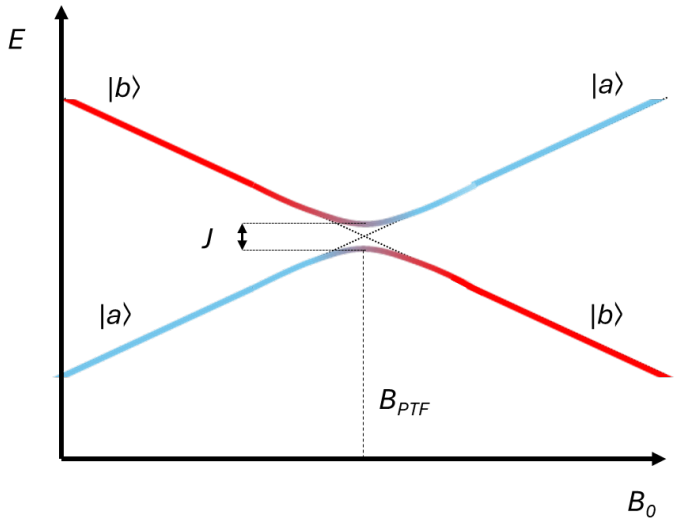

Figure 2.11: Illustration of LAC formation between $|a\rangle$ (blue) and $|b\rangle$ (red), two nuclear spin states strongly coupled by J. This interaction enables coherent polarisation transfer at the point of closest approach, B_{PTF}

Zeeman and J-coupling become comparable in magnitude. The pure spin states are no longer good eigenstates. Instead, the actual eigenstates become superpositions of these pure states. This allows coherent mixing of the wavefunctions of the two spin states.

Para-hydrogen is in a singlet nuclear spin state ($I = 0$), meaning its two protons have antiparallel spins and are in a coherent superposition. When enriched beyond its thermal equilibrium population, this singlet state represents a source of non-equilibrium spin order which can be exploited to generate hyperpolarisation. Within the transient SABRE complex, the two protons from *para*-hydrogen become hydride ligands (H_A and $H_{A'}$), and the substrate protons (B) are coupled through the J-coupling network, as shown in Figure 2.10. If we consider for now only transfer to ^{1}H, The J-coupling between the hydrides and substrate protons $J_{H_AH_B}$ is the dominant J-coupling in the network.

The energy levels of the nuclear spins within this coupled system are dependent on the applied magnetic field strength. As magnetic field decreases, the relative magnitudes of the Zeeman interaction and the J-couplings change. A LAC forms (and efficient spin transfer can occur) at a field B_0 such that the difference in Zeeman frequencies (chemical shift difference) between the coupled nuclei is comparable in magnitude to the J-coupling interaction. The formation of a LAC in this way is illustrated in Figure 2.11. At a LAC, the pure singlet character of the *para*-hydrogen-derived hydrides can mix coherently with the Zeeman energy levels of the substrate protons. This coherent mixing allows the non-equilibrium singlet spin order of *para*-hydrogen to be transferred into Zeeman polarisation of the substrate protons via the J-coupling network within the catalyst complex.[50,54,91]

Polarisation Transfer occurs when at Level Anti-Crossings (LACs) when the Polarisation Transfer Condition is met. A simplification of LAC theory allows the formation of a general equation which allows approximation of the field strength at which a LAC will form between the p-H_2 singlet state and the substrate target nuclei. The polarisation

transfer condition is given in Equation 2.21.[48,127]

$$J_{H_AH_{A'}} = \Delta\nu_{H_AB_{H,X}} \tag{2.21}$$

Where transfer is to another H atom:

$$\Delta\nu_{H_AB_H} = \frac{\gamma_H B_{PTF}(\delta_{H_A} - \delta_{B_H})}{2\pi} \tag{2.22}$$

where transfer is to a heteronucleus X:

$$\Delta\nu_{H_AB_X} = \frac{B_{PTF}(\gamma_H - \gamma_{B_X})}{2\pi} \tag{2.23}$$

In general, for transfer to substrate ^{1}H nuclei, the dominant J-coupling in the network on the SABRE catalyst is $J_{H_AH_{A'}} \approx 9$ Hz. For efficient mixing with the substrate, the hydride and substrate energy levels, $\gamma_H B_{PTF}(\delta_{H_A}\delta_B)$ must mix. The difference in chemical shift between hydride (-22 ppm) and substrate for most N-heterocycles, including pyridine (7-9 ppm), used throughout this thesis, is approximately 30 ppm. B_{PTF} for transfer to N-heterocycles using the Ir-IMes catalyst is therefore ≈ 6.6 mT.[123]

2.6.3 SABRE substrate range

SABRE is most effective for substrates, such as N-heterocyclic compounds, that exhibit optimal binding kinetics: strong enough to allow for efficient polarisation transfer during the catalyst residence time, but weak enough to ensure rapid exchange with the bulk solution. This explains the widespread success with molecules like pyridine. SABRE has had a significant broadening of its substrate range in recent years, particularly focussing on biological molecules for imaging potential. However, many biologically relevant molecules are challenging substrates due to poor binding kinetics or steric hindrance.[128,129] These limitations have been addressed through strategies such as SABRE-relay, where polarisation is transferred from a primary, easily hyperpolarised substrate (such as a "carrier amine"[130]) to a secondary target molecule in solution, or through the rational design of new catalysts with modified ancillary ligands to accommodate different classes of substrates.[49]

2.6.4 The SABRE catalyst in solution

The reversible exchange of the substrate (e.g., pyridine (py)) with the active catalyst $[Ir(H)_2(IMes)(py)_3]^+$ (CS_3) proceeds via a dissociative, S_N1-type mechanism.[131,132] This pathway is initiated by the rate-limiting dissociation of an equatorial pyridine ligand to form a transient, coordinatively unsaturated five-coordinate intermediate $[Ir(H)_2(IMes)(py)_2]^+$ (denoted CS_2). This reactive intermediate can then either be captured by a free substrate molecule from the bulk solution to reform the CS_3 complex, with fresh substrate, or can accept a molecule of H_2 to initiate hydride exchange.[45,131] The rates of these exchanges determine the efficiency of buildup of hyperpolarised substrate in solution. This mechanism

is supported by experimental kinetics: work by Cowley *et al.*[45] showed that the observed rate of H_2 loss from the reactive intermediate catalyst system decreases as the concentration of free pyridine increases, while it increases with rising H_2 pressure. This behaviour rules out a direct, unimolecular loss of H_2 from the saturated $[Ir(H)_2(IMes)(py)_3]^+$ complex. Instead, it points to a multi-step pathway that is initiated by the dissociation of a pyridine ligand to form the five-coordinate CS_2 intermediate. The vacant coordination site of the intermediate can then bind a molecule of H_2 from the solution to form a transient dihydrogen complex, $[Ir(H)_2(\eta^2\text{-}H_2)(IMes)(py)_2]^+$. This facilitates the exchange of the hydride ligands with the incoming p-H_2. Exchange of the η^2-H_2 molecule with the existing hydride ligands within the complex is an extremely rapid process with a very low activation barrier.[133] This shows that H_2 replenishment is rate-limited by pyridine dissociation, not H_2 binding.[134]

The highest signal enhancements are achieved at low substrate-to-catalyst ratios.[135] Conversely, increasing the substrate:catalyst ratio by adding an excess of substrate consistently leads to a significant reduction in the observed hyperpolarisation. This phenomenon can be explained by two primary kinetic effects.[65,135]

The most dominant effect is the competitive inhibition of the H_2 exchange pathway. The rebinding of a substrate molecule to the CS_2 intermediate becomes overwhelmingly faster than the binding of H_2, even if the latter is present at a high concentration. This effectively "starves" the H_2 exchange pathway. This is supported by the rate of H_2 loss decreasing with increasing pyridine concentration. Without efficient H_2 exchange, the p-H_2-derived spin order on the catalyst is not replenished, and the buildup of hyperpolarised substrate is inefficient.[45]

A second, competing effect is the catalyst allowing relaxation of hyperpolarisation as well as buildup. Binding to the catalyst also allows significant T_1 relaxation of hyperpolarised substrate in solution.[136] The observed T_1 of the free substrate in solution is a population-weighted average of its intrinsic, longer T_1 in bulk solution and the much shorter T_1 it experiences when transiently bound to the iridium centre, which behaves like a paramagnetic relaxation agent. At a fixed catalyst concentration, increasing the substrate concentration dilutes the influence of the catalyst on the total substrate pool, leading to a longer observed bulk T_1. This marginal gain in the lifetime of the polarisation is outweighed by the reduction in polarisation efficiency caused by the kinetic inhibition described above.[135,137] Studies have shown that the maximum attainable polarisation (P_{max}) is proportional to the ratio [Catalyst]/[Substrate] when substrate inhibition is the dominant kinetic limitation.[65]

2.6.5 Catalyst deactivation

While a low substrate:catalyst ratio is generally beneficial, operating at very low absolute substrate concentrations introduces a route to catalyst instability and deactivation. If the concentration of free substrate is too low, the lifetime of the reactive five-coordinate CS_2 intermediate increases,[128,135] providing a larger kinetic window for irreversible side reactions rather than productive rebinding of substrate or H_2.

The most prominent deactivation pathway is the formation of catalytically inactive or poorly active iridium dimers and oligomers.[131] These species form when two of the five-coordinate intermediates react with each other. A variety of such species, including chloride-bridged and hydride-bridged dimers, have been spectroscopically and crystallographically characterised. Their formation is often observed over long reaction times or at low substrate loadings and correlates with a decrease in SABRE activity.[138,139] For instance, in systems utilizing sulfoxide co-ligands for pyruvate hyperpolarisation, the dimerization of the reactive intermediate has been explicitly identified as a key deactivation route.[138,140]

2.6.5.1 *Para*-hydrogen pressure

Numerous studies conducted at conventional p-H_2 pressures (typically 1-10 bar) have reported a direct, often linear, relationship between the applied pressure and the magnitude of the observed signal enhancement.[45,59,141,142] Cowley *et al.* demonstrated a more than six-fold increase in the polarisation of pyridine when the p-H_2 pressure was increased from 1 atm to 3 atm.[45] In this "hydrogen-limited" low-pressure regime, the rate of the overall SABRE cycle is limited by the supply of p-H_2 to the catalyst. The concentration of dissolved H_2 in the solvent is governed by Henry's Law and is directly proportional to its partial pressure. Therefore, doubling the pressure effectively doubles the concentration of this key reactant. This leads to a proportional increase in the rate of the p-H_2 replenishment pathway and, consequently, a corresponding increase in the overall signal enhancement. The system is, in effect, "starved" for hydrogen, and any increase in its supply directly boosts performance.[65,141] As the pressure is increased into a "hydrogen-saturated" high-pressure regime, the signal enhancement reaches a plateau. Although the concentration of dissolved H_2 in the solvent continues to increase linearly with pressure across the entire 1-200 bar range, at high pressures, the system becomes saturated with H_2. Its availability is therefore no longer the rate-limiting factor.[135,136] In this regime the maximum rate of polarisation is governed by the rate of substrate dissociation, or T_1 relaxation on the catalyst complex.[132,135]

The kinetic landscape of SABRE is defined by a dynamic competition between a productive catalytic cycle and several parasitic loss pathways. The balance between these is dictated by the precise experimental conditions, primarily the reactant concentrations and the *para*-hydrogen pressure.

CHAPTER 3

Development of a *Para*-hydrogen Polariser Unit

3.1 Introduction

In order to develop *in situ* Signal Amplification By Reversible Exchange (SABRE), a device or series of devices are required which can be used cross-compatibly with any NMR instrument to bubble *para*-hydrogen through the SABRE reaction cell in time with an NMR pulse sequence. This requires: an independent supply of *para*-hydrogen, an electronically controlled valve manifold that can be triggered by the NMR spectrometer, and a SABRE reaction cell designed to allow in situ bubbling within that instrument without compromising field homogeneity around the sample.

3.2 *Para*-hydrogen delivery in literature

In situ Signal Amplification By Reversible Exchange (SABRE) experiments have been successfully implemented across a wide range of magnetic fields. The instrumentation varies significantly depending on the detection method, with examples ranging from conventional high-field spectrometers,[66] to low-field benchtop instruments,[143] Earth's field systems,[74] and even ultra-low-field setups using optically pumped magnetometers (OPMs) or SQUIDs.[64,144] All SABRE-enhanced NMR experiments share two fundamental instrumental requirements: a means to apply a polarisation transfer field to the sample to facilitate the transfer of spin order from *para*-hydrogen to the target substrate; and a method to detect the resulting hyperpolarised signal, which may involve physically transferring the sample between the PTF region and the detector. This section will summarise

key instrumental developments from the literature that address these two core challenges.

SABRE enhanced NMR experiments with both high and low-field detection require instrumentation to generate a SABRE polarisation transfer field or meet the SABRE PTF requirement, and to transfer the sample between the PTF and the detection region of a spectrometer. This section summarises the key instrumentation developments in this area from the literature.

3.2.1 Manual polarisation transfer approaches

The majority of work in SABRE has been done using *ex-situ* polarisation (outside the detector). In the simplest SABRE system, the head-space of an NMR tube is charged with *para*-hydrogen. To dissolve the *para*-hydrogen and achieve polarisation transfer, the sample is shaken in the stray field of a large NMR magnet for several seconds before being introduced into the NMR spectrometer for detection. This 'shake-and-drop' approach was used in the original SABRE experiments[43] and is convenient, but difficult to reproduce due to inconsistencies in stray field. In addition, it cannot be done using magnets that do not produce a significant stray field, for example benchtop NMR spectrometers.

A more rigorous approach is to provide a second controlled field for polarisation transfer, to give a reproducible PTF. This is the approach taken by more recent examples in the literature.[48,52,59,60,63] Richardson *et al.* describe a handheld unit that uses a Halbach array of permanent magnets to provide a fixed PTF during shaking.[47] This gives more efficient polarisation transfer, and is perhaps the simplest way to achieve a controlled field for polarisation transfer, minimising cost and complexity. Richardson *et al.* find their system can generate a 25% increase in SABRE enhancement compared to stray field shaking of a spectrometer.

Similarly, field cancelling can be used to apply sub-Earth's field PTFs, which are required for optimal transfer to heteronuclei such as ^{15}N. For example, Theis *et al.* implemented a manual transfer system, where *p*-H_2 is bubbled through an NMR tube placed inside a mu-metal shield.[48] This shields the sample from all external fields, including the Earth's field, giving a sub-microTesla PTF. In these experiments, the PTF is controlled by an electromagnet inside the mu-metal shield. Following polarisation transfer inside the shield, the sample is manually transported to a benchtop NMR spectrometer for detection. Theis *et al.*[48] give a manual transfer time of approximately 5s and suggest that this is limiting the observed level of polarisation, implying that the maximum polarization achievable by SABRE-SHEATH prior to sample transport is significantly higher than the 10% observed in practice. This effect would be expected to lead to more significant polarisation loss for faster relaxing heteronuclei polarised in a similar way, e.g. ^{19}F. A system that would allow faster consistent transfer times would thus significantly improve future observations made with SABRE-SHEATH hyperpolarisation.

Manual sample transfer is limited by the variability in the time taken and field experienced when moving the sample. It is generally only useful for single-shot experiments. For multi-step experiments, such as 2D spectroscopy, an automated approach is required.

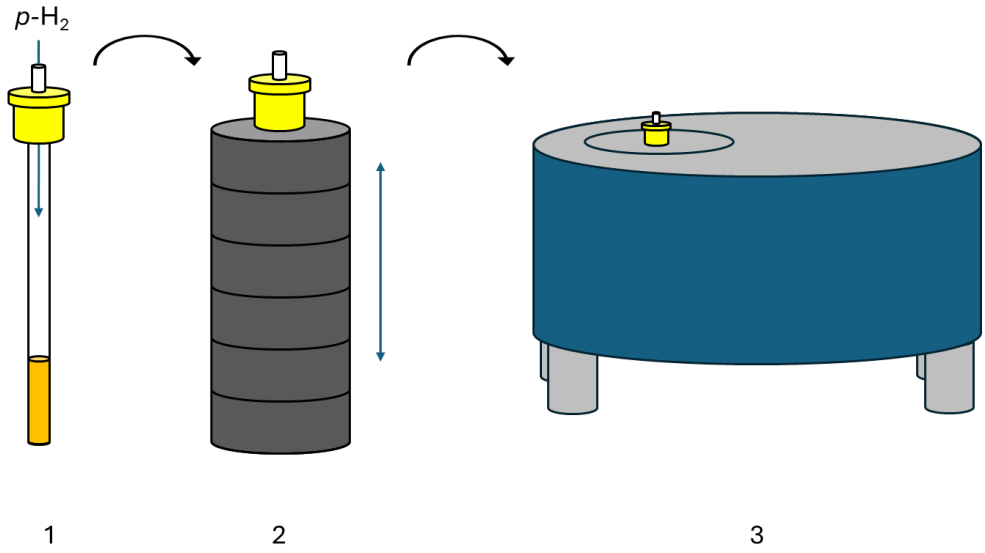

Figure 3.1: Shake and drop using a handheld Halbach array in the manner described by Richardson *et al.*. An NMR tube with Young's tap is charged with p-H_2 (1), shaken in a 6 mT Halbach array (2), and then placed in a spectrometer and detection occurs (3).

3.2.2 Automated polarisation transfer approaches

One approach to automating SABRE is to use a flow system to move the sample between the PTF and the NMR detector. For example, Mewis *et al.* used a variable power electromagnet to explore the effect of variable PTFs on polarisation transfer to ^{13}C in SABRE, using an apparatus shown in Figure 3.2.[59] In these experiments, p-H_2 is bubbled through the sample inside a mixing cell that is surrounded by the electromagnet, which generates the desired PTF. Following polarisation transfer, helium gas was used to push the sample from the mixing chamber to the NMR spectrometer for detection. The sample was returned to the mixing chamber following NMR detection (Figure. 3.2 parts 2 and 4), with a transport time of 2.9 s followed by a 1 s settling time in the probe head. This transfer and settling time is on a similar order to T_1, especially for ^1H nuclei, allowing significant relaxation of polarisation generated. The flow system will also drive solvent loss, reducing sample lifetime and potentially impacting sample concentrations.

A sample might also be moved mechanically between PTF and detector. This might be done pneumatically or mechanically. TomHon *et al.* show a pneumatic system,[60] using a sealed 'shuttling tube', into which N_2 can be pumped or vacuum applied to raise and lower the sample. An illustration of the system by TomHon *et al.* is reproduced in Figure 3.3.[60]

Raising and lowering the sample into the spectrometer allows adjustment of the PTF experienced as a gradient across the sample. Field can be controlled through use of the stray field, which weakens as the sample is lifted further away from the detection region, and through the addition of magnets above the spectrometer. TomHon *et al.* show the option of addition of an electromagnet or mu-metal shield for their system above the spectrometer, allowing controlled application of homogeneous millitesla or microtesla

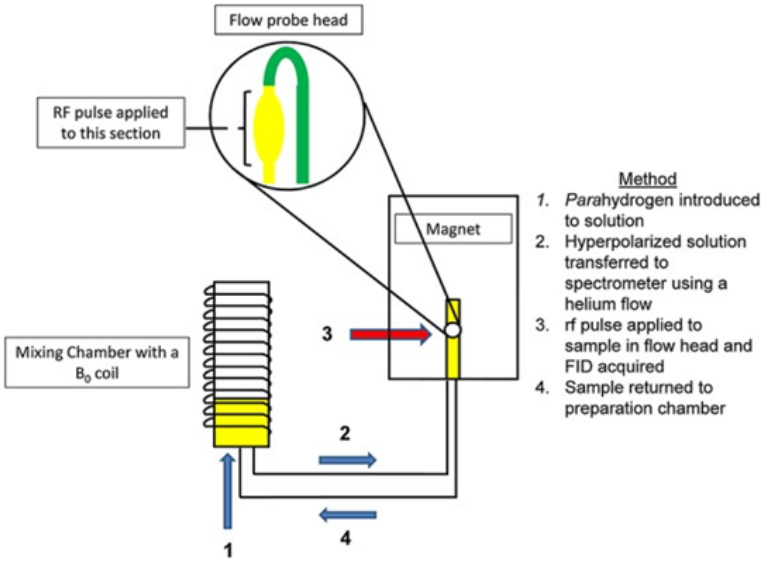

Figure 3.2: SABRE flow system with separate electromagnet for PTF as presented by Mewis *et al.*[59] A solenoid coil surrounds a mixing chamber containing SABRE catalyst and substrate in solution. Para-hydrogen can be bubbled into this solution through an inlet (1). Helium gas can be used to push the sample into the NMR probe (2) where NMR detection is executed (3) before the sample is flowed out with Helium. (4) Figure is reproduced without alteration from the publication by Mewis *et al.*[59] under the CC BY 3.0 license.

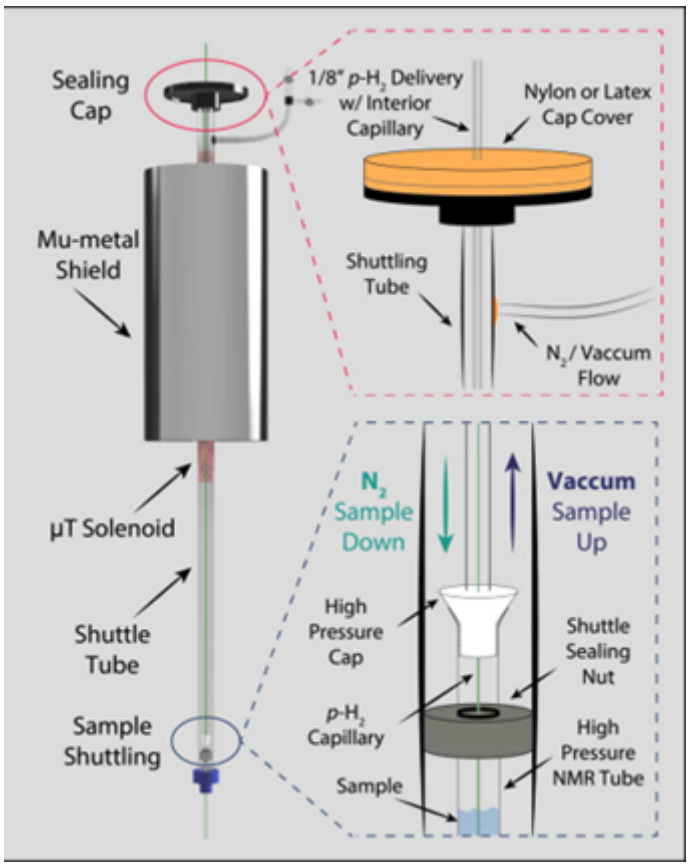

Figure 3.3: Bubbling system illustration edited from the graphical abstract of TomHon *et al.* (2020)[60] Reproduced from Ref. 59 with permission from Elsevier.

fields across the sample.[60] Kiryutin *et al.* describe a similar system, which instead uses a motor to mechanically shuttle the sample between a shielded electromagnet above the spectrometer, and the detection region.

Sample shuttling allows much faster movement of the sample and minimises solvent losses. Transfer through the stray field still allows some variability in the fields experienced by the sample during shuttling, which may give rise to some spontaneous polarisation transfer not driven by placing the sample in the PTF. Use of stray fields to generate PTF can give a broad inhomogeneity of transfer field across the sample, which may be mitigated by use of shallower sample depths. Use of electromagnets to generate the PTF increases the travel time between PTF and detection region, giving increased relaxation and making rapid processes more difficult to observe.

3.2.3 *In-situ* polarisation transfer

If SABRE is performed *in-situ*, inside the magnet, a transfer strategy is not needed. Barskiy *et al.* show a system in which bubbling is done directly into an NMR tube held *in-situ* in the NMR probe, with detection at 5.75mT, at which the spontaneous polarisation transfer condition is met.[68] This eliminates a number of the confounding factors that arise from changing field through use of shuttling methods, but *in-situ* bubbling at high field prevents the sample meeting the field requirement for spontaneous polarisation transfer via a level anticrossing. This can be overcome through use of RF-SABRE, in which level anticrossing conditions are met in the rotating reference frame under RF-field irradiation.

Pravdivtsev *et al.* use a similar system to Barskiy *et al.*, adding an RF pulse to the sequence between bubbling and detection to allow spontaneous polarisation transfer.[145] Figure 3.4 shows the illustration of this setup as presented by Pravdivtsev *et al.*.

Put *et al.*[64] and Myers *et al.*[71] give two examples of *in situ* polarisation transfer at ultra low field. Put *et al.* use an optically pumped magnetometer at 15 Hz, Myers *et al.* a SQUID which reaches sub-nT fields.

Put *et al.* illustrate a simple system for p-H_2 delivery using a network of solenoid valves to control gas flow. Gas is delivered into the NMR tube in-situ via a capillary submerged into the bottom of the sample solution. Gas is allowed to return through a Teflon tube stretched over the NMR tube. This gives a simple, controllable flow of p-H_2 gas into solution which can be performed in time with a NMR pulse sequence

The instrumentation presented by Myers *et al.* in 2024 is shown in figure 3.5.[71] They demonstrate a simple flow system similar to Mewis *et al.*, with an improved mixing system. The device is 3D-printed and uses a capillary to deliver p-H_2 gas into a Kenics mixer, using pairs of helices of alternating directions to improve p-H_2 dissolution in solution. The mixer is directly beneath the "sample volume", observed by the detector. A sample reservoir (d) is situated vertically above the detection reservoir ensures the sample volume remains full, while allowing p-H_2 gas to escape through capillary (c) and out through the headspace of the sample reservoir. This minimises sample loss while allowing experiments

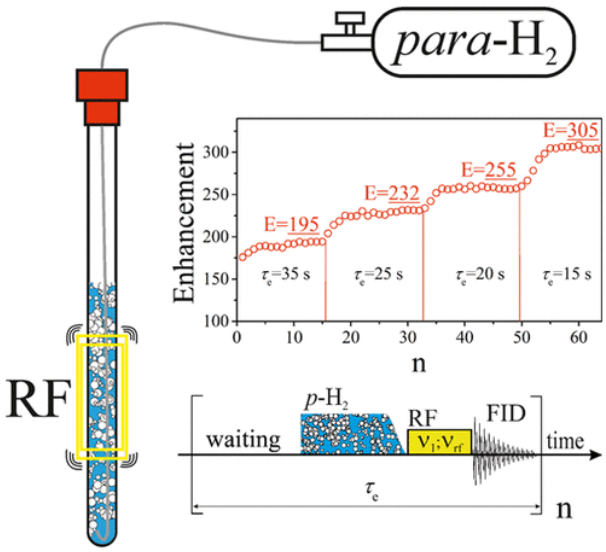

Figure 3.4: In-situ high field SABRE bubbling system with RF coil for polarisation transfer as presented by Pravdivtsev *et al.* (2015).[66] An RF coil is inserted into the NMR probe head of a high field instrument, directly around the NMR tube. This allows application of an RF field to generate polarisation transfer conditions. Reproduced from Ref. 65 with permission from the American Chemical Society.[66]

to be conducted during or after supply of p-H_2.

3.2.4 Concluison

Several polarisation transfer and bubbling systems have been implemented for SABRE, using both high and low field detection. All systems using external PTFs suffer from similar limitations, impacted both by the delay in changing from PTF to detection field, which allows for relaxation processes to occur following generation of hyperpolarisation; and restricting observation of short-lived intermediates. Transport from PTF to detection field exposes the sample to a field gradient between the PTF and detection field, which may allow unintended SABRE interactions including polarisation transfer to occur as the sample passes through fields in which transfer conditions are met. The former is solved either by exploration of longer-lived states or by implementing the fastest possible system of shuttling. The latter is solved exclusively by *in situ* detection. Either active field switching can be used to change from PTF to detection field immediately, or detection could be performed at the PTF to eliminate the need for change of field altogether.

While several such *in situ* systems now exist, at the inception of this project, solutions reported in the literature were bespoke developments, custom-built for a specific spectrometer and experiment. The only commercially available option, a Bruker delivery system, lacked the programming flexibility required for the pulse sequences planned for this research. This necessitated the development of our own system. Therefore, the aim is to create a robust and flexible solution with flexible timings for *in situ* gas delivery that could be applied to the full range of instrumentation within our group. This chapter details the development of such a *para*-hydrogen delivery system, designed to allow the

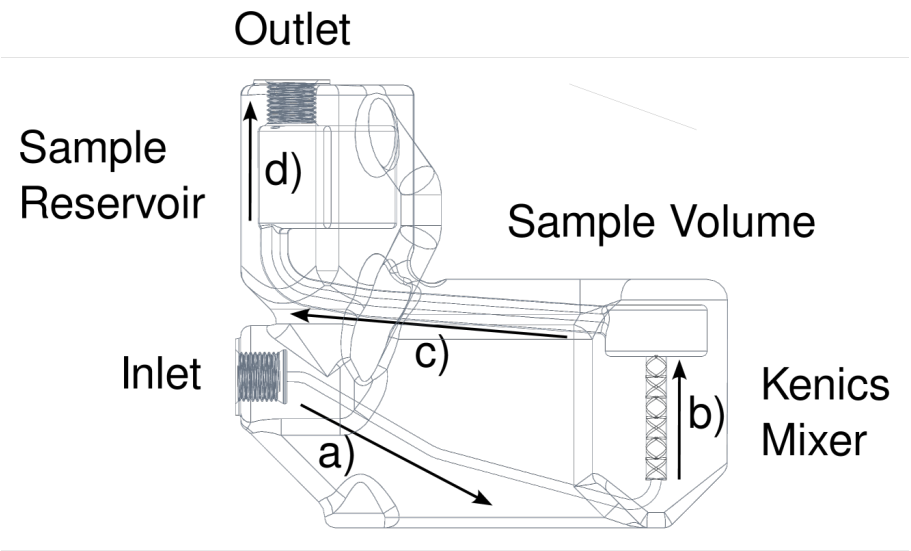

Figure 3.5: ZF/ULF SABRE instrumentation as reproduced from Myers *et al.* (2025).[71] © 2025 IEEE. A capillary inlet (a) allows p-H_2 gas flow into a Kenics mixer (b).

exploration of the very rapid interactions that follow polarisation transfer which have not as yet been explored.

3.3 *Para*-hydrogen generation and delivery

As described in Chapter 2, *para*-hydrogen is used as a source of spin-order for PHIP and SABRE hyperpolarisation experiments. p-H_2 can be generated by passing H_2 gas over a paramagnetic catalyst at a low temperature, where the lower energy singlet state is energetically favoured. Association of p-H_2 onto the surface of the paramagnetic catalyst breaks the symmetry of H_2, allowing spontaneous conversion between the *ortho*- and *para*- states, enriching the fraction of *para*-hydrogen in the gas.[146] For simplicity, enriched H_2 gas is referred to as *para*-hydrogen (p-H_2). To achieve a continuous supply of p-H_2 a system is required that can achieve a flow of *para*-hydrogen at low temperature across a catalyst. The enrichment of *para*-hydrogen is temperature dependent. In practice the conversion catalyst can be cooled using liquid nitrogen[147] or closed-loop liquid helium[147,148] as a cryogen, generating 51% or 94.3% respectively. The apparatus described here will use liquid nitrogen cooling, as it is significantly cheaper and less complex to set up than a closed loop helium system.

3.3.1 *Para*-hydrogen generation and the conversion manifold

Through all experiments in this thesis, p-H_2 was generated using a liquid N_2 conversion manifold. This was built by Dr. Fraser Hill-Casey and has not been altered as part of this thesis. The design, shown in Figure 3.6, has not been published previously and so is included here for completeness.

Hydrogen is generated through a commercial hydrogen generator. Both a Peak Scientific Precision 100 generator and an Erredue Mars 600N H_2 Generator have been used during this project. The Peak Scientific can provide up to 7.0 bar H_2 supply pressure at up to 0.1 L air min^{-1}. The Mars generator can supply 2 - 10 bar of pressure at up to 650 mL min^{-1}, and was incorporated into later developments. The higher pressure and flow rate on the Mars generator allow for more robust p-H_2 flow through the apparatus, achieved through setting the generator pressure higher than needed and down-regulating pressure and flow rate, but limit the exploration of SABRE processes at very low pressure (Chapter 5). The generator is connected to the manifold through steel gas lines and Swagelok valves (Figure 3.6). The gas lines on the manifold itself are similarly constructed. The manifold is clamped to a fixed clamp stand. This allows the entire system (shown in the schematic in Figure 3.6, between the dotted lines) to be raised and lowered relative to the liquid N_2 dewar.

The conversion coils are connected via Swagelok to the manifold. The coils consist of 16 turns of copper piping, packed with iron III oxide, stoppered at each end with glass wool. The iron oxide allows spontaneous conversion between *ortho*- and *para*-hydrogen. Lowering the manifold via the clamp allows the conversion coils to be submerged in the dewar of liquid nitrogen (pictured in Figure 3.6). At 77 K, H_2 gas passing through the coils while they are submerged allows enrichment to 50% *para*-hydrogen.[112] An Edwards E2m28 vacuum pump and external vent line are connected to the manifold through valves [2] and [3]. Valve [9] leads to a Young's tap, allowing p-H_2 to be added to the head-space

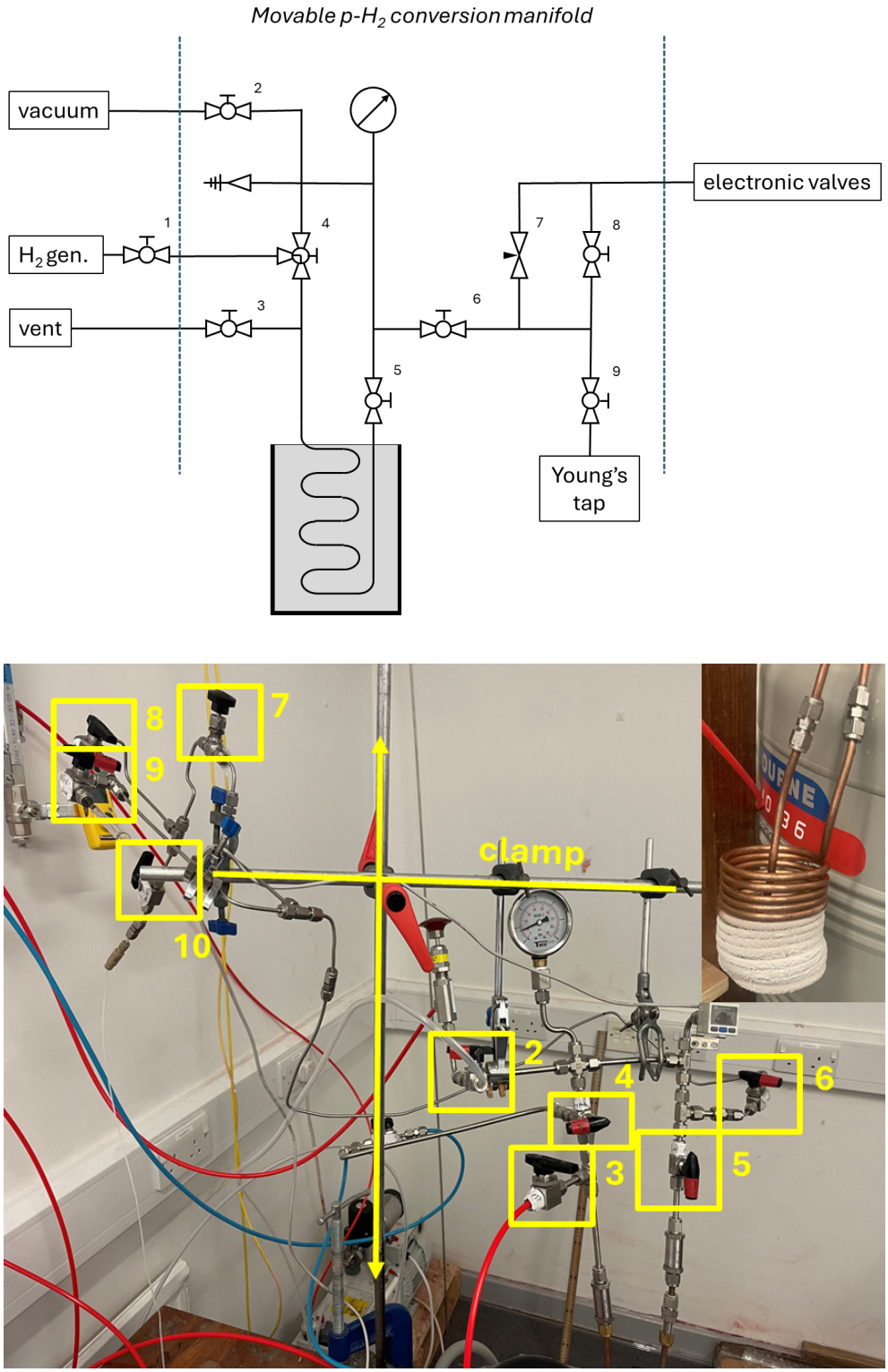

Figure 3.6: (Top) Schematic of the *para*-hydrogen conversion rig built by Hill Casey. (Bottom) Photograph of the conversion rig with values labelled. Inset upper right is the packed copper coil, pictured shortly after removal from liquid nitrogen.

of an NMR tube such that shake-and-drop experiments can be performed.

3.3.2 Normal experimental procedure

At the start of each experimental session, the *para*-hydrogen rig was set up using the following general procedure.

- The coil and valve manifold is put under vacuum for 10 minutes, with valve [2] open, the vacuum pump on, and valves [1], [4], and [6] closed. This step is of importance because failing to remove contaminants from the rig can result in the condensation of liquid oxygen in the conversion coils, which presents a safety concern if mixed with H_2 gas. Furthermore, the presence of any water in the lines will lead to ice blockages when submerged in liquid nitrogen.
- Valve [2] is closed and valve [1] is opened, filling the vacuumed coils with H_2.
- The manifold is lowered along the clamp stand to submerge the coils in liquid nitrogen. The top of the liquid nitrogen must be below the join. Submerging the join itself may cause leaks. Not submerging the coil enough can reduce the level of p-H_2 produced if the iron oxide is not sufficiently submerged for the entire mass to cool fully to 77 K.
- Valves [6] and [7] or [8] are opened, allowing flow of *para*-hydrogen to the electronic valve manifold.

The system is now set up and can be left for the duration of any experiments.

3.3.3 Electronic valve layout for gas delivery to cell

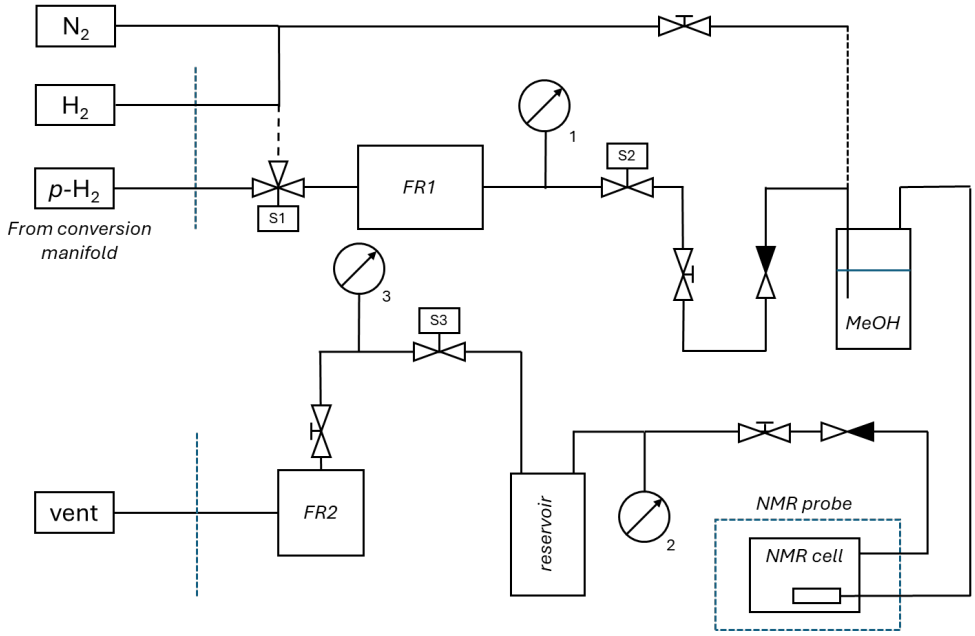

Figure 3.7: Diagram of current valve network. Clockwise from top left: p-H_2, H_2, N_2 are delivered from the p-H_2 conversion rig. Electronic valves are labelled S1 - S5 in order of flow. FR1 is the mass controller, FR2 the flow regulator. A solvent reservoir (discussed in Section 4.8) and an empty reservoir are included either side of the reaction cell. Manual valves, not numbered here, can be used to restrict flow across parts of the system for further control of gas flow.

Para-hydrogen generated in the conversion manifold is passed to an electronic valve network to allow electronic control of gas flow through the NMR cell. The schematic of this board is shown in 3.7 along with a photograph. This board is an adaptation of work by Dr. Hill Casey. It is designed to be modular, easily adaptable, and easy to identify problems and repair. Adaptations and improvements made to optimise performance are discussed in Chapter 4, Section 4.8.

The network is fixed to a laser-cut plastic base board containing a number of holes as mounting points. The network consists of a series of valves, reservoirs, pressure gauges and flow regulators, connected by $\frac{1}{16}^{\text{th}}$ inch PTFE tubing with IDEX connectors. Manually-operated and one-way valves are also IDEX components. The electronically switchable valves are NResearch HP225PK032 3-way isolation valves (Figure 3.7, S1-S3), screwed into the base board. FR-1 is a SMC M5 Pneumatic Regulator, set to limit outlet pressure at 7 bar. FR-2 is a flow regulator, set to 0.1 L air min^{-1}. Pressure gauges are NXP MPX5700GP (0 - 7 bar detection range) connected by greased push-fit 3/8" tubing. The in-line MeOH cell and sample reservoir are 25x25x40 mm blown glass cells with two 40 mm extensions for IDEX connections. The sample reservoir is empty, the solvent reservoir contains c. 18 mL (approximately 3/4 depth) of solvent. PTFE tubing extends to the bottom of the reservoir. These adaptations are discussed further in Chapter 4 Section 4.8.

Para-hydrogen is supplied to the system by the *para*-hydrogen generator detailed in section 3.3.1. H_2 can be supplied via the bypass from the generator. N_2 can be supplied from a nitrogen line. Electronically controlled switchable valve S1 allows changes between *para*-hydrogen, and hydrogen that has not been passed through the conversion coil. Switchable valves S2 (inlet) and S3 (outlet) control flow in and out of the cell. Flow regulator 2 (FR2) controls the rate of flow of gas immediately prior to exit through the vent. This is normally set to 0.1 L min^{-1}, matching the maximum output flow of the Peak Scientific hydrogen generator.

The electronic valve network, as illustrated in Figure 3.7, allows for electronic control of gas flow through the reaction cell. Software to control valve openings and additional functionality is outlined below. The valves have a response time of 5-20 ms (power on) and 30-5 ms (power off).[149] The flow regulator, in combination with the pressure set at the hydrogen generator, give broad control of the rate of flow of gas through the system, with the pressure capped to prevent damage to glassware.

3.4 Design and construction of electronic control box

A method of delivering controlled gas flow in time with a pulse sequence is needed. This control system must be able to interface between computer, spectrometer, and the physical valves. This can be done by using a microcontroller, to which information is passed from the computer and from which valve actuation is driven.

Fast processing speeds on the microcontroller are uninhibited by any peripheral computer operations, giving us highly responsive valve control in reaction to pulse sequence or spectrometer commands. A microcontroller with dedicated power supplied and digital outputs can also be used to directly provide power to valves and electronic peripherals in the electronic valve network such as pressure gauges.

This section details the changes made to a prototype valve controller system originally built by Dr. Hill-Casey. An Arduino Mega 2560 microcontroller was mounted on a breadboard, to give controllable gas flow in parallel to an NMR experiment or pulse sequence. The breadboard also housed valve driver cards and digital pressure gauges. Software written in Labview was used to control the Arduino. A number of improvements were needed to this prototype, to give improved robustness, moving away from fragile prototype design on the breadboard, improved portability, and improved code adaptability and responsiveness.

To do this, the prototype was redesigned and built in collaboration with Chris Rhodes in the Department of Chemistry Electronics workshop. The breadboard wiring was repackaged into an electronics control box, with improved scope for development and adaptability. This is detailed in section 3.4.1. New software was developed including a control script loaded directly onto the Arduino (Section 3.4.2) and a Graphical User Interface written in MATLAB (Figure 3.10).

3.4.1 Arduino valve controller unit

The Arduino Mega 2560 microcontroller ("the Arduino") remains the central device in the valve controller system. This device is shown in Figure 3.8.

The Arduino Mega 2560 microcontroller housing also includes a 24 V power supply, five NResearch CDS-V01 valve driver cards, and 16 programmable status LEDs on the front panel. The rear panel includes TTL connections, 8 stereo jack ports for valve power, a Serial connection for the interface to PC, and connections to the three digital pressure gauges PG1-3 as well as PG-0 on the p-H_2 conversion manifold. There is additional space inside the device to allow for independent control of up to 8 valves.

3.4.2 Valve controller software

All valves are controlled by an Arduino Mega 2560 programmable microcontroller. This allows observation of the network state and provides rapid response to manual or automated inputs for automated gas flow through cells in time with NMR pulse sequences. The software developed for this microcontroller allows the user to interface with the pressure sensors and valves via Serial input or through TTL (transistor-transistor logic) input pulses. The user can interact with the software directly, through the Graphical User Interface (GUI) (Section 3.4.3), or indirectly via the NMR spectrometer using either TTL digital logic inputs (Section 3.4.4) or pre-loaded bubbling sequences (Chapter 6, Section 6.4.1). The Arduino device runs software in two stages: an initial "setup" procedure followed by a continuous loop, where it waits for user input. Figure 3.9 illustrates the decision tree the script follows while running.

In this software, setup initialises a connection over a Serial line. The loop then continuously checks for Serial inputs, followed by TTL inputs when enabled, and can be asked to output pressures read from pressure gauges. The loop function runs continuously, as fast as the Arduino is able to process commands at the Arduino's 16 MHz clock frequency.[150] The script has two control modes: a TTL control mode, in which TTL inputs to the microcontroller determine valve state, and a Serial mode, in which user input through the User Interface (Figure 3.10) or pre-loaded bubbling sequences (Chapter 6) are used to determine valve state. The valve states can be output continuously alongside the pressures when pressure logging is enabled. Measured pressure is shown directly on the user Interface and can be saved for post-hoc analysis through the UI through user input or automatically as part of a pulse sequence. Pressure logging may only occur after a fixed, hard-coded interval $t_{(log)}$ has passed since the previous logging event.

3.4.3 Manual control

The manual control mode of the Arduino script allows the user to change all valve states through a graphical user interface (GUI). This provides options for testing, debugging, and running experiments that do not need precise time control in their gas delivery. The

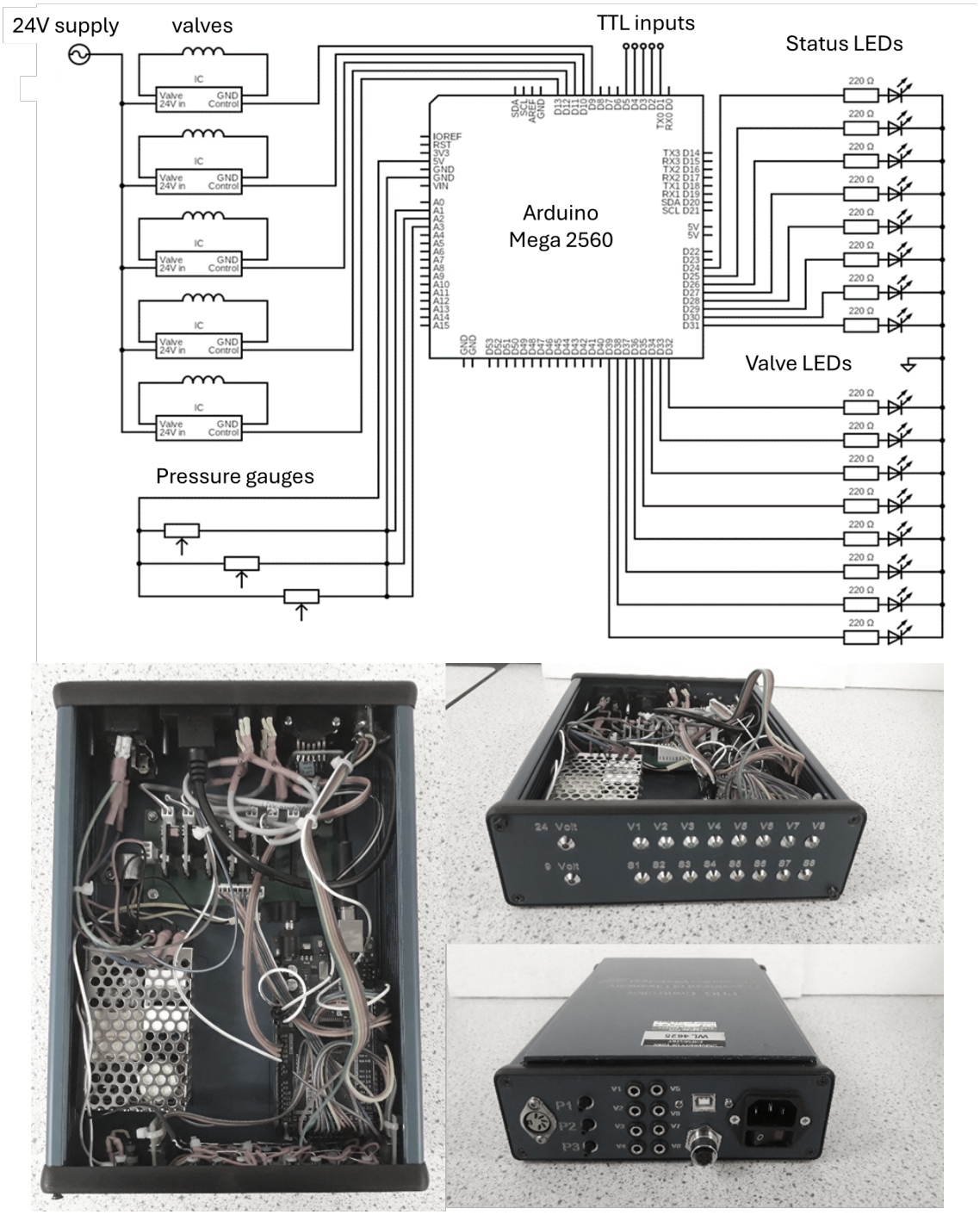

Figure 3.8: Valve controller unit. Top: Circuit diagram of the internal electronics of the valve controller unit, centred on the Arduino Electronics schematic. Bottom: Photographs of the device.

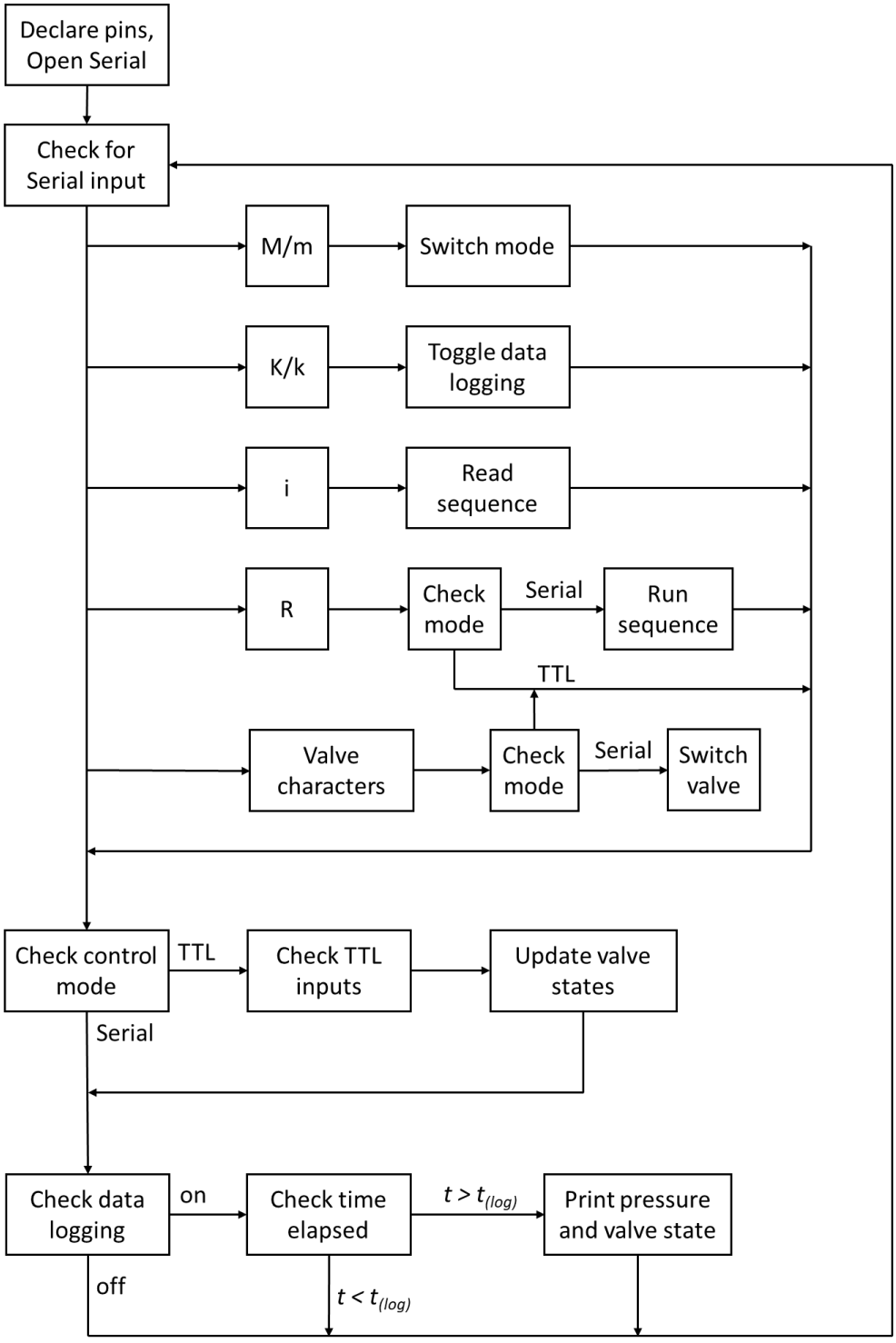

Figure 3.9: Flow chart illustrating the sequence of processes followed by the Arduino running the valve controller software. Summaries of input characters are given in Table 3.1, and the characters for switching individual valve states ("Valve Characters") in Table 3.2. The reading and running of pre-loaded sequences is discussed in Chapter 6. $t_{(log)}$ is the hard-coded elapsed duration after which pressure logging may be executed. The full script is given in Appendix A

Table 3.1: Table of Serial input characters to VCU and their effects

Character input	Function
M	Run in Automatic mode, ignoring Serial commands for valve switching
m	Run in Manual mode, ignoring TTL inputs
K	Record and print gauge pressures over Serial
k	Stop recording & printing system pressures
i	Initialise semi-automatic sequence; wait for remainder of sequence input.
R	Run currently loaded semi-automatic sequence

GUI also provides a live plot of the pressures as recorded by the pressure gauges to allow a user to monitor the ongoing state of the gas manifold. This interface is shown in Figure 3.10.

For all GUI functionality, a Serial port must be specified and a Serial connection must be opened. The UI then provides options to switch between automated TTL control, pre-loaded sequence control ("Spinsolve control", discussed in Chapter 6), and manual control. Pressure reporting for all or individual pressure gauges can be toggled. Recorded pressure data can be recorded manually or automatically at the end of an experiment. The mode can be toggled over the Serial connection at any time. Pressure logging, and semi-automated bubbling sequences, can likewise be input to the microcontroller at any time. These Serial inputs are detailed in Table 3.1. The semi-automated bubbling sequence procedure is detailed further in Chapter 6 Section 6.4.1.

The input characters and their corresponding function are detailed in Table 3.1. While accepting manual inputs, the Arduino will not check for TTL inputs. If the Arduino is set to manual mode, valves will be open and closed in response to the character inputs laid out in Table 3.2.

Table 3.2: Table of Serial input characters for switching valve states while the Arduino is in manual control mode.

Character input	Function	Valve
Z	Open Short valve	S5
z	Close short valve	
C	Open inlet valve to cell	S2
c	Close inlet valve to cell	
V	Open cell outlet valve	S3
v	Close cell outlet valve	
X	Open Nitrogen Inlet	S4
x	Close Nitrogen inlet	
H	Switch to non-polarised H_2	S1
h	Switch to *para*-hydrogen	

3.4.4 Automatic control

When set to automatic/TTL control, manual control of valves is disabled. The Arduino instead continually checks for voltage applied to the TTL pins. The response to each pin is customisable. There are 5 TTL input pins, each assigned a value from 1 - 16 to allow a maximum of 32 different valve states, according to the sum of the value of the input pins. The assigned value of each pin combination in the current setup is given in table 3.3, alongside TTL inputs to functions. Valve switching takes up to 30 μs.

Table 3.3: Valve state responses to each combination of TTL inputs

sum of pin values	Active pins	Valves/sequence
0	none	All closed
1	0x10	Fill & bubble (inlet open, 3s delay, outlet open)
2	0x20	Open bubble (inlet & outlet open)
3	0x10 and 0x20	Fill cell (inlet open)
4	0x08	Drain cell (outlet open)
5	0x08 and 0x10	Flush with nitrogen (nitrogen, inlet and outlet on)
6	0x08 and 0x20	Available (all closed)
7	0x08, 0x10, 0x20	Available

Manual control of the Arduino is achieved through a custom developed MATLAB application graphical user interface (GUI). The GUI (version 9.S5) is shown in Figure 3.10. The left side gives options for managing the Serial connections (blue box), changing control modes and changing valve state when in manual mode (pink box), and toggling pressure gauge display (orange box). The system is by default in automatic/TTL control mode until another control mode is selected.

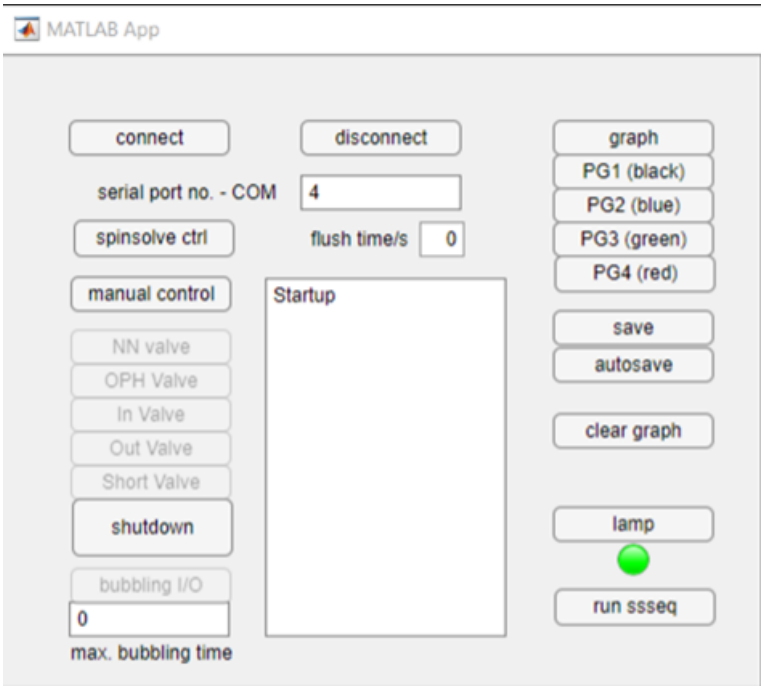

Figure 3.10: MATLAB application graphical user interface (version 9.S5)

3.5 Pressure gauge calibration and data-logging

The Arduino reads pressure gauge inputs into the analogue pins as 10-bit digital values. To convert these inputs into pressures for display, the pressure gauges were calibrated against the digital pressure gauge PG-0 on the movable conversion manifold, which displays relative pressure.

Using these calibration data, pressure can be determined from voltage using equation 3.1, where V_{obs} is the observed voltage, V_0 is the offset voltage at $P = 0$, and c is the calibration constant.

$$V_{obs} = V_0 + cP \tag{3.1}$$

Voltage is given in arbitrary units as a 10-bit number reported from the Arduino's analogue input pins. Figure 3.11 shows the calibration plot used to calculate output pressures for pressure gauges 1-3. The calibration values for each pressure gauge are given in Table 3.4.

Below 0.5 bar, the relationship between supplied voltage and pressure is no longer linear. For PG-1, under 0.5 bar of pressure there is a sudden drop away from the linear pressure voltage relationship, with the pressure gauge recording a voltage value of 25 at zero pressure instead of the expected 98. This non-linear region has not been characterized due to the difficulty in supplying pressures under 0.5 bar using the nitrogen regulator and the H_2 generators' minimum supply pressure of 1 bar. The Mars H_2 generator has a minimum supply pressure of 2 bar. For PG2 the residual voltage value at zero pressure is 80 as expected. To avoid recording spurious negative relative pressures for PG1, the

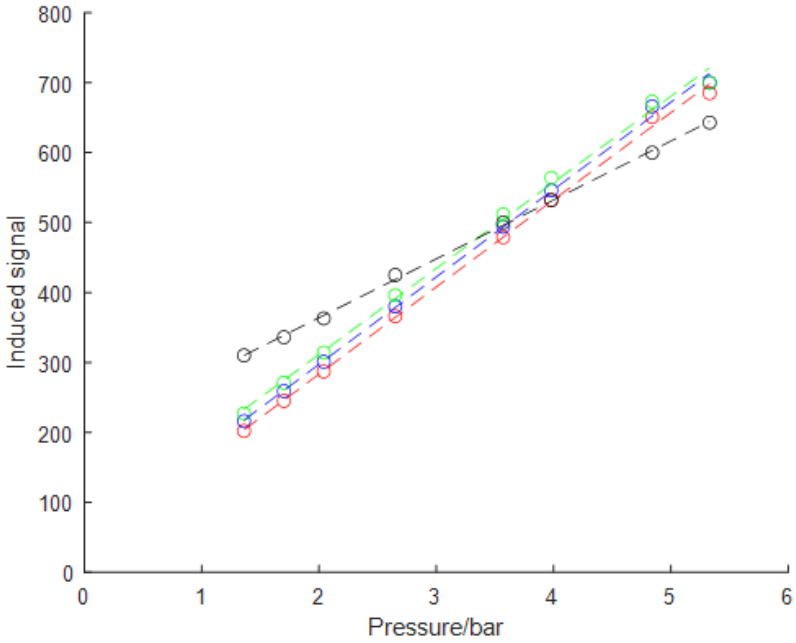

Figure 3.11: Pressure gauge calibration plot. Digital input recorded on the Arduino vs gauge pressure recorded by PG-0 on the p-H_2 conversion manifold. Black: PG-0, Red: PG-1, Blue: PG-2, Green: PG-3. Calibration values are given in Table 3.4.

Table 3.4: Calibration values for pressure gauges.

Pressure gauge	$\mathbf{V_0}$**/a.u.**	**c/bar**$^{-1}$
PG-0	194	84.5
PG-1	29.7	125.7
PG-2	41.6	128.6
PG-3	43.2	128.6

output is set to 0 for any readings below 98. No experiments were conducted with a supplied pressure below 2 bar. Future iterations of the Valve controller unit may use upgraded pressure gauges to allow improved recording.

3.5.1 Pressure recording during experiments

Pressure recorded by the Arduino is added to the Arduino's data recording string, which also monitors changing valve states. This string is returned to the GUI via the Serial line, where it can be displayed, saved manually, and saved automatically as part of an experiment. This allows for manual testing of the system, to observe gas flow and check for leaks. Examples of system tests without and with leaks in gas flow when the system is held at pressure are shown in figures 3.12 and 3.13.

Live pressure monitoring throughout the course of an experiment allows for an accurate calculation of the concentration of H_2 in solution in a sample cell, which is required to understand reaction kinetics (Chapter 5)

Using the UI and manual manipulation of the valves, a SABRE-type gas bubbling sequence can be mimicked, and the pressure response of the system can be observed. The state of the switchable valves is reported during the experiment and can be plotted alongside the pressures.

An example monitoring experiment is presented in Figure 3.12. N_2 is used instead of p-H_2, and all cells are empty. In part 0, all valves are closed, and there is no nitrogen pressure in the system. In Part 1, the N_2 supply valve SV-2 is opened, and the inlet network is pressurized with nitrogen. This is indicated by the sharp rise in pressure monitored on PG-1. In part 2, the inlet valve is opened, allowing N_2 flow into the cell network (pink in Figure 10). The drop in pressure in the inlet occurs as gas flows into the cells, resulting in the corresponding rise in pressure in the cell network at PG-2. In part 3, the N_2 supply valve is turned off, isolating the gas in the inlet and cell networks. The pressure remains constant until part 4, where the outlet valve SV-4 is opened. This allows the cell network to drain to vent, causing the observed drop to 0 pressure. In part 5, the inlet valve is opened, exposing the inlet to vent and causing the pressure in the inlet network to fall. The pressure in the outlet network briefly rises as the inlet volume is connected before both falling together to 0. (A summary of these steps is given in Table 3.5.)

This monitoring experiment demonstrates that the inlet and cell sections of the valve network can be pressurised and isolated to hold gas without leaking.

3.5.2 Leak testing

A similar monitoring experiment to that described above can be used in conjunction with manual valve switching to detect and resolve gas leaks in the system. Manual control

Table 3.5: Valve openings and effects.

Stage	Valves open	Effect (no leak)	effect (leak)
0	none	no gas movement	no gas movement
1	1	inlet network fills	inlet network fills
2	1, 2	cell fills	cell fills
3	2	cell holds with supply	cell holds with supply
4	none	cell holds at pressure	pressure in cell falls through leak
5	3	gas drains from cell	gas drains from cell
6	2, 3	gas drains from whole network	gas drains from whole network

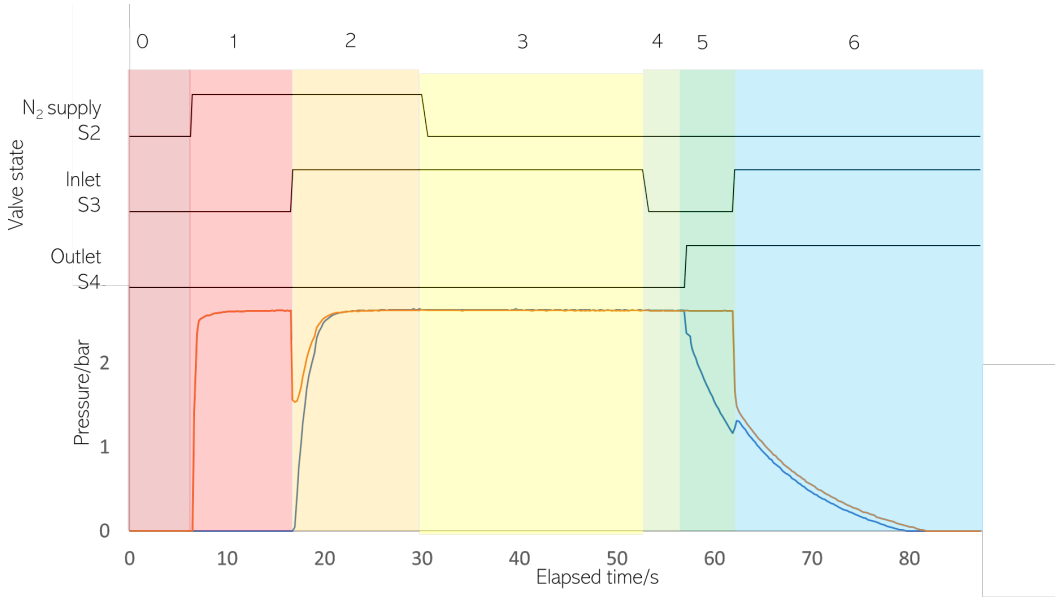

Figure 3.12: A pressure monitoring experiment which can be used to show correct functioning of the gas control system. Pressure (bar) is plotted against time (s) for inlet pressure (orange) and cell pressure (blue) with Nitrogen (5.2 bar supply). Changes in valve state are shown above. The effects of each change are given in Table 3.5.

of the valves can be used to pressurise and then isolate a portion of the network. Once a section of the line has been pressurised, the electronic pressure gauge for that section of line can be monitored, with falling pressure indicating a leak. Leak location can be isolated through use of leak detector fluid, and in some cases through audible hissing. Once a leak has been repaired the test can be repeated. Figure 3.13 shows an example of a pressure trace with a leak introduced through loosening a joint in the gas lines at the connection to the cell, with the effects of changing valve states detailed in Table 3.5. The pressure trace follows similarly to 3.12, being charged sequentially with nitrogen through the inlet and cell networks. Once the cell is isolated from supply of fresh gas the pressure inside falls rapidly, before gas is allowed to flow out through the outlet. For unknown leaks, the manual valves in-line can be used to further narrow down the affected section of gas line.

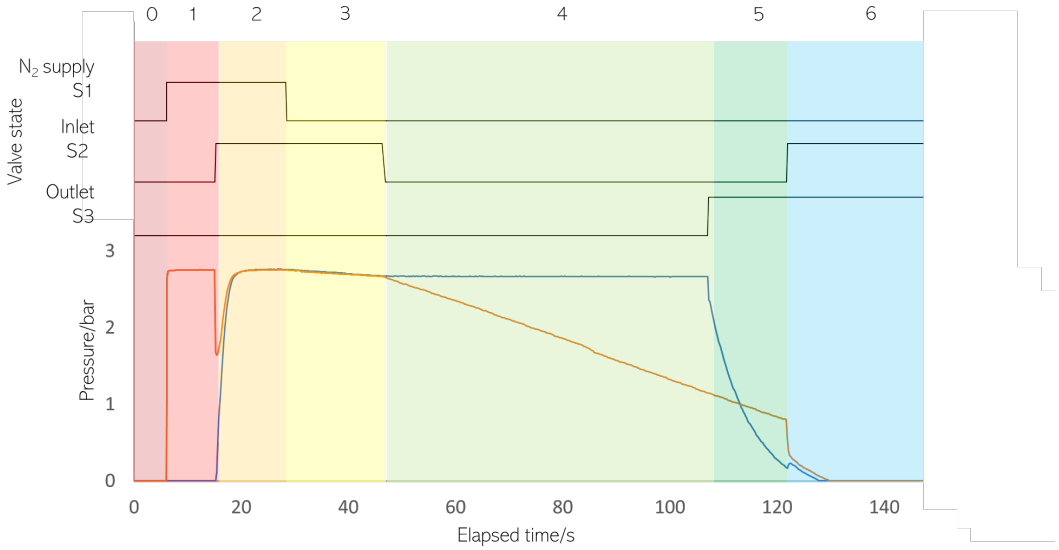

Figure 3.13: Leak test of the outlet region (white in Figure 10). Pressure (bar) is plotted against time (s) for inlet pressure (orange) and cell pressure (blue) with nitrogen (5.2 bar supply). Valve switches are shown above. For this test the manual valve immediately prior to FR-2 (Figure 3.7) was closed initially to prevent the outlet manifold draining to vent. 1 and 2: The inlet and cell networks are charged with nitrogen. 3: the outlet valve is opened, pressurizing the phase separator. The large dead volume in the vessel gives the large pressure drop and long recovery time to stable. 4: The N_2 supply is cut, shortly followed by the inlet valve. This leaves the cell and outlet networks connected while the inlet is isolated, remaining stable after the initial drop caused by brief exposure to vent without supply. The cell and outlet networks leak through 4 via the phase separator. 5: the manual valve is opened exposing the system to vent. 6: the inlet valve is also opened, exposing the inlet network to vent also and allowing all pressure to return to 0.

3.6 Flow rate and pressure differential

The final element of the system to be explored is the flow regulator situated at the end of the outlet section. The flow regulator is a manually tuned device which can be set to

allow between 0 and 0.5 L min^{-1} air to flow out the cell supply manifold to vent, through a screw-thread valve. This flow regulator can be used to controls the pressure differential between the two measuring points, PG-1 and PG-2, hence across the cell. The effect of tuning the flow regulator on inlet and cell pressures, and hence pressure differential, is shown in Figure 3.14, with flow rate set at 0.1 to 0.5 L min^{-1} air. Regulators with different graduations (0 – 0.1 L min^{-1} air for example) can also be introduced into the system should larger or smaller pressure differentials become necessary.

Higher flow rates slightly reduce inlet pressure to the cell, and more significantly reduce outlet pressure. This pressure differential varies linearly with flow rate, as shown in Figure 3.14. Pressure differential changes by 0.51 kPa L^{-1} min air.

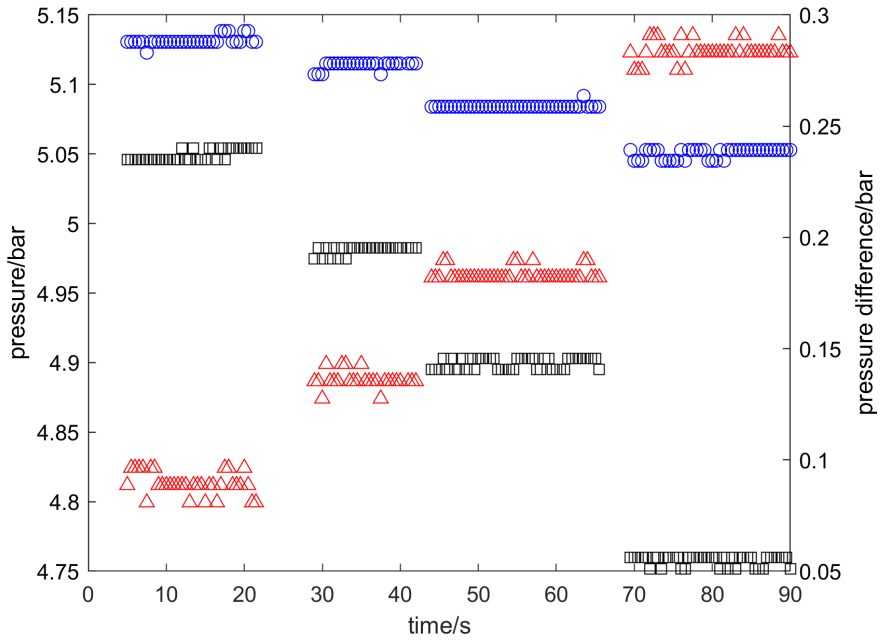

Figure 3.14: Plot of pressure against time for the flow regulator set at 0.1, 0.2. 0.3 and 0.5 L min^{-1} air, at the inlet (blue ○) and cell (black □) pressure gauges. 5.15 bar of inlet pressure was set. The flow regulator is changed manually at between each setting. The difference in pressure is overlaid (red Δ), with the pressure difference on the right axis.

3.7 Conclusion

A gas flow system, including a p-H_2 generator, electronic gas valve network, microcontroller system were developed, to give controlled, time-precise flow of p-H_2 or an alternative gas through a cell in an NMR spectrometer. The relevant software has also been developed for a user interface, automated running of the microcontroller, direct interface of the microcontroller with systems capable of supplying TTL pulses, and partially automated scripts to allow for time-resolved controlled bubbling when interfacing with systems that do not have this capability.

This system allows the performance of several novel capabilities when attempting SABRE-hyperpolarised NMR experiments. The system can be safety checked and leak-tested. This allows confirmation that gas flow is one directional through the system, and to prevent back-flow of sample out of a sample cell. Sample volume forced into the outlet in handling errors or due to excessively vigorous bubbling can be trapped in a small reservoir before it reaches electronics.

NMR experiments can be performed with bubbling added as part of the pulse sequence, allowing control of gas delivery in time with NMR pulses and control over timing of SABRE hyperpolarisation generation relative to acquisition.

2D experiments, or multiple-scan 1D experiments which include a bubbling step can be performed *in situ* in an NMR spectrometer, with timing and pressure delivery to give consistent concentration of gas into solution. This allows for SABRE experiments in low-field (Chapter 4) instruments. Performance of SABRE with polarisation transfer at the PTF using a high-field instrument will require a field cycling/shuttling mechanism. The development of such a system is shown in Chapter 6.

The system can be interfaced with a variety of instrumentation. Instruments capable of outputting TTL pulses can be connected directly, and any other device can be directed through its software to delivery gas in time-controlled sequences over a Serial connection, allowing the potential to interface with any spectrometer. The adaptations made to enable this automated Serial control are detailed in Chapter 6. The live pressure monitoring system allows for p-H_2 concentration monitoring during experiments. The system will be demonstrated on an Earth's field and benchtop spectrometer. Chapter 4 will illustrate this bubbling system being interfaced with a Magritek Terranova Earth's Field spectrometer, demonstrating the bubbling capability offered and using the system to optimise p-H_2 delivery for performance of SABRE in the Earth's field.

Some improvements to this system could be made should future work necessitate them. For example, the flow regulators and the system pressure, driven by the generator, are set manually and cannot in this setup be adjusted electronically; hypothetical experiments which require mid-sequence changes in gas discharge would require an alternative system. No need for such a system was identified during this project, though software control of supplied H_2 pressure would offer reductions overall experiment time and potential for further control should it be needed.

CHAPTER 4

EFNMR optimisation

4.1 Introduction

The previous chapter established a delivery system for *para*-hydrogen to a reaction cell in time with an NMR pulse sequence. In this chapter, the effectiveness of the new instrumentation will be demonstrated through *in situ* SABRE hyperpolarised experiments using an Earth's Field spectrometer, facilitating the exploration of SABRE dynamics in the low-field (LF) and ultra-low-field (ULF) regimes. Following this initial demonstration of capability, the instrumentation is then used to develop methodology for reaching a consistent, reproducible concentration of p-H_2 in solution, which will allow deeper studies of the dynamics of the SABRE reaction in controlled conditions not otherwise possible. This work focusses in particular on detection in the Earth's magnetic field. Packard and Varian in 1954[151] offered the first suggestion that the Earth's field could be used for detection of nuclear precession, making Earth's field NMR (EFNMR) almost as old as NMR itself. The Earth's field offers a number of advantages for the performance of NMR spectroscopy, being highly homogeneous, globally available, and free. However, Earth's field spectroscopy is limited by its insensitivity even in the context of already insensitive NMR. With a field of around 50 μT, a sample in the Earth's field would have a thermal polarisation well under 1 ppb. This very low field also makes EFNMR very susceptible to interference from ferrous and magnetic objects, and sources of ultra-low frequency noise such as electronic devices.[152] Further, at ultra-low field, chemical shift collapses, which results in spectra showing only heteronuclear J-coupling.

To overcome the extremely low sensitivity, EFNMR is almost always coupled with hyperpolarisation techniques to allow generation of sufficient polarisation to be readily detectable. The most common approach involves using a much stronger, temporary pre-

polarising field to increase the initial magnetisation before detection in the Earth's field. When coupled to brute force pre-polarisation, the Earth provides a very homogeneous B_0 field over relatively large sample volumes, (hundreds of mL vs. hundreds of μL for standard NMR) allowing for sub-Hz line-widths that are stable over the timescale of an NMR experiment. This is difficult to achieve using, for example, an electromagnet to provide the main magnetic field.

Practical uses of EFNMR are very limited. It has proved useful for educational purposes but has found little further application. The Magritek Terranova EFNMR spectrometer was released in 2005, based on work in Antarctica measuring brine in sea ice[152] as a portable device which could be easily operated in harsh, remote environments. Foundational studies soon established its utility for complex experiments beyond simple detection. For instance, Robinson *et al.*[85] demonstrated the viability of two-dimensional NMR at Earth's field by observing magnetisation transfer from heteronuclear J-couplings. This work was also significant because it showed that EFNMR instruments could be used indoors in lab settings, provided adequate screening was used to work around interference from electronics. In studies closer to its original design purpose, Callaghan *et al.*[152] used EFNMR spin echoes and CPMG trains to analyse molecular diffusion. This was applied to studies of brine volume and diffusivity in Antarctic sea ice for climate and ecology modelling, where the minimal ULF interference made the technique particularly effective. Pushing the instrumentation further, Halse *et al.*[153] demonstrated 3D MRI using the Terranova to take low-resolution 3D images of a capsicum. This was achieved through the use of pre-polarisation and ULF noise shielding to allow broad applicability, less limited by noise sources or interference from ferrous magnets, as might be found indoors in the laboratory setting.

Beyond pre-polarisation, the Terranova has also served as a platform for other advanced hyperpolarisation methods. Early experiments by Halse and Callaghan,[154] for example, coupled the instrument with Dynamic Nuclear Polarisation (DNP). They achieved signal enhancements of 3100 compared to thermal equilibrium on 100 mL water samples doped with TEMPO. This work demonstrates the viability of applying more complex hyperpolarisation techniques at ULF, the successful implementation of *Para*-hydrogen Induced Polarisation (PHIP) in the Earth's field soon followed,[155] setting a precedent for the subsequent exploration of the related SABRE technique in the same regime.

The first implementation of *in situ* SABRE on the Terranova spectrometer was reported by Hill-Casey *et al.* in 2019.[74] This work adapted a commercial p-H_2 delivery system originally developed for high-field NMR flow applications[59] for use in the low-field regime. Using this setup, the activation of the SABRE catalyst was observed and the dependence of signal enhancement on the Polarisation Transfer Field (PTF) strength was explored.

However, the adapted commercial system presented significant limitations for studying SABRE dynamics, as it does not allow bubbling to be switched during the pulse sequence. Rossetto describes the system as prone to blockage, and with inconsistent pressures and flow rates.[156] These challenges formed the primary motivation for developing the bespoke instrumentation detailed in this thesis. The work presented here is therefore a direct development of the instrumentation detailed by Rossetto and Hill-

Casey[156], designed specifically to overcome these previous limitations and enable a more controlled exploration of SABRE dynamics in the Earth's Field.

All Earth's field NMR experiments in this thesis were conducted on a Magritek Terranova MRI spectrometer programmed through the manufacturer's controlling software, Prospa (Magritek Ltd, Aachen, Germany). This chapter will demonstrate integration of the custom-built *para*-hydrogen delivery system (detailed in Chapter 3) with the Terranova EFNMR spectrometer to create a platform for *in situ* SABRE studies. Key experimental parameters, including gas pressure, bubbling duration, and Polarisation Transfer Field (PTF) application time, are optimised. This allows a robust methodology to be established for achieving maximum, reproducible signal enhancement. The effectiveness of gas mixing to generate even hyperpolarisation throughout solution is explored, using MRI to visualise the spatial distribution of hyperpolarisation. Finally, methods for extending sample lifetime by minimising solvent loss and catalyst degradation are explored and validated.

4.2 The Terranova Earth's field NMR Spectrometer

4.2.1 Terranova components

The Terranova system consists of two main components: a box of control electronics, typically referred to as the "spectrometer" or "Digital Signal Processor" (DSP), and a set of concentric coils for exciting and detecting the NMR signals, into which the sample is inserted, called the "probe". The DSP performs signal acquisition, supplies power to the probe coils, and is the interface to the controlling PC. The probe is centred inside a set of 3 Helmholtz coils, oriented along the x', y', and z'-axes of the laboratory frame of reference, as shown in Figure 4.1(a).

The three coils that make up the probe are shown in Figure 4.1(b). The largest, outer coil is the B_P polarising coil, which generates a magnetic field down the bore, along the x-axis, ranging from 0 to 18.8 mT. The purpose of this polarising coil is to generate a pre-polarising pulse for brute-force polarisation, generating much larger bulk polarisation than exists thermally in the Earth's field. The inner coil is the B_1 transmit-receive coil. This coil generates the RF pulses and detects the NMR signal. The middle part is a set of gradient coils. These are used to apply linear magnetic field gradients along the x, y, and z axes. Application of gradients can be used to remove magnetic field inhomogeneities from the field inside the probe, minimising signal line-width and maximising spectral amplitude and resolution for higher-quality NMR data. Gradients can also be applied to a sample to spatially encode frequency across the sample in MRI.

(a) (b)

Figure 4.1: (a) Photograph of external additions surrounding the Terranova probe. Shielding coils (black) are wrapped concentrically about the x'-axis. Helmholtz coils are centred on the probe in the x'-, y'- and z'-axes. (b) Primary components of the Terranova probe. Left: B_0 polarising coils. Centre: Shim/gradient coils. Right: B_1 RF transmit/receive coils. When assembled these coils are seated concentrically inside each other from inside/right to outside/left.

4.2.2 External additions for field control and noise reduction

Two additions have been made around the probe in order to improve field homogeneity, reduce noise, and improve the utility of the instrument inside a lab environment. Both of these additions were covered in detail in the PhD thesis of Matheus Rossetto[156], but are covered again here for completeness. Adjustments made to the system outlined by Rossetto are highlighted.

Field can be applied in either direction in any coil through reversal of the direction of current flow. In Earth's field NMR, there is an inherent misalignment between the spin and lab frames of reference. The lab frame can be represented in 3D space by x'y'z' axes, with the B_1 coil the point of reference along the x'y' plane. By NMR convention, B_0 is aligned positively along the longitudinal z axis of the spin frame which is represented by xyz axes. In the literature, the probe has been rotated to align the x'z' and xz planes.[153] In this system, due to spatial constraints, small adjustment fields using the Helmholtz coils are used instead to drive this alignment.[156]

Six concentric Helmholtz coils, shown in Figure 4.2.1 are added in pairs around the instrument, in the x', y' and z' axes. These coils have a radius of $\sim$ 60 cm and are separated by $\sim$ 30 cm, centred on the middle of the probe. These are powered by a GW-Instek GPP-4323 external programmable power supply. Power is supplied at 5 V and a range of $\pm$200 mA.

This alignment along the z'-axis is particularly useful because it allows for linear

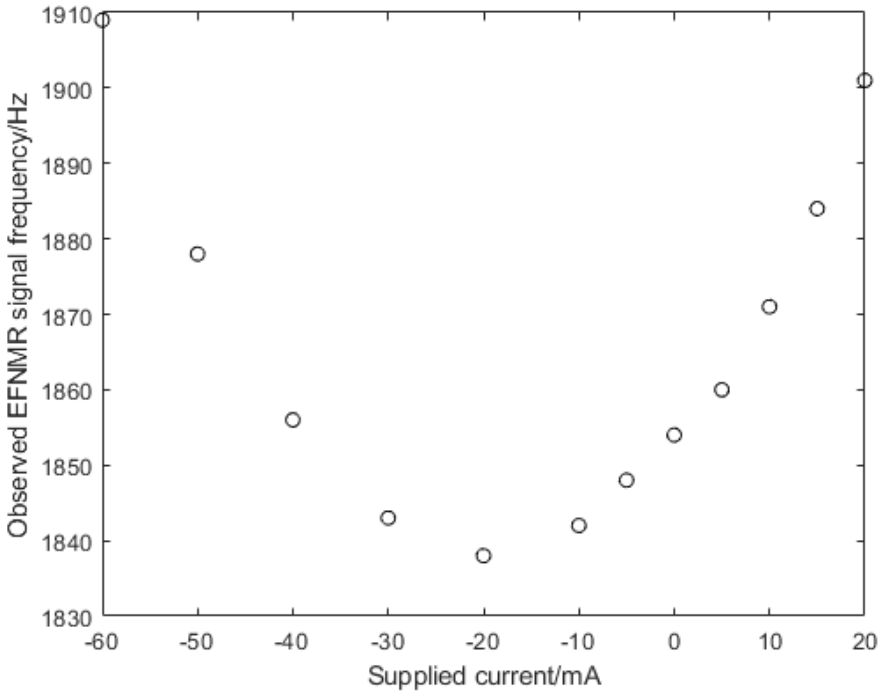

Figure 4.2: Frequency dependence of observed ^{1}H EFNMR signal against applied current through the x Helmholtz coil. A minimum is observed at -20 mA. 0 A current is supplied through both y- and z- coils. Negative current is supplied by reversing the direction of flow through the coils from the power supply.

adjustments to the B_0 field strength by changing the current applied through the z-Helmholtz coil. This allows rapid, linear changes to the B_1 frequency. Experiments in this thesis are performed at approximately 2210 Hz, in line with the setup described by Rossetto. Adjustments were made where necessary in supplied z-Helmholtz coil current to maintain this approximate frequency across all experiments.

This allows for studies of the SABRE reaction to be performed *in situ*, allowing for repeatability, 2D experiments, and zero-delay PTF-detection timings.

To align the field along the z' axis, the fields B_x and B_y must be 0. Observation of the Larmor frequency of the peak as a function of current applied to each Helmholtz coil can be used to determine the optimal field to apply through each Helmholtz coil in each axis to align the spin frame with the lab frame. The field is at zero in an axis when the Larmor frequency reaches a minimum. Figures 4.2 and 4.3 show the frequency change of the observed EFNMR peak of 500 mL of water as the applied current is changed through each Helmholtz coil. Frequency minima occur at -16 mA for the X coil and 55 mA for the Y coil, aligning the field along the z-axis at these values. Figure 4.4 shows the linear change in field with applied current in the Z Helmholtz coil when these X and Y values are applied, confirming the desired alignment of the field along the z-axis. This calibration can also be achieved by rotating the entire probe apparatus so that the Earth's field aligns with the probe x-axis, thus eliminating the need for application of an X-Helmholtz field.[153,156] This has not been done here due to space constraints in the current laboratory setup an noise directionality.

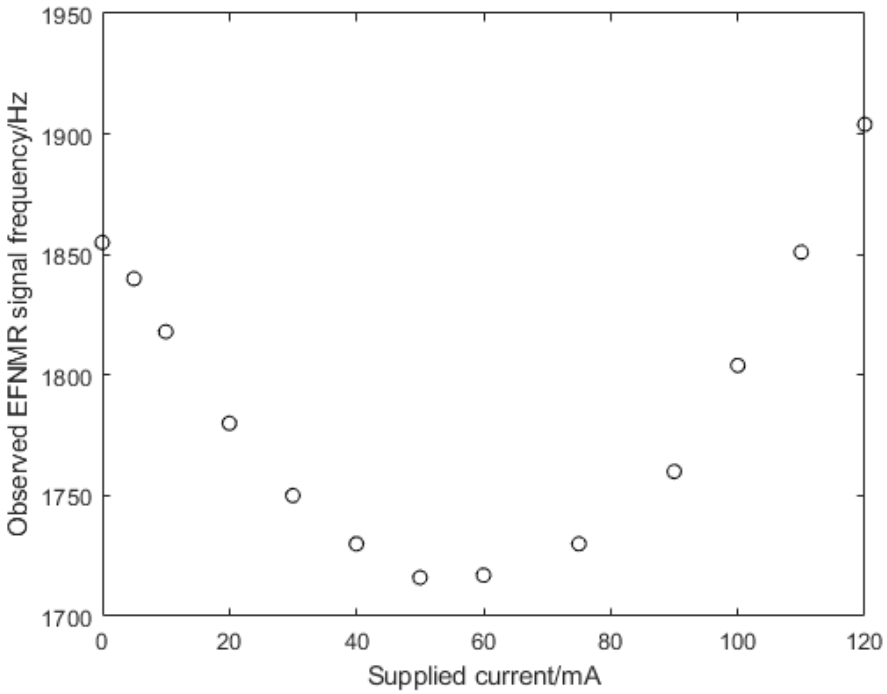

Figure 4.3: Frequency dependence of the observed ^{1}H EFNMR signal against applied current through Y Helmholtz coil. A minimum is observed at 55 mA. 0 A current is supplied through both X- and Z- coils.

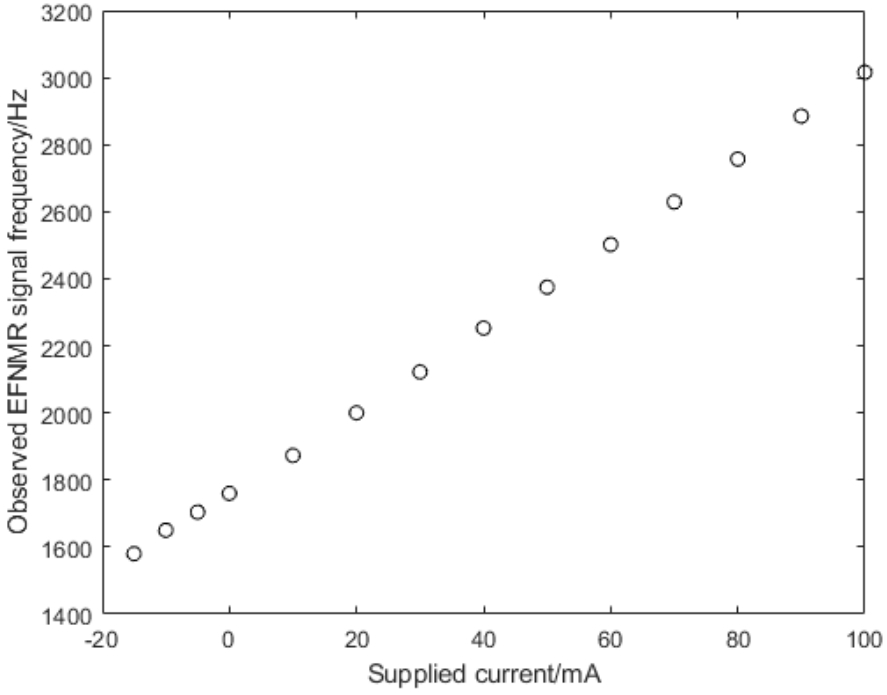

Figure 4.4: Frequency dependence of observed ^{1}H EFNMR signal against applied current through Z Helmholtz coil. Currents of 55 mA and -16 mA are supplied through the Y and X-Helmholtz coils, respectively, to cancel field along these axes. Negative current is supplied by reversing the direction of flow through the coils from the power supply.

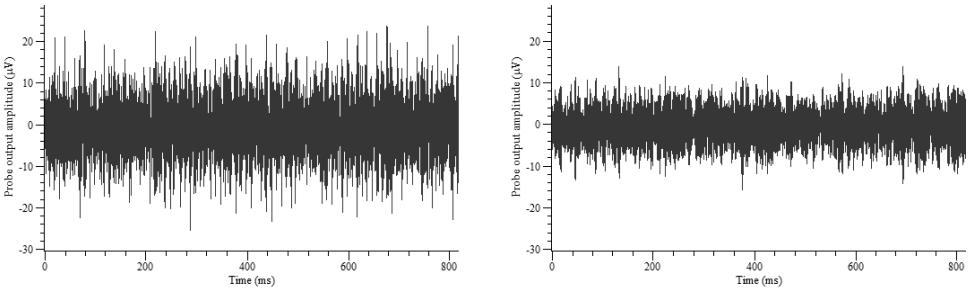

Figure 4.5: FIDs of white noise recorded on the Terranova with the insulating cable disconnected (left) and connected (right). Noise: 6.1 μV (left), 3.9 μV (right).

A large, thick copper cable has been wound around the supporting frame. This acts as a Faraday cage, creating a continuous current path. This minimises coupling from external electrical noise to the x-Helmholtz coil and detection coil, reducing noise in the NMR spectra. A comparison of two noise spectra is shown in figure 4.5, showing the visual reduction in noise when the coil is connected. Ten noise spectra were taken and the RMS noise was recorded. With the cable connected, the mean noise amplitude is 3.9$\pm$0.11 μV. When the cable is disconnected, it is $6.2 \pm 0.15\,\mu$V. Thus the cable gives a clear reduction in noise and will improve signal-to-noise ration (SNR) in all subsequent experiments. This is in addition to the B_P coil being shorted during detection, which provides a near 100-fold decrease in induced noise in the B_1 coil.

The large bore of the B_1 coil allows for a variety of reaction cell designs compared to the much more restrictive 5 mm diameter of a conventional high field NMR probe. This allows for exploration of different methods for gas delivery and mixing. In addition, the low magnitude of the Earth's field, typically around 50 μT, means that our peak linewidths are not affected by magnetic susceptibility mismatch so arbitrary cell geometries can be used. The Terranova B_P coil is also very useful, as it allows generation of the SABRE PTF. The range 0-18.8 mT allows simple generation of the coupling field for ^{1}H transfer, and the z-Helmholtz coil can be used to counteract the Earth's field, allowing the generation of sub-Earth's field transfer fields for heteronuclei, as described by Rossetto.[156] Shorting the B_P coil during detection also provides additional noise screening to the detection coil during detection. This significant noise insulation is what allows the performance of EFNMR in the lab environment, which would otherwise make recording EFNMR data practically infeasible.[87,153,154,157]

4.2.3 Terranova software

The Terranova is programmed in Prospa, a proprietary language for Magritek spectrometers. NMR experiments are formed of two parts: the Pulse Program and the Experiment Control macro.

The Pulse Program is a script that defines the user inputs, experimental parameters, and the sequence of pulses, delays, and other hardware events. To run an experiment, the Experiment Control macro executes the Pulse Program by sending the compiled

```
# Accumulate scan
for(scans = 0 to nrScans-1)
   # Note the time at scan start
   t1 = time()
   # Set phases for this scan
   (ppList,pAcq) = tnRun:setPPPhase(ppList,scans,pcList,pcIndex)
   # Send phase parameters to DSP
   dspwrite("x",0x00,ppList)
   # Collect the data
   (status,data) = tnRun:getData(totPnts,guipar)
   if(status != "ok")
      return(0)
   endif
   # Filter the data
   data = data .* flt
   # Accumlate the data
   sumData = tnRun:accumulate(accumulate,pAcq,sumData,data)
   # Process data
   (phasedTimeData,spectrum) = tnRun:transformData(sumData,fAxis,guipar,"fid")
   # Save the data
   tnFiles:savePlot(prt,:getPlotInfo("pt1"),guipar,"noReport")
   tnFiles:savePlot(prf,:getPlotInfo("pt2"),guipar,"simpleReport")

   # Check timing
   check = tnRun:checkTimeAndAbort(guipar,t1,scans,pcList)
   if(check == "abort")
      return(0)
   elseif(check == "finish")
      scans = scans+1
      exitfor()
   endif

next(scans)
```

```
# Pulse sequence
   initpp(dir)        # Reset internal parameter list

   cleardata(n4)      # Clear the data area
   grad(n1,g1)        # Set the x shim
   grad(n2,g2)        # Set the y shim
   grad(n3,g3)        # Set the z shim
   offseton(g4)       # offset coil

   polzpulse(c1,d1)   # Apply pre-poalrising current for duration

   delay(d7)          # Field stabilisation delay

   pulse(a1,p1,d2)    # 90 degree RF pulse
   delay(d4)          # Ringdown delay
   acquire(append,n4) # Acquire FID


   lst = endpp() # Return parameter list

# Phase cycle
  phaseList = [0,2; # p1 phase
               0,2] # Acquire phase
```

Figure 4.6: Prospa Experiment control (left) and Pulse Program (right) scripts for a multiple scan Pulse-and-Collect sequence, as shown in Figure 4.11. Pulse program instructions are sent to the DSP at the `dspwrite` step, and the pulse sequence subsequently executed.

instructions to the Digital Signal Processor (DSP). Following acquisition, the macro also handles the processing, display, and saving of the data. An example of the core of an Experiment Control and Pulse Program macros is shown in Figure 4.6.

Transistor-transistor logic (TTL) outputs are integrated into the spectrometer and can be toggled within a pulse sequence to interface with other devices, which is leveraged here to provide near-instantaneous interface with the p-H_2 bubbling system.

While the Pulse Program (pulse sequence, sequence) is being executed by the DSP, no other interactions with Prospa can occur. This limits any real-time external control to only those commands explicitly written into the pulse sequence itself, such as the switching of Transistor-Transistor Logic (TTL) outputs. Running of commands not explicitly allowed within the Pulse Program, such as output of Serial commands, is not possible in Prospa during DSP execution.

4.2.4 Reaction cells

Two primary reaction cell designs were employed in this work to facilitate *in situ* gas bubbling and subsequent NMR analysis. The first design incorporates a porous glass frit for gas dispersion, while the second utilizes a simple capillary inlet to explore different mixing regimes. Both are detailed below.

The primary cell used for initial optimisation and many subsequent experiments, referred to as the "frit cell," is shown in figure 4.7. The cell is a 24 mm x 24 mm x 28 mm cylinder, with inlet and outlet connections on the top face of the cylinder for gas flow. The inlet connection extends into the cylinder as a glass capillary. A porous glass

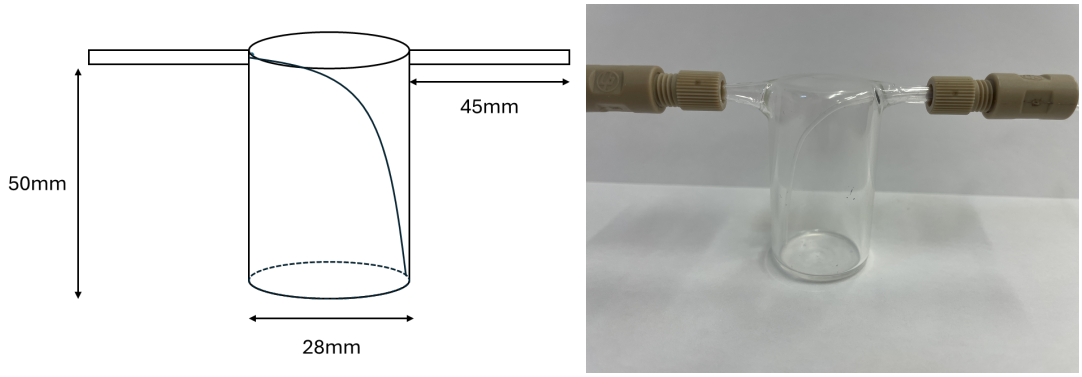

Figure 4.8: Capillary bubbling cell or "capillary cell"; cylinder of dimensions 28 mm diameter × 50 mm height with two arms of diameter 4 mm; diagram (left) and photograph (right).

frit (cylinder of dimensions 5×15 mm) is fused to the end of this capillary. The frit acts as a sparger, to give much improved mixing of gas flowing through the inlet into solution in the cell.

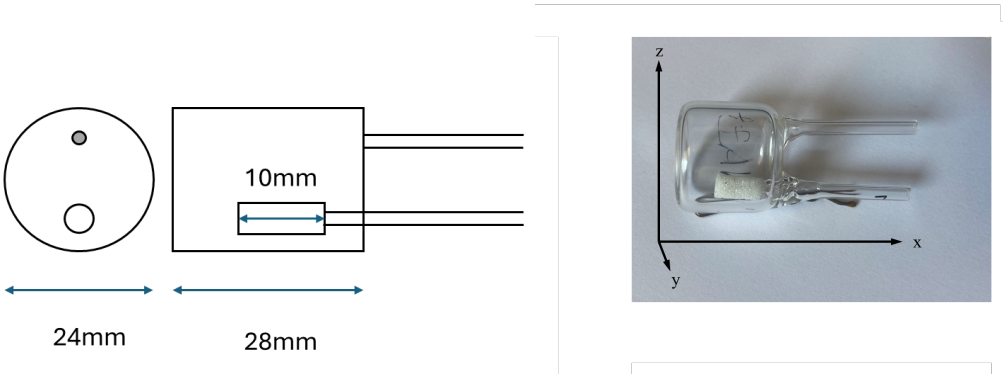

Figure 4.7: Diagram of the reaction cell for the Terranova (frit cell). Left: end-on and side-on diagram. The reaction cell used to allow bubbling of p-H_2 through the SABRE sample. The main body of the cell is a cylinder of 25×25 mm, with a 5×15 mm cylindrical frit in the centre of the lower half. A typical sample volume of 4 mL typically fills the cell halfway (to above the top of the frit). The relative axes used in imaging are shown.

The second cell, designed to investigate the impact of a different gas delivery mechanism, is referred to as the "capillary cell" (Figure 4.8). It consists of a glass cylinder of dimensions 28 mm diameter × 50 mm height with two arms of diameter 4 mm. Gas is delivered via a 1/16" outer diameter PTFE capillary tube extending through one arm to the base of the cell.

4.3 Standard Terranova experiments

Due to the very weak nature of the Earth's field, the Terranova system uses pre-polarisation (also known as brute-force hyperpolarisation) to generate enough signal. In a typical Terranova experiment 6 A is applied to the B_P coil to generate an 18.8 mT magnetic field for a period of 4 s. During this time, bulk polarisation is built up in the sample as it comes to equilibrium in the 18.8 mT field due to T_1 relaxation. In principle the pre-polarisation duration (t_{pol}) should exceed $5 \times T_1$ to maximise signal. In practice, to prevent damage to the coils through resistive heating, this value is limited to a maximum of 4-5 s, depending on the overall duty cycle of the experiment. In addition to the pre-polarisation, to generate sufficient population difference for observable signal, a very large number of spins must be used. In this example, a 500 mL bottle of water is placed in the bore of the probe. The pre-polarising field is applied to the sample along the x-axis and switched off adiabatically to allow the hyperpolarised magnetisation to reorient along the z-axis.

A short ringdown delay t_A follows to allow the B_0 field to stabilise at B_E inside the probe prior to excitation. The B_1 coil is then used to produce and subsequently detect transverse magnetisation of the samples' spins through application of a $\pi/2$ (90°) nutation pulse. The pulse application and spectral acquisition are separated by a ringdown delay t_R to prevent induction of current (ringing) in the transmit/receive coil by the B_1 pulse, which would interfere with induction of NMR signal. "Shim" fields are applied through the gradient coils for the duration of the pulse sequence to maintain the most homogeneous field possible, maximising signal and minimising line-width. The full pulse sequence is shown in Figure 4.9, and the resulting free induction decay (FID) and spectrum are shown in Figure 4.10.

In the Earth's field, there is insufficient strength to differentiate nuclear environments through chemical shift, so all nuclei of the same type appear at the same frequency. J-coupling to heteronuclei can still be observed.[87] The ^{1}H Larmor frequency is prone to mild drift of a few Hz as the Earth's field changes throughout the day.

Also observable in this spectrum is the electrical coupling from resonances in electrical cabling in the laboratory walls. While these have been reduced (see the copper shielding cable implemented in Section 4.2.1), some noise spikes remain observable in all spectra, as can be observed in Figure 4.10.

The large lift opposite the group's laboratory was also found to significantly disrupt the local magnetic field. When in motion, it generates a time-dependent field leading to distorted peaks. The motion also causes the ^{1}H Larmor frequency to shift by approximately 50 Hz. For this reason, some affected results in long or 2D experiments have been removed from their data sets.

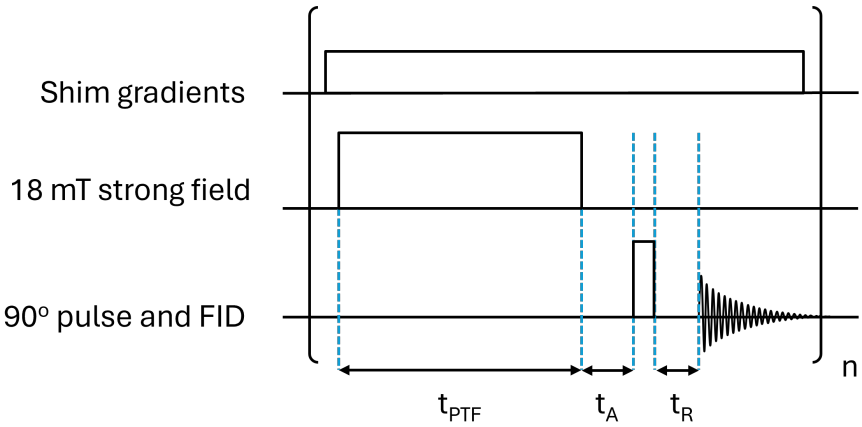

Figure 4.9: Pulse sequence for the simplest experiment on the Terranova, a brute force polarised 90° -pulse-and-collect experiment on the Terranova. Shim fields are applied through the gradient coils for the duration of the experiment. A short, intense pre-polarising pulse of 18 mT is applied for time t_{pol}, followed by a field settling delay t_A, a 90° pulse, ringdown delay t_R, and detection of transverse magnetisation using the B_1 coil.

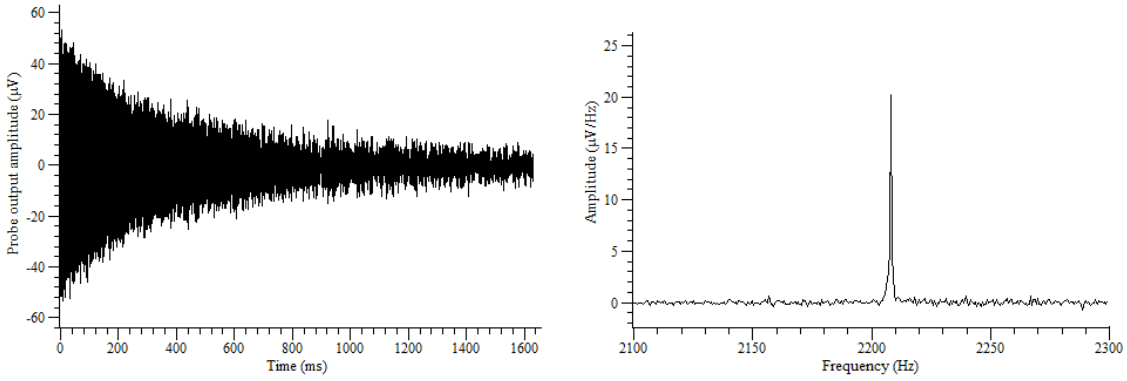

Figure 4.10: Left: Brute-force polarised FID. Right: resultant spectrum of a 500 mL bottle of water (line-width: 1.22 Hz, SNR: 29.6)

4.4 SABRE hyperpolarised experiments – bubbling, PTF, and detection

Chapter 3 showed the development of our own *para*-hydrogen delivery system. This can now be integrated with the Terranova to demonstrate effectiveness and to allow optimisation of p-H_2 delivery as part of NMR experiments. This section explores this optimisation process, in which a repeatable method for reaching a consistent, reproducible level of p-H_2 in solution is developed for use in future experiments.

4.4.1 Standard sample

Samples for NMR analysis were prepared through dissolution of 10.8 mg (4.2 mM) [IrCl(COD)(IMes)] (where COD = 1,5 cyclooctadiene and IMes = 1,3-bis(2,4,6-trimethylphenyl)-imidazol-2-ylidine) in 4 mL methanol, followed by addition of pyridine (80 μL, 250 mM, 59.5 eq.). Where necessary the sample was sonicated until homogeneous. Pyridine was purchased from Sigma-Aldrich (St. Louis, MO, USA). The pre-catalyst was synthesized in-house by Dr Vicky Annis according to a published procedure.[158]

Following preparation, the sample is injected using a syringe into the bubbling cell shown in Figure 4.7, which is inserted into Earth's field NMR probe for gas bubbling and detection *in situ*. The bubbling cell is supported inside the centre of the bore of the probe using a cylindrical plastic housing.

Pyridine is known to be a highly efficient SABRE substrate with the [IrCl(COD)(IMes)] catalyst and so was used as a model system throughout this thesis.[45]

4.4.2 The *In-Situ* SABRE Experiment

Performance of a SABRE-enhanced experiment on the Terranova system is analogous to the brute-force experiment, where the pre-polarisation step is replaced by SABRE hyperpolarisation. The standard pulse-and-collect sequence is shown in Figure 4.11. To achieve polarisation transfer to ^{1}H, a Polarisation Transfer Field (PTF) of approximately 6 mT is applied using the B_P coil (2 A) while p-H_2 is simultaneously bubbled through solution. This gas flow is controlled within the pulse sequence via synchronised TTL pulses from the spectrometer that operate the valves on the polariser unit. Following the combined bubbling and PTF period, a short delay (t_A) allows the field to settle before a 90° RF pulse is applied to detect the SABRE-enhanced NMR signal.

A typical FID and the resulting spectrum from the standard pyridine sample are shown in Figure 4.12. The SABRE-enhanced signal is remarkably intense, especially when compared to a brute-force polarised water sample. Despite the SABRE sample containing approximately 28 000 times fewer molecules (0.99 mmol pyridine vs 27.8 mol H_2O), it produces a signal with roughly double the SNR, a 3-fold higher FID amplitude,

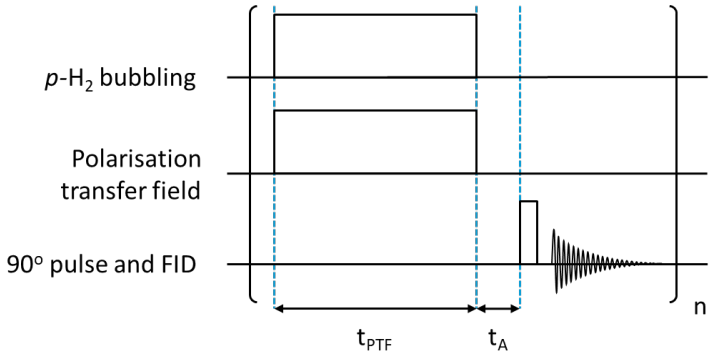

Figure 4.11: Simplest SABRE pulse and collect pulse sequence. p-H_2 is bubbled into the sample while a 6 mT PTF is applied. A 90° pulse is applied after a short settling delay, followed by detection.

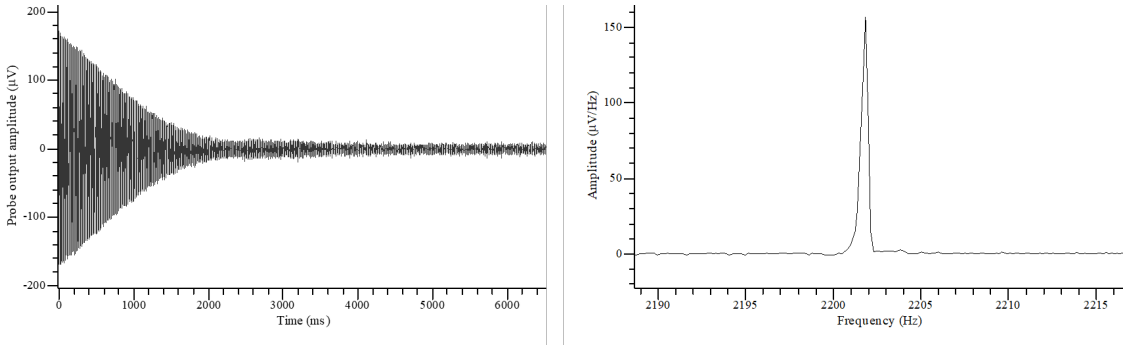

Figure 4.12: Left: Free induction decay (FID) and Right: NMR spectrum of SABRE-hyperpolarised pyridine (using the standard 80 μL pyridine sample) collected using the pulse sequence outlined in Figure 4.11. (line-width: 0.25 Hz, SNR: 63.2)

and a 5-fold narrower line-width (1.22 Hz compared to 0.25 Hz). This significant enhancement arises from the high polarisation achieved through SABRE, which is estimated to be around 0.02-0.25%, several orders of magnitude greater than the calculated thermal polarisation of water in the Earth's field (5.3×10^{-8}).[74] The improved line-width is also a result of the more homogeneous field across the smaller sample volume, which allows for finer shimming.

For the subsequent optimisation experiments, the sequence using in Figure 4.11 was used as a reference experiment, with the observed SABRE enhancement quantified using the integrated area of the spectral peak. Peak integral was chosen as the primary metric because it provides a robust measure of the total hyperpolarised magnetisation, being less susceptible than peak amplitude to variations in line-width that might arise from small disruptions in magnetic field homogeneity, field drift, or other minor alterations in sample conditions. Over short experimental timescales where the catalyst and substrate concentrations are stable; the SABRE peak integral can be used as a reliable proxy for the concentration of p-H_2 dissolved in the solution. However, over longer periods, confounding factors must be considered, such as solvent evaporation and catalyst degradation. The activated SABRE catalyst is known to decay over extended periods through dimerisation[138–140] and oxidation to Ir(III) in the presence of oxygen,[159] effects which will be explored in Section 4.8.

4.5 Establishing a consistent concentration of *para*-hydrogen in solution

To ensure maximum sensitivity for subsequent experiments, to facilitate ease of observation, and to enhance the versatility of the setup for benchtop applications, the system should be optimised to produce the maximum possible reproducible signal for each experiment as efficiently as possible.

There are several options in the instrumental setup which can be adjusted to impact the delivery of p-H_2 into the system. Hydrogen pressure and bubbling time can be changed, PTF time changed in parallel and in series with bubbling, and the sample cell can be purged with nitrogen, displacing dissolved hydrogen, to ensure a complete refresh of supplied hydrogen or *para*-hydrogen.

This section will begin by looking at each aspect in isolation, and then combining these findings in order to determine best set-up options for the most efficient experimental conditions.

4.5.1 Optimising supply pressure

The reference experiment shown in Figure 4.11 can be used to show the effect of changing p-H_2 pressure on sample signal. The aim is to maximise the SABRE signal output from a given experiment. A series of 10 reference experiments were run at each pressure. Between each set of experiments, 200 s of bubbling was performed to allow equilibration of pressure within the cell to the new level. Figure 4.13 shows a plot of SABRE signal against supplied pressure, as measured from PG-0 (as shown on Chapter 3 Figure 3.7). Flow rate was set to a constant 0.1 L min^{-1} air at flow regulator FR-2. Changing generator pressure does not alter the flow rate.

In this range, the SABRE signal exhibits a linear correlation with p-H_2 pressure. This relationship is expected,[141] as the concentration of p-H_2 in solution is linearly dependent on the partial pressure of p-H_2 above the solution. In all future experiments, unless otherwise noted, the generator is therefore set to supply 6.5 bar H_2 to maximise output signal. The 6.5 bar pressure level was chosen as this is the maximum output of the Peak Scientific generator. The Mars Generator can supply up to 10 bar, but the IDEX connections to the glass cell arms would require further safety testing to minimise risk of forcible disconnection of a cell from the system.

4.5.2 Optimising combined *para*-hydrogen and PTF application

SABRE experiments with *in situ* bubbling are often run with simultaneous p-H_2 delivery and PTF application. This allows continuous, flow of fresh p-H_2 into solution for generation of hyperpolarised substrate in solution. Appleby *et al.*[160] and Pravdivtsev *et*

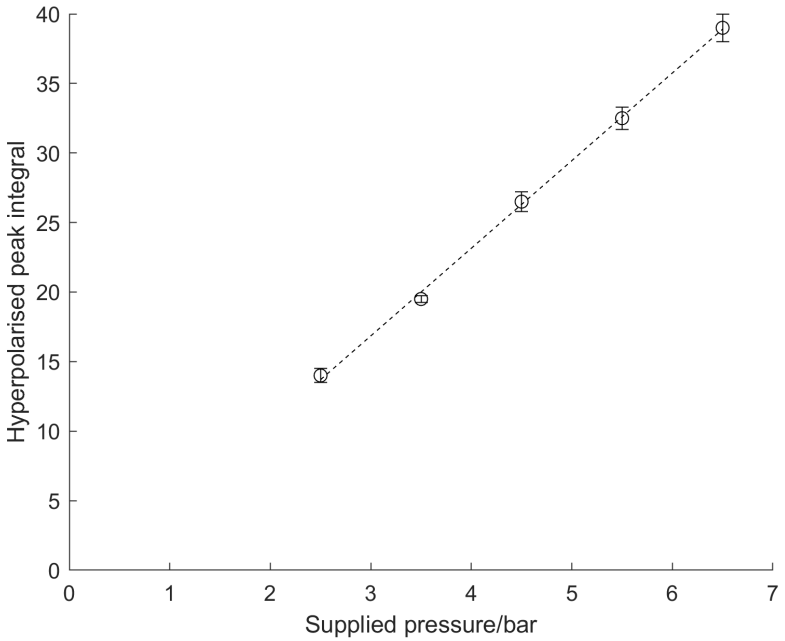

Figure 4.13: Pressure vs peak integral, recorded using pulse sequence in Figure 4.11. Pressure set at H_2 generation.

al.[161] show that increasing p-H_2 bubbling time gives increased SABRE signal. To determine the optimal duration for conditions where p-H_2 bubbling and PTF application are concurrent the pulse sequence shown in Figure 4.11 can be used, in which t_{PTF} is varied across experiments. To ensure a representative concentration of p-H_2 in solution at the start of the sequence, 10 repetitions of the sequence in Figure 4.11 were run prior to the 2D experiment starting, with $t_{PTF} = 30$ s. The resulting peak integral, plotted against t_{PTF}, is shown in Figure 4.14. It shows that SABRE signal builds proportionally to t_{PTF} until $t_{PTF} = 30$s, after which signal plateaus.

This experiment is useful for maximising signal in general SABRE experiments but does not allow for observing independent effects of p-H_2 bubbling and PTF application, or understanding the interactions occurring between the two. For this, separated p-H_2 - PTF sequences are needed.

4.5.3 Nitrogen purges to remove *para*-hydrogen from solution for a consistent starting point

To establish a consistent starting point for delivery of H_2 in optimisation experiments, nitrogen bubbling can be used to displace dissolved H_2 from solution. A consistent starting point can be found when a given N_2 bubbling time fully displaces all H_2 from solution. For this experiment, the pulse sequence shown in Figure 4.15 is used. p-H_2 is bubbled into solution for fixed duration $t_{p\text{-}H_2}$, followed by a variable duration of N_2 bubbling, t_{N_2}. A short polarisation transfer field (PTF) is applied to allow SABRE signal to be generated from any p-H_2 remaining in solution. Since the PTF amplitude

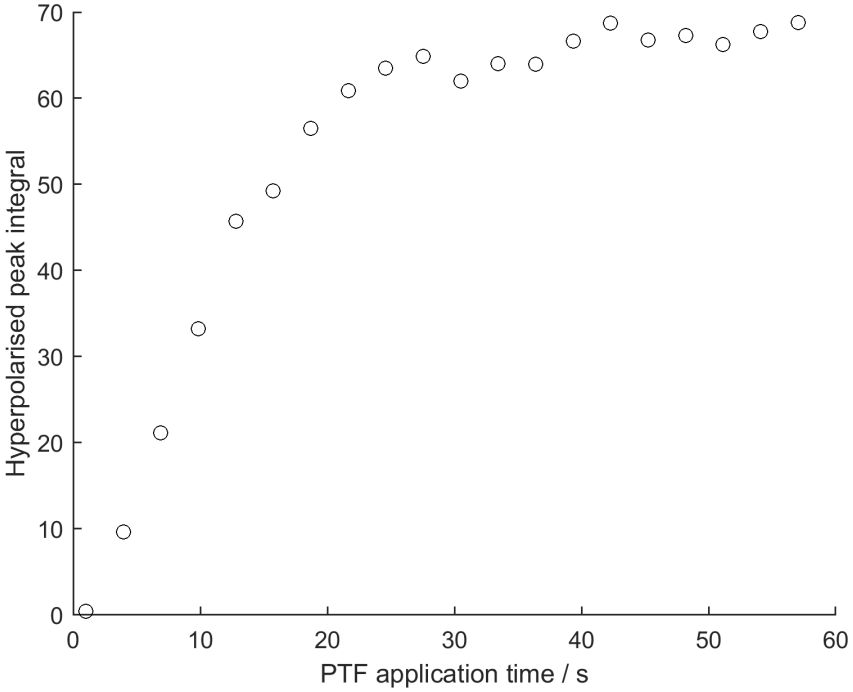

Figure 4.14: Observed SABRE-enhanced peak integral against combined PTF and p-H_2 bubbling time. data was acquired using the pulse sequence in Figure 4.11 with variable time t_{PTF}.

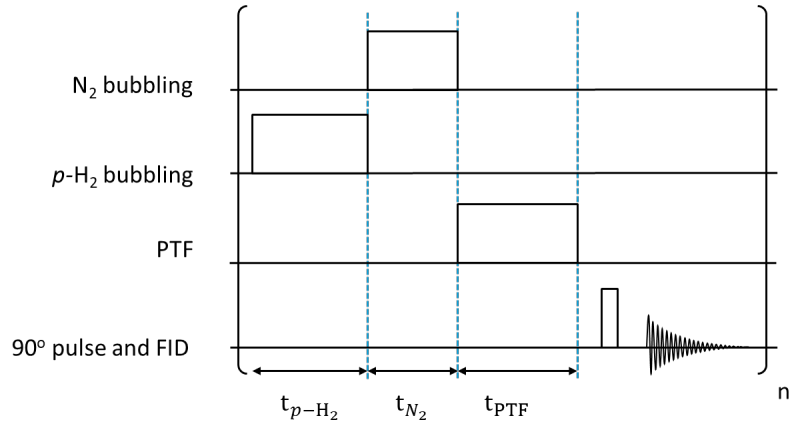

Figure 4.15: Pulse sequence used for determining N_2 bubbling time required to fully displace p-H_2 from solution. 30 s p-H_2 delivery is followed by variable time N_2 bubbling. A 10 s, 6 mT PTF pulse is followed by a 90° pulse and NMR detection.

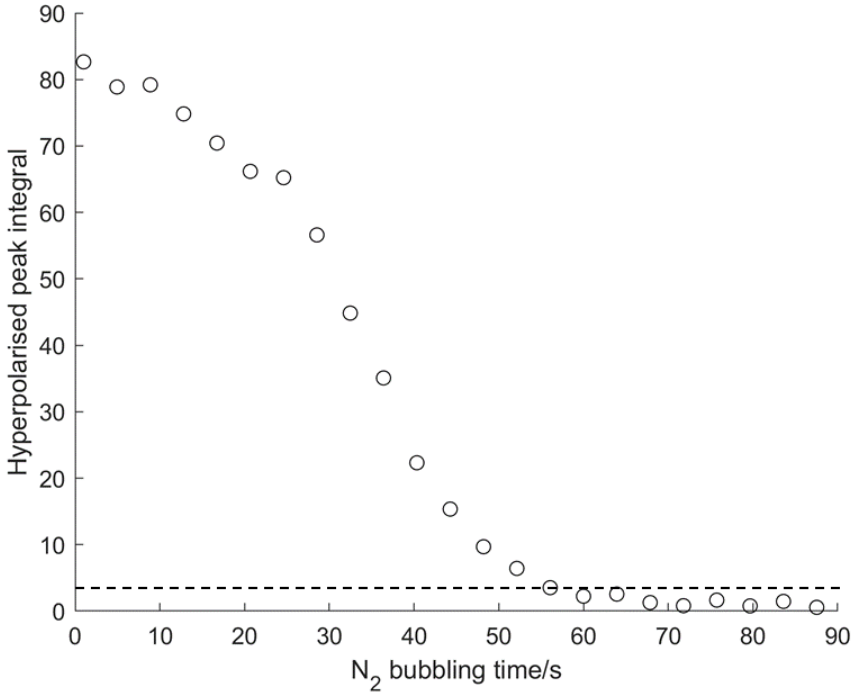

Figure 4.16: Plot of hyperpolarised SABRE peak integral against nitrogen displacement time, (t_{N_2}). Dashed line marks the baseline noise limit at which signal can no longer be distinguished.

and duration are kept constant for each measurement, the SABRE transfer efficiency is also assumed to be constant.[27] The resulting signal intensity is therefore assumed to be directly proportional to the concentration of p-H_2 remaining in the solution. (This assumes that all p-H_2 delivered is at a consistent enrichment, 51 % from the liquid nitrogen generator.) For a constant PTF amplitude and duration, it can also be assumed that for a fixed duration of p-H_2 bubbling, SABRE efficiency remains constant, and therefore the observed signal will correlate with the proportion of p-H_2 in solution.[146]

Figure 4.16 shows the resultant SABRE peak integral plotted against duration of N_2 bubbling time. From this, it can be seen that SABRE signal (from 30 s of p-H_2 bubbling) is reduced to intensity below spectral noise after 60 seconds of N_2 bubbling. Therefore, a 60 s N_2 purge can be used in all experiments where a consistent starting point zero p-H_2 in solution is needed.

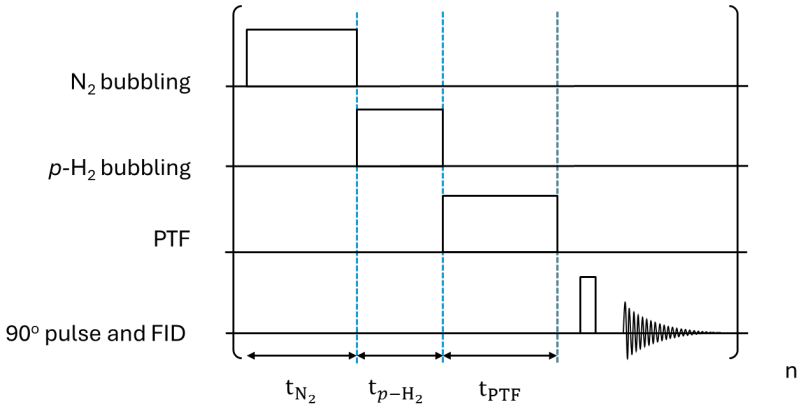

Figure 4.17: Pulse sequence for optimisation of p-H_2 bubbling time when PTF application is a separate, subsequent step. 60 s of N_2 bubbling is followed by a variable duration of p-H_2 bubbling, then 10 s of a polarisation transfer pulse. Signal is generated through a 90° pulse and detected.

4.5.4 Optimising *para*-hydrogen bubbling time

Experiments require an optimal, reproducible level of p-H_2 in solution without excessively long bubbling times. By beginning with a consistent baseline of no p-H_2 dissolved in the SABRE reaction solution (achieved through 60 s N_2 bubbling, as described in Section 4.5.3), it becomes possible to optimize bubbling duration to maximize the SABRE signal in the minimum possible duration. To do this, the pulse sequence in Figure 4.17 is used. N_2 is bubbled for 60 seconds to remove all p-H_2 from solution. A variable time of p-H_2 bubbling is then applied, followed by a 10 s PTF.

Figure 4.18 (□) shows the resultant integral of the hyperpolarised peak against each p-H_2 bubbling time, $t_{p\text{-}H_2}$. This produces a sigmoidal curve showing an initial induction period, in which no hyperpolarisation is built as N_2 is displaced from solution. Following this period, there is an increase in signal with bubbling time, eventually reaching a plateau at $t_{p-H_2} \approx 90$ s.

For day-to-day running of experiments, reaching consistent p-H_2 concentrations through displacement with N_2 followed by p-H_2 bubbling is a highly impractical approach resulting in a minimum experiment duration of 150 s. If it is assumed that p-H_2 in solution is largely consumed by polarisation transfer, consistent levels of p-H_2 in solution can be reached without N_2 displacement, instead simply by bubbling p-H_2 to replenish with fresh p-H_2 for each experiment. This duration can be optimised using the same pulse sequence in Figure 4.17, with N_2 bubbling time $t_{N_2} = 0$ s. This experiment was preceded by the running of 10 pulse-and-collect experiments (300 s total p-H_2 bubbling, sequence in Figure 4.11) to ensure a representative initial concentration of p-H_2 in solution. The resulting integrals are shown in Figure 4.18(○). The baseline noise limit is marked on the figure by a dashed line.

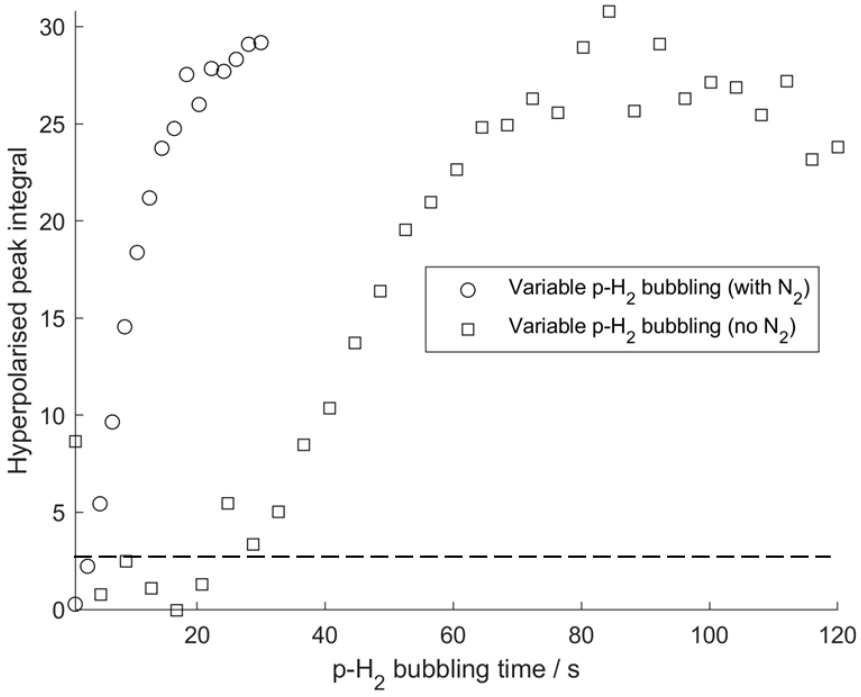

Figure 4.18: Observed hyperpolarised peak integral against p-H_2 delivery time, using the pulse sequence in Figure 4.17 with variable t_{p-H_2}. Dashed line marks the baseline noise limit at which signal can no longer be distinguished.
(○): Peak integral against p-H_2 bubbling time (t_{p-H_2}) with no N_2 displacement bubbling; $t_{N_2} = 0$.
(□): Peak integral against p-H_2 bubbling time (t_{p-H_2}) with 60 s N_2 displacement bubbling applied; $t_{N_2} = 60\,\text{s}$.

With this approach, hyperpolarised signal intensity builds at a higher rate, and without a latency period of displacement. The steep rise levels off after approximately 20 s of bubbling, after which signal continues to increase at a much gentler rate. For maximum signal in minimum time, 20 s of bubbling is optimal. Note that the resulting integrals for sequential p-H_2 - PTF experiments are much weaker than for parallel application (for example in Figure 4.16). This could be attributed to the more limited availability of p-H_2 in separated experiments, as the continuous flow for parallel bubbling can replenish depleted p-H_2, and provide a larger total volume of p-H_2 which will allow for a larger build-up of hyperpolarised substrate in solution.

4.5.5 Optimising PTF duration

The PTF duration can be optimised using the pulse sequence given in Figure 4.17, with a fixed t_{N_2} and t_{p-H_2}. The previously optimised times of $t_{N_2} = 60$ s and $t_{p-H_2} = 60$ s are used to ensure a consistent concentration of p-H_2 in solution for each experiment. The resulting SABRE integrals are shown plotted against t_{PTF} in Figure 4.19. This shows a sharp rise in signal up to $t_{PTF} \approx 7$ s, followed by a plateau. To ensure consistency of

signal reached through PTF application, a PTF application time of 10 s is used in all experiments where p-H_2 bubbling and polarisation transfer are performed sequentially. However, this result is of limited utility when p-H_2 bubbling and polarisation transfer are performed in parallel, as building p-H_2 concentration correlates with increased observed signal (as shown in Figure 4.13). Note that a small integral is observed at 0 s PTF because of the integration of noise. The baseline noise limit is marked on the figures by a dashed line.

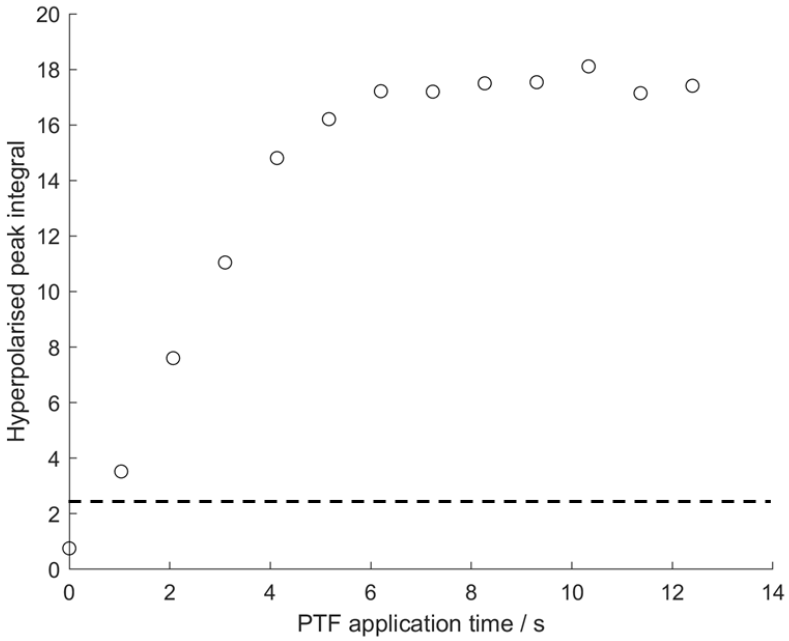

Figure 4.19: SABRE peak integral against PTF application time (t_{PTF}) when PTF is applied sequentially to p-H_2 bubbling.

4.5.6 Discussion of optimal bubbling conditions for maximum reproducible signal

The preceding sections systematically investigate the key experimental parameters for the delivery of p-H_2 and the subsequent generation of SABRE-enhanced magnetisation. This section consolidates these findings to establish a set of optimal conditions tailored for achieving either maximum signal intensity for p-H_2 delivery in parallel with or prior to application of a PTF pulse. The parameters are optimised for the standard sample composition detailed in Section 4.4.1.

Flow rate is set to match the flow rate output of the hydrogen generator, 0.1 L min^{-1} air. While higher flow rates yield higher peak integrals, this is at the expense of prolonged repetition time to allow system pressure to recover to initial level. Higher flow rates will also cause pressure fluctuations in the cell over the duration of the bubbling phase of the experiment, making p-H_2 concentration measurements (and reactions dependent on this) more difficult. SABRE signal exhibits a linear dependence on the supplied p-H_2 pressure, as demonstrated in Figure 4.13. The Peak Scientific p-H_2 generator used here is limited

to a maximum of 6.5 bar supply pressure. To maximise the available p-H_2 and therefore the potential signal enhancement, the generator pressure is set to its maximum of 6.5 bar for all experiments unless otherwise stated. The Mars H_2 generator has a higher supply limit, so when in use, the generator is set to 8.5 bar and down-regulated at the pressure regulator to 6.5 bar. This ensures a more consistent flow of p-H_2 through the system. The Mars generator was also limited to 0.1 L min^{-1} air at FR-2 to ensure comparability between experiments run using different generators.

4.5.6.1 Duration of p-H_2 bubbling

For experiments in which the only requirement is maximum possible SABRE signal, a simultaneous PTF - p-H_2 bubbling approach is used. This gives much stronger signal intensity than separating the two steps due to the higher total available volume of p-H_2, and the better availability of fresh p-H_2 in solution due to continuous replenishment. This can be observed through comparison of integral intensity in Figures 4.14 and 4.19. When the two are combined an application of 30 s combined p-H_2 bubbling/PTF gives maximum SABRE signal in minimum time, though incremental gains in signal can be made extending the bubbling time toward 60 s. This effect mirrors the signal plateauing with extending bubbling time observed by Appleby *et al.*.[160] This parallel approach does not allow for observation of kinetic processes, convoluting the effects of gas dissolution and polarisation transfer. To allow independent control of the two processes, a sequential approach to bubbling is necessary. When a baseline starting point of zero p-H_2 in solution is required, 60 s of N_2 bubbling can be applied to fully displace any residual p-H_2 in solution, as shown in Figure 4.16. Following full displacement, a consistent p-H_2 concentration in solution can be reached with 90 s of p-H_2 bubbling (Figure 4.18). Where the goal is simply to replenish the p-H_2 consumed in the previous scan, a much shorter duration is needed. Figure 4.18 shows that the signal plateaus after approximately 20 s of p-H_2 bubbling. This 20 s duration is therefore optimal for achieving a consistent, high level of signal in a time-efficient manner for decoupled p-H_2-PTF experiments, combined with a 10 s duration PTF application to maximise SABRE signal from p-H_2 in solution (Figure 4.19).

4.6 Implementation of MRI and polariser to explore flow cell mixing

With the system's parameters now optimised for signal generation, its capabilities can be applied to investigate physical phenomena within the reaction cell, beginning with the dynamics of gas mixing The mixing of p-H_2 within the reaction cell may be a driver of variability and inconsistency in signal produced, if mixing is not even. The distribution and intensity of mixing across the reaction cell may impact the overall quantity of SABRE reactions that occur in the reaction cell. An ideal distribution would give a consistent number of polarisation transfer reactions for each catalyst molecule across the cell. An uneven p-H_2 distribution between experiments may result in a variable level of polari-

sation reached across experiments. The *in situ* bubbling setup implemented here allows the performance of magnetic resonance imaging experiments on the cell. These imaging experiments indicate the quality of gas mixing and how well p-H_2 is distributed in solution. The intensity of the hyperpolarised signal in the MR images is proportional to the local concentration of hyperpolarised pyridine. Assuming that for each scan in an image, there is consistent overall H_2 concentration in the sample, the intensity of the image will correspond to the local concentration of p-H_2, with higher local availability of p-H_2 giving a larger build-up of hyperpolarised pyridine and more intense spots on the image. This can be used to qualitatively assess the effectiveness of bubbling at distributing p-H_2 in solution.

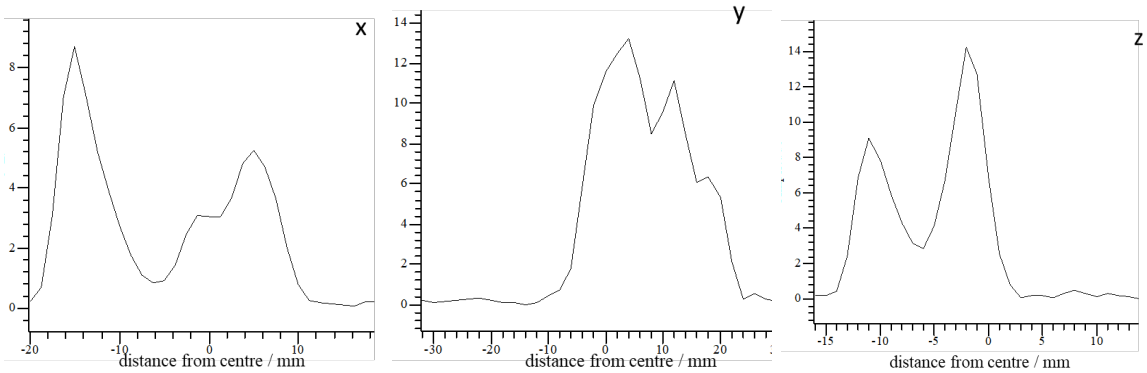

Figure 4.20: 1D images of a pyridine SABRE sample inside the bubbling cell (frit cell) in the x, y, and z directions, as given in Figure 4.7, shown as signal intensity against distance from centre of the probe. Signal intensity is not comparable between images.

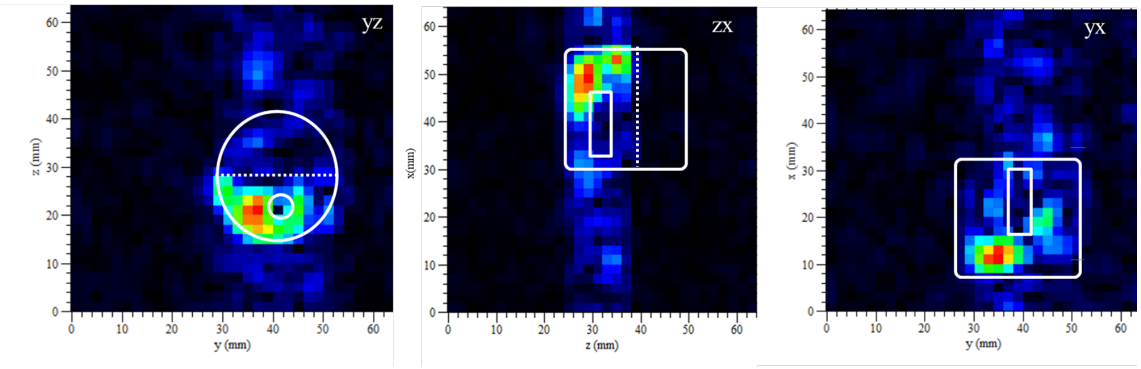

Figure 4.21: 2D images of a pyridine SABRE sample in the frit bubbling cell in yz, zx, and yx planes. Axes as shown in Figure 4.7. The colour scale represents the relative ^{1}H SABRE signal intensity, ranging from blue (low intensity) to red (high intensity). The position of the bubbling cell is overlaid in white, and the approximate position of the surface boundary of the SABRE solution is indicated with a dashed line on the xz and yz images.

The intensity of the image must be bounded by the edges of the cell, with intensity correlating to space in which we have best dissolution of p-H_2. Figure 4.7 presents a schematic of the frit cell being used to obtain images. Figure 4.20 shows 1D images of

the cell in x, y and z directions. Figure 4.21 shows 2D images of the glass cell in the yz, zx and yx planes. The silhouette of the cell and the frit is overlaid on the image. The images show inconsistent intensity of SABRE signal across the space of the cell. This is likely caused by uneven *para*-hydrogen mixing across the complete volume of the solution, resulting in "hot spots", regions of more intense p-H_2 dissolution and hence more intense SABRE signal. This can in part be attributed to the bubbling frit displacing a volume in the lower centre of the cell, reducing the volume available for signal. This can be seen in Figure 4.20 in the x dimension, and in Figures 4.21 in the yx and zx images, where the higher volume at the unoccupied end of the cell allows a larger number of spins to contribute to a more intense signal. The inconsistency in p-H_2 dissolution can be seen best in Figure 4.21 - yz, which shows an image of the cell as seen from above. A pair of hot spots of signal intensity are clearly visible, along with the higher intensity space beyond the end of the frit. These are likely caused by the manner in which bubbles escape the frit glass, concentrated in a small number of locations which would appear to roughly correspond with the locations of the hot spots in the images. To achieve better mixing, alternative cell designs may be considered, to ensure a wider range of space for gas delivery into solution to result in better mixing. Alternatively, a higher flow rate would result in more vigorous bubbling action which may drive wider p-H_2 distribution, though this is limited by the ability of the generator to supply H_2 at the requisite flow rate, and by potential sample loss through the outlet if bubbling becomes too vigorous.

4.7 Capillary cell

Prior experimental work by other members of the research group has primarily been conducted using the frit cell (Figure 4.7),[74,156,162] leaving the impact of mixing quality and efficiency on the SABRE reaction uncharacterised. To investigate how the quality of p-H_2 mixing and the gas-liquid interface surface area affect signal enhancement and stability, a comparative study was undertaken using an alternative cell design.

A new flow cell was designed, the "capillary cell". The cell is a cylinder of dimensions 28 mm diameter × 50 mm height that uses a capillary rather than a frit to mix the gas into solution. This changes the interaction of p-H_2 to allow dissolution only by a single stream of bubbles. The cell is shown in Figure 4.8. A capillary is made by extending the PTFE gas tubing through the inlet and from there down to the base of the cell, allowing p-H_2 delivery into solution via a single stream of bubbles out the capillary. This allows a comparison of bubbling efficiency between cells of different design through changing peak intensity and imaging.

The efficiency of bubbling in the capillary cell can be assessed by comparison of the 1D spectral intensity of the capillary cell peak integrals vs frit cell peak integrals. Figure 4.22 shows a comparison of the integrals recorded in the capillary cell and frit cell using the standard sample. This yielded hyperpolarised peak integrals in the frit cell with an average relative intensity of 127±2, compared to 64±2 in the capillary cell. This is a decrease of approximately 50% signal intensity, attributable to the poorer dissolution of p-H_2 in the capillary cell from a smaller surface interface between delivered p-H_2 gas

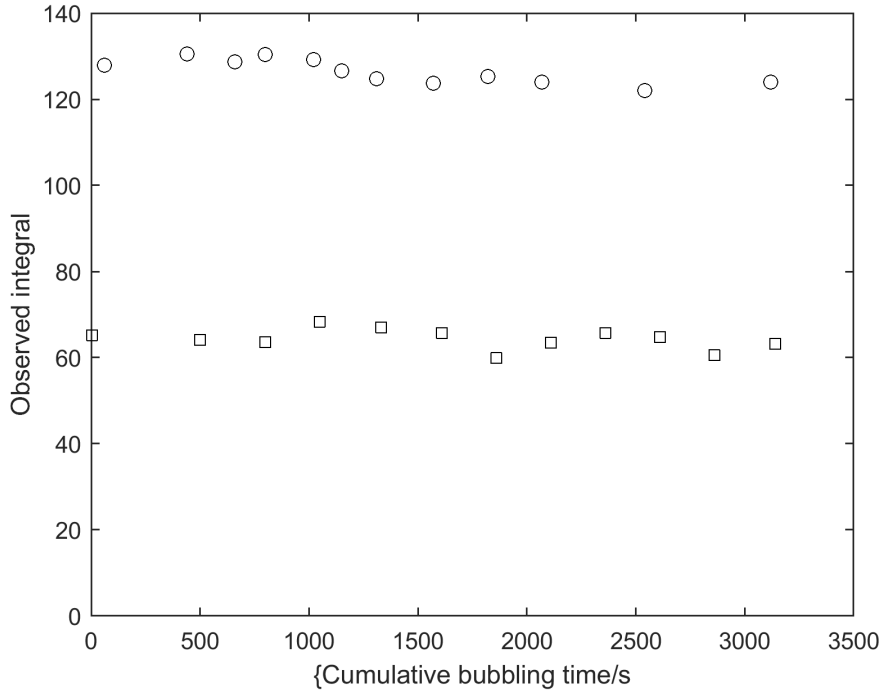

Figure 4.22: comparison of capillary cell (□) and frit cell integrals (∘) when running the standard 90° pulse and collect experiment on a standard sample.

(due to larger bubbles) and weaker mixing across the solution from poorer agitation from the single bubbling column. The capillary cell also does not have a dedicated support for inside the probe and therefore is supported using padding (carved polystyrene, or bubble wrap and a roll of electrical tape). The shallow depth and makeshift support make the capillary cell more sensitive to orientation, with any deviation from flat along the xy plane leading to inconsistent or excessively shallow bubbling into solution, further contributing to signal variability across multiple samples and potentially reaching sub-optimal signal intensities.

The quality of mixing can also be assessed through imaging of the capillary cell, similar to the frit cell. 2D images of the capillary cell were taken in yz and yz planes. These images are shown in Figure 4.23. Figure 4.23 (a) shows the image across the zy plane. It shows an even distribution of signal intensity. This suggests that mixing is consistent across the depth of the sample. The image of the yx plane shows a hot spot around the point at which the capillary is inserted into the solution and an apparent semicircular, anticlockwise flow of intensity away from this point. The small region of weaker signal around $y = 18$ mm in Figure 4.23 (a) correlates with the low intensity area in Figure 4.23 (b) and is suggestive of a directional flow of solution most likely driven by the angle of insertion of the capillary into solution.

The 2D images of the capillary cell show a single "hotspot" in the yx-plane where the capillary enters the solution, along with a "cold spot" at low y-values suggestive of a bulk circular flow of solution. When compared to the frit cell images (Figure 4.21), which show multiple, more intense hotspots corresponding to the many bubble streams emerging from the frit surface, a key difference emerges. While the signal distribution

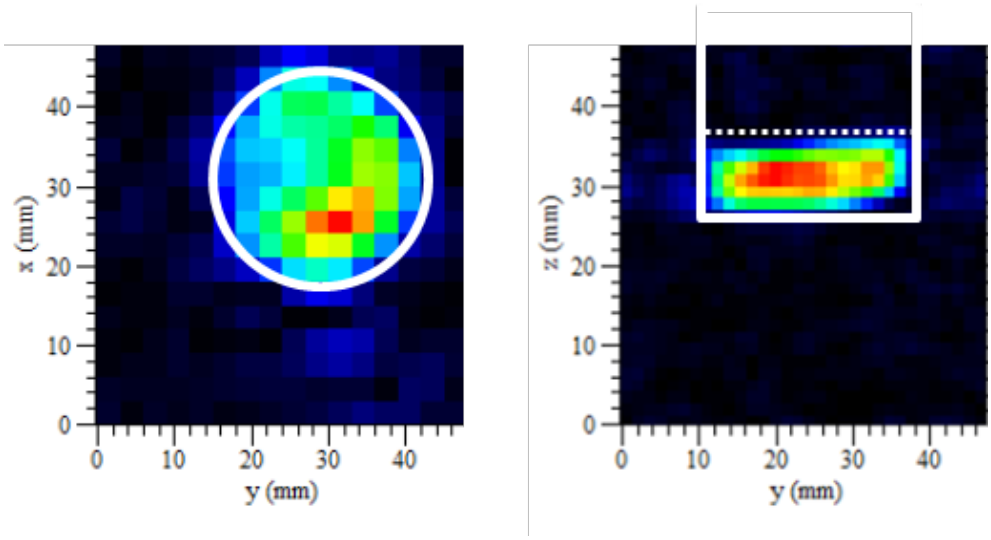

Figure 4.23: capillary cell images 2D images of a 250 mM pyridine SABRE sample in the capillary cell (photographed in Figure 4.8) in yz (top down) and yx (side on) planes. The approximate position of the cell is overlaid in white. The colour scale represents the relative ^{1}H SABRE signal intensity, ranging from blue (low intensity) to red (high intensity). The approximate position of the surface boundary of the SABRE solution is indicated with a dashed line on the yz image.

in the capillary cell is consequently more globally homogeneous, both cell designs clearly show that hyperpolarisation is most effective at the immediate point of p-H_2 introduction, with much weaker signal where dissolution relies on convection.

This visual evidence correlates with the quantitative differences observed in the 1D spectra (Figure 4.22). The integral intensity in the frit cell is approximately twice that of the capillary cell, which can be attributed to the greater gas-liquid surface area provided by the frit. This larger surface area leads to more efficient overall p-H_2 dissolution and more effective hyperpolarisation within the multiple, intense hotspots.

4.8 Extending sample lifetimes

SABRE is a reversible process and so in theory the same sample can be measured over many days. However, in practice catalyst degradation and solvent evaporation causes observed SABRE signal intensity to diminish over time. This decay is shown in Figure 4.24, which plots reference signal intensity against cumulative bubbling time over three days of experimental work. Gradual decay can be observed across each day, with sharp drops in signal overnight. Potential sources of the decay in signal intensity include solvent evaporation (during bubbling) and catalyst degradation (occurring most noticeably overnight, even without bubbling, giving the apparent step change in Figure 4.24). It is useful to maximise sample lifetime to make the most of each sample and to maintain a consistent SABRE response. Extended sample lifetimes also enable much longer experiments using the same sample, or complex 2D experiments where samples cannot be replaced partway through. This section will explore implementation of strategies to mitigate both solvent evaporation and catalyst degradation, beginning with evaporation.

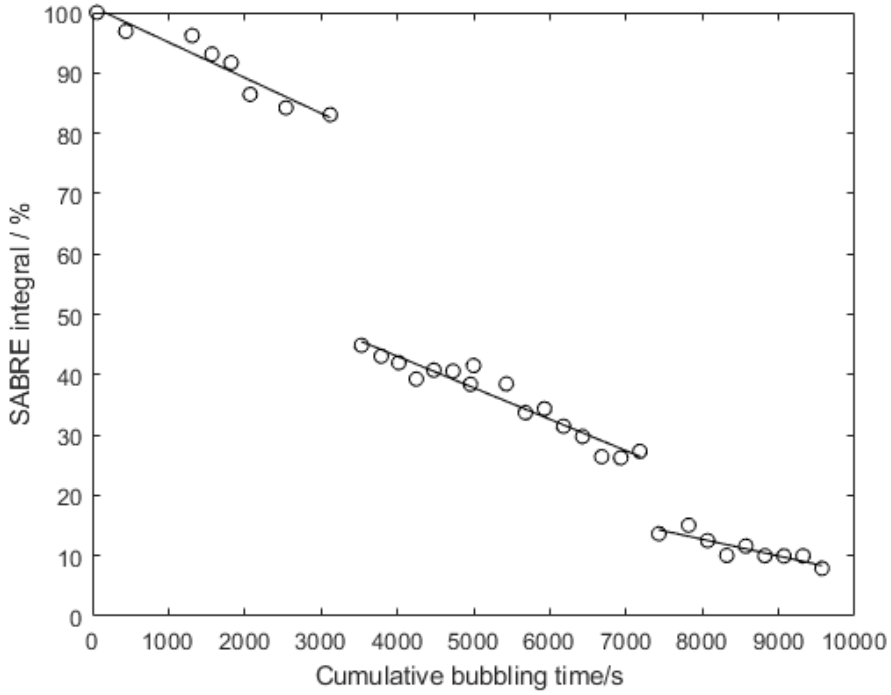

Figure 4.24: Reference peak integral against cumulative bubbling time, showing signal decay across three days of bubbling experiments

The impact of solvent loss is clearly illustrated when comparing the two cell designs used in this work. Linear fits of the integrals shown in Figure 4.22 shows the frit cell integral decays at 0.0019 ± 0.0006 % s^{-1} bubbling, compared to 0.0015 ± 0.00011 % s^{-1} bubbling for the capillary cell. This can be attributed to the weaker evaporation from the smaller stream of bubbles through the capillary cell. Figure 4.24 summarises the decay of the reference signal integrals recorded over multiple days. This data highlights two distinct issues that must be mitigated for consistent, long-term studies: first, the decline in

signal intensity that occurs during prolonged bubbling within a single session, and second, the more gradual degradation in catalytic performance observed across subsequent days.

4.8.1 Addition of an in-line methanol reservoir

Bubbling gas through the SABRE reaction solution drives evaporation of solvent and substrate (methanol and pyridine). This evaporation of sample diminishes the observed SABRE integral. Evaporation of pyridine substrate reduces the number of molecules available for hyperpolarisation, while the evaporation of the methanol solvent decreases the solution volume, limiting the amount of p-H_2 that can dissolve. While both methanol and pyridine will evaporate to some extent, methanol has a significantly lower boiling point (approx. 65 °C) compared to pyridine (approx. 115 °C). It is reasonable to assume that sample evaporation is overwhelmingly dominated by the loss of methanol. Therefore, the primary effect of bubbling is a continuous increase in the concentration of the pyridine substrate and catalyst.

To quantify the impact of solvent evaporation on the stability of the hyperpolarised signal, an experiment was designed to correlate the rate of solvent loss with the decay of the SABRE signal. A 4 mL sample of neat methanol was subjected to a continuous flow of hydrogen gas, simulating the conditions of a typical SABRE experiment. The rate of solvent evaporation was measured over time. This rate of mass loss was then cross-referenced against the decay of the integrated SABRE-enhanced pyridine signal from a separate experiment, using the standard SABRE sample. This direct comparison makes it possible to determine how significantly the loss of sample volume contributes to the observed decay in SABRE enhancement.

Rate of loss of solvent can be determined by bubbling for an extended period and then measuring the change in either sample mass or sample volume, which can be approximated by depth of solvent in the cell. Mass measurements are limited by the necessity to depressurise and repressurise the cell for each mass measurement. Volume measurements assume cell dimensions are consistent for the extent of the measurement. For both methods, the frit cell shown in Figure 4.7 was used. The cell was set on its side with the frit submerged at the lowest point, as is the case when performing experiments. The cell is then stood upright. For mass measurements once gas flow is stopped the cell is disconnected at the IDEX fittings on its neck and mass recorded. For volume measurements digital callipers were used to record solvent depth.

The solvent volume (V_t) at any intermediate time t was calculated using the interpolation method shown in Equation 4.1. In this equation, ρ is the solvent density and M_{cell} is the mass of the empty cell. The values M_{ini} and M_{final} are the masses of the cell plus solvent recorded only at the start and end of the entire experiment, while D_{ini}, D_{final}, and D_t are the corresponding solvent depths. This calculation determines the initial solvent mass ($M_{ini} - M_{cell}$) and subtracts the portion of the total mass loss ($M_{ini} - M_{final}$) that has occurred up to time t, as interpolated by the fractional loss of solvent depth. This method avoids the systematic error introduced by repeatedly depressurising the cell for

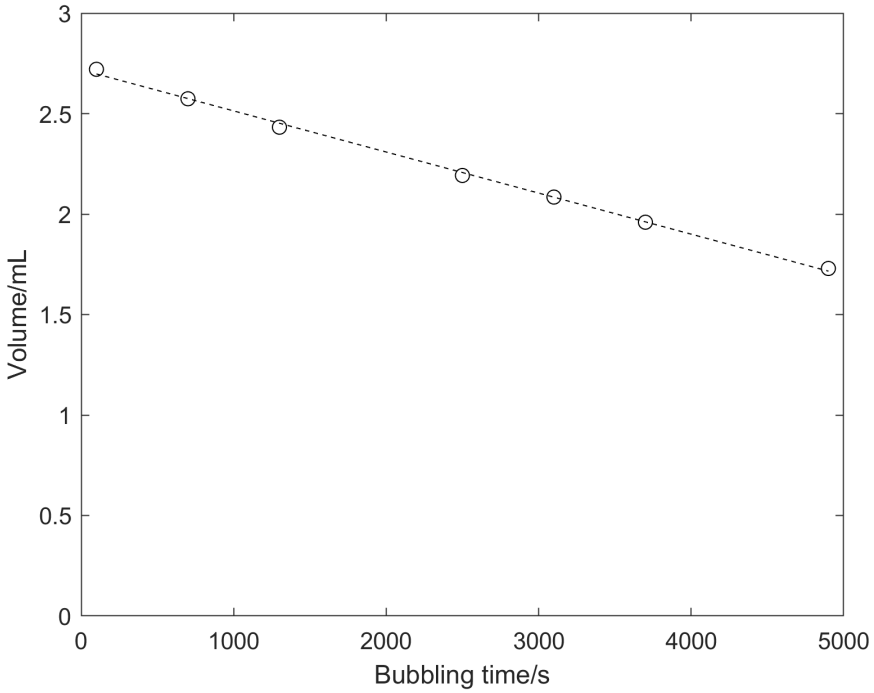

Figure 4.25: Volume of methanol contained in frit cell vs cumulative bubbling time. Volume calculated from mass measurements, less empty cell weight of 18.617 g. Volume depletes at $0.2\,\mu\mathrm{L\,s^{-1}}$ of bubbling.

intermediate mass measurements.

$$V_t = \frac{1}{\rho}\left[(M_{ini} - M_{cell}) - (M_{ini} - M_{final}) \times \frac{D_{ini} - D_t}{D_{ini} - D_{final}}\right] \tag{4.1}$$

Depth measurements were only recorded while a part the frit was submerged below the solvent surface while the cell was stood on end, to minimise inconsistency in volume change. The result of the mass measurement is shown in Figure 4.25. Solvent volume depletes at a rate of $0.2\,\mu\mathrm{L\ s^{-1}}$.

The depth measurement results are shown in Figure 4.26. Solvent is lost at a rate of $0.07\,\mu\mathrm{L\,s^{-1}}$. This is 35 % the rate of loss calculated through the mass measurements. The depth measurements are less precise but are more representative of the change in solvent volume as solvent vaporised into the cell head-space is not lost to atmosphere upon measurement, maintaining the shallower concentration gradients during the test that would be observed during normal experimentation. Each experiment used 4.0 mL MeOH as initial volume (V_{ini}).

To mitigate the loss of sample through evaporation, a solvent reservoir can be added in-line into the gas flow supply. The capillary cell is used for this reservoir, and is filled to approximately $\frac{3}{4}$ full with solvent (to prevent vigorous bubbling splashing solvent into the cell inlet line). When using MeOH, approximately 18 mL is used. This reservoir is included in Figure 3.7, labelled containing methanol. This saturates gas inbound to the sample with solvent before it reaches the reaction cell, limiting the volume of solvent that

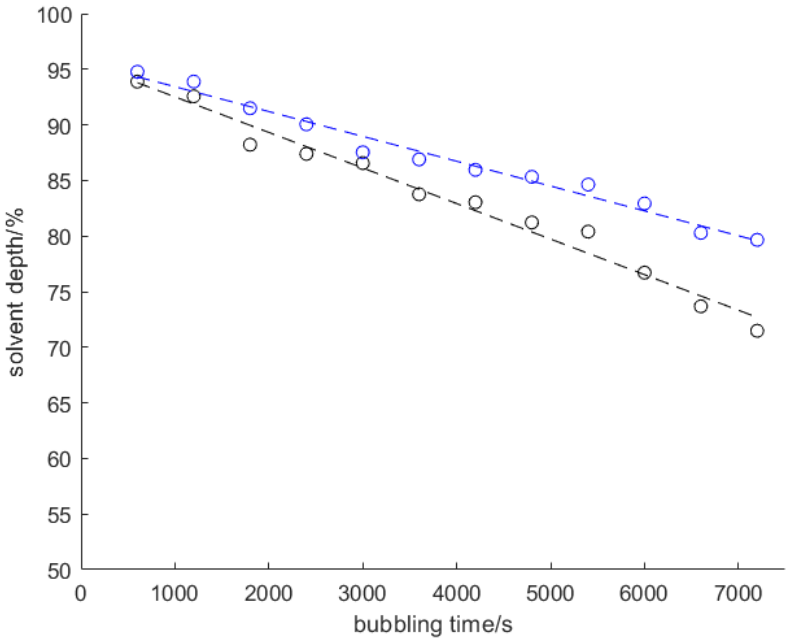

Figure 4.26: Change in solvent depth vs bubbling time for a frit cell containing 4 mL MeOH, with 18 mL of MeOH in the in-line solvent reservoir (black circles); and with an empty oslvent reservoir (blue circles) . Signal decays at 8.3 % h^{-1} (0.0023% s^{-1}) bubbling with the reservoir in-line and 11.5% h^{-1} (0.0032% s^{-1}) bubbling without.

Table 4.1: Rates of decay of reference peak signal across multiple experimental days.

Experimental Day	% Decay Rate per second Bubbling	% Initial Signal	% Decay/Hour since Activation	% Decay/Hour from Start of Day
1	0.0212	100	5.2	5.2
2	0.0188	64	3.14	7.0
3	0.01	29	1.13	14.8

is then evaporated from the reaction cell. Measurements of change in solvent depth were recorded with the methanol reservoir in-line and out of line.

Figure 4.26 shows methanol is lost at 0.0032% s^{-1} bubbling with the solvent reservoir excluded, equal to 0.135 μL s^{-1}. With the solvent reservoir included, rate of solvent loss is 0.0023 % s^{-1} bubbling or 0.101 μL s^{-1}; a 33 % improvement in rate of solvent loss. Thus a solvent reservoir is included in all subsequent experiments to limit solvent loss and maximise potential SABRE signal over extended experimental sessions.

4.8.2 Correlation of sample volume with SABRE signal

The previous section demonstrated that bubbling-driven methanol evaporation can be mitigated with the addition of the inline reservoir to deliver wet rather than dry hydrogen

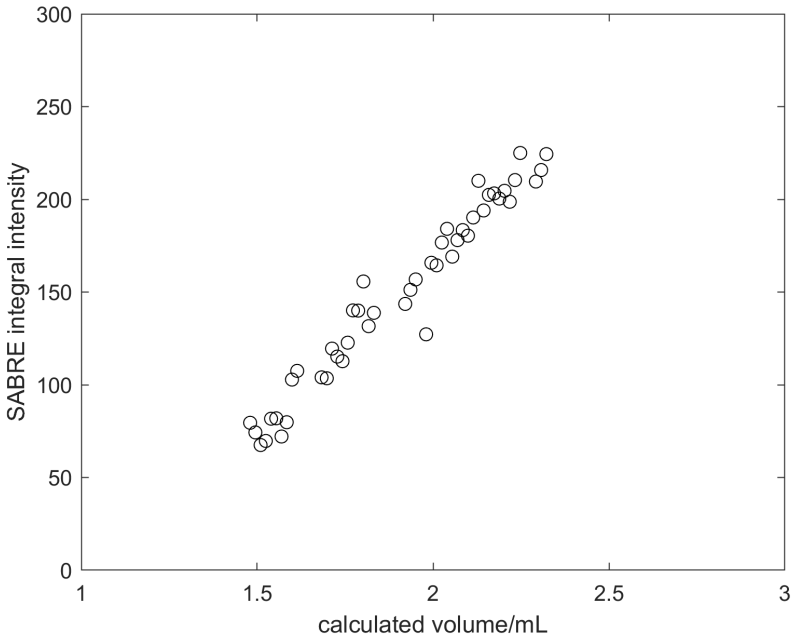

Figure 4.27: Calculated sample volume vs observed SABRE signal intensity (SABRE integral) from reference experiments taken after sample activation. The sample consisted of 10.80 mg catalyst and 80 μL pyridine, with no solvent reservoir in-line, beginning with 4 mL MeOH. The initial calculated volume is less than the prepared 4.0 mL due to solvent loss during catalyst activation prior to the experiment.

to the sample cell. Solvent boils off at a linear rate with respect to cumulative bubbling time t_B. Sample volume can therefore be calculated against cumulative bubbling time. In this manner, SABRE signal intensity can be correlated against sample volume. A series of standard reference experiments (Section 4.4.2 and Figure 4.11) were performed on a standard SABRE sample, with 60 s of p-H_2 bubbling between experiments. To correlate the SABRE signal intensity with sample volume, the volume at the time of each measurement was first estimated. This was based on the linear rate of solvent evaporation determined from the depth measurements in Section 8.1. The data for the cell without an in-line reservoir (Figure 4.26, blue data) shows a solvent depth decrease of 0.0032% per second of bubbling. The initial volume for the observations in Figure 4.27 is calculated at ≈ 2.45 mL by applying this evaporation rate to the bubbling time used for catalyst activation. The volume $V(t_B)$ at a given cumulative bubbling time t_B was calculated from the initial volume ($V_{ini} = 4.0$ mL) using the following relationship:

$$V(t_B) = V_{ini} \times \left(1 - \frac{0.0032 \times t_B}{100}\right) \tag{4.2}$$

As shown in Figure 4.27, there is a strong positive linear relationship between the calculated sample volume and the observed SABRE integral intensity. As the methanol solvent evaporates and the total sample volume decreases, the achievable hyperpolarised signal drops proportionally. This trend can be explained by considering the changing concentrations of the species involved in the catalytic cycle. While the concentration

of dissolved H_2, governed by Henry's Law, remains constant due to the fixed pressure, the concentrations of both the pyridine substrate and the catalyst increase as the solvent volume diminishes. This higher concentration of pyridine leads to it out-competing H_2 for binding sites on the catalyst. Consequently, the rate of H_2 exchange is slowed, reducing the efficiency of the SABRE catalytic cycle and leading to the observed drop in signal intensity.

A linear regression analysis of the data yields the relationship: $S = 181 \pm 4V - 196 \pm 9$, where the slope represents the signal enhancement (S) generated per millilitre of solvent (V). This value serves as a metric for the efficiency of the SABRE process under these specific conditions. While a linear extrapolation of this trend predicts the signal would reach zero at approximately 1.1 mL, this point is unlikely to be reached in practice. A more dominant, practical limitation exists: once the solvent volume drops below the gas delivery frit, *para*-hydrogen is no longer delivered into solution, preventing any further SABRE hyperpolarisation.

The preceding sections established a linear relationship between sample volume and SABRE signal intensity. The direct impact of mitigating this solvent loss is demonstrated in Figure 4.28, which compares the SABRE integral over time for samples with and without the in-line solvent reservoir. With the reservoir, the signal decay rate improves from $0.015 \pm 0.001\,\%\,s^{-1}$ to $0.0036 \pm 0.0004\,\%\,s^{-1}$. This represents a signal stabilization of nearly 76%, confirming that managing evaporation is critical for long-duration experiments.

The improvement in signal stability is significantly greater than the ∼28% reduction in the solvent evaporation rate alone. This disparity suggests the pre-saturated gas stream gives additional benefits beyond reducing the net loss of the methanol solvent. Potential explanations for this improved stability include the solvent-saturated gas limiting the evaporation of pyridine substrate, or the greater solvent volume improving long-term p-H_2 mixing and dissolution from bubbling through the frit. Given its effect on signal stability, the in-line solvent reservoir was adopted as an essential component for all subsequent experiments.

4.8.3 Limiting catalyst decay

The active SABRE catalyst is air sensitive.[50,74] The SABRE catalyst also irreversibly deactivates when there is a lack of substrate, through the dimerisation and oligomerisation of activated catalyst molecules.[122]

Degradation of the SABRE catalyst naturally results in fewer catalytic interactions during an experiment, and thus reducing the intensity of the observed SABRE signal. The decrease in observed SABRE signal levels can be tracked through the use of the reference experiment described in Section 4.4.2.

Figures 4.24 and 4.29 show the decay in signal intensity over the course of a sample lifetime, over time frames of hours and of several days, plotted respectively against time since catalyst activation and cumulative bubbling time. The decay profile in Figure

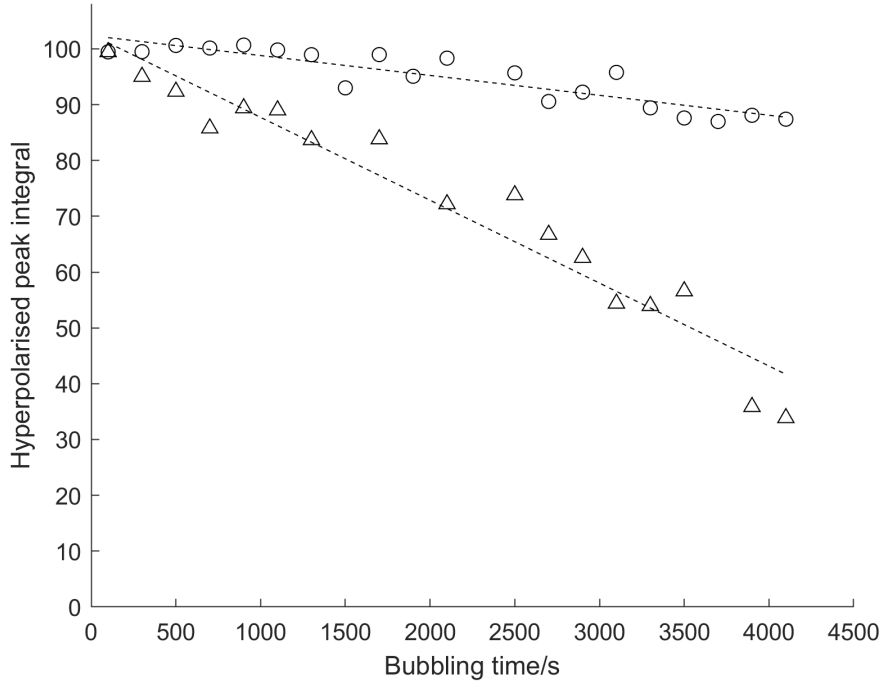

Figure 4.28: Plot of normalised hyperpolarised peak integral against cumulative p-H_2 bubbling time for a standard SABRE sample with (○) and without (△) the solvent reservoir in-line.

4.29, which plots signal against absolute time rather than cumulative bubbling time, clearly shows that significant signal loss occurs overnight. This supports the hypothesis of a bubbling-independent decay mechanism, such as the slow oxidation of the catalyst, which degrades the sample even when it is not in active use. Table 4.1 gives the decay rates for each day of experiments for bubbling time and for time since activation. The overnight decay rate is 3.7 % hour^{-1}. The rate of signal decay becomes proportionally worse with each subsequent day of use. While the absolute signal loss per hour decreases over the three days, the decay rate relative to the starting signal of that day increases significantly, from 5.2% per hour on Day 1 to 14.8% per hour on Day 3. This suggests that the catalyst degradation occurring overnight reduces the amount of active catalyst and renders the remaining catalyst less stable. Limiting catalyst decay therefore offers a significant extension in potential sample lifetime.

The SABRE signal can be seen to decay at consistent rates across the course of a day, with additional decay overnight.

When a sample is in use over multiple days, standard practice is to leave the gas delivery system at low pressure with all valves closed. Very small leaks and the porosity of the PTFE tubing allow gas to leak out of the cell and surrounding gas network, and oxygen can diffuse into the system once equilibrium pressure is reached. The oxygen-sensitive SABRE catalyst then degrades, limiting the use of any SABRE sample across multiple days of experiments.

To mitigate against air introduction into the sample during long periods between

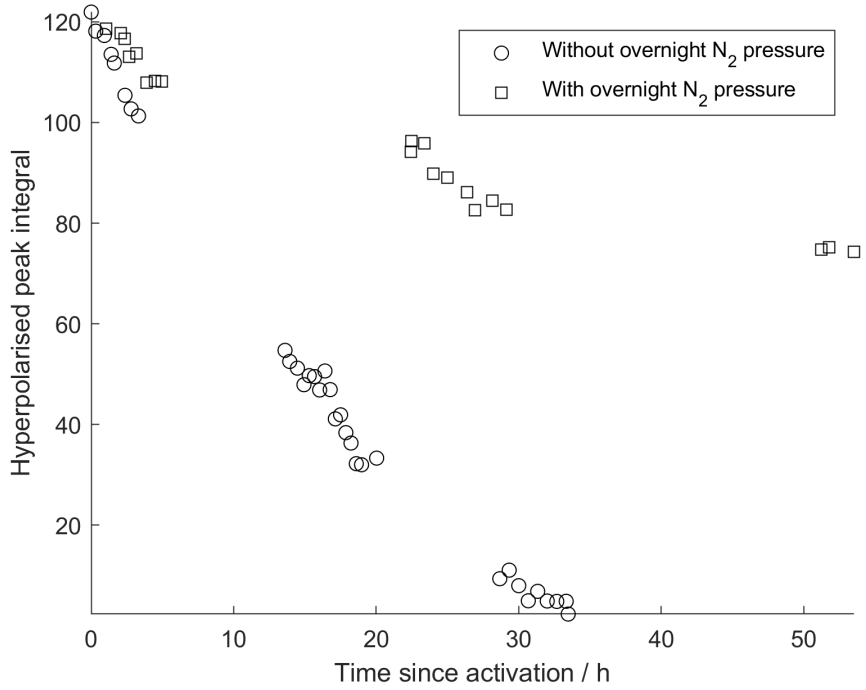

Figure 4.29: Comparison of decay of reference peak integral (from a standard sample with in-line solvent reservoir) against time since SABRE catalyst activation with H_2, over three days of experimental work, with solvent reservoir in-line containing 18mL MeOH.
(○) Sample left overnight without application of N_2 pressure.
(□) : identical sample with nitrogen pressure applied overnight.

experiments, the cell network can be pressurised to give a constant positive internal pressure in the cell and gas lines. This was done through addition of a nitrogen inlet to the cell network, which allows charging of the cell with nitrogen through opening of manual valves. The inlet connection is shown in Chapter 3 Figure 3.7. When left for long periods, all electronic valves are closed and the manual nitrogen inlet is opened. Nitrogen pressure is generally set to 3 bar (gauge pressure). The effectiveness of this strategy is demonstrated in Figure 4.29, which shows the signal decay for a sample stored under nitrogen pressure over multiple days.

This continuous pressurisation significantly extends the sample lifetime by reducing the overnight signal losses observed previously. A quantitative comparison with the data from the unpressurised sample (Figure 4.29) shows that the overnight signal decay rate decreases from 3.7 % hour^{-1} to 0.55 % hour^{-1}. This represents a nearly seven-fold improvement in catalyst lifetime. This significant extension of the catalyst's useful lifetime is attributed to the constant positive pressure of inert nitrogen, which effectively prevents the ingress of atmospheric oxygen. By inhibiting these oxidative degradation pathways, the catalyst retains a much higher level of activity for subsequent days of experiments, improving its utility in multi-day studies.

4.9 Conclusions

This chapter detailed the integration of a custom bubbling control system with a Magritek Terranova EFNMR spectrometer to conduct *in situ* SABRE experiments. Experimental parameters were optimised using a 250 mM pyridine standard, providing a methodological baseline for subsequent work.
The optimisation of p-H_2 delivery and PTF application was performed. A 60-second N_2 purge was found to fully remove dissolved p-H_2, but is inefficient for routine use. For maximum signal, a 30-second simultaneous bubbling and PTF application is recommended. For sequential bubbling - polarisation transfer experiments, a 20-second p-H_2 bubbling period followed by a 10-second PTF application yields maximum consistent signal in minimum time.
MRI was used to investigate mixing dynamics. A comparison between the standard frit cell and a single-capillary cell showed that the frit cell yields a two-fold increase in signal intensity. Imaging data attributed this to the larger gas-liquid surface area of the frit, which creates multiple regions of high hyperpolarisation. This suggests that maximising effective mixing of p-H_2 bubbles into solution is a more significant factor for best signal enhancement in this setup over achieving a uniform mixing pattern.
Methods to reduce signal decay were also evaluated. An in-line solvent reservoir reduced methanol loss by 33%, and pressurising the system with nitrogen overnight significantly extends the useful sample lifetime. This provides a basis for conducting *in situ* SABRE experiments with the highest possible reproducible signal and longest sample lifetime.

CHAPTER 5

Exploring the dynamics of *in situ* SABRE polarisation

5.1 Introduction

During work performed for Chapter 4, it was observed that while running multiple experiments in sequence, the intensity of an observed peak integral could vary significantly, appearing to depend on the length of delay between experiments. It can also be seen that the integral is greatly diminished when p-H_2 bubbling and the Polarisation Transfer Field (PTF) are separated, by as much as 80%. This observation suggests that an uncharacterised relaxation process occurring at the Earth's magnetic field (Earth's field) is a factor in the reproducibility and efficiency of *in situ* SABRE experiments.

A key concern is the effect of this relaxation on the level of hyperpolarisation observed once *para*-hydrogen has been introduced into solution. Any changes in p-H_2 concentration while the sample experiences stray fields has the potential to confound subsequent peak intensity, reducing the reliability of results, particularly for quantitative experiments or sequential scans (for example, T_1 measurements or imaging).

The SABRE process is governed by a relationship between spin physics and chemical exchange kinetics. As detailed in Chapter 2, the exchange of ligands proceeds via a dissociative mechanism where *para*-hydrogen and pyridine compete for a vacant coordination site on the catalyst. It can therefore be hypothesised that any relaxation of *para*-hydrogen spin order will be a catalyst-mediated process. The rate of this relaxation should be dependent on the relative concentrations of both pyridine and dissolved hydrogen, as these dictate the competitive binding kinetics that govern the interaction time between *para*-hydrogen and the catalyst.

While gaseous *para*-hydrogen can have a lifetime of weeks, its lifetime in solution is shorter (minutes to hours) and is strongly influenced by the presence of the SABRE catalyst.[163,164] Association with the catalyst in a magnetic field breaks the symmetry of the p-H_2 molecule, which, in the presence of a weak polarisation transfer field, enables the desired polarisation transfer to substrate and allows relaxation of H_2 to thermal equilibrium.[50]

The primary aim of this chapter is to investigate the relaxation of p-H_2 spin order in a SABRE solution at Earth's magnetic field. Specifically, to measure the rate of this relaxation and better understand the underlying mechanisms by probing its dependence on reactant concentrations.

To understand this relaxation behaviour, we must first understand features of the spin isomers of hydrogen. *Ortho-* and *para*-hydrogen were initially discussed in Chapter 2. A molecule of hydrogen gas can exist as one of two spin isomers, *ortho*-hydrogenand *para*-hydrogen, respectively a spin-symmetric triplet state coupled to the odd, and spin-antisymmetric singlet state coupled to the even rotational states. Interconversion between the two spin isomers is symmetry forbidden, allowing volumes of hydrogen with enhanced *para*-hydrogen fractions to be stored for long periods of time (weeks or longer) in the absence on any mechanism for interconversion.[165] Interconversion between spin isomers is permitted when the symmetry of the molecule is broken, for example this can occur through interaction with paramagnetic materials. Magnetic dipole-dipole coupling between the nuclear magnetic moment and an unpaired electron spin magnetic moment can break the symmetry of the H_2 molecule, allowing interconversion between spin states at a distance. The interaction intensity is proportional with the distance (R^{-4}).[165] Orbital overlap between the nuclei in H_2 and a paramagnetic species allows interconversion through the Fermi contact interaction. Interconversion only occurs when the induced overlap is different for the two nuclei in H_2, thus breaking its symmetry.[165] This interconversion can occur through heterogeneous routes such as near paramagnetic surfaces in activated carbon or iron oxide, as well as homogeneous routes such as O_2 or dissolved paramagnetic ions and complexes in solution. Interconversion can also occur through interactions with nuclear spins in diamagnetic materials,[166] exchange of H atoms,[167] and interactions with iMQCs (though interactions are much weaker due to a much lower γ).[168] Conversion kinetics depend on temperature (affecting equilibrium and mechanism rates), pressure (collision frequency, surface coverage), catalyst properties (nature, magnetic moment, surface area, activation state), and the presence of paramagnetic impurities (for example, O_2 or metal ions in glass).[169] Reconversion has been found to occur in seconds in the presence of a paramagnetic catalyst (iron oxide), minutes in the presence of oxygen,[165] hours in glass (due to paramagnetic impurities), though this can be alleviated through surface coatings which act to isolate the fluid contained from any paramagnetic surface species.[170]

5.1.1 Conversion Dynamics in SABRE

Chapter 2, Section 2.6.4 discussed the mechanism of ligand exchange in SABRE. Pyridine dissociates through a S_N1 type mechanism to leave a vacant site on the catalyst. The

rate of this dissociation depends only on catalyst concentration $[C]$. Substrate and free H_2 in solution can compete for this vacant site, driving substrate and hydride exchange. η^2 addition of p-H_2 to the substrate does not necessarily force reductive elimination of bound hydrides, but the brief binding can be enough to allow relaxation of the p-H_2 molecule. Relaxation occurs through symmetry breaking by different couplings of each H atom to the catalyst and bound substrate ligands. In the Earth's field, there are no differences in chemical shift among the hydrides and substrate protons, so it isn't clear that the catalyst breaks the symmetry of bound hydrides in the usual SABRE way. This presents the question of whether in Earth's field the SABRE catalyst would be expected to efficiently relax p-H_2 in solution. However, there are other potential routes to symmetry breaking and relaxation mechanisms available to p-H_2 in solution, including dipolar interactions and scalar relaxation of second kind (through interactions with ^{14}N, for example).[171]

This chapter will explore the lifetime of p-H_2 in SABRE solution in the Earth's field. If catalyst-mediated relaxation pathways are available, we might expect to see a very short relaxation time on the order of a few seconds, comparable to the hyperpolarisation lifetime in solution at higher field.[50] If, however, these relaxation pathways are quenched in the ULF regime, the relaxation of p-H_2 in solution might be expected to be comparable to the lifetime of p-H_2 in neat MeOH, around 300 minutes.[163] The observed lifetime of p-H_2 in low and ultra-low fields will have significant impact on reproducibility for experiments where p-H_2 bubbling is decoupled from polarisation transfer.

5.2 Experimental Methods

5.2.1 Hydrogen concentration and *para*-hydrogen enrichment in solution

To understand the kinetics and reactant dependencies investigated in this chapter, it is essential to have an accurate measure of the concentration of H_2 dissolved in the solution. An accurate calculation of H_2 concentration in solution will allow estimation of rates of interaction between all substrates and catalyst, giving a clearer picture of the way that changing these ratios impacts the SABRE process. The H_2 supply pressure from the Peak Scientific generator can be changed between 2.0 bar and 6.5 bar relative pressure. Higher pressures are available from the Mars hydrogen generator of up to 10 bar relative pressure, but the testing of equipment, particularly the IDEX connections to the cell arms, limits the safe working limits of the system to a maximum pressure of 6.5 bar.

The standard sample used in set-up and testing was composed of 10.80 ± 0.05 mg (4.2 mM) SABRE pre-catalyst, 80±0.8 μL (250 mM) pyridine (99.5%) in 4±0.2 mL MeOH (99.8%). To calculate the concentration of p-H_2 in solution, the mole fraction can be used to calculate moles of H_2 from the moles of MeOH present in the sample. Dividing this by the volume of the sample will give $[H_2]$ at 1 atm within the sample.[172] Equation 5.1 is a condensed version of this calculation where $C_{(g)}$ is the gas concentration, $\rho_{MeOH} = 792$

g dm^{-3} is solvent density, $M_{(l)}$ = 32.04 g $mol^{-1}$is the solvent molar mass for MeOH;[173] and $x_1(g)$ is the mole fraction of the gas.

$$C_{(g)} = \frac{\rho_{(l)}}{M_l} \times \mathtt{x}_{1(g)} \tag{5.1}$$

The IUPAC-NIST Solubility Data Series[174] gives the mole fraction $x_1(g)$ of H_2 at 1 atm and 298 K = 0.000161. The concentration of hydrogen in solution at 298 K can thus be calculated as 0.00398 M atm^{-1} = 3.93 mM bar^{-1}. Multiplication of this value by the recorded pressure of hydrogen in the cell allows calculation of [H_2] in SABRE solution in the reaction cell for a given pressure, following the proportionality shown in Henry's law. These calculated values are given in Table 5.1 for the range of supply pressures used in this chapter. The pressure after coil was recorded at each supply pressure using the cell pressure gauge PG-2 as shown in Chapter 3 Section 3.3.3.

Table 5.1: Reference table of supplied generator pressure, cell pressure and p-H_2 concentration in 4 mL MeOH

H_2 gen. relative pressure/bar	P(H_2) after coil/bar	[H_2] in cell/mM
6.5	5.87	23.1
5.5	4.88	19.2
4.5	3.89	15.3
3.5	2.91	11.4
2.5	1.92	7.5
2	1.44	5.7
-	1	3.9

These calculations assume that the temperature in the laboratory remains constant and thus that the sample temperature is constant, and is not significantly cooled by incoming gas or subject to variations over multiple experimental days or months. Small variations in temperature would have only a minor impact on H_2 concentration in solution. If we assume a 5 K change in temperature over the course of a day, we can re-calculate [H_2]. The IUPAC-NIST solubility series gives mole fraction of H_2 in MeOH at 293 K of 0.000157. This gives [H_2] as 0.00388 M atm^{-1} = 3.83 mM bar^{-1}, a difference of 2.5 %.

While Henry's law provides a method to estimate the concentration of hydrogen in solution from the pressure, a method is also needed to measure the relative level of p-H_2 enrichment. *Para*-hydrogen enrichment cannot be directly measured in solution in this experimental set-up. Enrichment can be measured using Raman spectroscopy,[175] but such a system is infeasible to implement here. Instead, a proxy measurement can be used: hyperpolarised peak integral from NMR detection. Richardson *et al.*[146] show that observed polarisation levels are linearly dependent on p-H_2 enrichment levels. For this experiment, the linear dependence of SABRE signal on p-H_2 under otherwise identical conditions allows the use of observed SABRE peak integral as a proxy measurement for relative enrichment of p-H_2 in solution. This proxy relies on the assumption that the concentration of H_2 in solution is consistent for a given bubbling time t_{p-H_2}.

5.3 Investigating *para*-hydrogen relaxation dynamics at Earth's field

To investigate how p-H_2 relaxes in Earth's field, we can decouple p-H_2 delivery from the bubbling system (Chapter 3) and PTF application in a pulse sequence. The supplied pressure of H_2 can be varied, which changes [H_2] in solution and affects the exchange rates. The concentration of pyridine can also be varied, which will also impact competition for vacant catalyst sites. The change in these interactions can then be used to observe how signal intensity and relaxation rates are impacted. A controlled, variable delay between p-H_2 delivery and PTF application allows for the direct measurement of signal loss during this period. The pulse sequence shown in Figure 5.1 was employed. This sequence introduces a variable delay (d_1) between p-H_2 bubbling ($t_{p\text{-}H_2}$), and PTF application (t_{PTF}).

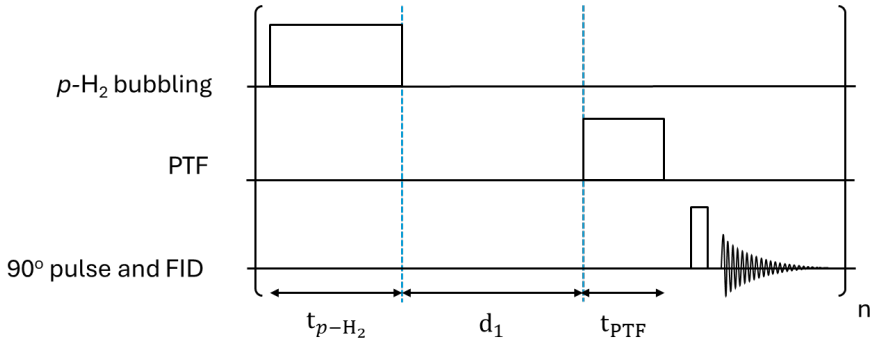

Figure 5.1: p-H_2 decay pulse sequence. *Para*-hydrogen is bubbled for a fixed duration of 20 s, followed by a variable relaxation delay d_1, then polarisation transfer and detection.

In all experiments $t_{p\text{-}H_2}$ = 20 s and t_{PTF} = 10 s. This is in line with the minimum effective bubbling time and PTF observed in Chapter 4. Allowing saturation of the solution with p-H_2 in the minimum time, to reach a fixed [H_2] in solution. It is also assumed that from this fixed H_2 concentration in solution, a consistent resultant SABRE peak integral will be observed.

Figure 5.2, presents an example result of this experiment on a sample of 4.2 mM (10.80 mg) Ir(IMes) SABRE catalyst, 250 mM (80 μL) pyridine in 4 mL MeOH. Two decay regimes are shown: an initial decay in the observed SABRE signal as d_1 increases to 20 s (inset), and a much slower decay of the signal across a much longer timescale (several minutes). The data was processed as described in Section 5.3.1. The integrals show two clear regimes: a fast decay to approximately 25 % initial intensity and an apparent second, much slower decay ill-characterised across an 11-minute $d_{1(max)}$ timescale. This suggests two separate relaxation processes are occurring. Therefore, a biexponential model was chosen to model the processes. The model is given in Equation 5.2, where $I(t)$ is the peak integral at time t, A_α is the amplitude of the first (α) process and t_α is the relaxation time constant, A_β is the amplitude of the second (β) process, and t_β is the relaxation time constant. The fit of the data shown in Figure 5.2 to this model is very strong

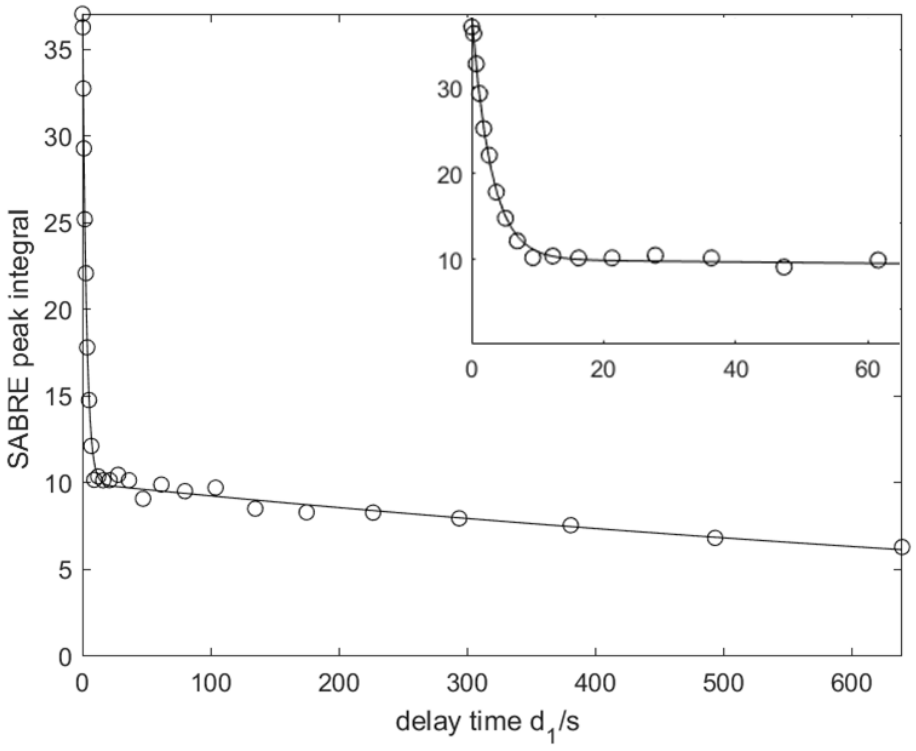

Figure 5.2: SABRE signal integral against delay time d_1 acquired using the pulse sequence in Figure 5.1. Data shown for a sample containing 250 mM pyridine and 4.2 mM Ir(IMes) SABRE catalyst. Insert shows the integral over $d_1 = 0$ to 61 s. The values for a fit to equation 5.2 are given in Table 5.2. $t_{p-H_2} = 20$ s, $t_{PTF} = 10$ s

($R^2 = 0.9974$), suggesting this is a highly effective model for the phenomena observed.

$$I(t) = A_\alpha \exp\left(-\frac{t}{t_\alpha}\right) + A_\beta \exp\left(-\frac{t}{t_\beta}\right) \tag{5.2}$$

The time window ($d_{1_{max}} = 640$ s) does not capture the full decay of SABRE signal through the slow relaxation process. However, its relative amplitude, A_β, can be effectively captured by the model, where the total signal at time $t = 0$ is the sum of the amplitudes ($A_{total} = A_\alpha + A_\beta$). This data implies the existence of at least two distinct relaxation pathways or environments for p-H_2 within the SABRE solution.

This observation leads to the central hypothesis of this chapter: that the fast-decaying component (α) represents a catalyst-mediated relaxation pathway governed by ligand exchange kinetics, while the slow-decaying component (β) represents a background relaxation process.

The fit data from Figure 5.2 is shown in Table 5.2. The fast decay process has a time constant $t_\alpha = 2.8 \pm 0.2$ s, and the slow process a time constant $t_\beta = 1300 \pm 300$ s. Accurate measurement of this time constant is limited by the timescale - it is very ill defined by this dataset. The fast component magnitude A_α accounts for the majority of the signal loss ($A_\alpha = 28.7 \pm 0.8$, 74% of the initial amplitude A_{total}), compared to A_β, 26% of A_{total} ($A_\beta = 10.0 \pm 0.4$). The fast-decaying component, which accounts for the majority of the signal loss, is hypothesised to represent the relaxation of p-H_2 that

Table 5.2: Biexponential decay (Equation 5.2) fitting values for data shown in Figure 5.2

Parameter	Value
A_α	28.7 ± 0.8, 74%
t_α	2.96 ± 0.20 s
A_β	10.0 ± 0.4, 26%
t_β	1300 ± 300 s

is actively exchanging with the Ir(IMes) SABRE catalyst. In contrast, the slow-decaying component may correspond to several phenomena, including the reintroduction of p-H_2 to solution, or relaxation mediated by a less active catalyst species. The following sections will test this hypothesis by systematically investigating how each component responds to changes in reactant concentrations. Table 5.3 gives details of the samples' reactant quantities used in these experiments.

Table 5.3: Table of pyridine and catalyst concentrations and supply pressure range used in relaxation measurements throughout this chapter.

Sample	[Pyridine]	[Catalyst]	Pressure H_2 / bar
1	250 mM	4.2 mM	2.0 - 6.5
2	200 mM	4.2 mM	2.0 - 6.5
3	125 mM	4.2 mM	2.0 - 6.5
4	50 mM	4.2 mM	2.5 - 6.5
5	25 mM	4.2 mM	2.0 - 6.5

5.3.1 Data Processing and Analysis

To efficiently and accurately compare experimental data, automated data processing macros were developed in Prospa and Matlab to allow for consistent processing of raw FID data into comparable spectra. This allows large data sets and experiments on different samples to be efficiently compared and trends to be observed. Spectra can be handled individually, or the same processing can be applied to a pseudo-2D array of FIDs.

Raw FIDs of 2D data sets from the sequence in Figure 5.1 are recorded through the TerranovaExpert software from Magritek. A macro was written in Prospa to systematically process all data in the same manner. This macro is provided in Appendix B. Spectra are Fourier transformed, phased, and integrated, to give a series of integrals for each variation in the 2D sequence.

Phasing can be performed in two ways: in "auto-phase" mode, which maximises peak amplitude of all spectra in a 2D experiment individually, or in "fixed - phase" mode, which maximises the peak of a reference spectrum (typically the first), and then applies the same phase adjustment to all subsequent spectra. A fixed-width integral is then

applied to the spectrum, which can be exported for further analysis. As Earth's field spectra of pyridine contain only a single peak at the Larmor frequency, spectral peaks are integrated by a fixed frequency width about a pre-set peak centre to give reproducible integrals consistent across multiple spectra. The biexponential fit described in equation 5.2 was calculated in MATLAB (Appendix C)

5.3.2 Characterisation of Initial Signal at $d_1 = 0$

We can first consider the size of the initial observed signal, $A_\alpha + A_\beta$ or A_{total}. The variation of relative amplitudes with the reactant concentrations provides insight into the two processes.

First considering the standard 250 mM pyridine/4.2 mM catalyst sample, the change in A_α, A_β, and the total integral can be observed under changing supply pressure over the range 2.0 - 6.5 bar as given in Table 5.1. Figure 5.3(a) shows the relationship between p-H_2 supply pressure (linearly related to p-H_2 concentration) using sample 1 (250 mM pyridine) against A_α, A_β, and A_{total}. Both components show a broadly linear dependence on pressure. However, the effect is dominated by the fast component, with A_α increasing significantly more than A_β. This indicates that the fast relaxation process is strongly linked to the concentration of available p-H_2 in solution. The intensity of A_β also shows a dependence on pressure, but the effect is far weaker. Some of this can be attributed to the changing pressure affecting reaction kinetics, but it appears that the A_β magnitude is largely unaffected by the concentration of p-H_2 in solution. This can also be seen in the data for the other pyridine concentrations given in Figure 5.3. This suggests that the intensity of A_β is not dependent on p-H_2 concentration; that the process is proportionally the same for all pressures.

The data presented in Figure 5.3 can also be presented as a function of pyridine concentration. This is shown in Figure 5.4. This shows a similar dependency of A_α, A_β, and A_{total} on [py] as [H_2], again dominated by the A_α component, while A_β shows only a very weak dependence if any at all. This again suggests A_α is catalyst mediated and A_β is catalyst independent.

Figure 5.4 shows much weaker trends than Figure 5.3. The changing pyridine concentration adds several confounding factors to deep interpretation, as the solution dynamics are all affected. An increase in pyridine concentration is expected to give more signal due to more spins available in solution to hyperpolarise. However, more pyridine molecules means stronger pyridine competition for vacant catalyst sites, causing changes in SABRE efficiency between samples. This will be further complicated by small differences in catalyst mass and, at low pressure, shim linewidth between samples.

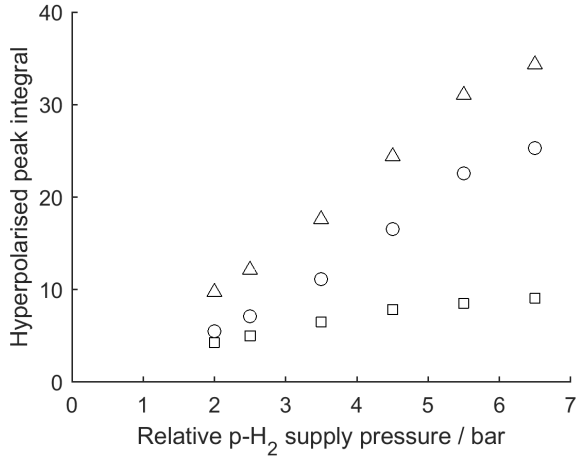

(a) Sample 1 (250 mM [py])

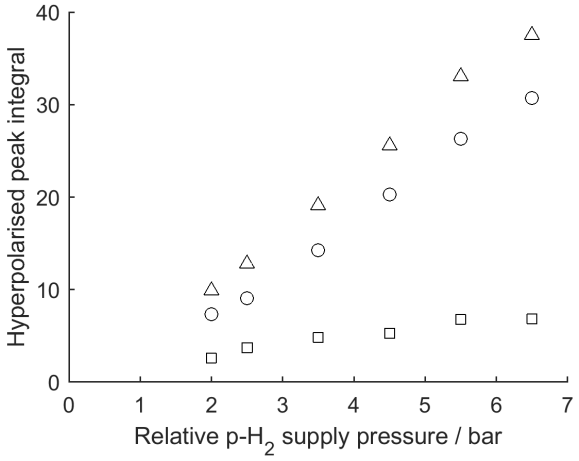

(b) Sample 2 (200 mM [py])

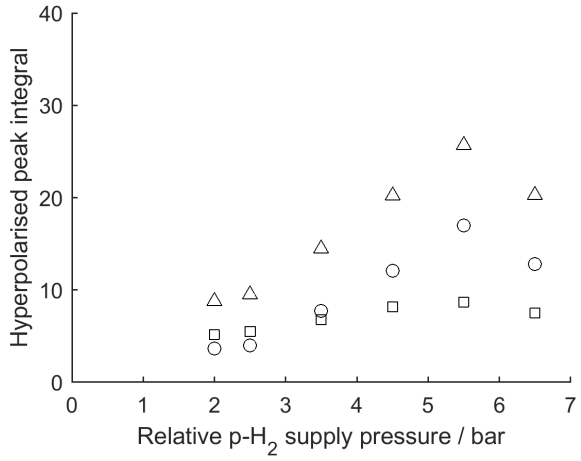

(c) Sample 3 (125 mM [py])

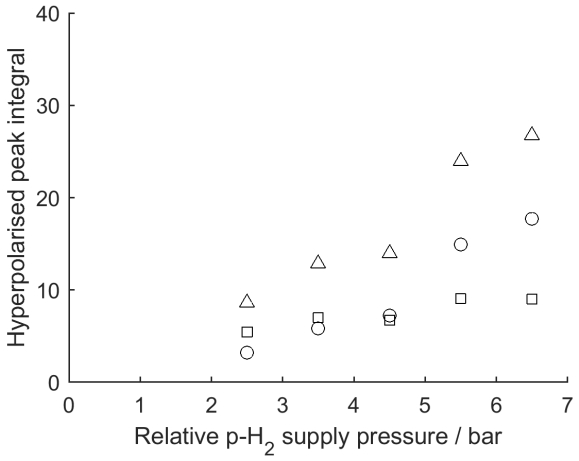

(d) Sample 4 (50 mM [py])

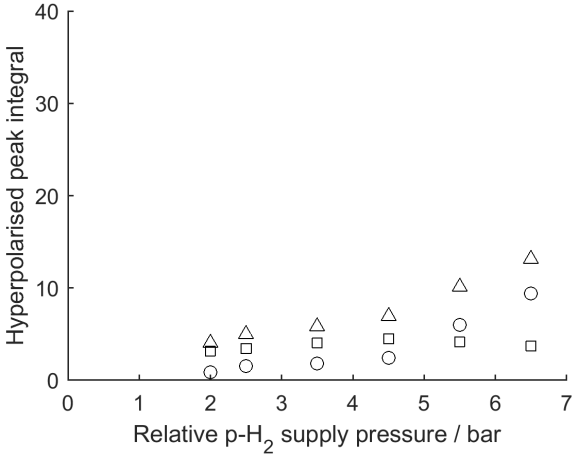

(e) Sample 5 (25 mM [py])

Figure 5.3: Plot of A_α (□), A_β (○), and A_{total} (△) against relative p-H_2 supply pressure. All samples contained 4mL MeOH and 4.2 mM Ir(IMes) SABRE catalyst, with pyridine concentrations: Sample 1 (250 mM (a)), Sample 2 (200 mM (b), Sample 3 (125 mM (c)), Sample 4 (50 mM (d)), Sample 5 (25 mM (e)).

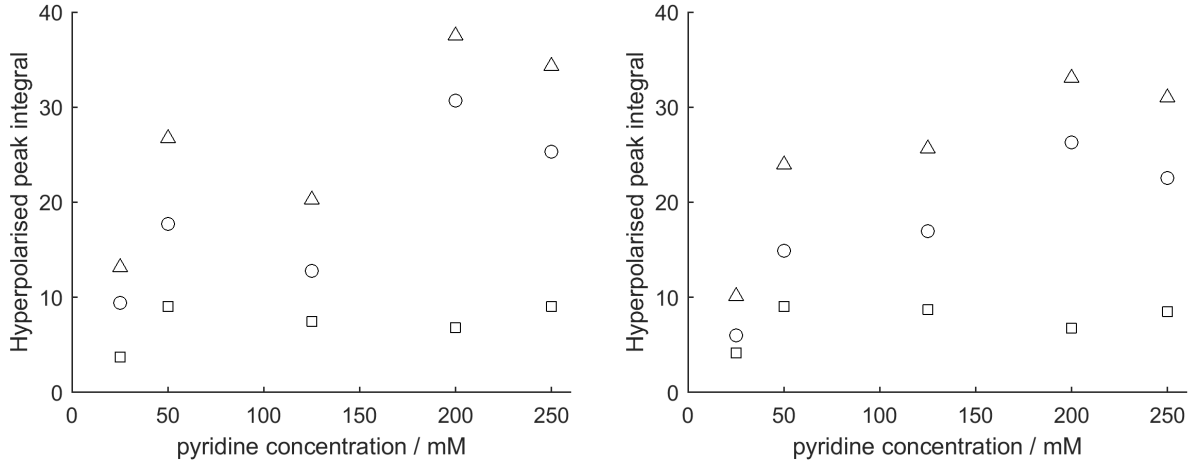

(a) 6.5 bar p-H_2

(b) 5.5 bar p-H_2

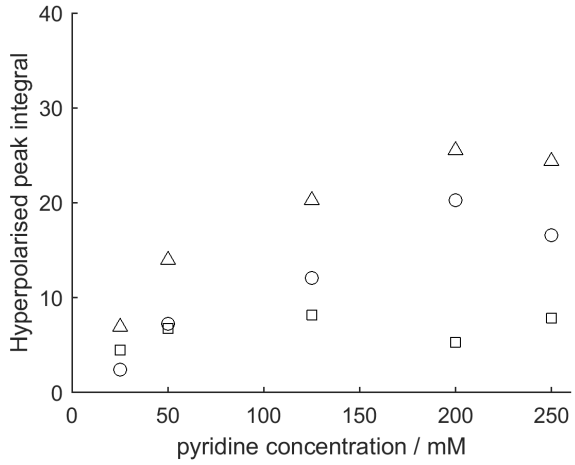

(c) 4.5 bar p-H_2

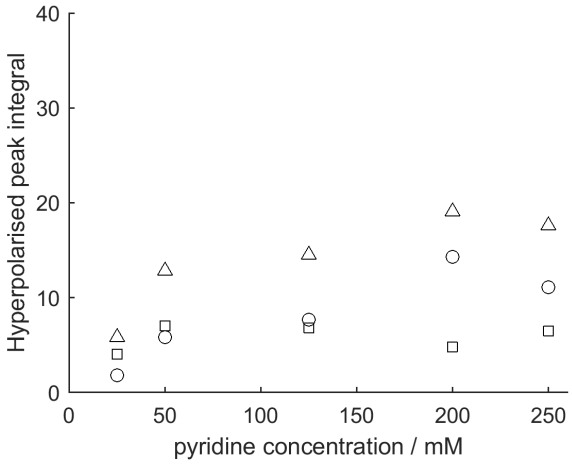

(d) 3.5 bar p-H_2

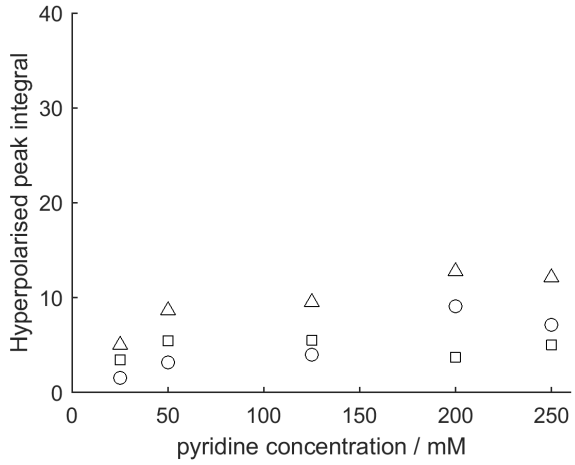

(e) 2.5 bar p-H_2

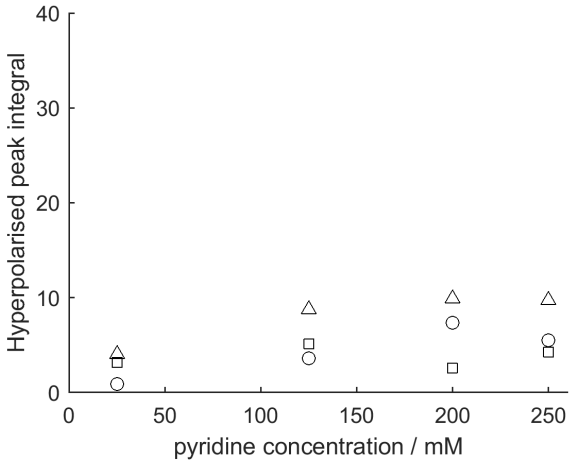

(f) 2.0 bar p-H_2

Figure 5.4: Plot of A_α (□), A_β (○), and A_{total} (△) against sample pyridine concentration. All samples contained 4mL MeOH and 4.2 mM Ir(IMes) SABRE catalyst, with p-H_2 supplied at: 6.5 bar (a), 5.5 bar(b), 4.5 bar (c), 3.5 bar (d), 2.5 bar (e), 2.0 bar (f).

5.4 Relaxation of SABRE signal

Having characterised the amplitudes of the two decay processes, the relaxation time constant of the fast-decaying component, t_α, can be analysed. This section examines the way in which t_α changes with changing substrate concentrations. This will enable an understanding of how substrate and catalyst interactions affect the relaxation of p-H_2 in solution while static in the Earth's field.

5.4.1 Effect of changing *para*-hydrogen concentration on t_α

First, we can observe the effect of changing [H_2] on t_α. Figure 5.5(a) shows how t_α changes with pressure. It shows that t_α is positively correlated with pressure, and hence on H_2 concentration. The relaxation time t_α becomes longer (relaxation is slower) at higher H_2 concentrations.

This result provides support for the hypothesis that the fast relaxation process is a catalyst-mediated process limited by the rate of pyridine dissociation. While a higher [H_2] concentration is expected to increase the rate of H_2 association to a vacant catalyst site, which would, in isolation, shorten t_α, the observed trend suggests this is not the dominant factor. Instead, the data is better explained by a model where pyridine dissociation is the rate-limiting step. As discussed in Chapter 2, the rate of this dissociation is independent of [H_2], suggesting that during both p-H_2 and t_{PTF} catalyst offers a relatively fixed number of vacant sites for interaction per unit of time. At higher pressures, the total pool of dissolved, hyperpolarised p-H_2 is larger. Consequently, this fixed number of relaxation events depletes a smaller fraction of the total p-H_2 pool over the same time period. This effect appears to outweigh the increased association rate, leading to the longer observed bulk relaxation time constant (t_α) and reinforcing the model of a catalyst-mediated, dissociation-limited process.

Figure 5.5 shows the dependence of the decay time constant t_α on p-H_2 supply pressure at all pyridine concentrations 25-250mM. Similar correlation trends are shown for each concentration, but the absolute value of t_α appears shorter at lower [py] as well as lower p-H_2 pressure. This variation in t_α with [py] in each sample indicates a dependence on [py]. The nature of this dependence is explored in the next section.

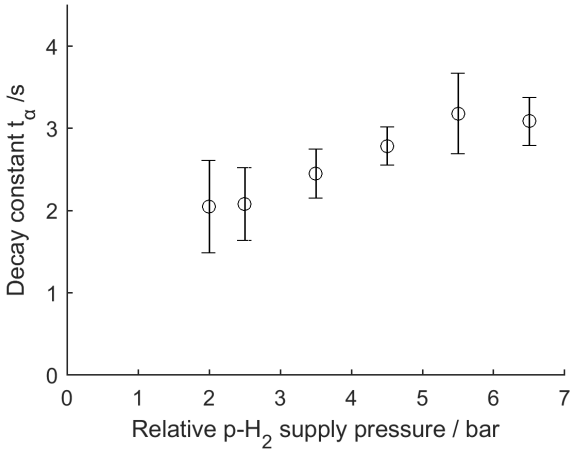

(a) Sample 1 (250 mM [py])

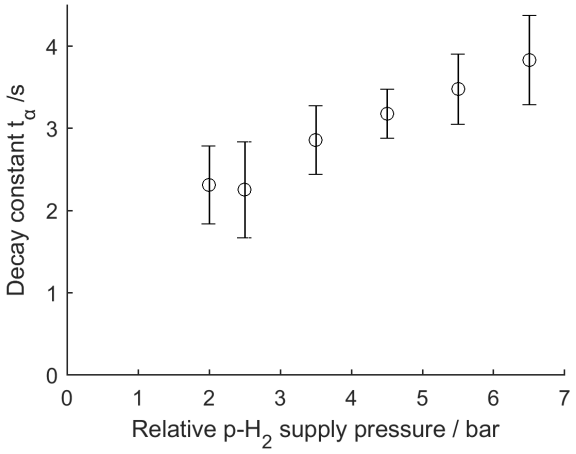

(b) Sample 2 (200 mM [py])

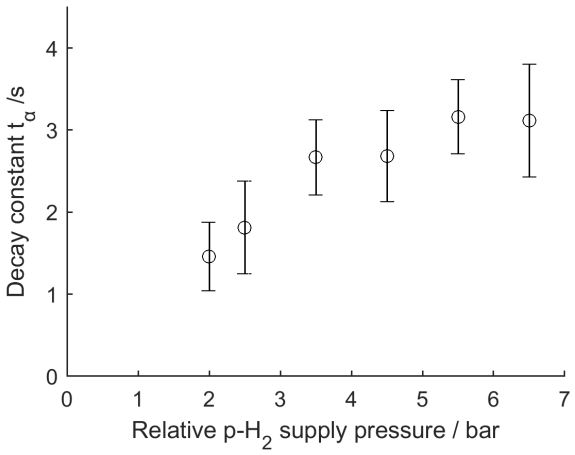

(c) Sample 3 (125 mM [py])

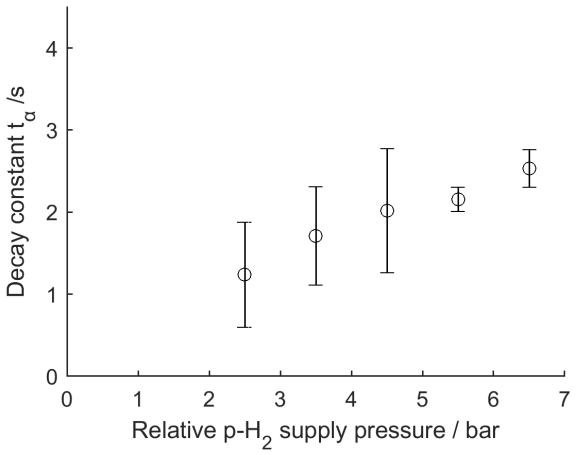

(d) Sample 4 (50 mM [py])

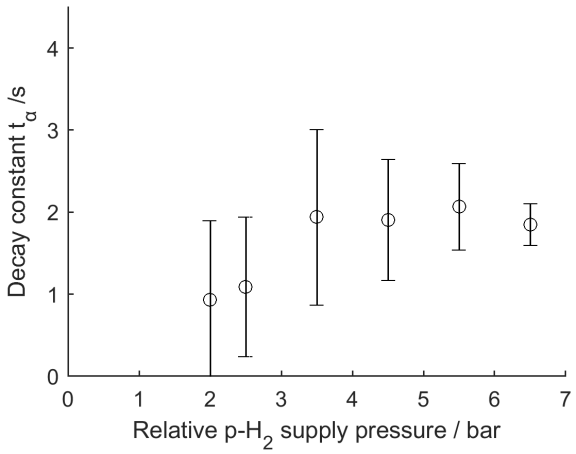

(e) Sample 5 (25 mM [py])

Figure 5.5: Plot of t_α against relative p-H_2 supply pressure. Error calculated from 95 % confidence interval of the fit. All samples contained 4mL MeOH and 4.2 mM Ir(IMes) SABRE catalyst, with pyridine concentrations: Sample 1 (250 mM (a)), Sample 2 (200 mM (b), Sample 3 (125 mM (c)), Sample 4 (50 mM (d)), Sample 5 (25 mM (e)).

5.4.2 Effects of changing pyridine concentration on t_α

To further probe the role of ligand exchange, we now examine the effect of pyridine concentration on the decay constant t_α. In Figure 5.6 the data from Figure 5.5 is re-plotted against pyridine concentration at fixed supply pressure. A general trend in Figure 5.6 can be observed where t_α is shorter at lower pyridine concentrations, although the data is noisier. This can be attributed in part to the data being recorded across multiple samples on different days, introducing greater uncertainty from minor variations in catalyst mass, field homogeneity, and other conditions compared to simply varying pressure for a single sample. Interpreting this trend is further complicated because the signal intensity is a function of both the number of available spins and the altered catalytic efficiency due to competition at higher pyridine concentrations. Despite the noise, this trend is consistent with the catalyst-mediated relaxation hypothesis. At higher pyridine concentrations, pyridine is better able to compete for vacant sites following dissociation, reducing the frequency of catalyst-H_2 interactions and thus the rate of relaxation. A higher pyridine concentration leads to an increased rate of rebinding to the coordinatively unsaturated catalyst intermediate. This outcompetes the binding of p-H_2, reducing the frequency of catalyst-mediated relaxation events for any given p-H_2 molecule and thus lengthening the observed relaxation time t_α.

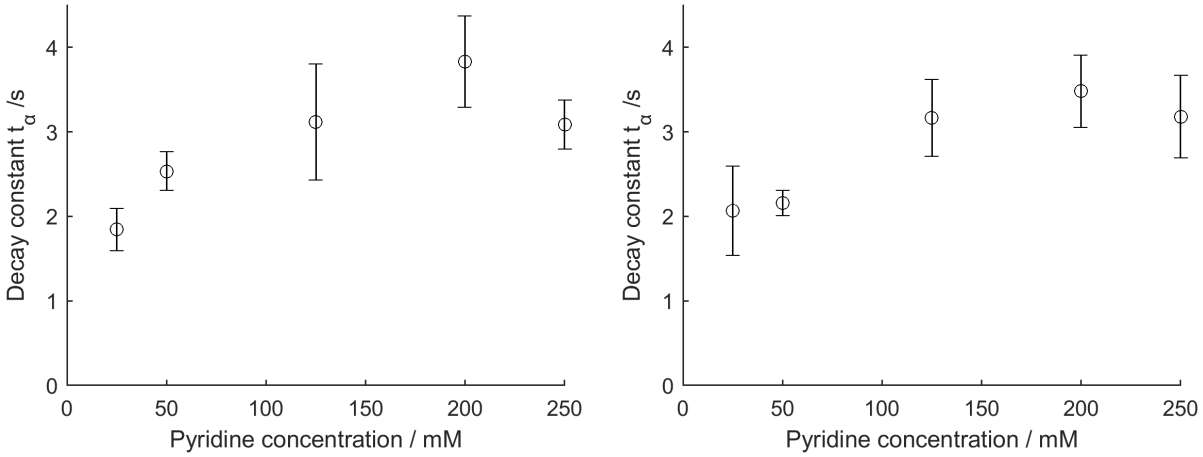

(a) 6.5 bar p-H_2

(b) 5.5 bar p-H_2

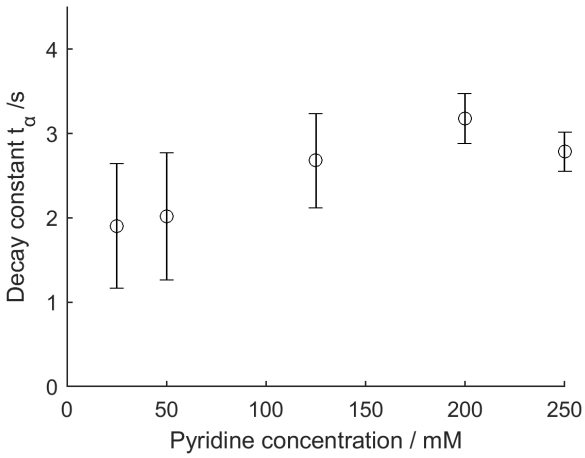

(c) 4.5 bar p-H_2

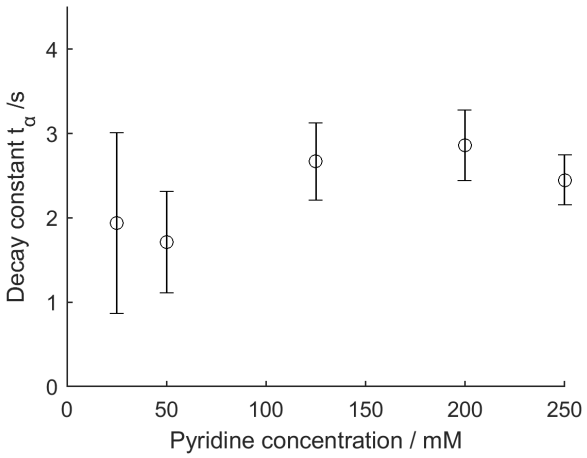

(d) 3.5 bar p-H_2

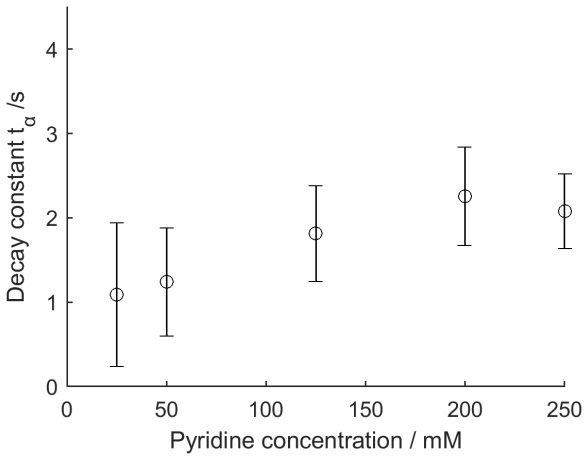

(e) 2.5 bar p-H_2

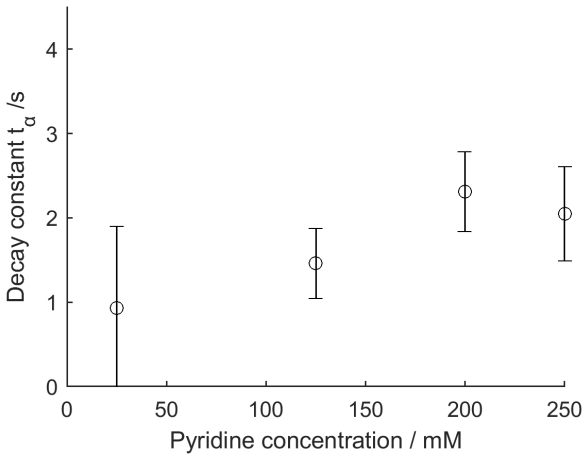

(f) 2.0 bar p-H_2

Figure 5.6: Plot of t_α against sample pyridine concentration. Error from 95% confidence interval of the fit All samples contained 4mL MeOH and 4.2 mM Ir(IMes) SABRE catalyst, with p-H_2 supplied at:6.5 bar (a), 5.5 bar(b), 4.5 bar (c), 3.5 bar (d), 2.5 bar (e), 2.0 bar (f).

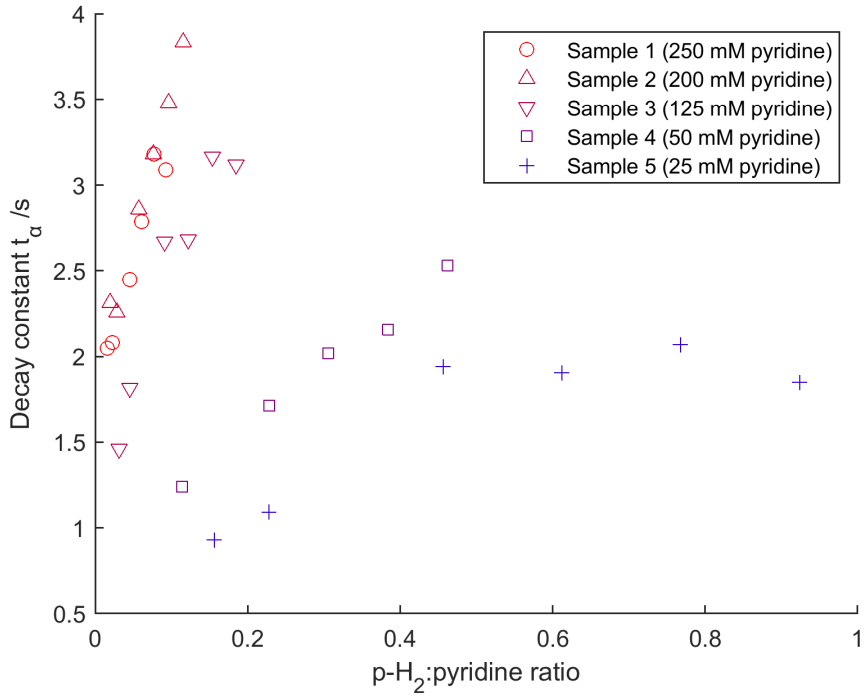

Figure 5.7: Relaxation constant t_α against [p-H_2]/[pyr] for all samples 1-5 (25 - 250 mM pyridine).

5.4.3 Modelling relaxation with reactant ratio

Since t_α depends on both [p-H_2] and [py], it is insightful to plot t_α against the ratio of these two exchanging species. However, plotting t_α against the simple ratio of [p-H_2]/[py], shown in Figure 5.7, shows significant sample-to-sample variation, indicating that the relaxation rate is also influenced by the absolute concentrations, not just their ratio.

To account for the competitive binding effect of pyridine, the relaxation time $t_\alpha$can be normalised by the pyridine concentration. Figure 5.8 shows a plot of this normalised relaxation time, t_α/[py], against the reactant ratio, [H_2]/[py]. This normalisation collapses the data from multiple experiments onto a single, clearer trend. This suggests that the fast relaxation process is driven by the interaction of p-H_2 with the SABRE catalyst, and its rate is dictated by the relative concentrations of all exchanging species.

The data for sample 5 (25 mM pyridine) appears somewhat anomalous, potentially approaching an asymptotic limit where the large excess of p-H_2 means the exchange rate is no longer dependent on the ratio. Excluding this dataset, as shown in Figure 5.9, reveals a much stronger linear trend for the samples with pyridine concentrations from 50 to 250 mM. This linear relationship provides a means to predict the rate of decay for a given H_2:py ratio within this concentration regime and further supports the model of a competitive, catalyst-driven relaxation mechanism.

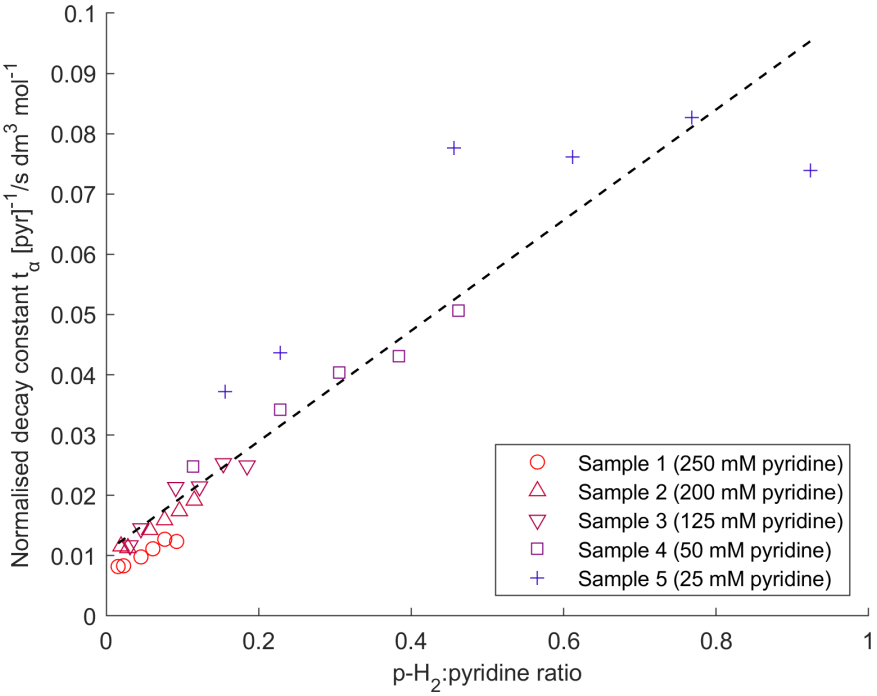

Figure 5.8: Plot of normalised relaxation time t_α/[py] against reaction ratio [p-H$_2$]/[py]]

5.4.4 Analysis of the slow relaxation process

A full quantitative analysis of the slow relaxation time, (t_β) was not practical. Most fittings yielded t_β values on the order of 1000 s with a $> 50\%$ error. An accurate fitting would need to take recordings with $d_{1(max)}$ up to 5 t_β, which would require an experiment with a maximum $d_{1(max)}$ on the order of 1-2 hours. A single well-defined curve over this time would require therefore approximately eight hours to record. With d_1 this long, there arise a number of other issues in recording accurate data, including catalyst decay, including through permeability of the gas lines to air, and experimentally significant drift of the Earth's magnetic field both between scans and between application for PTF and acquisition, during which time the field cannot be adjusted. The relaxation constant for t_β is therefore not characterised here, and analysis of the slow relaxation process uses its relative contribution to the overall decay A_β.

As shown previously (Figures 5.3 & 5.4), the amplitude A_β varies very little with reactant concentrations. This suggests the slow relaxation process is largely independent of the catalyst-substrate interactions that govern the fast relaxation process. The slow relaxation process appears in effect to be counteracting the complete relaxation of signal from the fast relaxation process. A plausible hypothesis for this mechanism is the presence of a reservoir of p-H$_2$ which undergoes exchange with the p-H$_2$ dissolved in solution. Therefore, higher pressure brings more p-H$_2$ into the reservoir. We can conjecture that the slow relaxation process is a process of exchange between a reservoir of fresh p-H$_2$ in the headspace of the cell and depleting p-H$_2$ in solution. This slowly replenishes the p-H$_2$, and is the reason we do not see complete relaxation through the fast relaxation process.

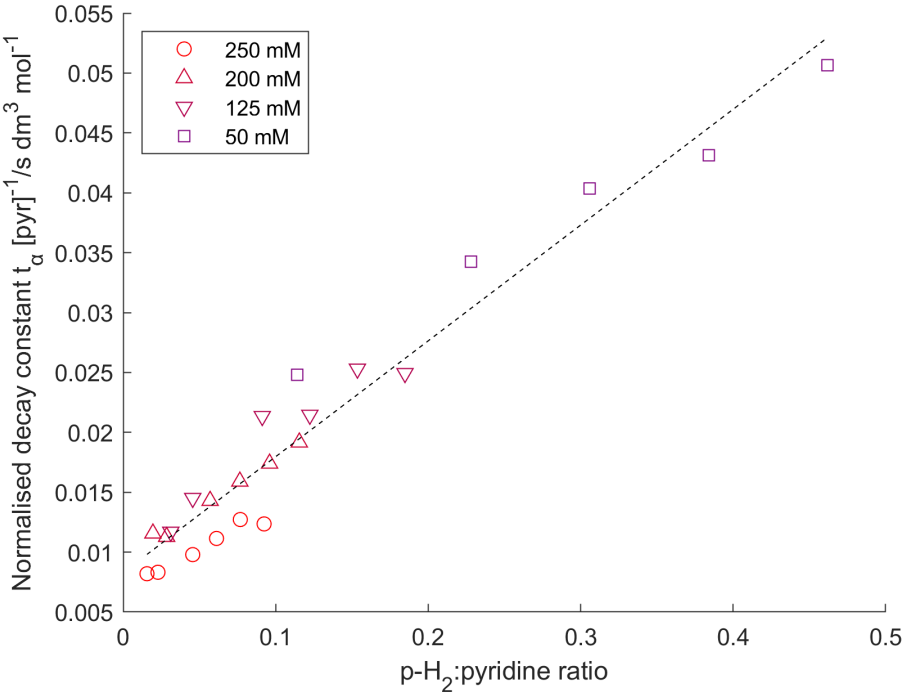

Figure 5.9: Plot of normalised relaxation time t_α/[py] against reaction ratio [p-H$_2$]/[py], for samples 1-4 (50 - 250 mM [py]).

5.5 Relative contribution of the relaxation processes

Having characterised the fast relaxation components $A_\alpha$and t_α, and hypothesised an origin for the slow process, we now examine the relative contribution of these two processes by analysing the ratio $\frac{A_\beta}{(A_\alpha+A_\beta)}$. This ratio represents the fraction of the initial signal that persists after the fast relaxation process is complete, effectively a "plateau" value.

Figure 5.10 shows the contribution for A_β to A_{total} against p-H$_2$ supply pressure in solution for all experimental samples (25 - 250 mM pyridine). Across all samples, at increasing p-H$_2$ supply pressure, the relative contribution of A_β is weaker leading to a lower plateau. The absolute intensity of A_β does not change significantly across pyridine concentrations, as was shown in Figure 5.4.

In addition, the biexponential fit model used here, while providing strong correlation, does not necessarily accurately represent the physical phenomena occurring in solution; other models may equally well fit the phenomena observed here and provide more insights into the underlying processes.

To quantify the trend observed in Figure 5.10, the gradient of the plateau percentage versus p-H$_2$ concentration was calculated via a linear fit for each series of pyridine concentrations. These gradients, plotted in Table 5.4, represent how strongly the relative contribution of the slow process (A_β) increases with higher concentrations of dissolved para-hydrogen.

As shown in Table 5.4, the value of this gradient is similar across all pyridine concentrations tested, remaining consistently around 2 % mM^{-1}. This uniformity reinforces the conclusion that while the absolute signal intensity depends on both reactants, the balance between the fast and slow relaxation pathways is primarily dictated by the total amount of p-H_2 in the system, regardless of the pyridine concentration.

To further probe the dynamics of the slow relaxation process, the dependence of $\frac{A_\beta}{A_\alpha+A_\beta}$ on pyridine concentration can also be analysed by looking at the data presented above as a function of pyridine concentration at constant pressure. Table 5.5 gives the gradient of the plateau percentage for each series of constant p-H_2 pressures. The gradient is very shallow across all pressures, suggesting that the plateau's value has no significant dependence on the pyridine concentration, and so is a process independent of pyridine/catalyst interaction.

Table 5.4: Gradient of percentage contribution of A_β to A_{total} against p-H_2 supply pressure.

Concentration	Gradient / % bar^{-1}
250	1.9 ± 0.3
200	1.9 ± 0.3
125	2.1 ± 0.6
50	2.5 ± 0.3
25	2.3 ± 0.4

Table 5.5: Gradient of percentage contribution of A_β to A_{total} against pyridine concentration.

Pressure	Gradient / % mM^{-1}
6.5	0.04 ± 0.06
5.5	0.04 ± 0.03
4.5	0.12 ± 0.07
3.5	0.08 ± 0.04
2.5	0.12 ± 0.04
2	0.09 ± 0.04

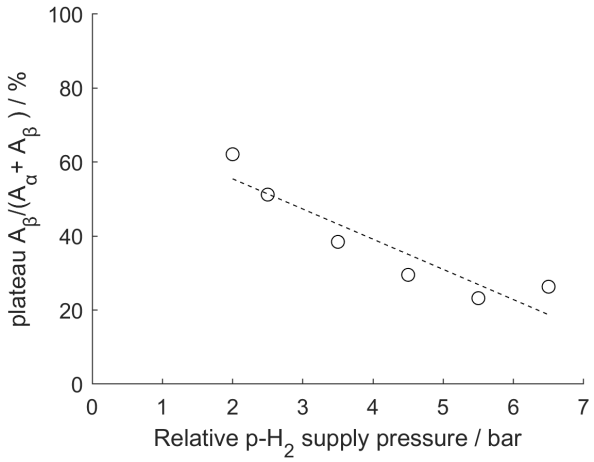

(a) Sample 1 (250 mM [py])

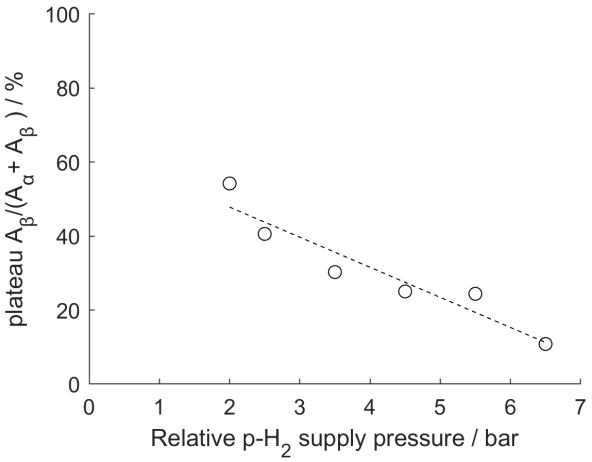

(b) Sample 2 (200 mM [py])

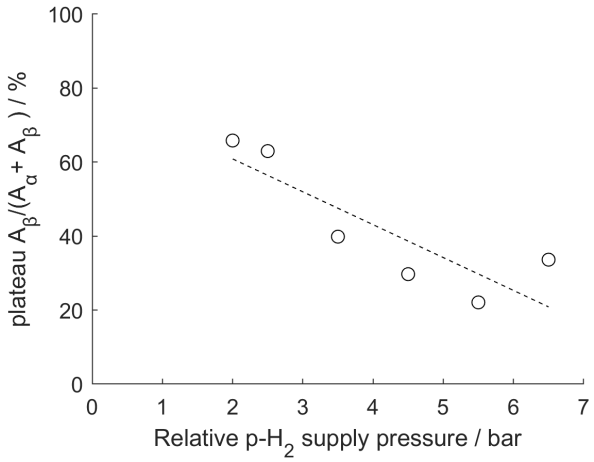

(c) Sample 3 (125 mM [py])

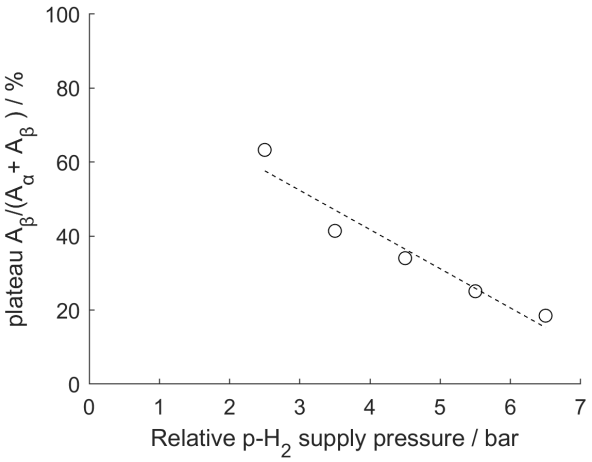

(d) Sample 4 50 mM [py])

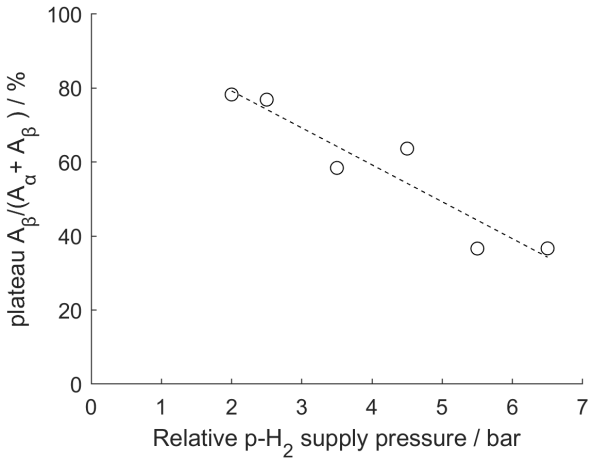

(e) Sample 5 25 mM [py])

Figure 5.10: Plot of percentage contribution of A_β to the overall signal intensity; plot of $\frac{A_\beta}{A_\alpha + A_\beta}$ against pyridine concentration for all samples, with pyridine concentrations: Sample 1 (250 mM (a)), Sample 2 (200 mM (b), Sample 3 (125 mM (c)), Sample 4 (50 mM (d)), Sample 5 (25 mM (e)).

5.6 Conclusion

This chapter has demonstrated that the observed SABRE-enhanced EFNMR signal diminishes significantly with the introduction of a decay between p-H_2 delivery and the application of the PTF, confirming the presence of a rapid relaxation process for p-H_2 in the Earth's magnetic field. As *para*-hydrogen has a long lifetime in pure methanol, this relaxation must be driven by interactions with the SABRE catalyst in solution. This signal decay follows a biexponential model, indicating at least two distinct relaxation pathways. The dominant pathway is a fast process responsible for the majority of the signal loss, with a time constant (t_α) on the order of 1 - 4 seconds under typical conditions. The amplitude of this component, A_α, was shown to be strongly dependent on both p-H_2 pressure and substrate concentration, consistent with the source of the relaxation being the SABRE catalysis process, similar to the dependence of the observed SABRE signal on substrate concentration and *para*-hydrogen pressure.

The relaxation rate of t_α was also shown to be dependent on p-H_2 pressure and [py]. t_α lengthens with increasing concentrations of both p-H_2 and pyridine, which indicates a mechanism which is limited by competitive kinetic exchange for vacant sites at the SABRE catalyst following substrate dissociation. In contrast, the second, slower process, is characterised by a smaller amplitude component, A_β which is much less sensitive to reactant concentrations. It is possible that this component may arise from a slow re-equilibration with a reservoir of unrelaxed p-H_2, such as the gas in the sample headspace, which acts to refresh the concentration of p-H_2 in solution during the experimental window. Further testing of this hypothesis would require development of a cell that has limited or no headspace or gas-liquid interface, but does not drive the sample through the outlet capillary upon gas delivery.

In conclusion, the relaxation of hyperpolarised p-H_2 in the Earth's field is consistent with a catalyst-mediated process that represents a mechanism for potentially unexpected signal loss in SABRE experiments. This relaxation may be of particular significance to SABRE experiments in which p-H_2 delivery and PTF application are separated in time and space. This relaxation is also significant when performing quantitative work even with *in situ* detection. These relaxation effects can be minimised by as much as possible reducing and standardising variations in time between p-H_2 delivery and PTF application, making sure to fully re-saturate the solution with fresh p-H_2 between experiments. Further characterisation of these experiments could be performed using low-field benchtop detection, if sample shuttling is available to move between EF and detector. The next chapter will detail development of such a system.

CHAPTER 6

Benchtop *in situ* bubbling and sample shuttling

6.1 Introduction

The gas delivery system built and developed in Chapters 3 and 4 was demonstrated for integration with an Earth's Field NMR (EFNMR) spectrometer. However, the goal is to make the system as versatile and applicable to as broad a range of instrumentation as possible. This means that it must be able to communicate with the widest possible range of spectrometers. Our research group uses Magritek Spinsolve benchtop spectrometers for SABRE-hyperpolarised NMR experiments at B_0 fields of 1-1.9 T. SABRE experiments employing benchtop NMR detection have predominantly relied on manual 'shake-and-drop' methods. A method to allow controllable, repeatable SABRE experiments using *in situ* or *ex situ* *p*-H_2 bubbling with benchtop NMR detection was therefore needed. The benchtop NMR spectrometers lack TTL (Transistor-Transistor Logic) output capability, so an alternative software architecture is required to control gas flow as part of pulse sequences.

In addition, the bubbling system alone would only allow for *in situ* RF-SABRE (Radiofrequency SABRE)[66] in a benchtop spectrometer. To perform standard SABRE with spontaneous polarisation transfer, a shuttling system is needed to move the sample from the strong B_0 field at the magnet's centre to a weaker Polarisation Transfer Field (PTF). This is typically achieved by either repositioning the sample within the magnet's stray field or by moving it to a dedicated external field source, such as a solenoid[48,59,60,63].

6.2 Background of SABRE with Benchtop NMR Detection

Benchtop NMR spectrometers are becoming increasingly popular as an alternative to HF NMR spectrometers due being cheaper, smaller and less complex to operate. This comes at the expense of weaker sensitivity and more complex spectra due to strong coupling. Hyperpolarisation techniques including SABRE have been used as a way to overcome the sensitivity limitations.[13] SABRE has been demonstrated on benchtop spectrometers for a range of substrates, including pyridine, nitriles, amino acids, and oligopeptides.[13,69] SABRE-Relay[49] further broadens the range of potential SABRE substrates and thus SABRE applications. The simplest way of performing SABRE on benchtop is to fit an NMR tube containing SABRE solution with a Young's tap, charge with p-H_2 and shake. This approach was widely used in early SABRE experiments.[27,35] Polarisation transfer to ^{1}H can be generated through a purpose built Halbach array[47] or generated using a solenoid electromagnet[52]. For transfer to heteronuclei mu-metal shields are used to produce the required microtesla PTFs. Shake and drop SABRE experiments on benchtop have found applications in forensics for detection of fentalogues[53,94] and reaction monitoring.[50] In forensics, the simplicity and portability of benchtop instrumentation is particularly attractive. However, shake-and-drop experiments are limited in their practicality and repeatability, requiring significant training and care. There is also operator-dependent variability, making reproducing measurements challenging. For SABRE experiments requiring precise timing, or multiple scans, an alternative system is needed which allows more precision in p-H_2 delivery. For precision or very high pressure p-H_2 delivery a capillary can be used to allow gas flow into solution with solenoid valves used to control flow timings.[141,176] This approach is also common with hydrogenative PHIP methods.[13]

To perform SABRE with spontaneous polarisation transfer there must be a mechanism by which the sample can be moved between PTF and detector. As discussed above this can be performed manually, but variations in the force and duration of shaking, the time taken to transfer the sample to the magnet, and the orientation of the tube during transfer all introduce significant variability into the final measured signal enhancement. Since the hyperpolarised state is transient, any delay or inconsistency in the transfer time leads to unpredictable relaxation losses, rendering comparisons between experiments unreliable. These factors make manual shuttling unsuitable for automated workflows, high-throughput screening, or advanced multi-scan experiments that require consistent signal levels over time. Several automated shuttling approaches have been published previously, which are reviewed here.[56] Automated methods provide much broader scope for experiments, allowing for control of timing and multidimensional NMR. Shuttling can be performed through mechanical or hydraulic methods. Prior to the commencement of this work, only Richardson *et al.*[27] had performed SABRE experiments with automated sample shuttling, but alternative methods have since emerged in the literature and are discussed below.

At the high magnetic fields of an NMR spectrometer, the large Zeeman energy difference ($\Delta\omega$) between the hydride and substrate spins effectively quenches the spontaneous, J-coupling mediated polarisation transfer that defines conventional SABRE. The LAC

condition for polarisation transfer can be re-established by applying a continuous-wave (CW) RF field resonant with one of the spins in the SABRE complex. The RF irradiation "dresses" the spin states, creating a new effective Hamiltonian where the energy levels are altered.[177,178] At the correct frequency and amplitude of RF field, the effective energy levels of the hydride and substrate spins can be brought into near-degeneracy, recreating the LAC condition and enabling efficient polarisation transfer directly at high field.[66,158,179] The entire experiment, from polarisation buildup to signal detection, occurs *in situ* within the high-field magnet. This dramatically simplifies the required hardware, removing the need for external PTF generators and complex shuttling mechanics. Several variants of this technique have been demonstrated, using various RF schemes and power applications (such as Spin-Lock Induced Crossing SABRE, SLIC-SABRE schemes) to meet the polarisation transfer requirement in different RF regimes.[66,121,135,180–182]

RF-SABRE signal enhancements are generally lower than those obtained with optimal low-field shuttling methods. For instance, early reports demonstrated enhancements of around 100 fold at 4.7 T,[66] which is substantial but less than the thousands-fold enhancements routinely achieved with transfer at low field. The process is also highly sensitive to the homogeneity and power stability of the applied RF field and requires sophisticated pulse sequence programming, making it technically more demanding to implement than a simple shuttling experiment. it is therefore desirable to be able to perform SABRE with benchtop detection with polarisation transfer occurring at the low-field PTF to access the higher potential enhancements.

6.2.1 Shuttling approaches

Implementations range from stepper motor-driven lifts,[55,60] which vertically raise and lower the sample tube between a PTF generator located below or above the magnet and the detection region inside the bore, to more sophisticated multi-axis robotic arms that provide greater flexibility in the transfer path.[56–58,183]

6.2.2 Pneumatic shuttling

Pneumatic shuttles can operate either through liquid transfer or tube transfer. Liquid transfer systems, originally designed for high field NMR, have also been implemented on benchtop.[47] Such a flow system by Richardson *et al.*[27] uses nitrogen pressure to flow the sample between a reaction cell, in which a PTF can be applied, and a detection region inside the spectrometer. This flow approach gives highly reproducible enhancements, with relative standard deviations of around 5% over 30 repeat measurements).[27] allowing multiple step experiments such as signal averaging and multidimensional spectroscopy (e.g. 2D COSY). Sample shuttling in this manner gave significantly lower (1200 × vs 17 000 ×) enhancements than manual shaking and transfer on comparable samples, caused by poorer mixing and longer transfer times. Enhancements were still very large, around 1200 × improvements over thermally acquired spectra. Flow-based systems present their own set of engineering challenges. This includes potential introduction of gas bubbles

into the NMR detection cell during the liquid transfer, which can severely degrade the magnetic field homogeneity, leading to poor spectral line shape and resolution. There are also risks of contamination between experiments if fluid lines are not properly flushed.

The entire NMR tube can also be pneumatically shuttled, as demonstrated by TomHon *et al.*.[60] This minimises the risk of formation of bubbles and line contamination inherent to sample flow systems. In their work, a vacuum pump and pressurised nitrogen were used to shuttle the sample on a Bruker 400 MHz spectrometer, achieving rapid transfer from the polarisation transfer field to the detector in approximately 0.5 seconds. This automated system enabled reproducible hyperpolarisation, achieving, for example, a ^{1}H signal polarisation of 2.9% for pyridine. While such systems offer high precision, they also require careful alignment and control to mitigate the mechanical stress of repeated high-speed sample insertion.

6.2.3 Mechanical shuttles

Mechanical shuttles are systems that physically transport the entire sealed NMR tube. These systems offer the highest degree of precision and control over the shuttling process, giving the best reproducibility in speed and timing of sample movement. Design considerations include maximizing transfer speed to minimise relaxation losses and ensuring smooth motion to prevent sample agitation or mechanical shock.

One implementation by Ellermann *et al.* uses a stepper motor driven lift,[55] which vertically raises and lowers the sample tube between a PTF outside the magnet and the detection region inside the bore. This gives faster shuttling between detector and PTF than with pneumatic shuttling (380 ms vs 500 ms). The schematic of the device presented by Ellermann *et al.* is reproduced in Figure 6.1.

Ellermann's system is designed to be inexpensive and simple to set up. There is risk with this kind of system that the motor "slips" or micro-jams while under load, which would cause mis-alignment of the sample and potentially risk damage to the tube or spectrometer. This can be controlled for through step-loss detection in the driver and guides to limit sample cell deviation.[55] Access to the sample tube in this design is limited, and the bore of the magnet can only be reached by removal of the shuttling apparatus.

Multi-axis robotic arms that provide greater flexibility in the transfer path have also been demonstrated by multiple groups.[56–58] These give much greater flexibility in the transfer path and are less spectrometer specific than integrated shuttles, allowing the arms to be rapidly reconfigured for different experiments—such as photo-CIDNP and SABRE—and paired with various detection systems, like benchtop and zero- to ultralow-field (ZULF) NMR spectrometers.[183] However, this flexibility comes with a significant risk of misalignment and accidents. Because the robotic arm holds the NMR tube only at the top, the bottom of the tube is not fixed and can swing out of alignment. This creates a high probability that the sample can be crushed upon transfer, especially when being inserted into a tight space like the bore of a spectrometer. To prevent this, a 3D-printed guide cone can be fixed at the entrance of the device, which directs the NMR tube

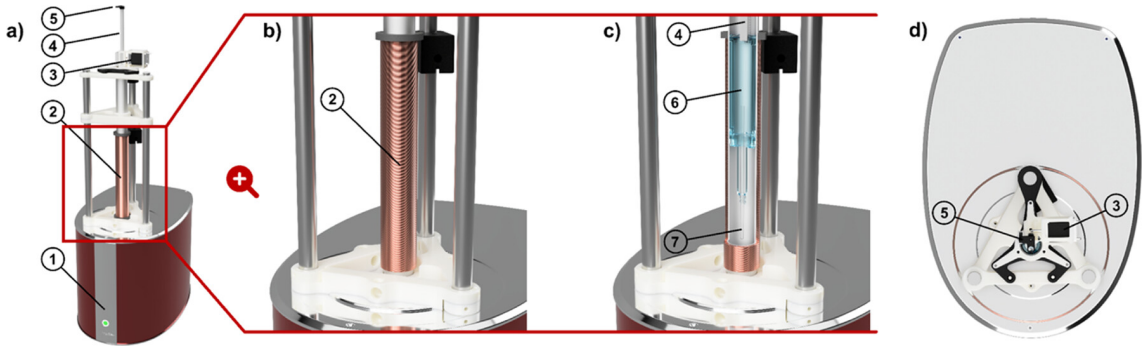

Figure 6.1: 3D rendering of mechanical shuttling apparatus as presented by Ellermann *et al.*. A resistive coil (2) is used to generate the PTF. A stepper motor (3) moves a gear rack, which moves the NMR tube and holder (6,7) inside the coil and into the detection region. Reproduced from Ref. 54 with permission from the American Chemical Society.[55]

into the bore. The timing of transfer can also be inconsistent, especially when complex movements involving multiple motors on an arm are used.[183]

6.2.4 PTF generation

The ability to generate a precise and stable magnetic field for the polarisation transfer step is as crucial as the shuttling mechanism itself. The hardware used for this purpose must be capable of producing fields in the appropriate range, milliTesla for ^{1}H SABRE or microTesla for heteronuclear SABRE-SHEATH, with sufficient homogeneity over the sample volume. The choice of technology for PTF generation is directly dictated by the underlying spin physics of the target nucleus.

The simplest way of reaching a mT PTF is to use the fringe field of the magnet. The field profile can be measured and sample shuttled to the required PTF. This is done at high field, where the distance down the bore is much longer so using an electromagnet is less feasible. Examples of this approach have been shown on high field instruments by Peters *et al.*[184] and Dücker *et al.*.[124] and Kiryutin *et al.*[185] The most flexible method for generating the PTF is through the use of an electromagnet, typically a wire-wound solenoid. This allows for automated "field sweep" experiments, where the SABRE enhancement is measured as a function of the PTF to empirically determine the optimal field for a given catalyst-substrate system.[27,47,50,60] For applications where a fixed, stable PTF is sufficient and system portability or cost is a primary concern, permanent magnet assemblies offer an excellent alternative to electromagnets. Halbach arrays are frequently used in manual shuttling setups to provide a constant and stable PTF, typically around 6 mT, which is near-optimal for ^{1}H polarisation of many common substrates like pyridine derivatives. This avoids the resistive heating and timing control issues of electromagnets, providing a permanent, stable, reproducible field of consistent homogeneity, intensity and direction.

6.3 Motivations

The preceding review illustrates that automated benchtop SABRE is typically performed using bespoke, in-house systems. These custom instruments feature diverse approaches to sample shuttling and polarisation transfer field generation, tailored to the specific needs of individual research groups. The lack of a commercially available, versatile, and non-flow-based shuttling system necessitated the development of a novel, custom-built solution. The primary goals for this new system were to create an instrument that was robust, flexible in its application, inexpensive to construct, and integrated with the precise pressure monitoring capabilities of the gas delivery system developed previously.

This chapter details the design, construction, and integration of a complete system for automated SABRE experiments on a benchtop spectrometer. It begins by discussing the integration of the gas delivery system for in situ RF-SABRE experiments. It then describes the development of a novel mechanical sample shuttling system, designed to move the sample between the high field of the spectrometer and a PTF generated in the fringe field. This work was a collaborative effort with Dr. Daniel Taylor; the design and physical implementation of the shuttle were carried out by Dr. Taylor, while the author developed the control software and worked collaboratively to integrate the shuttle with the gas delivery apparatus and NMR pulse sequences. The resulting system provides a highly reproducible and flexible platform for a wide range of SABRE experiments.

Our system is comparable to Ellermann *et al.*'s and developed following their publication. The initial design aimed to mimic theirs, but it was found adaptations to the design were needed for our system, including a change to a linear actuator with an externally mounted sample cradle, with the aim of making a more robust system with reduced complexity, particularly with the use of a lead screw to drive sample movement over a rack system.

6.4 Integration of Bubbling System with Benchtop NMR Spectrometer

6.4.1 Automated Serial Control of the Bubbling System

Chapter 3 illustrated the development of a p-H_2 delivery system for in situ SABRE experiments performed within a pulse sequence, and Chapter 4 detailed the optimisation of this system with an EFNMR spectrometer. Not all instruments in use have the facility for TTL outputs for automatic valve control. To use *in situ* bubbling without this facility, an alternative approach is needed. All instruments used in our group are programmed in Prospa. As discussed previously in Chapter 4, Section 4.2.1, Prospa cannot perform external operations while an NMR pulse sequence is running. Therefore, sets of instructions for the p-H_2 delivery system, referred to as bubbling sequences, must be pre-written and initiated synchronously with the NMR pulse sequence. A procedure is needed for

loading a bubbling sequence to the Arduino and a means of initiating this sequence from the Spinsolve pulse sequence software. This capability is necessary to allow us to open and close valves (e.g. to enable bubbling) during or between the application of RF pulses. The strategy implemented here involves establishing direct communication between the spectrometer's control software and the bubbling system's Arduino microcontroller. To achieve this, a Serial connection is opened directly in Prospa. A bubbling sequence is generated in Prospa through a series of commands in the Experiment Control macro, illustrated in Figure 6.3 and compiled into a string, which is then passed to the Arduino microcontroller. A final command to initiate the bubbling sequence can then be sent over the Serial connection to the Arduino immediately before the execution of the NMR pulse sequence in Prospa, minimising delay and establishing synchronisation between the two programs (the Arduino script "electronics_control" and Prospa macro "ssbubble" are provided in Appendix A and Appendix D respectively).

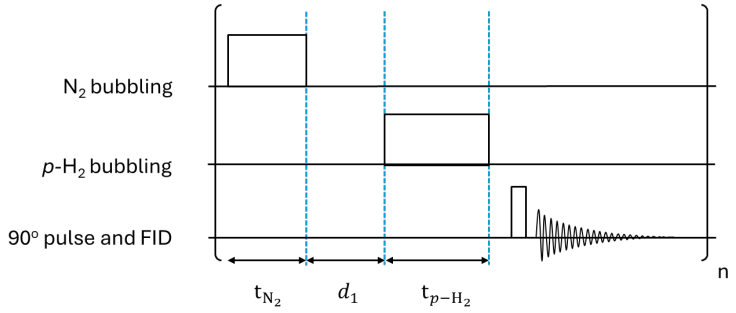

Figure 6.2: Example pulse sequence requiring N_2 bubbling followed by p-H_2 bubbling after a short delay. $t_{N_2} = 10\,\text{s}$, $d_1 = 1\,\text{s}$, $t_{p-H_2} = 10\,\text{s}$.

For example, consider the sequence in Figure 6.2 that requires 10 seconds of bubbling with an alternate gas (H_2 or N_2), followed by a 1-second delay, and then 10 seconds of p-H_2 bubbling.

This can be set in the Experiment Control macro in Prospa using the following commands, which calls from the macro "ssbubble" in Appendix D:

```
d1 = 10; d2 = 1; d3 = 10; port = "COM1"; mode = 0
s = ssbubble:setBubSeq(port, mode)
s = ssbubble:bublStep(s, d1)
s = ssbubble:delStep(s, d2)
s = ssbubble:altStep(s, d3)
ssbubble:sendSeq(port, s, mode)
ssbubble:runSeq(port,mode)
```

The first line defines the variable times and the Serial port address. The next initialises the variable length string which encodes the sequence. All strings start with "i", followed by an integer and "s", which gives the number of steps in the sequence. The rest of the string is broken down into numbers immediately followed by a single character that defines the action associated with the number. The character definitions are given in Table 6.1. To understand how this works consider the example bubbling sequence in Figure 6.3 which is encoded by the string i3s10n1d10b.

Broken down, the Arduino is prompted to load the string into memory with "i", and it is given the number of steps in the sequence, "3s". The commands "10n" and

"10b" specify 10 seconds of alternate gas and p-H_2 bubbling, respectively. The command "1d" introduces a 1-second delay between the two bubbling steps with no gas flow. This is illustrated in Figure 6.3. The Arduino compiles the command list into an array in memory containing the step type and duration. When initiated by sending the single character "R" over the Serial connection at any time following loading of a bubbling sequence, the Arduino will proceed line-by-line through the array, changing the valves to the appropriate position for the specified duration. Single characters are fastest for the Arduino to process over the Serial connection, making this the most robust option for precise timing with Prospa control. Table 6.1 provides a complete list of commands usable in pre-loaded bubbling sequences. All commands for a change in bubbling state are preceded by their duration. Additional commands could be added to the script where needed through specifying an additional character in Prospa and a case in the Arduino code that details the valve states associated with the new character.

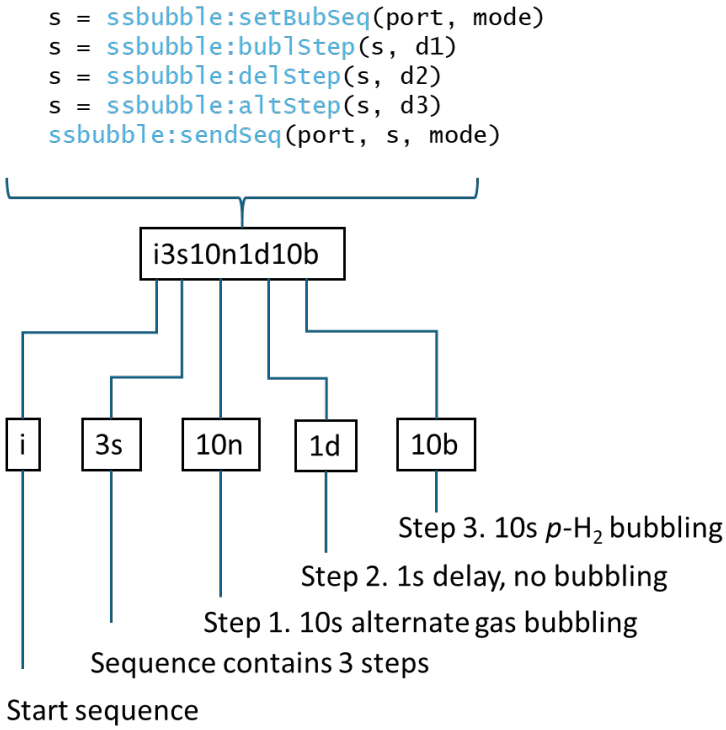

Figure 6.3: Example of a pre-loaded bubbling sequence transmitted to the Arduino for semi-automatic control. The Prospa commands above generate the string to be sent over the Serial connection. The first command creates the string to be sent, and the connection to the Arduino. Subsequent commands concatenate bubbling instructions onto the string, until it is complete and sent to the Arduino in the final step. The string is shown broken down into its constituent parts, generating a three-step bubbling sequence: 10s of alternate gas bubbling, a 1s delay, and 10s of p-H_2 bubbling.

Table 6.1: Commands for pre-loaded bubbling sequences under semi-automatic control.

Command	Function
`s`	Number of steps in the bubbling sequence
`b`	Bubble p-H_2 for the given duration
`d`	Delay between bubbling steps for given duration
`n`	Bubble alternate gas for the given duration

6.4.2 Adaptations to the Polariser Unit Components

To perform *in situ* SABRE experiments within a standard benchtop spectrometer, a new reaction cell had to be designed. The frit cell described in previous chapters (Chapters 3 and 4) is designed for the EFNMR spectrometer and is too wide for the standard 5 mm bore of the benchtop spectrometers. In addition, when positioned in the detection region of a benchtop spectrometer, differences in magnetic susceptibility at the boundary between a frit or capillary and the reaction solution as compared to the bulk sample create distortions in B_0 within the sample, disrupting field homogeneity in the detection region. While undetectable at ultra-low field, these become disruptive in the 1 - 2 T regime of a benchtop NMR spectrometer, resulting in broad, distorted peaks, particularly for ^{1}H spectra due to their narrow chemical shift range and higher gyromagnetic ratio. Thus, an approach to p-H_2 delivery is needed that allows the use of the bubbling system, fits into a 5 mm spectrometer bore, and does not contain any components of the bubbling apparatus in positions to disrupt the B_0 homogeneity in the spectrometer's detection region. To this end, a capillary bubbling tube was developed by Dr. Daniel Taylor and Izzy Hehir that meets both of these requirements, delivering p-H_2 into a modified 5 mm NMR tube via capillary. This is illustrated in Figure 6.4. A standard NMR tube was modified by Abby Mortimer of the University of York Chemistry Glassblowing Workshop to join to a GL-14 screw head. A connector, CNC-machined by Stuart Murray of University of York Chemistry Mechanical Workshop, is then fitted between the tube rim and the GL-14 lid to create a sealed flow path with space for a capillary. To complete the seal, a two-part head is used; an inner part, which interfaces with the NMR tube, screws into an outer part that holds the IDEX connections. The capillary, made of PFA (1/16" O.D., 0.040" I.D.), is routed in through an IDEX connector. Gas escapes through a second IDEX port to return to the valve manifold. This system allows controlled bubbling of p-H_2 into a SABRE sample, with no foreign materials within the detection region as long as the capillary terminates above the detection region. The system is simple, inexpensive, and easy to replicate, allowing integration with multiple tubes and p-H_2 delivery systems. The capillary depth is set to a fixed position during assembly by positioning it within the IDEX connector before the ferrules are tightened to form a seal, and the tube is cut to the desired length. Gas-tight seals are ensured through tight threading of the connector into the head and a washer built into the connector sandwiched between the GL-14 tube and lid. This set-up is shown in Figure 6.4.

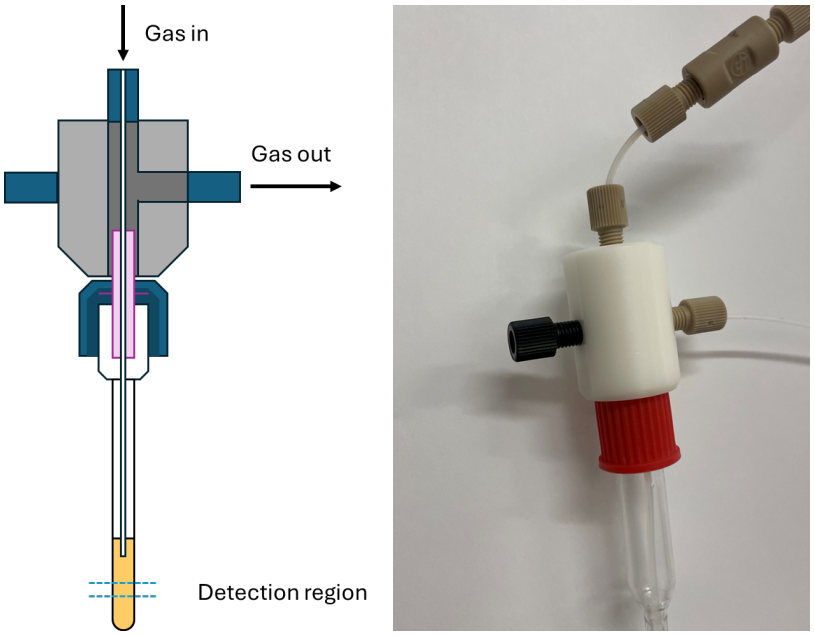

Figure 6.4: Left: Schematic of the capillary NMR tube assembly for in situ p-H_2 bubbling in a benchtop spectrometer, not to scale. A 3D printed head (grey) contains IDEX connections to inlet and outlet gas lines. A PTFE capillary is routed through the inlet into the sample. A 3D-printed connector (purple) threads into the head to connect to a GL-14 tread on top of a 5mm NMR tube. A washer integrated into this connector ensures a gas-tight seal between components. Gas flows into the sample through the capillary and returns to the outlet line via lateral space in the head and connector. Right: photograph of capillary NMR tube assembly.

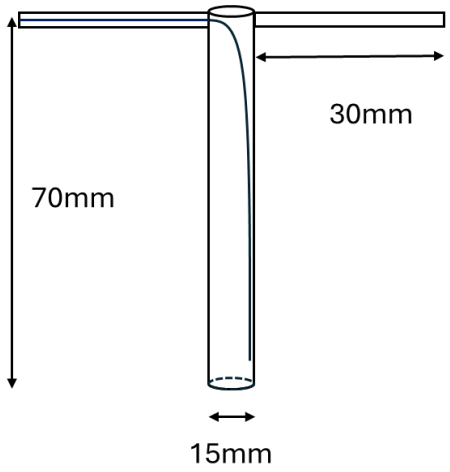

Figure 6.5: Capillary bubbling cell adapted for use with the p-H_2 delivery system when supplying the benchtop NMR cell.

6.4.3 Modified Solvent Reservoir

Bubbling through the sample drives solvent evaporation, which presents a significant challenge for the long-duration, multi-scan experiments enabled by an automated system. Solvent loss is typically negligible for manual shake-and-drop methods, as they are used for single-shot acquisitions where the cumulative effect of evaporation is insignificant.

The depth of the capillary is limited, as its end must remain above the NMR detection region. Once enough solvent has evaporated to reduce the liquid surface level below the capillary tip, gas mixing becomes ineffective. The solvent reservoir is therefore implemented to minimise evaporative losses and extend sample lifetimes. For the small benchtop cell, a new solvent reservoir was made by Abby Mortimer (University of York Chemistry Glassblowing Workshop). The modified reservoir is deeper and narrower and can be filled up to $\frac{3}{4}$ of its depth with solvent. The new reservoir has a main body of 15 mm outer diameter and 70 mm height, with inlet/outlet arms of 4 mm outer diameter and 30 mm length. The new design is illustrated in Figure 6.5 This design extends the travel path for gas passing through the reservoir while reducing the overall reservoir volume to 5 mL. A reduced overall reservoir volume, while maintaining a long bubble travel distance, improves the efficiency of solvent saturation and minimises dead volume. Reduced solvent consumption also increases the viability and cost-efficiency of using deuterated solvents, which are sometimes desirable in benchtop spectroscopy to avoid large solvent signals.

6.5 *In situ* bubbling on a benchtop NMR

To demonstrate that the bubbling system enables the controlled, in situ supply of *para*-hydrogen, the activation of a SABRE pre-catalyst was monitored by ^{1}H NMR spectroscopy on a 1.4 T Magritek Spinsolve benchtop spectrometer. The delivery of p-H_2 to the precursor initiates the formation of the active catalyst, which is distinguished by a

characteristic hyperpolarised iridium hydride resonance at approximately -23 ppm. The intermediate activation resonances following the displacement of Cl^- can also be seen at -17 and -12 ppm. This provides a direct method for tracking the progress of catalyst activation and assessing the reproducibility of the hyperpolarised signal. Using the pulse sequence depicted in Figure 6.6, the build-up of this hydride signal was measured over successive 15 s p-H_2 bubbling periods.

The *para*-hydrogen delivery system coupled with the automated Serial control enables replicable p-H_2 delivery for SABRE-hyperpolarised experiments Figure 6.7 shows the spectra of the bound hydride peak of a sample of 4-methylpyridine (4-Mepy) in methanol in a repeated bubbling experiment of catalyst activation, and then showing the plateau of signal. The pulse sequence for this experiment is given in Figure 6.6, with 60 s p-H_2 bubbling time between each scan. The hydride peaks for the activation intermediate $[Ir(H_2)(Cl)(IMes)]^+$ at -12.4 and -17.3 ppm become visible in the spectrum after 15 s of bubbling as catalyst activation begins, and diminish in intensity until activation is complete. After 75 s bubbling, the intermediate peaks can no longer be observed on the spectrum, and only the peak for the active SABRE catalyst remains, indicating complete activation.

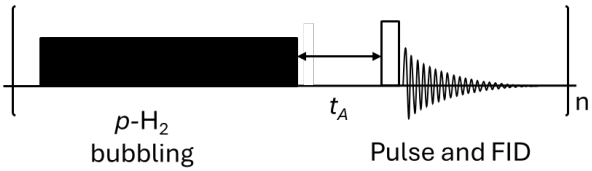

Figure 6.6: Bubble and acquire pulse sequence for observation of SABRE catalyst activation.

6.5.1 Discussion

The precision in timing offered by this approach is good, with delays measured at under 5 ms for initiation of pulse sequence. Timing restarting on every scan minimises chance of cumulative build-up of delays leading to a loss of synchronisation over the experiment. In practice, Serial communication proved highly robust, with transmission errors only occurring in cases of physical disconnection. A short settling delay (Figure 6.6 t_A) must be included to allow all bubbles to escape solution, as bubbles present cause significant field perturbations due to differences in magnetic susceptibility at the interface.

SABRE becomes no longer possible once the capillary is not submerged in solution, as fresh p-H_2 can no longer be mixed into solution. The in-line reservoir significantly reduced the rate of solvent boil-off in the same manner as the reservoir on the Earth's Field system, allowing for sample lifetimes to be extended from ca. 30 min to several hours. The system is limited by poor mixing quality from top-down gas delivery due to the shallow depth of insertion of the capillary into the sample; p-H_2 is ineffectively delivered into the detection region. A more effective means of p-H_2 delivery would be for bottom-up delivery through a gas-permeable membrane such as sintered glass, similar to

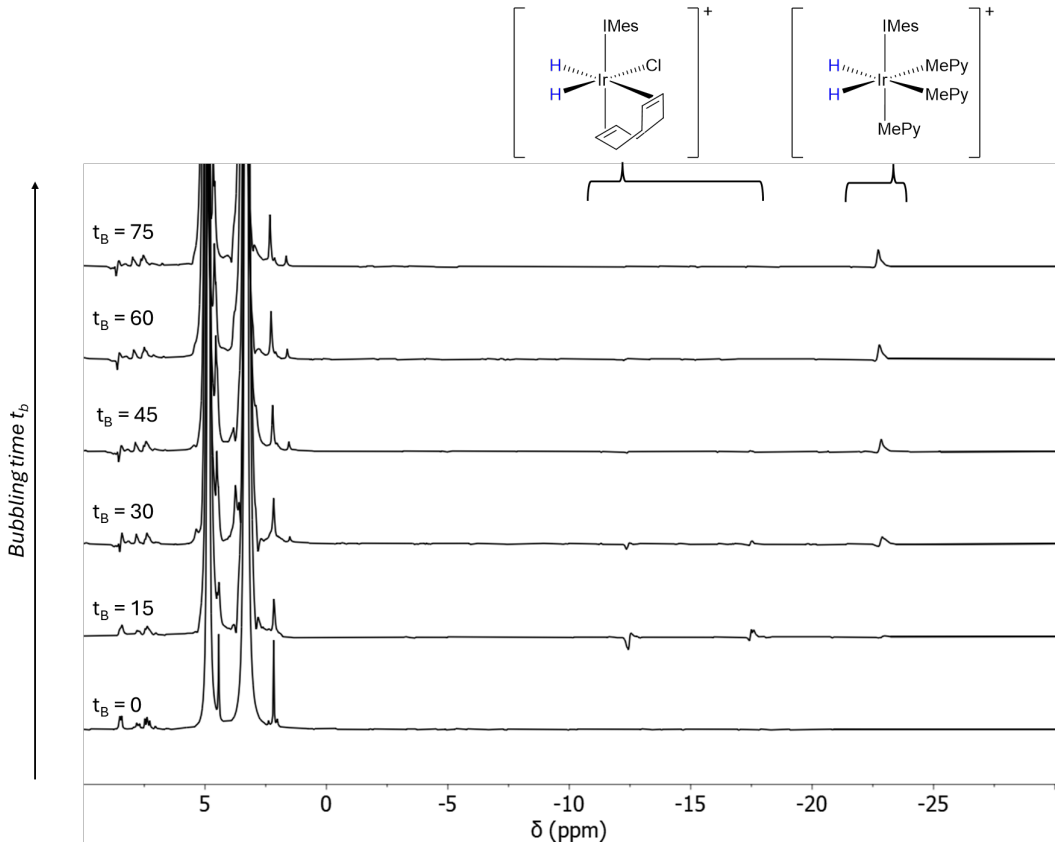

Figure 6.7: Hydride region of ^{1}H NMR spectra sample of 4-MePy (50 mM) and SABRE catalyst in methanol (0.7 mL) Data recorded by Izzy Hehir. Pressure supplied at 8.1 bar, down-regulated to 5.44 bar. p-H_2 supplied for 15 s between each spectrum recorded, using pulse sequence shown in Figure 6.6. The SABRE catalyst activation intermediates can be seen at -12.4 and -17.3 ppm. The fully activated SABRE catalyst hydride appears at -22.8 ppm.

the design published by Kiryutin *et al.*.[185] Explorations of a cell design to facilitate this are under way in the group at time of writing.

6.6 Integrated control of sample shuttling

To perform spontaneous transfer we must move the sample out of the detection region of the spectrometer. Spontaneous transfer to pyridine in our model sample occurs at 6.6 mT.[123] This can be reached either in the fringe field of the magnet, in a constructed magnet array, or a solenoid like that used in the Ellermann *et al.* shuttle design.[55] For this work the fringe field will be used, providing sufficient field to observe polarisation transfer and demonstrate system viability. Therefore, to perform spontaneous SABRE, a system is required to physically move the sample between the optimal polarisation transfer field (PTF) and the detection region. To enable this sample transport, a motor-driven shuttling system was developed. To shuttle the sample along the bore, a stepper motor assembly is mounted on top of the spectrometer. This motor drives a lead screw

that precisely controls the vertical position of the NMR tube holder, allowing for rapid, automated movement between the 6 mT polarisation region and the magnet's detection region. The following sections will detail the physical construction of this apparatus and the software developed for its integrated control.

6.6.1 Motor construction

This motor shuttle hardware was designed and built by Dr. Daniel Taylor. A diagram of the complete motor shuttling apparatus is shown in Figure 6.9. A frame structure is mounted on top of a benchtop spectrometer through three integrated mounting points in the base plate. The frame is made of 20×20 mm^2 T/V-slot aluminium extrusion profile. An Ooznest 24.5 kg-cm (345oz-in) 3.00A 1.8° NEMA23 Hybrid Bipolar Stepper Motor is fixed to a mount and coupled to an 8 mm ACME lead screw. The lead screw is threaded through an ACME anti-backlash nut block that is mounted to a gantry plate. Linear motion of the gantry plate upon rotation of the lead screw is supported by 40x80 mm (C-Beam) T/V-slot aluminium extrusion profile. The linear actuator is bolted into the top of the spectrometer ensuring consistent alignment of the NMR tube with the bore of the magnet, minimising risk of damage to either. A 3D printed bracket interfaces the gantry plate with the head of the NMR cell illustrated in Figure 6.4. IDEX 1/4-28 connections hold the cell in the 3D printed bracket. Rotation of the motor shaft causes rotation of the lead screw, which causes vertical motion of the nut block, gantry plate, 3D printed bracket, bubble head and NMR tube. The software written for the motor as part of this project is given in Appendix E. Further detail of the software is given in Section 6.6.2. Compatibility between the bubbling system and the shuttling system will need to be ensured in shuttling system development, ensuring timing remains precise and consistent with both. For manually controlled experiments this should not present an issue as the shuttle and bubbling will be controlled through separate Serial lines. For automated experiments the same parallel Serial lines will be used but care will need to be taken to ensure the timing of both remains synchronised with the spectrometer

6.6.2 Moving the motor

A system needed to move the sample to allow spontaneous polarisation transfer in the 6 mT regime and then transfer to the detection region of the spectrometer. Software was written to allow control of the motor in a manual mode, controlled by the user during the running of an experiment through the User Interface shown in Figure 6.8. Automated motor movements to be performed prior to the initiation of the pulse sequence can be programmed into the experiment Control macro, as discussed below. Development of an automatic mode, in which sequences of motor movements can be pre-loaded, analogous to the bubbling sequences described in Section 6.4.1, is ongoing at the end of this project. Manual control of the motor can be performed by a user through interaction with the MATLAB app (detailed in Chapter 3, Figure 6.8) which also controls the bubbling.

Opening and closure of the Serial connection is performed in the same manner as

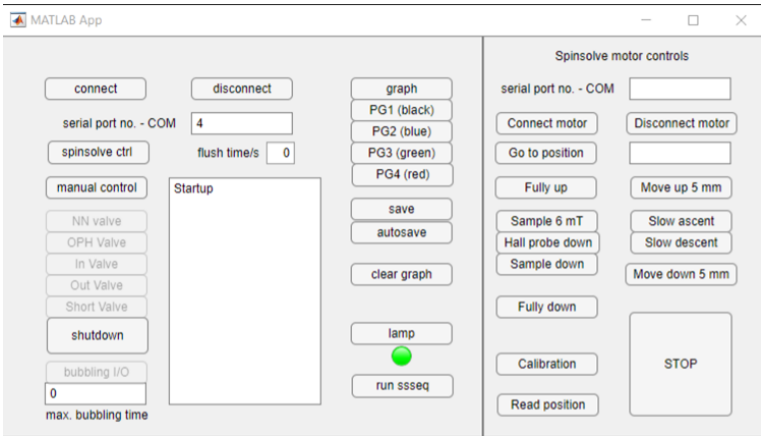

Figure 6.8: MATLAB application graphical user interface (version 9.S5).

with the bubbling system using a very similar script. The full Prospa macro is given in Appendix F. Following connection, motor calibration is a key function to prevent damage to samples or the spectrometer through forceful sample insertion into the spectrometer bore. The motor microcontroller library includes a calibration function that slowly rotates the lead screw, moving the sample holder up, detects the resistance on contact of the sample holder to the end of the lead screw, and returns the position value to the microcontroller. By including a calibration on each initialisation of the motor against the top of the lead screw, the known "top position" can be used to calculate each pre-set sample position relative to the top. This, combined with preventing users exceeding the calculated bottom position, minimises risk of driving the sample into the spectrometer and causing damage to the motor system or the magnet itself.

When connected, the motor microcontroller runs a script written in Arduino C++. This script powers on the motor on initial connection, and moves it to the top of the lead screw. The script then waits for input commands over the Serial port, returning to this waiting state following performance of any input commands. The top-level functions written in the motor control software are outlined in Table 6.2.

The functions "go to position" and "query motor" wait for second inputs to specify the position or information desired, respectively. Secondary arguments in "query motor" allow a user to request data such as the motor's current position or its calibration status.

6.6.3 Using the motor

6.6.3.1 Field mapping

The region of the stray B_0 field in the bore of the magnet that corresponds to the desired PTF = 6 mT is needed for spontaneous polarisation transfer in a SABRE experiment. A map of the stray field can be produced by interfacing a Gauss meter to the motor mount and using the fixed distance movement on the motor control to record the field measurement at fixed increments. In this manner, a field map was measured by Dr.

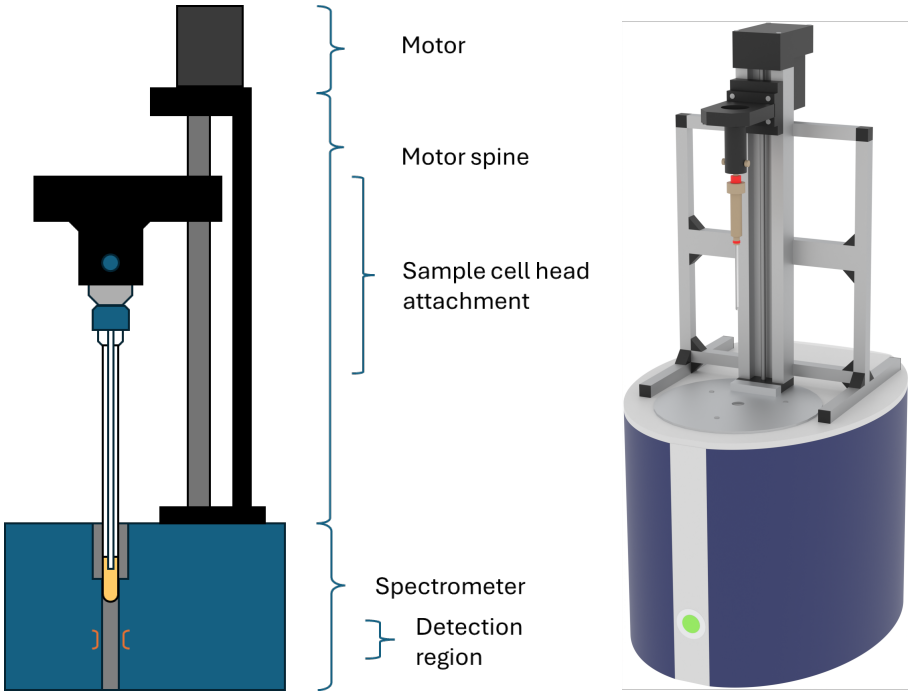

Figure 6.9: Cartoon (left) and render (right) of the motor-controlled shuttling set-up mounted on top of a benchtop spectrometer. The motor structure is mounted on top of the spectrometer, with a rotating lead screw (grey) driven directly by the motor. The sample mount is attached to this lead screw, allowing raising and lowering of the NMR tube by lead screw rotation. This allows movement of the sample (including the attached bubbling lines) into and out of the detection region of the spectrometer to access variable fields.

Table 6.2: Table of Serial input characters for controlling the motor.

Serial input character	Function
u	Slow rotate up
d	Slow rotate down
s	Emergency stop
e	Return to top and shut down
m	Perform field map movement
c	Calibrate field
p	Go to position
r	Read position
y	Move motor up 5mm
z	Move motor down 5mm
b	Move motor specified distance
i	Request information

Daniel Taylor, using a Hirst GM08 Gauss meter with a transverse probe, presented in Figure 6.10.

The position of the motor to hold a sample in the 6 mT region can be logged and its relative distance to the top position recorded as an argument to the "go to position" command in Table 6.2. This allows users or pulse sequences to rapidly shuttle to the PTF using simple inputs.

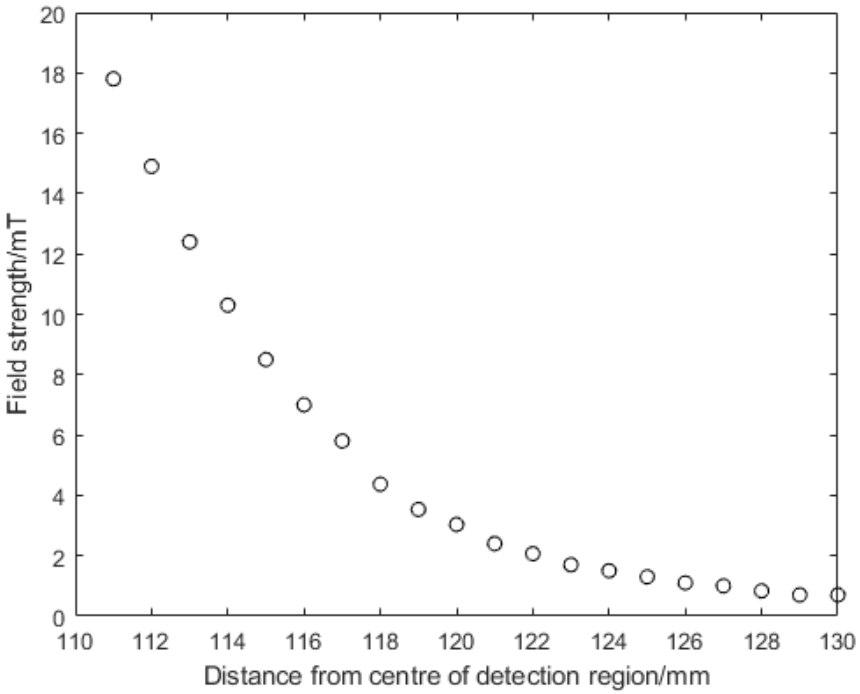

Figure 6.10: B_0 field intensity inside the bore of a Spinsolve 60, in distance from the centre of the detection region/mm, recorded by Dr. Daniel Taylor using a Hirst GM08 Gauss meter with transverse probe moved by the magnet. The SABRE PTF is reached at 117mm.

6.6.3.2 Limitations and Mitigations

Figure 6.10 shows that a 6 mT field is only reached in a very narrow band across the sample. For a typical sample depth of ≈60 mm, the full depth of the sample experiences 100 mT < PTF < 0.5 mT. Only 2.5 mm of the sample experiences a PTF of 6±2 mT and 1.5 mm of the sample experiences a PTF of 6±1 mT. This diminishes the effectiveness of SABRE transfer toward the higher and lower edges of a sample. This field heterogeneity is a significant factor that can diminish the overall achievable enhancement compared to methods where the entire sample volume resides in a more homogeneous field, such as through use of a separate magnet mounted above the spectrometer bore.

This is somewhat mitigated by the mixing of the sample during bubbling, which circulates sample through the tube. The quality of p-H_2 mixing is also reduced by the shallow depth from the top of the sample through which bubbles travel, diminishing mixing quality compared to sample shaking.[74] However, this region of effective PTF is still more than sufficient to generate large SABRE enhancements.

6.6.4 Manual shuttling

Using the field map to pre-calibrate the 6 mT position on the lead screw allows the performance of experiments using the motor system controlled by user input using the GUI (shown in Figure 6.8). This setup enables a direct comparison between two methods of PTF generation: the stray spectrometer field utilized by the motor-shuttling system and the Halbach array shaker[47] typically used in conventional shake-and-drop experiments. To carry out a SABRE experiment controlled using the GUI, the motor is connected through the serial port specified using the Connect Motor input, and after calibration, is moved to the "Sample 6 mT" position. A fixed p-H_2 bubbling duration can be applied using the options on the left side of the UI. following bubbling the sample can be moved to the detection region by the "Sample down" input, and detection initiated through Prospa. A pulse sequence representing this process is shown in Figure 6.11.

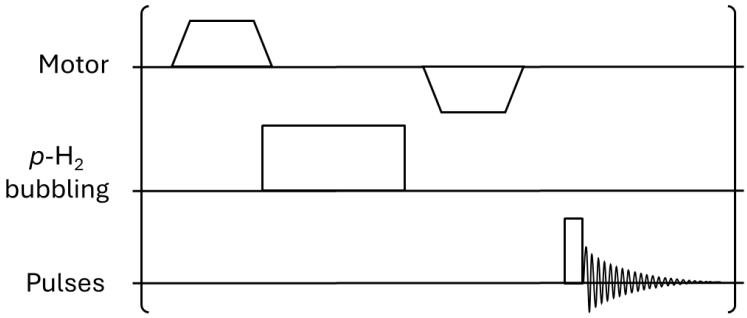

Figure 6.11: Pulse sequence for shuttled SABRE experiments. The motor moves up, lifting a sample to the 6 mT region of stray field. this allows polarisation transfer to occur concurrent with p-H_2 bubbling. The sample is then returned to the detection region, for application of a 90° pulse and detection.

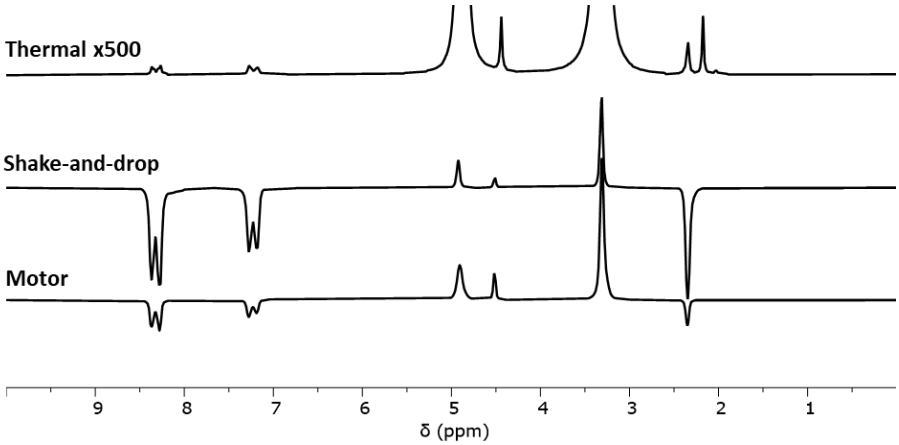

Figure 6.12: Comparison of ^{1}H NMR spectra for a solution containing 100 mM 4-methylpyridine with 5 mM [Ir(IMes)(COD)Cl] catalyst in methanol. Data recorded by Dr. Daniel Taylor. (Top) Thermal equilibrium spectrum (peak intensities magnified ×500). (Middle) Shake-and-drop hyperpolarised spectrum (magnified ×1). (Bottom) Spectrum acquired using the automated motor-driven shuttling system, with pulse sequence shown in Figure 6.11 using 10 s p-H_2 bubbling time (magnified ×1).

Figure 6.12 shows a SABRE - hyperpolarised spectrum of 4-methylpyridine recorded using this method by Dr. D. A. Taylor. Figure 6.12 also includes a thermally polarised and shake-and-drop spectrum of 4-methylpyridine. Both the motor-shuttled and shake-and-drop spectra show siginificant enhancement over thermal. The shake-and-drop sample experiences both better mixing (from shaking sample vs shallow capillary bubbling) and a more homogeneous field, yielding significantly stronger enhancements across all peaks.

A key feature of the motor-shuttled spectrum is the selective and strong enhancement of the ortho-protons relative to the other resonances. This occurs because the ortho-protons possess the broadest field range over which the polarisation transfer field (PTF) condition is met. The meta- and methyl-protons are only weakly enhanced due to their much narrower PTF requirement. Under these conditions, PTF requirements for positive enhancement for the meta- and methyl- are also met, which acts to cancel the primary negative enhancement, resulting in a weaker overall signal.[124]

As shown in Table 6.3, the enhancement from the motor-shuttled experiment is significant compared to a thermal spectrum but weaker than the enhancement achieved via the shake-and-drop method. For example, the ortho-protons are enhanced by a factor of 320 with the motor, compared to 1300 with the shake-and-drop method.

The much weaker signal enhancement observed from the shuttled spectrum compared to the shake-and-drop can be attributed to the very limited region across which the sample experiences 6 mT, compared to the Halbach array shaker which allows polarisation transfer across the entire sample. The mixing quality from the bubbling here is also of lower quality compared to vigorous sample shaking. This could be compensated for by extending bubbling times at the expense of reducing sample lifetime through driving evaporation.

Table 6.3: Table of enhancement factors of shake-and-drop and motor-shuttled SABRE spectra of 4-Mepy shown in Figure 6.12.

Peak	Enhancement factor (Shake & Drop)	Enhancement factor (motor)
Ortho	1300	320
Meta	690	140
Methyl	360	60

6.6.5 Fully integrated shuttling

While manual shuttling is effective for single-shot experiments, its inherent lack of reproducibility and precise timing control precludes more advanced applications. The key advantage of a motor-driven shuttle is that it allows the performance of spectrometer-controlled sequences, allowing for more complex experiments including 2D experiments with controlled timing. The simplest pulse sequence to run is the sequence given in Figure 6.11, performing a simple pulse-and detect. This is a useful proof of concept and allows performance of reference experiments.

For this simple pulse sequence, a Serial connection to the motor is established parallel to the connection to the polariser unit. Sample shuttling can be controlled step by step using characters over this Serial line. p-H_2 delivery can be implemented using the pre-loaded sequence approach outlined above. This may include a delay to account for shuttling time to the 6 mT region, or may be initiated following cell arrival at the 6mT region. Following bubbling, including the appropriate delay in pulse sequence script, the command to return the sample to the detection region can be sent over the Serial connection, and detection commenced. This process is illustrated in the script below. Motor movements are programmed to place the sample in the PTF region of the bore for 10 s of bubbling prior to detection.

```
bubbleTime = 10; port = "COM1"; mode = 0        # set up bubbling sequence parameters
motorPort = "COM2"                              # set motor port
s = ssbubble:setBubSeq(port, mode)
s = ssbubble:bublStep(s, d1)
ssbubble:sendSeq(port, s, mode)

ssMotor:connect_motor(motorPort)                # Connect and calibrate motor position
delay(10);

# Accumulate scans
for(scan = 0 to nrScans-1)
    ssMotor:position_motor(motorPort, "PTF")    # place sample in PTF
    delay(1.8)                                    # allow time for movement
    ssbubble:runSeq(port,mode)                  # begin bubbling with sample in PTF
    delay(bubbleTime)                                 # wait for bubbling to complete
    ssMotor:position_motor(motorPort, "bottom") # move to detection region
    delay(1.8)                                  # wait for motor to complete movement

    # Check timing, update the parameters, run the sequence and return the data
      (data,pAcq,status) = ucsRun:runSequence(guipar,ppList,pcList,pcIndex,scan)
next(scan)
```

Hard-coded delays are used to allow the motor sufficient time to position itself between steps. The 10 second delay after "connect motor" is added to give sufficient time to calibrate, and the 1.8 s movement delay is added to allow time for movement and stabilisation in the detection region. this also functions as the settling delay post-bubbling. This approach limits motor movements to the Experiment Control part of the Prospa NMR experiment, in which commands over the Serial connection can be sent. For more complex sequences involving motor movements occurring in time with or between NMR pulses in the detection region, the same strategy as the integrated bubbling could be implemented: to use pre-loaded sequences to fixed positions at fixed intervals. This would allow movements to occur while a pulse sequence is running in Prospa should it be needed. Multi-threading or careful control of initiation of bubbling and shuttling would be required to achieve the fine time control required for simultaneous or near-simultaneous bubble - shuttle - pulse timings.

6.7 Conclusion

In this chapter, the successful integration of the automated p-H_2 delivery system with a Magritek Spinsolve benchtop spectrometer has been demonstrated. The absence of TTL outputs on the spectrometer required the development of new software architecture to allow semi-automated control of gas bubbling directly from within a Prospa pulse sequence.

This is performed by pre-loading sequences of bubbling steps and delays to the delivery system's microcontroller via Serial communication. This adaptation makes the bubbling system developed in previous chapters compatible with any NMR instrumentation that is capable of sending text data over a serial connection.

To allow the system to perform spontaneous polarisation transfer, a motor-driven sample shuttling system was developed and implemented in collaboration with Dr. Daniel Taylor. The system enables precise and repeatable movement of a sample between the detection region and the PTF, which is reached in the stray field in the bore of the magnet. The hardware and control software for this shuttle were integrated with both the spectrometer and the existing bubbling apparatus.

From this, there are direct and relatively simple improvements that could be made to significantly improve the SNR of spectra obtained using this system. Inclusion of a magnet at the end of the detection bore of the spectrometer would simplify the PTF regime to be effective across the entire sample. Strategies involving a separate PTF magnet have been implemented by several authors, using electromagnets[48,59,60,63] and shielding for heteronuclear polarisation transfer.[56]

The mixing can be improved by using an alternative bubbling scheme. Space in the 5 mm bore is very limited but an alternative approach to gas delivery, for example from the bottom of the NMR tube (including a system to prevent unintentional displacement of the sample) would be expected to significantly improve mixing and signal intensity, in a similar manner to using the frit cell compared to the capillary cell described in Chapter 4.

During the course of development, unintended phantom movements were observed to occur sporadically on connection of the motor to a PC, in a manner that could not be easily replicated. To prevent phantom movement, since the conclusion of this project the "shut down motor" command included above has been added to the end of sequences of motor movements, which sets the motor power, maximum acceleration and maximum velocity to zero. The "restart motor" function allows the motor to be moved again when desired. From a mechanical perspective, a improvements have been made since the end of this project to make the system more robust and minimise risk of damage: Mechanical safeguards have been added to minimise risk of damage from phantom movements or other error, including adding optical sensors to prevent the motor exceeding pre-set limits at either end of the lead screw. This prevents mechanical damage to the spectrometer, sample or the motor system in the event of motor slip, failure, misalignment or power surge.

CHAPTER 7

Conclusions

7.1 Key Findings and Contributions

This thesis has detailed the successful design, construction, and validation of an automated and versatile platform for performing SABRE-enhanced low-field NMR. The system provides robust, repeatable *para*-hydrogen delivery that can be precisely synchronised with the pulse sequences of diverse NMR instruments, from ultra-low-field to benchtop spectrometers. This new capability enabled a study into the relaxation dynamics of *para*-hydrogen in a SABRE solution at the Earth's magnetic field, identifying rapid, catalyst-mediated pathway for NMR signal decay. More broadly, the instrumentation developed in this work provides a flexible toolkit for future SABRE research through the adaptation of the system for use with benchtop NMR spectrometers. This facilitates signal-averaged and multidimensional experiments that were not previously feasible with shake-and-drop p-H_2 delivery and polarisation transfer methods.

A robust, automated, and modular platform for *para*-hydrogen delivery for *in situ* SABRE was developed, comprised of a *para*-hydrogen generator and programmable valve network that together allow controllable p-H_2 delivery to a reaction cell to be incorporated directly into an NMR pulse sequence. This p-H_2 delivery platform enabled two key developments. First, it facilitated direct measurements of p-H_2 relaxation dynamics *in situ* within the Earth's magnetic field using a Magritek Terranova system. Second, by integrating the system with a rapid and controllable sample shuttling system, it allowed for SABRE with spontaneous polarisation transfer to be performed on a benchtop spectrometer. The *para*-hydrogen delivery system builds on an initial prototype constructed by Hill-Casey *et al.*[74] and Rossetto.[156]

The *para*-hydrogen delivery system comprises a controlling polariser unit which interfaces with a spectrometer, a network of controllable solenoid valves and gas lines, and a glass reaction cell which allows for efficient mixing of p-H_2 into a sample of SABRE solution (solvent, substrate, and catalyst). The polariser unit is built around a central Arduino microcontroller, which allows user control through a graphical user interface, direct control through electronic TTL signals, or software control through interaction with the NMR experiment control software over a Serial connection. These control methods allow for automated, precisely timed gas flow as part of an NMR experiment. Additionally, the user interface and the Serial interaction allow for real-time and post-hoc pressure monitoring to ensure a robust, leak-free design for gas flow. Real-time pressure monitoring can also be used to calculate H_2 concentration in the reaction solution. This forms a foundation for the optimisation experiments and SABRE dynamics explorations for all NMR experiments presented in this thesis, allowing the performance of multiple signal averaging, two-dimensional experiments, and multidimensional imaging coupled with SABRE hyperpolarisation.

The polariser unit was integrated with a Magritek Terranova EFNMR instrument and used to optimise experimental parameters for p-H_2 delivery in SABRE were optimised, including p-H_2 delivery times, PTF application times, and H_2 displacement from solution with nitrogen. *Para*-hydrogen delivery can be optimised separately from, or in parallel with, PTF application, with results indicating different optimal delivery times for each scenario. A higher signal intensity is observed when the two are applied in tandem, which can be attributed to a higher available volume of dissolved p-H_2 due to continuous replenishment through gas flow. The effectiveness of p-H_2 mixing was also studied through the use of MRI with two different designs of reaction cell: a frit cell commonly in use in the group and a capillary cell. While MR images of the capillary cell show more a homogeneous distribution hyperpolarisation, the corresponding spectra were of weaker intensity, with the frit cell showing a two-fold greater overall signal enhancement. This suggests that maximising the gas-liquid surface area for efficient p-H_2 dissolution is more critical for achieving high signal than ensuring perfectly uniform mixing.

To prolong sample lifetimes, a solvent reservoir was added in-line to the gas delivery system prior to the reaction cell, allowing gas to become "wet" before reaching the cell. This reduced the rate of solvent loss by 33% in the frit cell in the EFNMR system, slowing the rate of SABRE signal decay by nearly 76% (from $0.015\,\%s^{-1}$ to $0.0036\,\%s^{-1}$), significantly improving sample stability over long experiments. Sample lifetimes were further improved through addition of a nitrogen line connected to the cell allowed samples to be left under a nitrogen atmosphere overnight, significantly reducing the decay of hyperpolarised peak integral when samples were left for long periods, such as overnight. This is hypothesised to be due to nitrogen positive pressure in the cell preventing ingress of oxygen, which drives catalyst deactivation.

During optimisation experiments, inconsistencies were observed regarding the interactions of fresh p-H_2 in solution prior to polarisation transfer, where an apparent biexponential decay was seen. This behaviour indicates two distinct relaxation pathways. The dominant, rapid process was found to be highly dependent on both [H_2] and [substrate], consistent with a catalyst-mediated relaxation mechanism governed by competitive ligand exchange. Specifically, the rate and amplitude of this fast decay constant are limited

by the competitive exchange kinetics of H_2 and the substrate at the SABRE catalyst. At low substrate concentrations, the amplitude of the fast decay process is lowest and the decay is most rapid, as H_2 more effectively competes for vacant catalyst sites, leading to a faster relaxation rate. In contrast, the second, slower decay process has an amplitude that appears to be very weakly dependent on H_2 concentration and pyridine concentration, suggesting it arises from a background relaxation mechanism independent of the primary catalytic cycle. The time constant of this slow component was >1000 s, which is shorter than the lifetime of p-H_2 in degassed methanol, suggesting another interaction is driving the relaxation. This rapid, catalyst-mediated relaxation will impact the design and reproducibility of all *in situ* SABRE experiments, particularly those where p-H_2 delivery and polarisation transfer are decoupled in time or space.

A key achievement in this chapter was the development of a software control protocol based on serial communication. This innovation decouples the delivery system from the spectrometer's hardware, removing the reliance on TTL pulses. This creates a universal interface, allowing the platform to be controlled by any instrument or computer capable of sending simple text commands over a serial port. This dramatically increases the system's versatility and applicability to a wide range of existing and future NMR systems. This communication protocol was coupled with a Magritek Spinsolve benchtop spectrometer and a custom-built 5 mm NMR tube. The controllable gas delivery used to monitor the activation of the SABRE catalyst *in situ* by monitoring the growing integral of the hydride peak at -23 ppm.

To allow spontaneous SABRE polarisation transfer coupled with detection on the benchtop spectrometer, software was written to allow control of a motor-driven sample shuttling apparatus constructed by Dr. Daniel Taylor. The motor shuttling was used with an interfaced Gauss probe to create a field map of the bore of the spectrometer, creating a reference point for which a SABRE sample could be shuttled between 6 mT and the detection region. User control of the motor through the interface was combined with the controlled bubbling to allow performance of a spontaneous SABRE hyperpolarisation of 4-Mepy. The development of fully automated sample shuttling inside the Prospa pulse sequence was ongoing at the conclusion of this project and has since been implemented, facilitating highly reproducible and multidimensional SABRE-hyperpolarised NMR with benchtop detection.

7.2 Future work

Further development of the gas flow system could include a change to the layout of the valve network to allow back-pressurisation of the cell. Routing the gas path to allow a bypass for back pressure could provide a more abrupt stop to bubbling, which reduces the settling delay required for stabilisation in higher-field systems that are prone to magnetic susceptibility artifacts in their spectra. To complement this, integrated digital in-line flow regulators would allow more precise control of flow to the cell, ensuring improved reproducibility of the *para*-hydrogen gas volume delivered and reducing the required pressure recovery time between experiments. This recovery time could also be reduced by

using the first pressure regulator currently in the system to allow a higher generator set pressure followed by down-regulation, thereby reducing the impact of generator lag and pressure depletion, particularly for long supply durations of p-H_2. However, even with these enhancements to the delivery system, the stochastic nature of bubble formation at the frit would likely remain a persistent source of inconsistency.

Another possible development is the integration of a higher-capacity H_2 generator for higher flow rates and the potential for increased pressure. A higher flow rate would yield a larger signal enhancement for combined bubbling/PTF experiments, as the signal in the low-pressure regime in which these experiments are conducted is linearly dependent on H_2 pressure. In addition, a larger reaction cell for EFNMR detection would give more intense signals.

Further improvements to the benchtop hardware could significantly boost performance. Adding a Halbach array or mu-metal shield above the spectrometer would create a homogeneous PTF across the entire sample, increasing signal enhancements and enabling transfer to heteronuclei. Signal could also be improved by implementing a bottom-up bubbling design for more efficient p-H_2 mixing. Finally, to make the motor system more robust, physical sensors could be added at each end of the lead screw to prevent the shuttle from moving out of bounds and provide a backstop against damage to the motor, sample, or spectrometer.

To better characterise the relaxation dynamics, the group possesses a simple 6 mT NMR spectrometer with a probe consisting of of two pairs of concentric Helmholtz coils around an orthogonal B_1 coil. The polariser unit can be coupled to this spectrometer to allow the acquisition of hyperpolarised NMR spectra at the SABRE PTF for ^{1}H nuclei. However, the peak width in the current iteration is very broad (250 Hz) with correspondingly poor SNR ($\approx$ 6)as compared to EFNMR spectra hyperpolarised by SABRE (SNR$\approx$ 60) or even brute force (SNR$\approx$ 20). Higher quality NMR spectra using this instrument could be acquired with the construction of gradient coils for the probe. This improved instrumentation would enable the study of relaxation dynamics within the PTF as they occur during NMR detection, which may paint a clearer picture of the dynamics compared to the observation in the Earth's field experiments presented here. Further measurements of the long decay process could be made on a system less susceptible to external interference, such as a benchtop spectrometer. This would also allow the longer-lived states to be better resolved with chemical shift information. The stability and higher field of a benchtop spectrometer make it an ideal platform for characterising both the fast and slow relaxation processes. The main advantage is chemical shift resolution, which would allow distinction of distinct relaxation behaviours in different chemical environments. The primary challenge is that this requires a robust and highly reproducible shuttling sequence to move the sample between the Earth's field and the benchtop's detection field. The current motor system provides the foundation for this, but motor movements would need to be fully automated within the pulse sequence synchronously with p-H_2 delivery. The rapid movement through a field gradient during shuttling might also introduce experimental complexities compared to the single field switch in the Earth's field instrument.

The bubbling system can also be leveraged to perform RF-SABRE experiments on

the benchtop. This would enable studies of SABRE transfer dynamics under continuous RF irradiation, providing a complementary approach to the spontaneous transfer methods explored in this thesis. More broadly, the fully integrated shuttling system unlocks a wide range of experiments previously impossible on this platform, including repeatable shuttling for signal averaged 1D spectra and multidimensional sequences, which cannot be performed without automated control. Implementing these capabilities in the benchtop regime is particularly advantageous as it lowers the barrier to entry for such hyperpolarisation experiments, making them more accessible and cost-effective compared to high-field alternatives.

Appendices

APPENDIX A

Arduino Control code

```
////////////////////////////////////////
//define variables
////////////////////////////////////////

int pollTime = 500;        //time between pressure reads
int pressureTime = 3000;  //time the outlet valve is closed to
    pressurise the cell before 'open' bubbling starts.

int simpleTTL = 0;         //use one-to-one TTL input to valve opening

//
String pollTimeS;
int bubbleT, seqT, leadT, reps;
String bubbleTS, seqTS, leadTS, repsS;

int outLEDIn = 34;
int oLI = outLEDIn;
int outLEDOut = 36;
int oLO = outLEDOut;
int outLEDshort = 40;          //sets pin number for LED outputs
int oLS = outLEDshort;             //contraction. used throughout
int outLEDNN = 38;
int oLN = outLEDNN;
int outLEDopH = 32;
int oLH = outLEDopH;
int V6 = 42;
int V7 = 44;
int V8 = 46;
int inMon = 0;
int outMon = 0;
int ophMon = 0;
int n2Mon = 0;
```

```
int shortMon = 0;
int T1n, T1b, T2n, T2b, T3n, T3b, T4n, T4b, T5n, T5b;
String inMo, outMo, ophMo, n2Mo, shortMo;
char startup = 'z';
//
int outValveIn = 9;
int oVI = outValveIn;
int outValveOut = 10;
int oVO = outValveOut;
int outValveShort = 52;
int oVS = outValveShort;    //pin nos for valve triggers
int outValveNN = 22;        //including contractions. if you need to add both will work
int oVN = outValveNN;
int outValveopH = 8;
int oVH = outValveopH;
int startupint;
//
int T1 = 2;  //0x10 TTL bit
int T2 = 3;  //0x20
int T3 = 4;  //0x08
int T4 = 51;
int T5 = 53;
//
int S1 = 5;  //pin numbers for LED status indicators
int S2 = 6;
int S3 = 7;
int S4 = 11;
int S5 = 12;
int S6 = 13;
int S7 = 23;
int S8 = 50;
//
bool TNcontrol = 1;      //Terranova control:when true valves are triggered by TTL pulses
bool PrintPressure = 0;  //sends presure readings over serial


int vA1 = 0;
int vA2 = 0;  //voltage from analog pin
int vA3 = 0;
int vA4 = 0;

String prOut;  //string that gives the pressure readings over serial
int pCount;
unsigned long tNow;
unsigned long tSt = 0;
String parameters;
int zeroTime;
int fillTime;


//Variables for spinsolver
String test, stepsStr, durationStr, sequence;
int steps, duration, acStepDur;
char stepType;
int stepno = 0;
int exec[9][2] = {
```

```
  { 0, 0 },
  { 0, 0 },
  { 0, 0 },
  { 0, 0 },
  { 0, 0 },
  { 0, 0 },
  { 0, 0 },
  { 0, 0 },
  { 0, 0 },
};
int steplocator = 1;
int seqLen;

//////////////////////////////////////////
void setup() {
  //////////////////////////////////////////
  // put your setup code here, to run once:
  DeclarePins();  // declares the pin numbers to the arduino
                  // these functions are defined after LOOP
  AllTheLights();

  Serial.begin(9600);   //opens the serial port at 9600baud (9600 bits/
   second)
  digitalWrite(S2, 1);  //TNcontrol is on by default
  digitalWrite(S3, 1);  //Print pressure is on by default
  tSt = millis();
}
//////////////////////////////////////////
void loop() {
  //////////////////////////////////////////

  tNow = millis();

  HandleSerial();

  TTLFunction();

  pressureFunction();

}  //end of the repeated code loop

//////////////////////////////////////////
void HandleSerial() {
  //////////////////////////////////////////

  char input;
  input = Serial.read();

  switch (input) {  //depending on *input*, do the following:
    //////////////////////////
    //manual,auto control functions
    //////////////////////////
    case 'i':
      digitalWrite(S4, HIGH);
      spinsolver(exec);
      //Serial.println("spinsolved");
      break;
    case 'R':
```

```
145       if { TNControl == 0 }
146       {
147         digitalWrite(S4, HIGH);
148         ssexecute(exec);
149       }
150       break;
151
152
153      case 'M':               //Capital M for auto(spec'r) control. lc *m
    * for manual control.
154       TNcontrol = 1;         //switches between manual and auto mode?
155       pCount = 0;
156       digitalWrite(S2, 1);  //S2 is on when we're running in auto.
157       // FullTTL();
158       break;
159      case 'm':  //activates manual control
160       TNcontrol = 0;
161       pCount = 0;
162       digitalWrite(S2, 0);
163      case 'K':             //turns on the plotting and the valve logging
    .
164       PrintPressure = 1;  //how we log comes later.
165       digitalWrite(S3, 1);
166       break;
167      case 'k':  //turns the logging off.
168       PrintPressure = 0;
169       digitalWrite(S3, 0);
170       break;
171       if (TNcontrol == 0) {      //when in manual mode:
172         case 'Z':                //capital letters for on, l/c for off
173           VLWrite(oVS, oLS, 1);  //turns on the short valve and the
    short LED.
174           shortMon = 1;          //logs the valve state
175           break;                 //this valve sytate is printed next to
     the pressures.
176         case 'z':
177           VLWrite(oVS, oLS, 0);
178           shortMon = 0;
179           break;
180         case 'C':
181           VLWrite(oVI, oLI, 1);
182           inMon = 1;
183           break;
184         case 'c':
185           VLWrite(oVI, oLI, 0);
186           inMon = 0;
187           break;
188         case 'V':
189           VLWrite(oVO, oLO, 1);
190           outMon = 1;
191           break;
192         case 'v':
193           VLWrite(oVO, oLO, 0);
194           outMon = 0;
195           break;
196         case 'H':
197           VLWrite(oVH, oLH, 1);
198           ophMon = 1;
```

```
199           break;
200         case 'h':
201           VLWrite(oVH, oLH, 0);
202           ophMon = 0;
203           break;
204         case 'X':
205           digitalWrite(S4, 1);
206           VLWrite(oVN, oLN, 1);
207           break;
208         case 'x':
209           // digitalWrite(S4, 0);
210           VLWrite(oVN, oLN, 0);
211           break;
212       }  //end of the manual control operation part of the code.
213   }
214 }
215
216 ////////////////////////////////////////
217 void TTLFunction() {
218   ////////////////////////////////////////
219   if (simpleTTL == 0 && TNcontrol == 1) {
220     /*
221       functions we need:
222       pressurise into bubble
223       drain cell
224       gas switch
225     */
226     // start of the auto control section
227     T3n = digitalRead(T3);  //usually does oph        0x20
228     T2n = digitalRead(T2);  //usually does inlet      0x08
229     T1n = digitalRead(T1);  //usually does short      0x04
230     T5n = digitalRead(T5);  //usually does outlet     0x40
231     T4n = digitalRead(T4);  //usually does outlet     0x10    //clearly
        wrong?
232
233     int TTLcode = TTLByter(T1n, T2n, T3n, T4n, T5n);
234     /*        Serial.println(TTLcode);
235         Serial.println("-------");*/
236     TTLCases(TTLcode);
237   }
238   if (simpleTTL == 1 && TNcontrol == 1) {
239     //start of the auto control section
240     //second 0x10
241     T1n = digitalRead(T1);
242     VLWrite(oVI, oLI, T1n);
243     shortMon = T1n;
244     //third 0x20
245     T2n = digitalRead(T2);
246     VLWrite(oVO, oLO, T2n);
247     inMon = T2n;
248     //first, 0x08
249     T3n = digitalRead(T3);
250     VLWrite(oVH, oLH, T3n);
251     ophMon = T3n;
252
253     //flips the h2 supply from thermal to para.
254     T4n = digitalRead(T4);
255     VLWrite(oVN, oLN, T4n);
```

```
256     inMon = T2n;
257     T5n = digitalRead(T5);
258     VLWrite(oVS, oLS, T5n);
259     outMon = T5n;
260   }
261 }
262
263 ////////////////////////////////////////
264 void pressureFunction() {
265   ////////////////////////////////////////
266
267
268   if (PrintPressure == 1) {  //allows recording of valves and pressures
      :
269     if (tNow - tSt >= pollTime) {
270       tSt = tNow;            //reset the timer after printing
271       vA1 = analogRead(A0);  //gets the pressures.
272       vA2 = analogRead(A2);
273       vA3 = analogRead(A4);
274       vA4 = analogRead(A6);
275       //vA4 = analogRead(A4);              //can be in if/when we get
      more pressure gauges.
276       String vsA1 = String(vA1);  //makes the recorded pressure integer
       into a string, bc can't concactenate integers into compound strings
      .
277       String vsA2 = String(vA2);
278       String vsA3 = String(vA3);
279       String vsA4 = String(vA4);
280       String ophMo = String(ophMon);
281       String inMo = String(inMon);  //does the same with the valve
      state indicator
282       String outMo = String(outMon);
283       String n2Mo = String(n2Mon);
284       String shortMo = String(shortMon);
285       prOut = "P " + vsA1 + ' ' + vsA2 + ' ' + vsA3 + ' ' + vsA4 + ' '
      + ophMon + ' ' + inMo + ' ' + outMo + ' ' + n2Mon + ' ' + shortMo +
      'C';  //prints the pressures, followed  y the valve states separated
       by a space for
286       Serial.println(prOut);
287       //we can add extra pressures read off to the end of the string
288     }
289   }
290 }
291 ////////////////////////////////////////
292 void VLWrite(int valve, int LED, int power) {
293   ////////////////////////////////////////
294
295   // turns on valve and led
296   if (power == 1) {
297     digitalWrite(valve, HIGH);
298     digitalWrite(LED, HIGH);
299   } else {
300     digitalWrite(valve, LOW);
301     digitalWrite(LED, LOW);
302   }
303 }
304
305 ////////////////////////////////////////
```

```
306 int TTLByter(int T1n, int T2n, int T3n, int T4n, int T5n) {
307   ////////////////////////////////////*/
308   byte result;
309   int a, s, d, f;
310   a = s = d = f = 0;
311   if (T1n == 1) {  //0x10
312     a = 1;
313   }
314   if (T2n == 1) {  //0x20
315     s = 2;
316   }
317   if (T3n == 1) {  //0x08
318     d = 4;
319   }
320   if (T4n == 1) {
321     f = 8;
322   }
323   result = a + s + d + f;
324   return result;
325 }
326
327
328 ////////////////////////////////////////
329 void TTLCases(int input) {
330   ////////////////////////////////////////
331
332   if (input != 1 && input != 7) {
333     fillTime = 0;
334     //these two code require a fixed delay after which a second step
      occurs. The timing used is fillTime (set at top)
335     //fillTime resets whenever a different case other than the two-step
      cases is running. To run the back-to-back, add in a +111 pulse or
      +000 gap
336   }
337
338   switch (input) {
339     case 0:  //000
340       VLWrite(oVI, oLI, 0);
341       inMon = 0;
342       VLWrite(oVH, oLH, 0);
343       ophMon = 0;
344       VLWrite(oVO, oLO, 0);
345       outMon = 0;
346       VLWrite(oVN, oLN, 0);
347       n2Mon = 0;
348       break;
349     //cell filling & bubbling
350     case 1:  //001          //0x10 only
351       VLWrite(oVI, oLI, 1);
352       inMon = 1;
353       VLWrite(oVH, oLH, 0);
354       ophMon = 0;
355       if (fillTime == 0) {
356         zeroTime = millis();
357       }
358       fillTime = millis() - zeroTime + 1;
359       if (fillTime >= pressureTime) {
360         VLWrite(oVO, oLO, 1);
```

```
361         outMon = 1;
362       } else {
363         VLWrite(oVO, oLO, 0);
364       }
365       break
366         //open bubbling. pH2 flow through cell.
367         case 2 :  //010          //0x20 only
368                   VLWrite(oVI, oLI, 1);
369       inMon = 1;
370       VLWrite(oVH, oLH, 0);
371       ophMon = 0;
372       VLWrite(oVO, oLO, 1);
373       outMon = 1;
374       break;
375
376     //cell filling. opens in. Used to open H2 too - will need to in
      future
377     case 3:  //011
378       VLWrite(oVI, oLI, 1);
379       inMon = 1;
380       VLWrite(oVH, oLH, 0);
381       ophMon = 0;
382       VLWrite(oVO, oLO, 0);
383       outMon = 0;
384       break;
385
386     //draining
387     case 4:  //100          //0x08 only
388       VLWrite(oVI, oLI, 0);
389       inMon = 0;
390       VLWrite(oVH, oLH, 0);
391       ophMon = 0;
392       VLWrite(oVO, oLO, 1);
393       outMon = 1;
394       break;
395
396     //alt gas bubbling flushout        //0x10 and 0x08 = 0x18
397     case 5:  //101
398       VLWrite(oVI, oLI, 1);
399       inMon = 1;
400       VLWrite(oVH, oLH, 1);
401       ophMon = 1;
402       VLWrite(oVO, oLO, 1);
403       outMon = 1;
404       VLWrite(oVN, oLN, 1);
405       ophMon = 1;
406       break;
407
408   }
409 }
410 ////////////////////////////////////////////
411 void DeclarePins() {
412   ////////////////////////////////////////////
413
414   pinMode(outLEDshort, OUTPUT);  //sets the corresponding pins to input
      or output
415   pinMode(outLEDNN, OUTPUT);
416   pinMode(outLEDopH, OUTPUT);
```

```
417   pinMode(outLEDIn, OUTPUT);
418   pinMode(outLEDOut, OUTPUT);
419   pinMode(V6, OUTPUT);
420   pinMode(V7, OUTPUT);
421   pinMode(V8, OUTPUT);
422
423   pinMode(outValveShort, OUTPUT);
424   pinMode(outValveNN, OUTPUT);
425   pinMode(outValveopH, OUTPUT);
426   pinMode(outValveIn, OUTPUT);
427   pinMode(outValveOut, OUTPUT);
428
429   pinMode(T1, INPUT);
430   pinMode(T2, INPUT);
431   pinMode(T3, INPUT);
432   pinMode(T4, INPUT);
433   pinMode(T5, INPUT);
434
435   pinMode(S1, OUTPUT);
436   pinMode(S2, OUTPUT);
437   pinMode(S3, OUTPUT);
438   pinMode(S4, OUTPUT);
439   pinMode(S5, OUTPUT);
440   pinMode(S6, OUTPUT);
441   pinMode(S7, OUTPUT);
442   pinMode(S8, OUTPUT);
443 }
444
445
446 void spinsolver(int exec[9][2]) {
447   Serial.println("active");
448   //if (Serial.available() > 0) {
449
450   sequence = Serial.readString();
451   Serial.println(sequence);
452
453   //sequence = (Serial.readString());
454   Serial.println("string loaded");
455   digitalWrite(S6, HIGH);
456   //decompile the string into an array of command steps
457   stepsStr = sequence.substring(0);
458   steps = stepsStr.toInt();
459   //String stepsStr = String(steps);
460   Serial.println(stepsStr);
461
462   //for (int i = 0; i < steps; i++) {
463   int steplocator = sequence.indexOf('s');
464   int seqLen = sequence.length();
465   int start = steplocator + 1;
466   stepno = 0;
467   Serial.print("seq length is: ");
468   Serial.println(seqLen);
469   //for position in string x
470   for (int x = (steplocator + 1); x < seqLen; x++) {
471
472     //read each position in the string.
473     //once a character is reached, step is complete. calculated here
      and loaded into exec array
```

```
474     if (isAlpha(sequence.charAt(x))) {
475       int end = x;
476       durationStr = sequence.substring(start, end);
477       int stepDur = durationStr.toInt();
478       acStepDur = stepDur * 100;
479       exec[stepno][0] = acStepDur;
480       //character declares what type of step to process. They are
      processed here and loaded into exec array
481       char StepType = sequence.charAt(x);
482       start = x + 1;
483       if (StepType == 'b') {
484         //load bubbling step into executable
485         exec[stepno][1] = 1;
486       }
487       if (StepType == 'd') {
488         exec[stepno][1] = 2;
489       }
490       if (StepType == 'n') {
491         //load alt bubble time step into executable
492         exec[stepno][1] = 3;
493       }
494       stepno = stepno + 1;
495     }
496   }
497   Serial.print("sequence loaded: ");
498   Serial.println(sequence);
499   digitalWrite(S7, HIGH);
500 }
501
502 void ssexecute(int executable[9][2]) {
503   if (executable[0][0] != 0 && executable[0][0] != 0) {
504     for (int i = 0; i < 10; i++) {
505       int time = executable[i][0];
506       int type = executable[i][1];
507       if (type == 0) {
508         //Serial.println("ard. seq. done");
509         break;
510       }
511       if (type == 1) {
512         VLWrite(oVI, oLI, 1);
513         inMon = 1;
514         VLWrite(oVO, oLO, 1);
515         outMon = 1;
516         //digitalWrite(S4, 1);
517         VLWrite(oVN, oLN, 1);
518
519         //this is a less than ideal way of doing  things because it
      stops all code execution during the bubbling time
520         delay(time);
521
522         digitalWrite(S4, 0);
523         VLWrite(oVN, oLN, 0);
524         VLWrite(oVO, oLO, 0);
525         outMon = 0;
526         VLWrite(oVI, oLI, 0);
527         inMon = 0;
528
529         //Serial.print("bubbling ");
```

```
530         //Serial.println(i);
531       }
532       if (type == 2) {
533         VLWrite(oVI, oLI, 0);
534         inMon = 0;
535         VLWrite(oVH, oLH, 0);
536         ophMon = 0;
537         VLWrite(oVO, oLO, 0);
538         outMon = 0;
539         delay(time);
540       }
541     }
542   }
543   digitalWrite(S4, LOW);
544 }
```

APPENDIX B

2D spectral Processing - Prospa

```
procedure(curvefit_spectra_3)
   # multi experiment flag
   multiEx = 1
   if multiEx = 0
      folder = "C:\\a_name" # location of experiment folder
      :procTNspectra2023(folder, savename)
   elseif multiEx = 1
      target = "2024-12-25-experiments"
      Parent = "Z:\\Terranova2\\TN2 data\\James\\2024\\$target$"
      outFolder = "Z:\James M\dataprocessing\\2025\\output-folder\\"
      setcwd(Parent)
      count = 0
      #make a list of each experiemnt folder in the current Date
   directory
      exptlist = getdirlist(".")
      pr exptlist
      #for each experiment folder:
      for y = 0 to (size(exptlist) - 1)
          # pr nrPnts
         #construct the name of the folder
         exptfolder = exptlist[y]
         exptpath = Parent + "\\" + exptfolder
         setcwd(exptpath)
         if issubstr(exptpath, "ttl_Bp_relaxn")
            count = count + 1
            pr count
            if issubstr(exptpath, "emma")
              errFlag = 0
              count = count - 1
            else
               errFlag = :procTNSpectra_2023(target, exptfolder, count,
    outFolder)
```

```
31              endif
32              if errFlag > 0
33                 pr "Could not process data from $exptlist[y]$\n"
34                 count = count - 1
35              endif
36           endif
37        next(y)
38     endif
39  endproc()
40
41  procedure(procTNSpectra_2023, folder, savename, count, outFolder)
42     errFlag = 0
43     # file containing acq pars
44     parFile = "acqu.par.bak"
45     dataFile = "fid.2d"
46     timeStamps = "integrals.csv.1d"
47     try
48        (expPars,data2D,xAx) = :loadData(folder,parFile,dataFile,
       timeStamps)
49     catch
50        pr "Could not load data from $folder$$savename$"
51        return(1)
52     endtry
53     (nrPnts,nSteps) = size(data2D)
54     assignlist(expPars)
55     pr b1Freq
56     # Processing parameters
57     zfFac = 4                # Zero-filling factor, applied after any
       power-of-2 correction
58     phCorr = 0               # Fixed phase correction
59     decimateFlag = 1         # Decimate data according to the pars below
60     specWidth = 80          # Hz
61     intWidth = 20            # Hz
62     centreFreq = b1Freq +4    # Hz
63     labFrameFlag = 0
64     autophasing = 1
65     if labFrameFlag == 1
66        minDel = 0
67        maxDel = maxDelay
68        del = linvec(0,maxDel,nSteps)
69        del[0] = minDel
70     endif
71     filterType = "cosinebellsquared"
72
73   # Process data
74
75   # Set-up zero-filling (check power of 2)
76     if (frac(log2(nrPnts)) != 0)   # ZF if data not a power of 2
77        nTemp = 2^round(log2(nrPnts)+0.5) # round up to nearest power of
       2
78        temp = data2D
79        data2D = matrix(nTemp,nSteps)
80        data2D[0:nPoints-1,~] = temp    # ZF up to the next power of 2
81        nrPnts = nTemp
82     endif
83     nZF = nrPnts*zfFac
84
85   # Calculate time/frequency axes
```

```
86    tAxis = [0:nrPnts-1]*dwellTime*1e-6            # in s
87    fAxis = [0:nZF/2-1]*bandwidth*1000/nZF         # in Hz
88
89  # Get filter
90    if(filterType == "none")
91       flt = matrix(nrPnts)+1
92    else
93       flt = filters:get_filter(filterType,"FTFid",nrPnts)
94    endif
95
96 # set up parameters for lab frame correction
97    for nn = 0 to nSteps -1
98       try
99       # pr nn
100      # pr "correcting"
101         tDataCorr = matrix(nZF)
102         tDataCorr[0:nrPnts-1] = data2D[:,nn].*flt
103         tDataCorr[0] = tDataCorr[0]/2
104         spectrum = rft(tDataCorr)/(bandwidth*500) # bandwidth divided
    by 2 because only +ve frequencies kept by rft
105
106         if labFrameFlag
107            spectrum = spectrum*exp(i*2*pi*del[nn]*b1Freq)
108         endif
109      catch
110         pr "frame corr err"
111         return(2)
112      endtry
113      if autophasing == 1
114           #spectrum = spectrum*exp(-i*phCorr*pi/180)
115            left = findindex(fAxis,b1Freq-2*intWidth)
116            right = findindex(fAxis,b1Freq+2*intWidth)
117            if (left >= right)
118               phCorr = autophase(spectrum,0,totPnts-1,"maximise")
119            else
120               phCorr = autophase(spectrum,left,right,"maximise")
121            endif
122            spectrum = spectrum*exp(-i*phCorr*pi/180)
123      endif
124      if autophasing == 0
125       if phCorr != 0    # Apply fixed phase
126          spectrum = spectrum*exp(-i*phCorr*pi/180)
127       else
128         if  nn == 0    # Auto-phase first spectrum to get phCorr value
129            try
130               left = findindex(fAxis,b1Freq-2*intWidth)
131               right = findindex(fAxis,b1Freq+2*intWidth)
132            catch
133               pr "find index failed"
134            endtry
135            try
136               if (left >= right)
137                  phCorr = autophase(spectrum,0,totPnts-1,"maximise")
138                  # pr "first case"
139               else
140                  phCorr = autophase(spectrum,left,right,"maximise")
141                  # pr "scnd case"
142               endif
```

```
143             catch
144                return(2)
145                pr "phase failed"
146             endtry
147             spectrum = spectrum*exp(-i*phCorr*pi/180)
148          endif
149       endif
150    endif
151 try
152    if (decimateFlag & specWidth > 0 )
153 
154             if nn == 0
155              # get location of the B1 frequency
156                centreInt = findindex(fAxis,centreFreq)
157              # determine number of points in the dispRange
158                delf = fAxis[1]-fAxis[0]
159                tempPnts = round(specWidth/delf)
160              # get next largest power of two for processing
161                nDecimate = 2^round(log2(tempPnts))
162                fOut = submatrix(fAxis,centreInt-(nDecimate/2),centreInt
    +(nDecimate/2)-1)
163                swhNew = abs(fOut[-1]-fOut[0])
164                dwNew = 1/swhNew
165              # declare output arrays
166                fidOut = cmatrix(nDecimate,nSteps)
167                specOut = cmatrix(nDecimate,nSteps)
168                tOut = [0:1:nDecimate-1]*dwNew
169             endif
170 
171           # Extract region of spectrum
172             specOut[:,nn] = submatrix(spectrum,centreInt-(nDecimate/2),
    centreInt+(nDecimate/2)-1)
173             temp = ift(specOut[:,nn])*swhNew
174             fidOut[:,nn] = temp[0:nDecimate-1]
175             fidOut[0,nn] = 2*fidOut[0,nn]
176             totPnts = nDecimate
177 
178    else
179 
180             if nn == 0
181                totPnts = size(spectrum)
182                specOut = cmatrix(totPnts,nSteps)
183                fidOut = data2D
184                tOut = tAxis
185                fOut = fAxis
186             endif
187             specOut[:,nn] = spectrum
188 
189    endif
190 
191 catch
192    pr "decimate fail"
193    return(3)
194 endtry
195 
196 
197 next(nn)
198 
```

```
199 # Strip zero points out of the results matrix
200 # Adjust for frequency drift
201 # Correct for frequency and phase shift
202   freqShift = matrix(nn)
203   indShift = matrix(nn)
204   for nn = 0 to nSteps-1
205      (freqShift[nn],indShift[nn]) = :getFreqShift(fidOut[:,0],fidOut
      [:,nn],fOut,centreFreq)
206      if autophasing == 1
207         specOut[:,nn] = rotate(specOut[:,nn],-indShift[nn])      #
      Shift without phase correction
208      else
209         fidOut[:,nn] = fidOut[:,nn]*exp(i*2*pi*freqShift[nn]*acqDelay
      /1000)   # shift with phase correction
210         specOut[:,nn] = rotate(specOut[:,nn]*exp(i*2*pi*freqShift[nn]*
      acqDelay/1000),-indShift[nn])
211      endif
212   next(nn)
213
214 # Integrate spectra
215   integral = cmatrix(nSteps)
216   if nSteps > 3
217      for nn = 0 to nSteps-1
218         integral[nn] = integvector(fOut,real(specOut[:,nn]),centreFreq
      -intWidth/2,centreFreq+intWidth/2)+i*integvector(fOut,imag(specOut
      [:,nn]),centreFreq-intWidth/2,centreFreq+intWidth/2)
219      # pr integral[nn]
220      next(nn)
221
222      multiplot("1d",2,1)
223      curplot("1d",1,1)
224
225      plot(xAx,integral)
226      title("exp number: $count$")
227
228    # plot average of spectra
229      specAvg = sum(specOut,"y")/nSteps
230      curplot("1d",2,1)
231      plot(fOut,specAvg)
232      # xAx = xAx/1000
233      multiplot("2d",2,1)
234      curplot("2d",1,1)
235      image(data2D)
236      curplot("2d",2,1)
237      ylim = [1,nSteps]
238      xlim = [fOut[0],fOut[nDecimate-1]]
239      image(specOut,xlim,ylim)
240      2dsave = getplotdata("2d")
241      # pr size(specOut)
242      wdir = getcwd()
243
244      try
245         cd outFolder
246      catch
247         pr "could not access $outFolder$"
248         pr "Saving to: $wdir$"
249      endtry
250
```

```
251       savename = "$folder$_$savename$"
252
253       if count < 10
254          savenameInt = "o00$count$_$savename$__$maxDelay$mD.csv"
255       elseif count < 100
256          savenameInt = "o0$count$_$savename$__$maxDelay$mD.csv"
257       else
258          savenameInt = "o$count$_$savename$__$maxDelay$mD.csv"
259       endif
260       savename2d = "d$count$.2d"
261    realInt = real(integral)
262   # pr xAx
263    export1dpar("ab", "ascii", "xyrc", "xydata", "delimiter", "comma", "
      machine", "win",
264             "fileheader",1)
265       export1d(xAx, realInt, savenameInt)
266       fac = max(realInt)
267    if fac == 0
268       fac = 1
269    endif
270    if xAx[2] > 10
271       xAx = xAx/1000
272    endif
273    export1d(xAx, realInt, savenameInt)r
274       normInt = realInt/fac
275       if count < 10
276          normName = "n00$count$_$savename$__$maxDelay$mD.csv"
277       elseif count < 100
278          normName = "n0$count$_$savename$__$maxDelay$mD.csv"
279       else
280          normName = "n$count$_$savename$__$maxDelay$mD.csv"
281       endif
282
283    export1d(xAx, normInt, normName)
284       #pr(vartype(xAx))
285       (szx, szy) = size(xAx)
286       nullCMat = cmatrix(szx,szy)
287       dataInts = xAx + nullCMat
288       #pr(vartype(integral))
289       # dataInts = join(dataInts, integral, "horiz")
290       # pr dataInts
291       save(savename2d, 2dsave)
292       realInt = real(integral)
293      # pr xAx
294      # pr realInt
295       export1dpar("ab", "ascii", "xyrc", "xydata", "delimiter", "comma"
      , "machine", "win",
296                "fileheader",1)
297     #  pr xAx
298       if xAx[2] > 10
299          xAx = xAx/1000
300       endif
301       export1d(xAx, realInt, savenameInt)
302     #  pr count
303       curDir = getcwd()
304       pr "\nsaved to $curDir$\n"
305       cd wdir
306
```

```
307     else
308        pr "Could not load data from $folder$"
309        pr "Not enough steps in data from $folder$. No steps = $nSteps$"
310        return(1)
311     endif
312
313
314
315 endproc(0)
316
317
318 procedure(getFreqShift, FIDRef, FIDNew, fAxis, freqCentre)
319
320 # Calculate CrossCorrelation function and relative fAxis
321     crossCorr = ft(conj(FIDRef).*FIDNew)
322     fRel = fAxis - freqCentre
323
324 # Magnitude of CrossCorrelation function
325     crossCorrMag = mag(crossCorr)
326
327 # Find maximum which is frequency shift
328     (maxPeak, maxIndex) = max(crossCorrMag)
329     freqShift = fRel[maxIndex]
330     indShift = round(freqShift/(fAxis[1]-fAxis[0]))
331
332 endproc(freqShift,indShift)
333
334 procedure(loadData,folder,parFile,filename, timestamp)
335
336     # Load experiment data and parameters
337     bak = getcwd()
338     cd(folder)
339     # pr getcwd()
340
341     # Load parameter file
342 try
343     expPars = load(parFile,"list")
344     assignlist(expPars)
345 catch
346     expPars = load("acqu.par","list")
347     assignlist(expPars)
348 endtry
349
350     # Load data file
351 try
352     data2D = load(filename)
353 catch
354     pr "2d load fail"
355 endtry
356   # pr "loaded 2d"
357 try
358     intTime = load("integrals.csv.1d")
359     # pr intTime
360 catch
361     pr "1d time axis load fail"
362 endtry
363     cd(bak)
364
```

```
365 endproc(expPars,data2D, intTime)
```

APPENDIX C

Decay fitting - MATLAB

```
basedir = "Z:\James M\data\2024\";
folder = "folder";
directory = basedir + folder;
date = datestr(now, 'yyyy-mm-dd');
output_location = directory + "\_" + date + folder + ".xlsx";
plotfig = 1;
fitEquation = 'A * exp(-x/B) + C *exp(-x/D) ';
count = 0;
% % Get a list of all CSV files in the directory
files = dir(fullfile(directory, '*.csv'));
nmls = 1;
results = {'no.', 'folder', 'file', 'size', 'maxDel', 'A', 'pmA', 'pctA
    ', 'B', 'pmB', 'pctB','C', 'pmC', 'pctC','D', 'pmD', 'pctD', 'mag',
     'plat', 'ini'};
% Loop through each CSV file
for i = 1:numel(files)
    try
        % Construct the full file path
        file_path = fullfile(directory, files(i).name);
        % Read the CSV data using the 'readtable' function
        data = readmatrix(file_path);
        % Logical index to find rows where the second column is not
   zero
        data;
        file_path;
        nonZeroRows = data(:, 2) > 0;
        % Extract rows where the second column is not zero
        filteredMatrix = data(nonZeroRows, :);
        newx = filteredMatrix(:,1);
        sz = size(newx, 1);
        mD = max(newx);
        y = filteredMatrix(:,2);
```

```
        files(i).name;
        filteredMatrix;

        flder = extractBetween(files(i).name, "2024-", '_ttl');
        flder = cell2mat(flder);

        fle = extractBetween(files(i).name, "2pulse", '.csv');
        fle = cell2mat(fle);

        if isempty(fle)
            fle = files(i).name;
        end
    catch
        "load error"
        count = extractBefore(files(i).name, '_202');
        count;
        continue
    end
    if sz > 2
        firstPt = filteredMatrix(1,2);
        try
            f = fit(newx, y, fitEquation, 'StartPoint',[1,1,1,1000]);
        catch
            count;
            "fit failed"
        end
        try
            % CALCULATE CONFIDENCE INTERVALS
            errors = confint(f, 0.95);
            e1 = errors(1, 1);
            e2 = errors(2, 1);
            pctA = 100*(f.A - e1)/f.A;
            delA = abs(f.A - e1);
            e3 = errors(1, 2);
            e4 = errors(2, 2);
            pctB = 100*(f.B - e3)/f.B;
            delB = abs(f.B - e3);
            e5 = errors(1, 3);
            e6 = errors(2, 3);
            pctC = 100*(f.C - e5)/f.C;
            delC = abs(f.C - e5);
            e7 = errors(1, 4);
            e8 = errors(2, 4);
            pctD = 100*(f.D - e7)/f.D;
            delD = abs(f.D - e7);
            str = "B1";
        catch
            "failed calculating errors"
        end
        try
            x = 0:1:(max(newx));
            z = f.A * exp(-x / (f.B)) + f.C * exp(-x / f.D);
            z0 = f.A + f.C;
            plat = f.C/z0;
            count = extractBefore(files(i).name, '_202');
            count(1);
            hold off;
            plot(newx, y, 'ok', x, z, '-k');
```

```
88              xlabel('delay time d_1/s ');
89              ylabel('SABRE peak integral ');
90              if count(1) == 'n'
91                  axis([0, max(newx), 0, 1])
92              else
93                  axis([0, max(newx), 0, max(y)])
94              end
95              dB = 1/f.B;
96              newresult = {count, flder, fle, sz, mD, f.A, delA, pctA, f.
    B, delB, pctB, f.C, delC, pctC,f.D, delD, pctD, z0, plat, firstPt};
97              size(newresult)
98              results = [results; newresult];
99              grNm = directory + "\graph_" + num2str(count) + '_' +
    folder + ".png";
100             grNm2 = directory + "\graph_" + num2str(count) + '_' +
    folder + ".fig";
101             ax = gca;
102             if plotfig
103                 saveas(ax, grNm2);
104                 "png saved";
105                 exportgraphics(ax, grNm);
106             end
107         catch
108             "an issue occured at:"
109             count
110         end
111     end
112 end
113 writecell(results, output_location);
```

APPENDIX D

Prospa/Spinsolve Bubbling Macro

```
1  ##################################################################
2  #############          SPINSOLVE MACROS             #############
3  ##################################################################
4
5  #
6  #    TEST    PROCEDURE
7  #
8
9  :test(port, mode, d1, d2, d3)
10 d1 = 5
11 d2 = 3
12 d3 = 2
13 port = "COM10"
14 mode = 0
15 procedure(test, port, mode, d1, d2, d3)
16 # this is an example of how a sequence would be constructed and
       initiated in the experiment macro, with a short, artificial delay.
17     s = :setBubSeq(port, mode)
18     s = :bublStep(s, d1)
19     s = :delStep(s, d2)
20     s = :altStep(s, d3)
21     :sendSeq(port, s, mode)
22     pr s
23     pause(2)
24    :runSeq(port,mode)
25
26 endproc(rslt)
27
28
29 procedure(integSingleBubble, duration, port, mode)# do one bubble step
       using the matlab handler
30
```

```
31
32 #     w2 is in us
33 #     bubblestep expects it in s
34       if duration > 1000000
35          duration = duration/1000000
36       endif
37
38      s = :setbubseq(port, mode)
39      s = :bublstep(s, duration)
40      :sendSeq(port, s, mode)
41      pause(2)
42
43 endproc(s)
44
45
46 ####  excerpt from bubble/acquire sequence
47 procedure(excerptTest)
48
49 # Bubbling
50    port = "com4"
51    mode = 0
52       ssbubble:integSingleBubble(w2, port, mode)
53
54     ## Collect the data
55
56 # Accumulate scans
57    for(scan = 0 to nrScans-1)
58     # begin the bubbling sequence
59       ssBubble:runseq(port, mode)
60     Check timing, update the parameters, run the sequence and return
       the data
61     (data,pAcq,status) = ucsRun:runSequence(guipar,ppList,pcList,
       pcIndex,scan)
62     next(scan)
63 endproc()
64
65 #######
66 ##   initialise sequence
67 #######
68 procedure(setBubSeq, port, mode)
69
70 # On spinsolve this line must be included for serial port lines to be
       opened
71    if mode == 0
72       try
73         serialmode("sync")
74       catch
75          pr "serial mode change failed - you may be using an old
       version of prospa. some commands may work incorrectly. \n"
76       endtry
77    endif
78 # mode = :getmode(mowd)
79 # cache the current folder
80    workingDir = getcwd()
81
82 # look for the file handler folder in C drive
83    try isdir("C:\ssbubble")
84       # pr "found dir"
```

```
85    catch mkdir ("C:\ssbubble")
86       pr "made dir"
87    endtry
88
89   cd("C:\ssbubble")
90
91 if mode == 1
92
93    if isfile("runSeq.txt")
94       rmfile("runSeq.txt")
95    endif
96    if isfile("sendSeq.txt")
97       rmfile("sendSeq.txt")
98    endif
99
100 endif
101
102    if isfile("sequence.txt")
103       save("sequence.txt", "")
104    else
105       save("sequence.txt", "")
106    endif
107    cd(workingDir)     #  return to the experiment folder
108   sequence = "0s"
109    if mode == 0
110    # default parameters for opening a serial connection.
111    baudrate = 9600
112    databits = 8
113    parity = "none"
114    stopbit = "1"
115    serialpars = [port, baudrate, databits, parity, stopbit]
116
117    # tries to close any open serial ports down the specified line.
118       try
119          closeserial(port)
120       pr "port closed"
121       catch
122          pr "port close fail. if using older Prospa (TN), "port" arg
     may be unneccessary"
123       endtry
124    # tries to open the serial port
125       try
126          openserial(port,baudrate,databits,parity,stopbit)
127          pr("connected to $port$\n")
128          pause(5)
129          pr "connected\n"
130       catch
131          abort("failed to open a connection to $port$")
132       endtry
133    endif
134
135 endproc(sequence)
136
137 #######
138 ##    do a bubbling step
139 #######
140
141 procedure(bublStep, sequence, btime)
```

```
142
143
144   # used to reduce length of string. limits time res to 100ms.
145   btimeMath = btime*10;
146   btimeStr = realtostr(btimeMath);
147
148   # makes an integer variable of the no. of steps in seq., then
       increments
149   count = eval(submatrix(sequence, 0, 0))
150   # pr count
151   count = count + 1
152
153   # error test for count over 9.
154   if count > 9
155       count = count - 1
156       abort("error: sequence is too long for current architecture")
157   endif
158
159   # adds the incremented step count & bubbling command with duration
       specified to the seq.
160   length = size(sequence)
161   subsequence = submatrix(sequence, 1, length-1)
162   # pr "subseq is " + subsequence
163   sequence = realtostr(count) + subsequence + btimeStr + "b";
164
165   # pr "sequence is " + sequence
166
167
168 endproc(sequence)
169
170
171
172
173 ###################
174 #   Alternate gas bubble step
175 ############
176
177 procedure(altBublStep, sequence, btime)
178   # used to reduce length of string. limits time resolution to 100ms.
179   btimeMath = btime*10;
180   btimeStr = realtostr(btimeMath);
181
182   # makes an integer variable of the no. of steps in seq., then
       increments
183   count = eval(submatrix(sequence, 0, 0))
184   pr count
185   count = count + 1
186
187   # error test for count over 9.
188   if count > 9
189   count = count - 1
190   abort("error":"sequence is too long for current architecture")
191   endif
192   # adds the incremented step count & bubbling command with duration
       specified to the seq.
193   length = size(sequence)
194   subsequence = submatrix(sequence, 1, length-1)
195   # pr "subseq is " + subsequence
```

```
196   sequence = realtostr(count) + subsequence + btimeStr + "n";
197
198   # pr "sequence is " + sequence
199
200
201 endproc(sequence)
202
203
204 ###
205 # do a delay step
206 ###
207 procedure(delStep, sequence, btime)
208   #used to reduce length of string. limits time res to 100ms.
209   btimeMath = btime*10;
210   btimeStr = realtostr(btimeMath);
211
212   #makes an integer variable of the no. of steps in seq., then
       increments
213   count = eval(submatrix(sequence, 0, 0))
214   pr count
215   count = count + 1
216
217   #error test for count over 9.
218   if count > 9
219   count = count - 1
220   abort("error":"sequence is too long for current architecture")
221   endif
222
223   #adds the incremented step count & bubbling command with duration
       specified to the seq.
224   length = size(sequence)
225   subsequence = submatrix(sequence, 1, length-1)
226   sequence = realtostr(count) + subsequence + btimeStr + "d";
227
228
229 endproc(sequence)
230
231
232 ###############
233 ##  procedure for making connection to the arduino
234 ###############
235
236 procedure(connect, port)
237 # serialmode("sync")
238 #   port = "COM4"
239
240 endproc(serialpars)
241
242
243
244 ###############
245 ##  procedure for loading the sequence and sending it to the arduino
246 ###############
247
248
249 procedure(sendSeq, port, str, mode)
250
251 if(mode == 0)
```

```
252     pr "loading sequence\n"
253     pr getcwd()
254     save("sequence.txt", str)
255     writestr = "i" + str
256     writeserial(port, writestr)
257     # pause(0.5)
258     pr "sent sequence $str$ \n"
259 
260 
261     endif
262 
263 if(mode == 1) # "matlab") #|| "Matlab" || "MATLAB")
264         save("sequence.txt", str)
265         workingDir = getcwd()
266 
267         cd "C:\ssbubble"
268         # save("newtest.txt")
269         savestr = "i" + str
270         pr str
271         pr getcwd()
272         save("sequence.txt", savestr)
273         # :filewait("sequence.txt")
274         save("sendseq.txt", "terranova gang")
275         :filewait("sendseq.txt")
276          cd = workingDir
277         pr "sequence saved\n"
278 
279 endif
280 
281 endproc()
282 
283 
284 ############
285 ##  procedure for sending an execute instruction to the ard
286 ############
287 
288 
289 procedure(runSeq, port, mode)
290 
291 workingDir = getcwd()
292 
293 if (mode == 0) #"prospa" || "Prospa" || "PROSPA" || "p" || 0)
294     # pause(2)
295     writeserial(port, "R")
296     # pr "runnng\n"
297 
298 endif
299 
300 if mode == 1
301 
302     workingDir = getcwd()
303     cd("C:\ssbubble")
304 
305     if isfile("sequence.txt")
306         # pr "okay"
307         save("runSeq.txt", "")
308         :filewait("runSeq.txt")
309         # pr "running"
```

```
310    else
311       pr("Error: no sequence file available")
312    endif
313 endif
314      #return to the experiment folder
315    cd(workingDir)
316
317 endproc()
318
319
320
321 procedure(filewait, file)
322    timer = 0;
323    while isfile(file)
324       pause(0.01)
325       timer = timer + 1
326       if timer > 3000
327
328          abort("an error has occured in saving/reading the initiator
    file. aborting due to timeout")
329          exitwhile
330       endif
331    endwhile
332    timest =  timer/100
333    pr timest
334 endproc()
335
336 procedure(initMLsave, dataDirectory, expName)
337
338  # saveloc = tnBubble:initMLsave(dataDirectory, expName)
339    workingDir = getcwd()
340
341
342 # checks for the directors
343    try isdir("C:\matlabsaves\_autosave")
344    catch mkdir ("C:\matlabsaves\_autosave")
345    endtry
346
347    cd(dataDirectory)
348       mkdir(expName)
349       cd(expName)
350    saveloc = getcwd()
351 #   pr saveloc
352    cd("C:\matlabsaves\_autosave")
353    save("autosave.txt", saveloc)
354    save("clear.txt", saveloc)
355    cd(workingDir)
356
357 endproc()
```

APPENDIX E

Arduino-style motor code

```
#include <UstepperS32.h>
#include <callbacks.h>
#include <UstepperS32.h>
UstepperS32 stepper;
/* Motor run parameters */
double runCurrent = 100; // Motor run current, % of maximum
double holdCurrent = 10;  // Motor hold current, % of maximum
double brakeCurrent = 10;
float maxAcceleration = 23250; //23250 Motor acceleration, steps/s^2
float maxDeceleration = 23250; //23250 Motor deceleration, steps/s^2
int maxVelocity = 6500; //6500
int contVelocity = 1000;
int stallSensitivity = 0; // Stall sensitivity, arbitrary (-64 to 63,
    lower number = higher sensitivity)
// Motor standby parameters
double standby_runCurrent = 0;
double standby_holdCurrent = 0;
float standby_maxAcceleration = 0;
float standby_maxDeceleration = 0;
int standby_maxVelocity = 0;
// Position definitions
int mmSteps = 6400;     //no of steps in 1 mm
int topPosition = -1;
int currentPosition;
int downPosition;
int downValue = 2475000;
int sixmTPosition;
int sixmTValue = 1190700; //2475000 - 1284300
int upPosition;
int upValue = 100000;
int setPosition;
int mapPositions;
```

```
int curPos;
int newPos;
//misc
bool contFlag;
bool movingFlag;
unsigned long startTime;
unsigned long endTime;
bool motorState1 = 0;
bool prevMotorS1 = 0;
void setup() {
  stepper.setup(NORMAL, 200);             // Initialize uStepper S32
  Serial.begin(9600);
  Serial.println("Initialising motor, finding top position!");
  stepper.moveToEnd(CW, 50, stallSensitivity);  // Find top reference
   position
  topPosition = stepper.getPosition();  // Set top reference position
  Serial.print("Top position: "); Serial.println(topPosition);  //
   Print top reference position
  calculatePositions(topPosition);
  stepper.movePosition(upPosition);

  stepper.setCurrent(runCurrent);                 // Set motor run
   current
  stepper.setHoldCurrent(holdCurrent);            // Set motor hold
   current
  stepper.setMaxAcceleration(maxAcceleration);  // Set maximum
   acceleration of motor
  stepper.setMaxDeceleration(maxDeceleration);  // Set maximum
   deceleration of motor
  stepper.setBrakeMode(COOLBRAKE);
  stepper.setMaxVelocity(maxVelocity);            // Set maximum velocity
    of motor
}
void loop() {
  motorState1 = stepper.getMotorState(POSITION_REACHED);
  bool motorState2 = stepper.getMotorState(VELOCITY_REACHED);
  bool motorState3 = stepper.getMotorState(STANDSTILL);
  char input;
  input = Serial.read();
  if (input == 'u' || input == 'd') {
    contFlag = 1;
    stepper.setMaxVelocity(contVelocity);
    Serial.println("low vel.");
  } else {
    contFlag = 0;
    stepper.setMaxVelocity(maxVelocity);
  }
  while (contFlag == 1 && Serial.available() == 0) {
    curPos = stepper.getPosition();
    Serial.println(curPos);
    if ((curPos > upPosition) || (curPos < downPosition)) {//dir == 1
   && .... dir == 0 &&
      Serial.println("Motor will crash!");
      stepper.stop(HARD);
      contFlag = 0;
      movingFlag = 0;
    }
  }
```

```
82  if (motorState1 && !prevMotorS1) {
83    startTime = millis();
84  } else if (!motorState1 && prevMotorS1) {
85    // Motor state just turned false, stop the timer
86    unsigned long elapsedTime = millis() - startTime;
87    Serial.print("Motor was on for: ");    Serial.print(elapsedTime);
     Serial.println(" milliseconds");
88  }
89  prevMotorS1 = motorState1;  // Update the previous motor state
90  switch (input) {
91    case 'u': // Move upwards continuously
92      contRotation(1);
93      break;
94
95    case 'd': // Move downwards continuously
96      contRotation(0);
97      break;
98
99    case 's': // Stop
100     stepper.stop(HARD);
101     Serial.println("Stop!");
102     curPos = stepper.getPosition();
103     Serial.print("Current position: ");
104     Serial.println(curPos);
105     break;
106   case 'e': // Shutdown. requires reinitialisation code 'i' to reset.
107     shutdownMotor();
108     break;
109   case 'm': // Perform field map
110     fieldMap();
111     break;
112   case 'c': // Calibrate positions
113     calibrateMotor();
114     break;
115   case 'p':             //position motor; position determined by next
     character in.
116     movingFlag = 1;
117     positionMotor();    //will want to include relative up & down
    commands.
118     break;
119   case 'r': // Read position
120     curPos = stepper.getPosition();
121     Serial.print("Current position: "); Serial.println(curPos);
122     break;
123   case 'z': // Move downwards by 5 mm
124     Serial.println("Moving downwards by 5 mm!");
125     bumpMotor(-5);
126     break;
127   // Move upwards by 5 mm
128   case 'y':
129     Serial.println("Moving upwards by 5 mm!");
130     bumpMotor(5);
131     break;
132   case 'b':
133     //movingFlag = 1;
134     bumpMotor(0);
135     break;
136   case 'i':
```

```
137       queryMotor();
138       break;
139   }
140 }
141 //////////
142 void calibrateMotor() {
143   //////////
144   stepper.setCurrent(runCurrent);          // Set motor run current
145   stepper.setHoldCurrent(holdCurrent);    // Set motor hold current
146   stepper.setMaxAcceleration(maxAcceleration);  // Set maximum
       acceleration of motor
147   stepper.setMaxDeceleration(maxDeceleration);  // Set maximum
       deceleration of motor
148   stepper.setBrakeMode(COOLBRAKE);
149   stepper.setMaxVelocity(maxVelocity); // Set maximum velocity of motor
150
151   Serial.println("Finding top position!");
152   stepper.moveToEnd(CW, 50, stallSensitivity);
153   topPosition = stepper.getPosition();
154   calculatePositions(topPosition);
155   Serial.print("Top position: ");
156   Serial.println(topPosition);
157   upPosition = topPosition - upValue;
158   stepper.movePosition(upPosition);
159 }
160 ////////////////////////
161 void positionMotor() {
162   ////////////////////
163   char nextin;
164   //if testing - first char is 'p'
165   nextin = Serial.read();
166   switch (nextin) {
167     case 'b': // Sample to down position
168       Serial.println("Sample down!");
169       downPosition = topPosition - downValue;
170       setPosition = downPosition;
171       stepper.movePosition(setPosition);
172       break;
173     case '6': // Sample to 6 mT position
174       Serial.println("6 mT position!");
175       sixmTPosition = topPosition - sixmTValue;
176       setPosition = sixmTPosition;
177       stepper.movePosition(setPosition);
178       break;
179     case 't': // Sample to top
180       Serial.println("Sample up!");
181       upPosition = topPosition - upValue;
182       setPosition = upPosition;
183       stepper.movePosition(setPosition);
184       break;
185     case 'a': {
186         int testPos1 = downPosition + 1500000;
187         stepper.movePosition(testPos1);
188         break;
189       }
190     case 's': {
191         int testPos2 = downPosition + 1750000;
192         stepper.movePosition(testPos2);
```

```
193         break;
194       }
195     case 'd': {
196         int testPos3 = downPosition + 2000000;
197         stepper.movePosition(testPos3);
198         break;
199       }
200     case 'f': {
201         int testPos4 = downPosition + 2250000;
202         stepper.movePosition(testPos4);
203         break;
204       }
205   }
206 }
207 ////////////////////////
208 void fieldMap() {
209   ////////////////////
210   Serial.println("Performing field map!");
211   downPosition = topPosition - downValue;
212   setPosition = downPosition;
213   stepper.movePosition(setPosition);
214   delay(5000);
215   //currentPosition = stepper.getPosition();
216   //Serial.println(currentPosition);
217 
218   mapPositions = 75;
219   for (int i = 0; i < mapPositions; i++) {
220     delay(5000);
221     stepper.moveAngle(225);
222     curPos = stepper.getPosition();
223     Serial.println(curPos);
224   }
225 }
226 ////////////////////////
227 void shutdownMotor() {
228   ////////////////////////
229   Serial.println("Shutting down!");
230   upPosition = topPosition - 100000;
231   setPosition = upPosition;
232   stepper.movePosition(setPosition);
233   delay(10000);
234   stepper.setCurrent(standby_runCurrent);                 // Set motor
       standby run current
235   stepper.setHoldCurrent(standby_holdCurrent);           // Set motor
       standby hold current
236   stepper.setMaxAcceleration(standby_maxAcceleration);  // Set standby
       maximum acceleration of motor
237   stepper.setMaxDeceleration(standby_maxDeceleration);  // Set standby
       maximum deceleration of motor
238   stepper.setBrakeMode(FREEWHEELBRAKE);
239   stepper.setMaxVelocity(standby_maxVelocity); // Set standby maximum
       velocity of motor
240 }
241 ////////////////////
242 void calculatePositions(int topPosition) {
243   ////////////////////
244   downPosition = topPosition - downValue;
245   sixmTPosition = topPosition - sixmTValue;
```

```
246   upPosition  = topPosition - upValue;
247 }
248 ////////////////////////
249 void bumpMotor(int distance) {
250   ////////////////////////
251   curPos = stepper.getPosition();
252   Serial.println(distance);
253   Serial.println(curPos);
254   if (distance == 0) {
255     String nextin;
256     // Serial.read();
257     if (Serial.available() > 0) {
258       nextin = Serial.readStringUntil('\n'); // Read the input string
     until a newline character
259       //Serial.println(nextin);
260       distance = nextin.toInt(); // Convert the input string to an
     integer
261       Serial.println(distance);
262     }
263   }
264   int  toMove = (distance * mmSteps);
265   newPos = curPos + toMove;
266   if (newPos > topPosition || newPos < downPosition) {
267     Serial.println("Motor will crash!");
268     return;
269   }
270    // startTime = millis();
271     stepper.movePosition(newPos); //      stepper.moveAngle(-225);
272 }
273
274
275 ////////////////////////
276 void queryMotor() {
277   /////////////////
278   char nextin;
279   //if testing - first char is 'i'
280   nextin = Serial.read();
281   switch (nextin) {
282     case 'a':
283       Serial.println(maxAcceleration);
284       break;
285     case 'v':
286       Serial.println(maxVelocity);
287       break;
288   }
289 }
290
291
292 //////////////////
293 void contRotation(bool dir) { //1 is up and dir 0 is down
294   ///////////////
295   String dirtext;
296   if (dir == 1) {
297     dirtext = "up";
298   }  else {
299     dirtext = "down";
300   }
301   stepper.runContinous(dir);
```

```
302   contFlag = 1;
303   //movingFlag = 1;
304   Serial.read();
305   while (contFlag == 1 && Serial.available() == 0) {
306
307     curPos = stepper.getPosition();
308     Serial.println(curPos);
309
310     if ((dir == 1 && curPos > upPosition) || (dir == 0 && curPos <
      downPosition)) {
311       Serial.println("Motor will crash!");
312       stepper.stop(HARD);
313       contFlag = 0;
314       movingFlag = 0;
315     }
316   }
317 }
```

APPENDIX F

Prospa Motor Control Code

```
    #######
# test
#######
port = "COM4"
procedure(test, port)

   :initialise_motor(port)
   # pause(5)
   pr "calibrating"
   # :command_motor(port, "cal")
#   pause(2.5)
#   :position_motor(port, "bottom")
#   pause(5)
#   :position_motor(port, "top")
#   pause(5)
#   :position_motor(port, "PTF")
#   pause(5)
   :query_motor(port, "top")
   :query_motor(port, "up")
   :query_motor(port, "bottom")
   :query_motor(port, "velocity")
   :query_motor(port, "acceleration")
   :disconnect_motor(port)
   pr "done"

endproc()

###########
#CONNECT MOTOR
###########

procedure(connect_motor, port)
```

```
33    try
34     serialmode("sync")
35    catch
36    endtry
37    baudrate = 9600
38    databits = 8
39    parity = "none"
40    stopbit = "1"
41    serialpars = [port, baudrate, databits, parity, stopbit]
42       try
43          closeserial(port)
44      pr "port closed "
45       catch
46       endtry
47
48       try
49          openserial(port,baudrate,databits,parity,stopbit)
50          pr("connected to $port$\n")
51       catch
52          pr "No device connected to $port$"
53          abort()
54       endtry
55 endproc()
56
57 procedure(disconnect_motor, port)
58       #try
59       #pr "finishing\n"
60       :command_motor(port, "end")
61       #pr "end sequence"
62       closeserial(port)
63       #pr "disconnected"
64       #catch
65
66       #endtry
67 endproc()
68
69 ##
70 #set motor pars
71 ##
72 procedure(set_motor_pars, standard_pars, command_names)
73
74 endproc()
75
76 #####
77 #position motor
78 ####
79 procedure(position_motor, port, position)
80
81    # does prospa have a switch/case function or must it be lists?
82    # read from list position name
83    # return character
84    if position == "top"
85       cmd = "t"
86    elseif position == "up"
87       cmd = "u"
88    elseif position == "PTF"
89       cmd = "p"
90    elseif position == "bottom"
```

```
91          cmd = "b"
92       endif
93       writeserial(port, "p$cmd$")
94    endproc()
95
96
97    #########
98    # COMMAND MOTOR
99    ##########
100
101   procedure(command_motor, port, command)
102   #this is a horrible way of doing this
103      list()
104      if command == "stop"
105         cmd = "s"
106      elseif command == "test"
107         cmd = "t"
108      elseif command == "up"
109         cmd = "u"
110      elseif command == "down"
111         cmd = "d"
112      elseif command == "read"
113         cmd = "g"
114      elseif command == "cal"
115         cmd = "c"
116      elseif command == "down"
117         cmd = "d"
118      elseif command == "ref"
119         cmd = "r"
120      elseif command == "end"
121         cmd = "e"
122      elseif command == "map"
123         cmd = "m"
124      elseif command == ""
125         cmd = ""
126         return()
127      else
128         cmd = command
129      endif
130      # pr "writing\n"
131      writeserial(cmd)
132      starttime = time()
133      while time() < (starttime + 1)
134         try
135             # readserial()
136         catch
137         endtry
138      endwhile
139   endproc()
140
141
142   #######
143   #GET MOTOR POSIITON
144   ########
145
146   procedure(get_motor_position, port)
147         :commmand_motor(port, "get")
148         pos = readserial()
```

```
149       pos = rmsubstr(pos, "g")
150       eval(pos)
151 endproc(pos)
152 
153 
154 ####
155 # check referencing
156 ####
157 
158 # this should check the calculated top position of the motor.
159 # If the top position has not been set this will trigger a top position
      referencing.
160 # this will fail in the unlikely event that the top position is
161 # exactly 1 microstep below the initial position.
162 
163 procedure(checkref)
164 
165    :command_motor(port, "info", ) # this probably wants to be better
      named
166    topCheck = readserial()
167    if topcheck == -1
168       :command_motor("c")
169    endif
170 
171 
172 endproc
173 
174 procedure(query_motor, port, command)
175 
176 #this is a horrible way of doing this
177    if command == "acceleration"
178       cmd = "a"
179    elseif command == "bottom"
180       cmd = "b"
181    elseif command == "current"
182       cmd = "c"
183    elseif command == "PTF"
184       cmd = "p"
185    elseif command == "top"
186       cmd = "t"
187    elseif command == "up"
188       cmd = "u"
189    elseif command == "velocity"
190       cmd = "v"
191    endif
192    writeserial("i$cmd$\r")
193    response = readserial()
194    pr response
195 
196 endproc(response)
197 
198 procedure(calculateTiming)
199    distance = currentPos - targetPos
200    endproc()
201 
202 
203 
204 procedure(initialise_motor, port)
```

```
205     try
206     :disconnect_motor(port)
207     catch
208     endtry
209     :connect_motor(port)
210     pause(1)
211     pr "connected"
212     #try
213        pr "checking"
214        check = :query_motor(port, "top")
215        pr check
216     #catch
217        check = 0
218        pr check
219     #endtry
220     if check == -1
221        pr "calibrating\n"
222        :command_motor(port, "cal")
223        check = :query_motor(port, "top")
224        pr check
225     endif
226 endproc()
```

List of Abbreviations

COD	cis,cis-1,5-cyclooctadiene
CSV	Comma Separated Values
DNP	Dynamic Nuclear Polarisation
DSP	Digital Signal Processor
EFNMR	Earth's Field NMR
FID	Free Induction Decay
IMes	1,3-bis(2,4,6-trimethylphenyl)imidazol-2-ylidine
LAC	Level Anti-Crossing
MRI	Magnetic Resonance Imaging
MePy	methylpyridine
NHC	N-Heterocyclic Carbene
NMR	Nuclear magnetic resonance
OPM	Optically Pumped Magnetometer
PHIP	*Para*-Hydrogen Induced Polarisation
PTC	Polarisation Transfer Condition
PTF	Polarisation Transfer Field
py	Pyridine
RF	Radio Frequency
RMS	Root Mean Square

SABRE	Signal Amplification By Reversible Exchange
SABRE-SHEATH	SABRE in SHield Enables Alignment Transfer to Heteronuclei
SEOP	Spin-Exchange Optical Pumping
SNR	Signal to Noise Ratio
TTL	Transistor-Transistor Logic
ULF	Ultra-Low-Field
ZF	Zero-field

Bibliography

[1] R. W. Brown, Y. C. N. Cheng, E. M. Haacke, M. R. Thompson and R. Venkatesan, *Magnetic Resonance Imaging: Physical Principles and Sequence Design: Second Edition*, 2014, **9780471720850**, 1–944.

[2] J. Keeler, *Understanding NMR Spectroscopy*, Wiley, Chichester, 2nd edn, 2010.

[3] M. H. Levitt, *Spin Dynamics*, John Wiley & Sons Ltd, Chichester, 2nd edn, 2008.

[4] Z. Huang, T. Bi, H. Jiang and H. Liu, *Phytochemical Analysis*, 2024, **35**, 5–16.

[5] S. Carlson, *Journal of Natural Products*, 2020, **83**, 3764–3764.

[6] M. Khajeh, M. A. Bernstein and G. A. Morris, *Magnetic Resonance in Chemistry*, 2010, **48**, 516–522.

[7] M. V. Gomez and A. De La Hoz, *Beilstein Journal of Organic Chemistry 13:31*, 2017, **13**, 285–300.

[8] A. L. Dunn and C. R. Landis, *Magnetic Resonance in Chemistry*, 2017, **55**, 329–336.

[9] D. A. Foley, A. L. Dunn and M. T. Zell, *Magnetic Resonance in Chemistry*, 2016, **54**, 451–456.

[10] U. Holzgrabe, R. Deubner, C. Schollmayer and B. Waibel, *Journal of Pharmaceutical and Biomedical Analysis*, 2005, **38**, 806–812.

[11] H. Schwalbe, *Angewandte Chemie - International Edition*, 2017, **56**, 10252–10253.

[12] E. Luchinat, L. Barbieri, M. Cremonini and L. Banci, *Journal of Biomolecular NMR*, 2021, **75**, 97–107.

[13] A. I. Silva Terra, D. A. Taylor and M. E. Halse, *Progress in Nuclear Magnetic Resonance Spectroscopy*, 2024, **144-145**, 153–178.

[14] E. Danieli, J. Mauler, J. Perlo, B. Blümich and F. Casanova, *Journal of Magnetic Resonance*, 2009, **198**, 80–87.

[15] A. McDowell and E. Fukushima, *Applied Magnetic Resonance*, 2008, **35**, 185–195.

[16] V. Demas and P. J. Prado, *Concepts in Magnetic Resonance Part A: Bridging Education and Research*, 2009, **34**, 48–59.

[17] E. Danieli, J. Perlo, B. Blümich and F. Casanova, *Angewandte Chemie - International Edition*, 2010, **49**, 4133–4135.

[18] K. Halbach, *Nuclear Instruments and Methods*, 1980, **169**, 1–10.

[19] H. Raich and P. Blümler, *Concepts in Magnetic Resonance Part B: Magnetic Resonance Engineering*, 2004, **23**, 16–25.

[20] A. J. Parker, W. Zia, C. W. Rehorn and B. Blümich, *Journal of Magnetic Resonance*, 2016, **265**, 83–89.

[21] T. Castaing-Cordier, D. Bouillaud, J. Farjon and P. Giraudeau, *Annual Reports on NMR Spectroscopy*, 2021, **103**, 191–258.

[22] B. Blümich, *Journal of Magnetic Resonance*, 2019, **306**, 27–35.

[23] A. D. Robinson, *PhD thesis*, University of York, York, 2022.

[24] K. Singh, E. Danieli and B. Blümich, *Analytical and Bioanalytical Chemistry*, 2017, **409**, 7223–7234.

[25] W. G. Lee, M. T. Zell, T. Ouchi and M. J. Milton, *Magnetic Resonance in Chemistry*, 2020, **58**, 1193–1202.

[26] K. Singh and B. Blümich, *TrAC Trends in Analytical Chemistry*, 2016, **83**, 12–26.

[27] P. M. Richardson, A. J. Parrott, O. Semenova, A. Nordon, S. B. Duckett and M. E. Halse, *Analyst*, 2018, **143**, 3442–3450.

[28] M. L. Hirsch, N. Kalechofsky, A. Belzer, M. Rosay and J. G. Kempf, *Journal of the American Chemical Society*, 2015, **137**, 8428–8434.

[29] A. H. Emwas, R. Roy, R. T. McKay, L. Tenori, E. Saccenti, G. A. Nagana Gowda, D. Raftery, F. Alahmari, L. Jaremko, M. Jaremko and D. S. Wishart, *Metabolites*, 2019, **9**, 123.

[30] J. H. Ardenkjær-Larsen, B. Fridlund, A. Gram, G. Hansson, L. Hansson, M. H. Lerche, R. Servin, M. Thaning and K. Golman, *Proceedings of the National Academy of Sciences of the United States of America*, 2003, **100**, 10158–10163.

[31] M. A. Bouchiat, T. R. Carver and C. M. Varnum, *Physical Review Letters*, 1960, **5**, 373.

[32] T. G. Walker and W. Happer, *Reviews of Modern Physics*, 1997, **69**, 629.

[33] B. M. Goodson, *Journal of Magnetic Resonance*, 2002, **155**, 157–216.

[34] A. S. Khan, R. L. Harvey, J. R. Birchall, R. K. Irwin, P. Nikolaou, G. Schrank, K. Emami, A. Dummer, M. J. Barlow, B. M. Goodson and E. Y. Chekmenev, *Angewandte Chemie (International ed. in English)*, 2021, **60**, 22126.

[35] M. E. Halse, *TrAC Trends in Analytical Chemistry*, 2016, **83**, 76–83.

[36] G. Buntkowsky, F. Theiss, J. Lins, Y. A. Miloslavina, L. Wienands, A. Kiryutin and A. Yurkovskaya, *RSC Advances*, 2022, **12**, 12477–12506.

[37] C. R. Bowers and D. P. Weitekamp, *Journal of the American Chemical Society*, 1987, **109**, 5541–5542.

[38] C. R. Bowers and D. P. Weitekamp, *Physical Review Letters*, 1986, **57**, 2645.

[39] R. W. Adams, S. B. Duckett, R. A. Green, D. C. Williamson and G. G. Green, *Journal of Chemical Physics*, 2009, **131**, 194505.

[40] R. A. Green, R. W. Adams, S. B. Duckett, R. E. Mewis, D. C. Williamson and G. G. Green, *Progress in Nuclear Magnetic Resonance Spectroscopy*, 2012, **67**, 1–48.

[41] T. C. Eisenschmid, R. U. Kirss, P. P. Deutsch, S. I. Hommeltoft, R. Eisenberg, J. Bargon, R. G. Lawler and A. L. Balch, *Journal of the American Chemical Society*, 1987, **109**, 8089–8091.

[42] R. V. Shchepin, A. M. Coffey, K. W. Waddell and E. Y. Chekmenev, *Journal of the American Chemical Society*, 2012, **134**, 3957–3960.

[43] R. W. Adams, J. A. Aguilar, K. D. Atkinson, M. J. Cowley, P. I. Elliott, S. B. Duckett, G. G. Green, I. G. Khazal, J. Lopez-Serrano and D. C. Williamson, *Science*, 2009, **323**, 1708–1711.

[44] A. N. Pravdivtsev, A. V. Yurkovskaya, H. M. Vieth, K. L. Ivanov and R. Kaptein, *ChemPhysChem*, 2013, **14**, 3327–3331.

[45] M. J. Cowley, R. W. Adams, K. D. Atkinson, M. C. R. Cockett, S. B. Duckett, G. G. R. Green, J. A. B. Lohman, R. Kerssebaum, D. Kilgour and R. E. Mewis, *Journal of the American Chemical Society*, 2011, **133**, 6134–6137.

[46] B. J. van Weerdenburg, S. Glöggler, N. Eshuis, A. H. Engwerda, J. M. Smits, R. de Gelder, S. Appelt, S. S. Wymenga, M. Tessari, M. C. Feiters, B. Blümich and F. P. Rutjes, *Chemical Communications*, 2013, **49**, 7388–7390.

[47] P. M. Richardson, S. Jackson, A. J. Parrott, A. Nordon, S. B. Duckett and M. E. Halse, *Magnetic Resonance in Chemistry*, 2018, **56**, 641–650.

[48] T. Theis, M. L. Truong, A. M. Coffey, R. V. Shchepin, K. W. Waddell, F. Shi, B. M. Goodson, W. S. Warren and E. Y. Chekmenev, *Journal of the American Chemical Society*, 2015, **137**, 1404–1407.

[49] S. S. Roy, K. M. Appleby, E. J. Fear and S. B. Duckett, *The Journal of Physical Chemistry Letters*, 2018, **9**, 1112–1117.

[50] O. Semenova, P. M. Richardson, A. J. Parrott, A. Nordon, M. E. Halse and S. B. Duckett, *PhD thesis*, University of York, York, 2019.

[51] P. J. Rayner, M. Fekete, C. A. Gater, F. Ahwal, N. Turner, A. J. Kennerley and S. B. Duckett, *Journal of the American Chemical Society*, 2022, **144**, 8756–8769.

[52] T. B. R. Robertson, L. H. Antonides, N. Gilbert, S. L. Benjamin, S. K. Langley, L. J. Munro, O. B. Sutcliffe and R. E. Mewis, *ChemistryOpen*, 2019, **8**, 1375–1382.

[53] T. Tennant, M. C. Hulme, T. B. Robertson, O. B. Sutcliffe and R. E. Mewis, *Magnetic Resonance in Chemistry*, 2020, **58**, 1151–1159.

[54] E. J. Fear, A. J. Kennerley, P. J. Rayner, P. Norcott, S. S. Roy and S. B. Duckett, *Magnetic Resonance in Medicine*, 2022, **88**, 11.

[55] F. Ellermann, P. Saul, J. B. Hövener and A. N. Pravdivtsev, *Analytical Chemistry*, 2023, **95**, 6244–6252.

[56] J. Yang, R. Xin, S. Lehmkuhl, J. G. Korvink and J. J. Brandner, *Scientific Reports*, 2024, **14**, 21022.

[57] S. Alcicek, E. Van Dyke, J. Xu, S. Pustelny and D. A. Barskiy, *Chemistry-Methods*, 2023, **3**, e202200075.

[58] E. T. Van Dyke, J. Eills, R. Picazo-Frutos, K. F. Sheberstov, Y. Hu, D. Budker and D. A. Barskiy, *Science Advances*, 2022, **8**,.

[59] R. E. Mewis, K. D. Atkinson, M. J. Cowley, S. B. Duckett, G. G. Green, R. A. Green, L. A. Highton, D. Kilgour, L. S. Lloyd, J. A. Lohman and D. C. Williamson, *Magnetic Resonance in Chemistry*, 2014, **52**, 358.

[60] P. TomHon, E. Akeroyd, S. Lehmkuhl, E. Y. Chekmenev and T. Theis, *Journal of magnetic resonance (San Diego, Calif. : 1997)*, 2020, **312**, 106700.

[61] P. Štěpánek, C. Sanchez-Perez, V. V. Telkki, V. V. Zhivonitko and A. M. Kantola, *Journal of Magnetic Resonance*, 2019, **300**, 8–17.

[62] J. Milani, B. Vuichoud, A. Bornet, P. Miéville, R. Mottier, S. Jannin and G. Bodenhausen, *Review of Scientific Instruments*, 2015, **86**, 024101.

[63] A. S. Kiryutin, A. V. Yurkovskaya, H. Zimmermann, H. M. Vieth and K. L. Ivanov, *Magnetic Resonance in Chemistry*, 2018, **56**, 651–662.

[64] P. Put, S. Alcicek, O. Bondar, L. Bodek, S. Duckett and S. Pustelny, *Communications Chemistry*, 2023, **6**, 1–7.

[65] M. L. Truong, T. Theis, A. M. Coffey, R. V. Shchepin, K. W. Waddell, F. Shi, B. M. Goodson, W. S. Warren and E. Y. Chekmenev, *Journal of Physical Chemistry C*, 2015, **119**, 8786–8797.

[66] A. N. Pravdivtsev, A. V. Yurkovskaya, H. M. Vieth and K. L. Ivanov, *Journal of Physical Chemistry B*, 2015, **119**, 13619–13629.

[67] D. A. Markelov, V. P. Kozinenko, A. V. Yurkovskaya and K. L. Ivanov, *Journal of Magnetic Resonance Open*, 2023, **16-17**, 100139.

[68] D. A. Barskiy, K. V. Kovtunov, I. V. Koptyug, P. He, K. A. Groome, Q. A. Best, F. Shi, B. M. Goodson, R. V. Shchepin, M. L. Truong, A. M. Coffey, K. W. Waddell and E. Y. Chekmenev, *ChemPhysChem*, 2014, **15**, 4100–4107.

[69] D. A. Barskiy, S. Knecht, A. V. Yurkovskaya and K. L. Ivanov, *Progress in Nuclear Magnetic Resonance Spectroscopy*, 2019, **114-115**, 33–70.

[70] D. A. Barskiy, M. C. Tayler, I. Marco-Rius, J. Kurhanewicz, D. B. Vigneron, S. Cikrikci, A. Aydogdu, M. Reh, A. N. Pravdivtsev, J. B. Hövener, J. W. Blanchard, T. Wu, D. Budker and A. Pines, *Nature Communications*, 2019, **10**, 1–9.

[71] J. Z. Myers, K. Buckenmaier, A. N. Pravdivtsev, M. Plaumann and R. Körber, *IEEE Transactions on Applied Superconductivity*, 2025, **35**, 1–5.

[72] R. Picazo-Frutos, R. Kircher, J. Eills, G. P. Centers, Y. Hu, J. Qin, S. J. Barker, M. Utz, K. F. Sheberstov, T. Kasajima, S. Okawa, M. Kami and D. Budker, 2025, DOI: 10.26434/CHEMRXIV-2025-DDQ2C.

[73] A. Ortmeier, K. MacCulloch, D. A. Barskiy, N. Kempf, J. Z. Myers, R. Körber, A. N. Pravdivtsev, K. Buckenmaier and T. Theis, *Journal of Magnetic Resonance Open*, 2024, **19**, 100149.

[74] F. Hill-Casey, A. Sakho, A. Mohammed, M. Rossetto, F. Ahwal, S. B. Duckett, R. O. John, P. M. Richardson, R. Virgo and M. E. Halse, *Molecules*, 2019, **24**, 4126.

[75] T. D. W. Claridge, *High-Resolution NMR Techniques in Organic Chemistry*, Elsevier, Amsterdam, 3rd edn, 2016.

[76] P. J. Hore, J. A. Jones and S. Wimperis, *NMR: The Toolkit*, Oxford University Press, Oxford, 2nd edn, 2015.

[77] S. Appelt, F. W. Häsing, U. Sieling, A. Gordji-Nejad, S. Glöggler and B. Blümich, *Physical Review A - Atomic, Molecular, and Optical Physics*, 2010, **81**, 023420.

[78] *J-Coupling (Scalar) - Chemistry LibreTexts*, `https://chem.libretexts.org/Bookshelves/Physical_and_Theoretical_Chemistry_Textbook_Maps/Supplemental_Modules_(Physical_and_Theoretical_Chemistry)/Spectroscopy/Magnetic_Resonance_Spectroscopies/Nuclear_Magnetic_Resonance/NMR_-_Theory/NMR_Interactions/J-Coupling_(Scalar)`.

[79] *UCL NMR Spectroscopy: Spin-Lattice and Spin-Spin Relaxation*, `https://www.ucl.ac.uk/nmr/sites/nmr/files/L5_3SH_web_shortened.pdf`, (Accessed: April 2025).

[80] E. Nimerovsky, K. T. Movellan, X. C. Zhang, M. C. Forster, E. Najbauer, K. Xue, R. Dervişoğlu, K. Giller, C. Griesinger, S. Becker and L. B. Andreas, *Biomolecules*, 2021, **11**, 752.

[81] K. Farahani, U. Sinha, S. Sinha, L. C. Chiu and R. B. Lufkin, *Computerized Medical Imaging and Graphics*, 1990, **14**, 409–413.

[82] K. M. Lüdeke, P. Röschmann and R. Tischler, *Magnetic Resonance Imaging*, 1985, **3**, 329–343.

[83] P. Kinsler, *Physics 2020, Vol. 2, Pages 150-163*, 2020, **2**, 150–163.

[84] R. Gimatdin, P. Kupriyanov, G. Mozzhukhin, B. Rameev and V. Chizhik, *2023 Photonics and Electromagnetics Research Symposium, PIERS 2023 - Proceedings*, 2023, 921–924.

[85] J. N. Robinson, A. Coy, R. Dykstra, C. D. Eccles, M. W. Hunter and P. T. Callaghan, *Journal of Magnetic Resonance*, 2006, **182**, 343–347.

[86] S. Appelt, F. W. Häsing, H. Kühn, U. Sieling and B. Blümich, *Chemical Physics Letters*, 2007, **440**, 308–312.

[87] M. E. Halse, P. T. Callaghan, B. C. Feland and R. E. Wasylishen, *Journal of Magnetic Resonance*, 2009, **200**, 88–94.

[88] A. Bielecki, D. B. Zax, A. M. Thayer, J. M. Millar and A. Pines, *Zeitschrift fur Naturforschung - Section A Journal of Physical Sciences*, 1986, **41**, 440–444.

[89] K. K. George Kurian, P. K. Madhu and G. Rajalakshmi, *Journal of Magnetic Resonance Open*, 2022, **10-11**, 100049.

[90] A. W. Overhauser, *Physical Review*, 1953, **92**, 411.

[91] J. Eills, D. Budker, S. Cavagnero, E. Y. Chekmenev, S. J. Elliott, S. Jannin, A. Lesage, J. Matysik, T. Meersmann, T. Prisner, J. A. Reimer, H. Yang and I. V. Koptyug, *Chemical Reviews*, 2023, **123**, 1417–1551.

[92] J. Ettedgui, K. Yamamoto, B. Blackman, N. Koyasu, N. Raju, O. Vasalatiy, H. Merkle, E. Y. Chekmenev, B. M. Goodson, M. C. Krishna and R. E. Swenson, *Angewandte Chemie - International Edition*, 2024, **63**, e202407349.

[93] V. Daniele, F. X. Legrand, P. Berthault, J. N. Dumez and G. Huber, *ChemPhysChem*, 2015, **16**, 3413–3417.

[94] T. B. R. Robertson, N. Gilbert, O. B. Sutcliffe and R. E. Mewis, *ChemPhysChem*, 2021, **22**, 1059–1064.

[95] T. R. Carver and C. P. Slichter, *Physical Review*, 1953, **92**, 212.

[96] A. Abragam and M. Goldman, *Reports on Progress in Physics*, 1978, **41**, 395–467.

[97] T. Maly, G. T. Debelouchina, V. S. Bajaj, K. N. Hu, C. G. Joo, M. L. Mak-Jurkauskas, J. R. Sirigiri, P. C. Van Der Wel, J. Herzfeld, R. J. Temkin and R. G. Griffin, *The Journal of chemical physics*, 2008, **128**, 052211.

[98] B. Plainchont, P. Berruyer, J. N. Dumez, S. Jannin and P. Giraudeau, *Analytical Chemistry*, 2018, **90**, 3639–3650.

[99] S. Pudakalakatti, P. Raj, T. C. Salzillo, J. S. Enriquez, D. Bourgeois, P. Dutta, M. Titus, S. Shams, P. Bhosale, M. Kim, F. McAllister and P. K. Bhattacharya, *Methods in molecular biology (Clifton, N.J.)*, 2022, **2435**, 169.

[100] D. Gauto, O. Dakhlaoui, I. Marin-Montesinos, S. Hediger and G. De Paëpe, *Chemical Science*, 2021, **12**, 6223.

[101] R. W. Hooper, B. A. Klein and V. K. Michaelis, *Chemistry of Materials*, 2020, **32**, 4425–4430.

[102] C. Y. Hsieh, Y. C. Lai, K. Y. Lu and G. Lin, *Biomedical Journal*, 2025, **48**, 100802.

[103] D. A. Barskiy, A. M. Coffey, P. Nikolaou, D. M. Mikhaylov, B. M. Goodson, R. T. Branca, G. J. Lu, M. G. Shapiro, V. V. Telkki, V. V. Zhivonitko, I. V. Koptyug, O. G. Salnikov, K. V. Kovtunov, V. I. Bukhtiyarov, M. S. Rosen, M. J. Barlow, S. Safavi, I. P. Hall, L. Schröder and E. Y. Chekmenev, *Chemistry (Weinheim an der Bergstrasse, Germany)*, 2017, **23**, 725.

[104] M. Kirby, L. Mathew, A. Wheatley, G. E. Santyr, D. G. McCormack and G. Parraga, *Radiology*, 2010, **256**, 280–289.

[105] J. P. Mugler, B. Driehuys, J. R. Brookeman, G. D. Cates, S. S. Berr, R. G. Bryant, T. M. Daniel, E. E. De Lange, J. H. Downs, C. J. Erickson, W. Happer, D. P. Hinton, N. F. Kassel, T. Maier, C. D. Phillips, B. T. Saam, K. L. Sauer and M. E. Wagshul, *Magnetic Resonance in Medicine*, 1997, **37**, 809–815.

[106] E. E. De Lange, T. A. Altes, J. T. Patrie, J. D. Gaare, J. J. Knake, J. P. Mugler and T. A. Platts-Mills, *Chest*, 2006, **130**, 1055–1062.

[107] P. Bachert, L. R. Schad, M. Bock, M. V. Knopp, M. Ebert, T. Großmann, W. Heil, D. Hofmann, R. Surkau and E. W. Otten, *Magnetic Resonance in Medicine*, 1996, **36**, 192–196.

[108] M. Salerno, T. A. Altes, J. P. Mugler, M. Nakatsu, H. Hatabu and E. E. de Lange, *European Journal of Radiology*, 2001, **40**, 33–44.

[109] J. L. MacLeod, H. M. Khan, A. Franklin, L. Myc and Y. M. Shim, *Diagnostics 2025, Vol. 15, Page 474*, 2025, **15**, 474.

[110] W. Pauli, *Zeitschrift für Physik*, 1925, **31**, 765–783.

[111] M. Born and J. R. Oppenheimer, *Annalen der Physik*, 1927, **389**, 457–484.

[112] A. Farkas, *Orthohydrogen, Parahydrogen and Heavy Hydrogen*, Cambridge University Press, Cambridge, 1935.

[113] C. Terenzi, S. Bouguet-Bonnet and D. Canet, *Journal of Physical Chemistry Letters*, 2015, **6**, 1611–1615.

[114] M. Matsumoto and J. H. Espenson, *Journal of the American Chemical Society*, 2005, **127**, 11447–11453.

[115] D. H. Weitzel and O. E. Park, *Review of Scientific Instruments*, 2004, **27**, 57.

[116] R. E. Svadlenak and A. B. Scott, *Journal of the American Chemical Society*, 1957, **79**, 5385–5388.

[117] K. F. Bonhoeffer and P. Harteck, *Zeitschrift für Physikalische Chemie*, 1929, **4B**, 113–141.

[118] G. E. Schmauch and A. H. Singleton, *Industrial and Engineering Chemistry*, 1964, **56**, 20–31.

[119] S. Wagner, *MAGMA*, 2014, **27**, 195–199.

[120] B. A. Tom, S. Bhasker, Y. Miyamoto, T. Momose and B. J. McCall, *Review of Scientific Instruments*, 2009, **80**, 016108.

[121] T. Theis, M. Truong, A. M. Coffey, E. Y. Chekmenev and W. S. Warren, *Journal of Magnetic Resonance*, 2014, **248**, 23–26.

[122] M. L. Truong, F. Shi, P. He, B. Yuan, K. N. Plunkett, A. M. Coffey, R. V. Shchepin, D. A. Barskiy, K. V. Kovtunov, I. V. Koptyug, K. W. Waddell, B. M. Goodson and E. Y. Chekmenev, *The Journal of Physical Chemistry. B*, 2014, **118**, 13882.

[123] L. S. Lloyd, A. Asghar, M. J. Burns, A. Charlton, S. Coombes, M. J. Cowley, G. J. Dear, S. B. Duckett, G. R. Genov, G. G. Green, L. A. Highton, A. J. Hooper, M. Khan, I. G. Khazal, R. J. Lewis, R. E. Mewis, A. D. Roberts and A. J. Ruddlesden, *Catalysis Science & Technology*, 2014, **4**, 3544–3554.

[124] E. B. Dücker, L. T. Kuhn, K. Münnemann and C. Griesinger, *Journal of Magnetic Resonance*, 2012, **214**, 159–165.

[125] K. L. Ivanov, A. N. Pravdivtsev, A. V. Yurkovskaya, H. M. Vieth and R. Kaptein, *Progress in Nuclear Magnetic Resonance Spectroscopy*, 2014, **81**, 1–36.

[126] J. R. Lindale, L. L. Smith, M. W. Mammen, S. L. Eriksson, L. M. Everhart and W. S. Warren, *Proceedings of the National Academy of Sciences of the United States of America*, 2024, **121**, e2400066121.

[127] S. S. Roy, P. Norcott, P. J. Rayner, G. G. Green and S. B. Duckett, *Chemistry - A European Journal*, 2017, **23**, 10496–10500.

[128] P. J. Rayner, J. P. Gillions, V. D. Hannibal, R. O. John and S. B. Duckett, *Chemical Science*, 2021, **12**, 5910–5917.

[129] P. Pham, C. Hilty, R. Li, . Chemcomm and C. Communication, *Chemical Communications*, 2020, **56**, 15466–15469.

[130] P. J. Rayner, B. J. Tickner, W. Iali, M. Fekete, A. D. Robinson and S. B. Duckett, *Chemical Science*, 2019, **10**, 7709–7717.

[131] O. G. Salnikov, C. D. Assaf, A. P. Yi, S. B. Duckett, E. Y. Chekmenev, J. B. Hövener, I. V. Koptyug and A. N. Pravdivtsev, *Analytical Chemistry*, 2024, **96**, 11790–11799.

[132] D. A. Barskiy, A. N. Pravdivtsev, K. L. Ivanov, K. V. Kovtunov and I. V. Koptyug, *Physical Chemistry Chemical Physics*, 2016, **18**, 89–93.

[133] M. E. Halse, B. Procacci, S. L. Henshaw, R. N. Perutz and S. B. Duckett, *Journal of Magnetic Resonance*, 2017, **278**, 25–38.

[134] K. Lin, P. TomHon, S. Lehmkuhl, R. Laasner, T. Theis and V. Blum, *Chemphyschem : a European journal of chemical physics and physical chemistry*, 2021, **22**, 1937.

[135] P. J. Rayner and S. B. Duckett, *Angewandte Chemie - International Edition*, 2018, **57**, 6742–6753.

[136] E. V. Stanbury, P. M. Richardson and S. B. Duckett, *Catalysis Science & Technology*, 2019, **9**, 3914–3922.

[137] P. J. Rayner, M. J. Burns, A. M. Olaru, P. Norcott, M. Fekete, G. G. Green, L. A. Highton, R. E. Mewis and S. B. Duckett, *Proceedings of the National Academy of Sciences of the United States of America*, 2017, **114**, E3188–E3194.

[138] B. J. Tickner and S. B. Duckett, *Chemical Science*, 2025, **16**, 1396–1404.

[139] W. Iali, G. G. Green, S. J. Hart, A. C. Whitwood and S. B. Duckett, *Inorganic Chemistry*, 2016, **55**, 11639–11643.

[140] B. v. Weerdenburg, *PhD thesis*, RU Radboud Universiteit, 2016.

[141] A. Duchowny, J. Denninger, L. Lohmann, T. Theis, S. Lehmkuhl and A. Adams, *International Journal of Molecular Sciences*, 2023, **24**, 2465.

[142] S. Lehmkuhl, M. Emondts, L. Schubert, P. Spannring, J. Klankermayer, B. Blümich and P. P. M. Schleker, *ChemPhysChem*, 2017, **18**, 2426–2429.

[143] R. Kircher, J. Xu and D. A. Barskiy, *Journal of the American Chemical Society*, 2024, **146**, 514–520.

[144] J. Z. Myers, F. Bullinger, N. Kempf, M. Plaumann, A. Ortmeier, T. Theis, P. Povolni, J. Romanowski, J. Engelmann, K. Scheffler, J. B. Hövener, K. Buckenmaier, R. Körber and A. N. Pravdivtsev, *Physical Review B*, 2024, **109**, 184443.

[145] A. N. Pravdivtsev, K. L. Ivanov, A. V. Yurkovskaya, P. A. Petrov, H.-H. Limbach, R. Kaptein and H.-M. Vieth, *Journal of Magnetic Resonance*, 2015, **261**, 73–82.

[146] P. M. Richardson, R. O. John, A. J. Parrott, P. J. Rayner, W. Iali, A. Nordon, M. E. Halse and S. B. Duckett, *Physical chemistry chemical physics : PCCP*, 2018, **20**, 26362–26371.

[147] Y. Mhaske, E. Sutter, J. Daley, C. Mahoney and N. Whiting, *Journal of Magnetic Resonance*, 2022, **341**, 107249.

[148] Y. Du, R. Zhou, M. J. Ferrer, M. Chen, J. Graham, B. Malphurs, G. Labbe, W. Huang and C. R. Bowers, *Journal of Magnetic Resonance*, 2020, **321**, 106869.

[149] NResearch, *HP225K032 data sheet*, 2022.

[150] *Arduino Mega 2560 Rev3 – 54 Digital I/O, 16 Analog Inputs, 256KB Flash — Arduino Official Store*, `https://store.arduino.cc/products/arduino-mega-2560-rev3?srsltid=AfmBOopRo-FCOwtYqIYTX7sjMc2pC7S6QAWyLCOEIMDOmkPh_WYPg_Th`.

[151] R. V. M. Packard, *Phys. Rev.*, 1954, **A93**, 941.

[152] P. T. Callaghan, A. Coy, R. Dykstra, C. D. Eccles, M. E. Halse, M. W. Hunter, O. R. Mercier and JNRobinson, *Applied Magnetic Resonance*, 2007, **32**, 63–74.

[153] M. E. Halse, A. Coy, R. Dykstra, C. Eccles, M. Hunter, R. Ward and P. T. Callaghan, *Journal of Magnetic Resonance*, 2006, **182**, 75–83.

[154] M. E. Halse and P. T. Callaghan, *Journal of Magnetic Resonance*, 2008, **195**, 162–168.

[155] B. C. Hamans, A. Andreychenko, A. Heerschap, S. S. Wijmenga and M. Tessari, *Journal of Magnetic Resonance*, 2011, **212**, 224–228.

[156] M. Rossetto, *PhD thesis*, University of York, 2022.

[157] P. T. Callaghan, . C. D. Eccles, J. D. Seymour and C. D. Eccles, *Rev. Sci. Instrum*, 1997, **68**, 4263–4270.

[158] D. A. Barskiy, K. V. Kovtunov, I. V. Koptyug, P. He, K. A. Groome, Q. A. Best, F. Shi, B. M. Goodson, R. V. Shchepin, A. M. Coffey, K. W. Waddell and E. Y. Chekmenev, *Journal of the American Chemical Society*, 2014, **136**, 3322–3325.

[159] C. Schiwek, J. Meiners, M. Förster, C. Würtele, M. Diefenbach, M. C. Holthausen and S. Schneider, *Angewandte Chemie - International Edition*, 2015, **54**, 15271–15275.

[160] K. M. Appleby, R. E. Mewis, A. M. Olaru, G. G. Green, I. J. Fairlamb and S. B. Duckett, *Chemical Science*, 2015, **6**, 3981–3993.

[161] A. N. Pravdivtsev, A. V. Yurkovskaya, P. A. Petrov, H. M. Vieth and K. L. Ivanov, *Applied Magnetic Resonance*, 2016, **47**, 711–725.

[162] A. Sakho, *PhD thesis*, University of York, 2022.

[163] A. B. Schmidt, J. Wörner, A. Pravdivtsev, S. Knecht, H. Scherer, S. Weber, J. Hennig, D. von Elverfeldt and J. Hövener, *ChemPhysChem*, 2019, **20**, 2408–2412.

[164] C. Aroulanda, L. Starovoytova and D. Canet, *Journal of Physical Chemistry A*, 2007, **111**, 10615–10624.

[165] X. Zhang, T. Karman, G. C. Groenenboom and A. van der Avoird, *Natural Sciences*, 2021, **1**, e10002.

[166] G. Buntkowsky, B. Walaszek, A. Adamczyk, Y. Xu, H.-H. Limbach and B. Chaudret, *Phys. Chem. Chem. Phys.*, 2006, **8**, 1929–1935.

[167] F. Lique, P. Honvault and A. Faure, *Journal of Chemical Physics*, 2012, **137**, 154303.

[168] S. Appelt, S. Lehmkuhl, S. Fleischer, B. Joalland, N. M. Ariyasingha, E. Y. Chekmenev and T. Theis, *Journal of Magnetic Resonance*, 2021, **322**, 106815.

[169] S. Wijnans, R. Zietara, E. Pearson, M. Boele and M. A. Reynolds, *Industrial and Engineering Chemistry Research*, 2024, **63**, 20065–20078.

[170] R. V. Chimenti, J. Daley, J. Sack, J. Necsutu and N. Whiting, *Molecules*, 2023, **28**, 2329.

[171] S. J. Elliott, C. Bengs, L. J. Brown, J. T. Hill-Cousins, D. J. O'Leary, G. Pileio and M. H. Levitt, *Journal of Chemical Physics*, 2019, **150**, 64315.

[172] A. S. Kiryutin, G. Sauer, A. V. Yurkovskaya, H. H. Limbach, K. L. Ivanov and G. Buntkowsky, *Journal of Physical Chemistry C*, 2017, **121**, 9879–9888.

[173] *Methanol Solvent Properties*, `https://macro.lsu.edu/howto/solvents/methanol.htm`.

[174] B. Scrosati, C. A. Vincent, E. M. Woolley, H. Z. Galus, C. Guminski, M. S. Shuman, J. W. Lorimer, A. L. Horvath, F. W. Getzen and H. Benzenes, *IUPAC Solubility Data Series*, Pergamon Press, Atlanta, 1981, vol. 5, p. 186.

[175] A. J. Parrott, P. Dallin, J. Andrews, P. M. Richardson, O. Semenova, M. E. Halse, S. B. Duckett and A. Nordon, *Applied Spectroscopy*, 2019, **73**, 88–97.

[176] H. J. Jeong, S. Min and K. Jeong, *Analyst*, 2020, **145**, 6478–6484.

[177] S. J. DeVience, R. L. Walsworth and M. S. Rosen, *Journal of Magnetic Resonance*, 2016, **262**, 42–49.

[178] A. N. Pravdivtsev, A. V. Yurkovskaya, N. N. Lukzen, H. M. Vieth and K. L. Ivanov, *Physical Chemistry Chemical Physics*, 2014, **16**, 18707–18719.

[179] A. N. Pravdivtsev, A. V. Yurkovskaya, H. M. Vieth and K. L. Ivanov, *Physical Chemistry Chemical Physics*, 2014, **16**, 24672–24675.

[180] S. Knecht, A. S. Kiryutin, A. V. Yurkovskaya and K. L. Ivanov, *Molecular Physics*, 2019, **117**, 2762–2771.

[181] S. S. Roy, G. Stevanato, P. J. Rayner and S. B. Duckett, *Journal of Magnetic Resonance*, 2017, **285**, 55–60.

[182] O. G. Salnikov, D. B. Burueva, I. V. Skovpin and I. V. Koptyug, *Mendeleev Communications*, 2023, **33**, 583–596.

[183] K. Sheberstov, E. Van Dyke, J. Xu, R. Kircher, L. Chuchkova, Y. Hu, S. Alvi, D. Budker and D. A. Barskiy, *Journal of Magnetic Resonance Open*, 2025, **23**, 100194.

[184] J. P. Peters, C. D. Assaf, J.-B. Hövener and A. N. Pravdivtsev, *Compact magnetic field cycling system with the range from nT to 9.4 T exemplified with 13C relaxation dispersion and SABRE-SHEATH hyperpolarization*, 2025, `https://arxiv.org/abs/2506.08711`.

[185] A. S. Kiryutin, A. N. Pravdivtsev, K. L. Ivanov, Y. A. Grishin, H. M. Vieth and A. V. Yurkovskaya, *Journal of Magnetic Resonance*, 2016, **263**, 79–91.